PSFC/RR-97-2

Global Modeling of Non-Axisymmetric Disruptions and Halo Currents in Tokamaks

J. McCarrick

Plasma Science and Fusion Center
Massachusetts Institute of Technology
Cambridge, Massachusetts 02139 USA

Global Modeling of Non-Axisymmetric Disruptions and Halo Currents in Tokamaks

by

James F. McCarrick

B. S. in Applied and Engineering Physics
Cornell University (1992)

Submitted to the Department of Nuclear Engineering
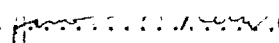in Partial Fulfillment of the Requirement for the Degree of
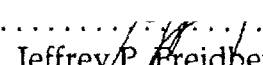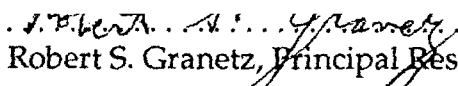
Doctor of Philosophy

at the

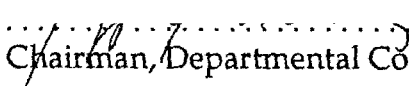MASSACHUSETTS INSTITUTE OF TECHNOLOGY

January 1997

Signature of Author . . . .
Department of Nuclear Engineering, January 15, 1997

Certified by . . . .
Jeffrey P. Freidberg, Professor of Engineering, Thesis Supervisor

Certified by. . . . .
Robert S. Granetz, Principal Research Scientist, Thesis Reader

Accepted by . . . .
Jeffrey P. Freidberg, Chairman, Departmental Committee on Graduate Students

Global Modeling of Non-Axisymmetric Disruptions and Halo Currents in Tokamaks

by

James F. McCarrick

Abstract

As tokamak plasmas become more robust with the development of increasingly advanced operating regimes, the occurrence of plasma disruptions places a greater demand on the tokamak structure. In particular, the flow of *halo currents*, large currents which appear in tokamak vacuum vessels as a result of direct contact with bulk plasma, has become a matter of increasing concern. Experimental measurements have confirmed the existence of large, toroidally asymmetric currents which flow poloidally in the wall, exerting strong localized forces on the wall as they interact with the toroidal magnetic field. A new model has been developed to study this phenomenon, based on the use of nested sheet currents to represent a disrupting plasma. This model contains the minimum number of degrees of freedom which permit the flow of continuous, non-axisymmetric poloidal and toroidal currents; furthermore, the model can be put into a compact integral formulation which allows rapid numerical solution even in the presence of complicated tokamak geometries. A fast code called TSPS-3D has been written to solve the sheet current model; the code has been matched against experimental data and used to examine basic scaling relationships of halo currents and the resulting $J \times B$ loads with plasma parameters.

Thesis Supervisor: Jeffrey P. Freidberg
Professor of Nuclear Engineering
Massachusetts Institute of Technology

Acknowledgments

In spite of what my ego would want you to believe, I did not perform this work in a vacuum! I would like to thank the many people at MIT who have offered their insight to me, and provided assistance along the way. In particular (but in no particular order), I wish to thank Joe Sorci, Manos Chaniotakis, Matt Ferri, Judy Chen, Len Myatt, Peter Titus, Steve Kochan, and Bob Pillsbury. A special tip of the hat goes to Bob Granetz for being my thesis reader, and to Professor Ian Hutchinson, who never hesitates to provide the critiques which are a necessary, albeit sometimes painful, part of the learning process.

I especially thank Ali Shajii and Constantine Hrousis, for sharing their friendship and many a long conversation on what it means to do science; and, of course, my advisor Professor Jeff Freidberg, a true role model as a scientist and as a person, and a prime example of what MIT is all about.

Finally, I could never have crossed the finish line of this marathon endeavor without knowing my wife Jennifer was there waiting for me, with all her love, patience, and support.

Dedicated to Mom and Dad - "Rock 'em and sock 'em", at last!

Table of Contents

Chapter 1.

Introduction

Chapter 1. Introduction

The goal of the international fusion program is to generate energy by means of controlled fusion reactions of light nuclei, using as an abundant fuel source two isotopes of hydrogen, called deuterium (D) and tritium (T). The most efficient way to do this is to create a *plasma* of D and T, where a plasma is a fully ionized gas with some unique physical properties, so that it is generally considered a distinct state of matter [1],[2]. By heating the plasma to very high temperatures one can "ignite" the fusion reactions. The problem is that "very high temperatures" can be hundreds of millions of degrees, so that it is not possible to confine the plasma with material walls. One technique which attempts to solve this problem is to hold the plasma in place by interacting induced electrical currents with external magnetic fields, taking advantage of the fact that a high-temperature plasma is an extremely good electrical conductor. Not surprisingly, this technique is called *magnetic confinement fusion*, or simply, magnetic fusion [3],[4].

Magnetic fusion presents an awkward design problem, since magnetic fields can only exert forces perpendicular to the field direction; it is therefore necessary to build configurations where the field wraps around on itself, forming a closed system. The most successful of these designs so far is a configuration called a *tokamak*, where the dominant magnetic field and the plasma it confines wrap around in the shape of a torus. A schematic of the basic components of a tokamak is shown in figure (1.1).

Since its inception in the late 1950s, the magnetic fusion program has produced some singularly contrasting good and bad news. The good news is that the amount of time that a hot plasma can be confined has grown by six orders of magnitude, a very impressive achievement. The bad news is that the earliest experiments could produce plasmas which lasted only microseconds, which means that modern plasmas linger only for a few seconds. In addition, the energy put into creating and confining the plasma still exceeds the energy released in D-T fusion reactions.
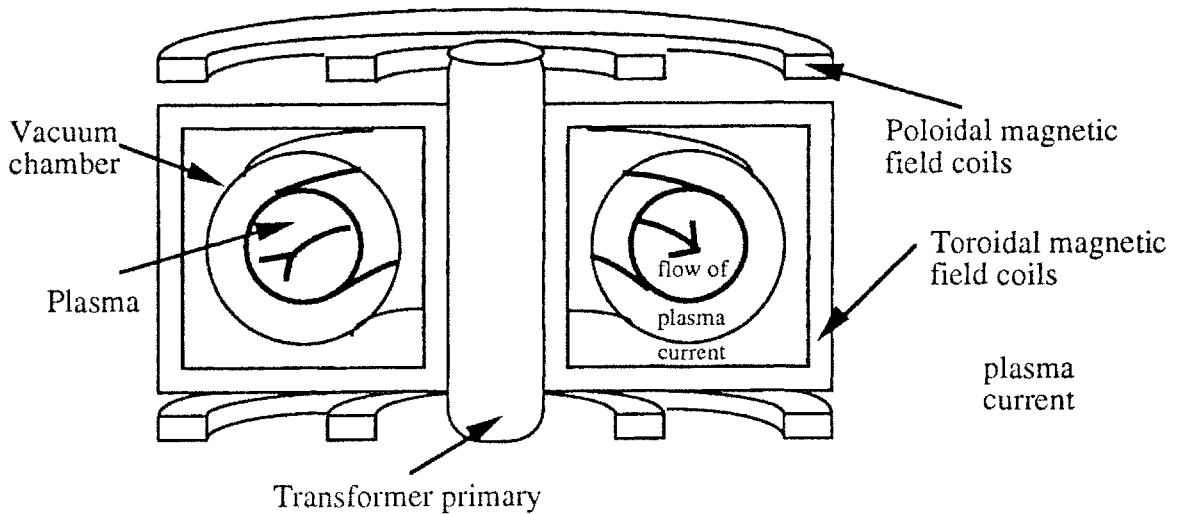
Figure 1.1. Schematic of basic tokamak components

The fact that controlled fusion has resisted the concerted attack of forty years of international effort shows that a fusion plasma can produce a wide array of befuddling behavior. It is also an indication, therefore, that the difficulties encountered in operating a tokamak experiment over several seconds are very different in nature from those encountered at the level of microseconds. In particular, tokamak plasmas have gotten robust enough that if they escape confinement, in a fast event called a *disruption*, they can damage a tokamak which is not properly designed. Thus the engineering of tokamaks is rapidly becoming an area as challenging as the physics of tokamaks, if not more so. The focus of this thesis is on one of the dominant engineering concerns in the design of modern experiments, the behavior of *halo currents* resulting from certain types of disruptions.

1.1 "Slow" Disruptions and Non-Axisymmetric Halo Currents

The macroscopic interaction between the plasma and magnetic fields is studied in the field of magnetohydrodynamics (MHD) [5]. MHD modeling is responsible for finding *equilibrium* configurations where the plasma is confined. It is one of the basic principles of MHD that if a plasma does not satisfy the MHD equilibrium conditions it can escape confinement at speeds equal to the thermal velocity of the ions in the plasma, on the order of 10^5 m/s. The "ideal MHD time" is defined to be the characteristic size of a

8

tokamak plasma divided by this velocity; for plasmas which are a few tens of centimeters across, the ideal MHD time is a few microseconds.

It is quite possible for a particular equilibrium to be *unstable*; that is, if some random perturbation changes the configuration just slightly, equilibrium is lost very rapidly. If the plasma is left to itself, the equilibrium will be destroyed on the ideal MHD time scale in a "disruption". In such disruptions where there is complete loss of confinement, the plasma loses its electrical current, thermal energy, pressure, and density, all on that fast time scale. Finding passively stable equilibria that avoid such disruptions has been one of the major accomplishments of the magnetic fusion program.

However, such "basic" disruptions are not the only kind. In order to achieve hotter and cleaner plasmas whose currents can be sustained for longer periods of time, advanced tokamaks employ novel methods of heating, fueling, and current drive, using physical effects which are outside of MHD modeling. As such, they represent perturbations which can radically change the character of an equilibrium without being as catastrophic as a "basic" disruption. The plasma can suddenly lose all of its thermal energy even though particle confinement remains relatively intact; the shape of its current profile or temperature profile can change rapidly; the transport of impurity ions can suddenly jump. Even though the dominant physical properties of the plasma state may remain unaffected, the efficiency with which the plasma undergoes fusion reactions, or its ability to do so at all, can be seriously degraded. While this type of disruption is troubling from the standpoint of fusion science, it poses little physical threat to the experiment.

Another type of disruption is especially troublesome. In an effort to improve the efficiency of a tokamak, it is necessary to employ equilibria which require dynamic feedback stabilization. All advanced tokamaks create elongated plasmas which are unstable to vertical displacements; sophisticated feedback systems are built into the external field systems to maintain stability. There are disruptions where there is a partial loss of feedback control, so that the plasma moves vertically and is gone in milliseconds. (Since the cause is generally rooted in the electronics rather than the plasma physics, this is sometimes distinguished as a "vertical displacement event," or VDE, rather than a disruption.) While this is fast relative to the entire seconds-long shot,

it is quite slow on the ideal MHD time scale; the plasma can be in a state of "quasi-equilibrium" where some if not all confinement characteristics are relatively intact. It is therefore possible for the plasma to impact the surrounding vacuum chamber while still carrying a significant fraction of its electrical current. When this current interacts with the metallic chamber and the magnetic fields, strong Lorentz forces can act on the chamber, causing structural damage.

A well-studied interaction between the plasma current and chamber is the generation of *eddy currents*, currents which attempt to preserve the original flux state in the chamber if the plasma current changes, as required by Maxwell's equations. The case of a "current dump" in a fixed-position plasma has often been examined; the resulting eddy currents tend to be distributed over fairly large regions of the chamber and also include any other nearby metallic structure. While the effects of these eddy currents on the machine are not necessarily benign, they are understood and usually well accounted for in the machine design. In a disruption where the plasma strikes the vacuum chamber, however, the eddy currents can be much more localized and dangerous.

Experimental evidence acquired over the past decade from many different tokamaks has brought to light the importance of another type of interaction, that of *halo currents* , which are usually defined to be poloidal currents which link both the vacuum vessel and the plasma, wrapping around the bulk plasma which has not yet impacted the wall (hence the "halo"). These currents flow through the wall only in the region overlapped by the plasma, and since poloidal current interacts with the large toroidal magnetic field, substantial localized forces can result. Many machines generally emerge from inspections with a list of broken bolts, loose insulating tiles, and possibly even bent plates, signifying the presence of strong local forces. The true scope of the problem was brought to the attention of the fusion community in spectacular fashion by a vertical disruption at the JET tokamak which lifted the multi-ton machine several millimeters [6]. Since that time, measurements of poloidal halo currents and estimates of the resulting forces have been undertaken at all major machines [7],[8],[9],[10]. In all cases, the peak halo currents reach significant fractions of the toroidal plasma current.

The halo current problem became of even greater concern following a recent experimental campaign on the Alcator C-MOD tokamak at MIT's Plasma Fusion Center.

10

J. Sorci and R. Granetz installed several new diagnostics specifically intended to study the poloidal and toroidal distribution of halo currents; extensive work revealed that the halo currents in C-MOD are not distributed symmetrically in the toroidal direction [10]. There is often a strong n=1 component, with peak-to-average ratios of about 2; see figures (1.2-3). This means the distribution of current over toroidal angle can be concentrated locally; since it is the current density which determines Lorentz forces, concentrated currents mean large forces. Present-day tokamaks are not designed with significant toroidal asymmetries in mind, so this additional localization of the forces is cause for worry.

1.2 Problem Statement

The appearance of large, non-axisymmetric poloidal halo currents has both an immediate and long-term effect on the fusion program. The immediate effect is felt most strongly at MIT's Alcator C-MOD experiment, which is a compact machine capable of operating at high plasma currents (2, possibly even 3 MA) and high magnetic field (9T on axis). The prospect of a potential 2MA of poloidal current interacting with inboard toroidal fields of 13T, possibly localized due to asymmetries, causes some concern about safe operation of the machine at full parameters [11],[12],[13],[14],[15]. Upgrades at other machines tried various methods of accounting for halo-current effects, although without addressing asymmetries [16],[17]. The long-term effect pertains to the designs of new experiments such as International Thermonuclear Experimental Reactor (ITER) [18], whose physical size corresponds to plasmas with large toroidal currents (21 MA) and high inboard toroidal fields. The sheer cost of an ITER-sized experiment demands a design which is robust enough to withstand all foreseeable loads.

There is a clear need for an accurate non-axisymmetric halo current model, including a rapid computational tool capable of doing parametric studies over a wide range of design parameters. Answers are desired for the following questions:

- Is the source of halo current correctly understood?
- Are there localized "toroidal halo currents" as well?
- What is the relationship between the magnitude of halo currents and plasma parameters, as well as machine geometry?

- How serious an effect is the non-axisymmetric nature of the problem?
- What are the forces on the vacuum chamber produced by the halo currents?
- Is there a reasonable way to design the vacuum chamber so as to minimize the consequences of halo currents?
- What are the effects of non-axisymmetric disruptions on eddy current behavior?

1.3 Existing Work

The halo current problem is not new, but there are no comprehensive, practical methods available to study it. Studies based on diagnostic data can have the most reliable numbers for certain quantities, but no existing machine is instrumented well enough to get *localized* measurements of *both* poloidal and toroidal current in the wall, especially with respect to the toroidal distribution [see prev. refs.].

The alternative is numerical modeling, but here, too, there are deficiencies. Experimental conditions can be reconstructed, including poloidal halo current, using codes such as EFIT [19]; however, the halo current contribution to the flux function is often modeled in simple form, and the resolution of toroidal vessel currents is often low [e.g. 9]. Usually there are a fair number of free parameters left to allow the matching of data. Finally, EFIT is a fully axisymmetric code.

For completely self-contained simulations, by far and away the most comprehensive code available in the fusion community is the Tokamak Simulation Code, TSC [20]. TSC has been used to simulate disruption events including poloidal halo currents (e.g. [21], [22]), but suffers from two drawbacks. Firstly, it is a fully axisymmetric code; secondly, it is designed to self-consistently model a complete plasma-tokamak system, including a very broad range of plasma physics. Complete non-linear flux-surface calculations are done at each time step. As a result, it requires a significant amount of time to run such a simulation, several hours on a Cray Y-MP C90. This does not lend itself to rapid parametric design studies at the engineering level.

Disruption codes intended to design vertical feedback and control systems have been written for C-MOD [23],[24], and run quite fast since the plasma is represented simply by a group of non-rigid toroidal filaments. However, filament models do not allow the flow of poloidal currents, and these particular codes are also purely axisymmetric.

There are many three-dimensional electrodynamics codes which are employed in tokamak design (e.g. [25]), but the 3-D modeling is restricted to the solid structures; the plasma is generally modeled quite simply, even as a single toroidal filament, and is assumed to behave in a fully axisymmetric way. The asymmetries of interest are in the resulting eddy currents (due to a current dump, for example), resulting from the asymmetries in the structures due to varying conductivity in the segments, access ports, and the like.

1.4 Goals of the Present Work: Global Modeling

The goal of this thesis is to introduce a novel method of modeling a plasma disruption and the generation of non-axisymmetric halo currents by using a *global* approach. The idea is to correctly capture the broad phenomena of interest, namely the distribution of halo currents and the resulting forces, without expending effort on a host of details not pertinent to the problem. No attempt will be made to study disruption physics, meaning the cause for and onset of a particular disruption; the only concern is the electrical interaction between the vacuum chamber and the plasma.

To strike a balance between the insufficiency of filament models and the extensive computation required by flux surface models, we introduce a *nested sheet current* model for the plasma. This yields the minimum number of degrees of freedom which enable the flow of continuous poloidal currents; it also allows considerable analytic reduction of the necessary equations to a compact integral form so that the only unknowns are the currents themselves. There is no need to "discretize the universe" as required by differential models with free-space boundary conditions. Since the experimental evidence on C-MOD indicates that the disruption asymmetries are dominantly n=1, the sheets themselves are constrained to remain symmetric about some axis (not necessarily that of the chamber), but are allowed to rigidly shift, tilt, rotate, contract, etc.

13

The wall is also treated as electrically thin so that it, too, can be incorporated into the sheet current model. Since asymmetries due to access ports and other variations would come in as significantly higher modes than n=1 (there are 10 ports, for example), the wall shape is treated as axisymmetric. The fact that the halo currents are observed to rotate rapidly rather than be associated with a particular toroidal location of the tokamak would seem to justify this assumption. However, the current distributions in the wall and the plasma sheets are allowed to be non-axisymmetric.

Plasma shapes and displacements can be parameterized directly from experimental data to satisfy the quasi-equilibrium condition, avoiding the need for flux-surface reconstruction at every time step of the simulation. The sole free parameter is the conductivity of the plasma; a Spitzer model based on temperature measurements will be used. All other details of plasma physics are assumed to not significantly affect the halo current problem. The global quantities of interest are the currents, magnetic fields, and associated forces; the elements of the system are the tokamak vacuum chamber, the external field system, and a mobile, current-carrying medium which is allowed to strike the wall; its motion is governed by satisfying quasi-equilibrium conditions prior to impact.

The result of this model is a fast, highly customized code called the Three-Dimensional Tokamak/Shell Plasma Simulator, or TSPS-3D. It was designed to be robust enough to handle the complicated geometry of Alcator C-MOD (see figure 1.4), but general enough to be quickly adapted to other machines, such as ITER.

A unique opportunity to benchmark the code is present in the form of the concurrent experimental work of Sorci and Granetz on C-MOD. The results of comparisons between TSPS-3D and data will be given, along with a number of numerical investigations on the dependence of halo currents and forces on various plasma parameters. Attention will be focused on the presence of toroidal halo current and strong, poloidally localized toroidal eddy currents, which C-MOD has no instrumentation to measure, and the role it plays in the loads on the vacuum chamber. It is therefore important to note that in the context of this thesis, the term *halo current* has a slightly broader definition than commonly used. It will refer to any current flowing in the vacuum vessel as a result of direct contact with bulk plasma. This extension covers

the flow of localized toroidal currents. Since these currents are localized, link both the wall and the plasma except in completely (current and displacement) axisymmetric cases, and have a significant contribution to the loads, it is felt that they must be treated on equal footing with poloidal halo current.

1.5 Organization

This thesis is composed of six chapters, organized in a "from the ground up" fashion with respect to deriving and subsequently solving the sheet-current model. A breakdown of the chapters succeeding this introduction is as follows:

Chapter 2 begins by introducing the underlying equations of the sheet current model, namely Maxwell's equations and the ideal MHD plasma model. The assumptions and approximations which enable the reduction to the sheet-current model are stated and justified, after which the specific manipulations are carried out to derive the sheet-current equations. The chapter concludes with a simple illustration about why the use of sheet currents and the resulting integral equations is more efficient than existing differential models.

Since the behavior of halo currents is linked more closely to geometry rather than simple circuit behavior, it is not easy to get a "feel" for the character of the sheet current equations, because the geometry does not enter in a simple fashion. Therefore, Chapter 3 is devoted to a series of simple examples which attempt to provide pictorial representations of basic halo current and disruption behavior. While none of the examples are quantitatively useful since they lack most of the complexities found in modern tokamaks, they do yield some qualitative understanding of experimentally observed phenomena and serve to sharpen one's intuition about what halo currents can and cannot do.

Chapter 4 deals with the methods used to solve the sheet-current equations numerically for realistic applications. The "in principle" reduction to a linear algebra system masks a number of complications, so a significant portion of this chapter is devoted to specific problems which arise due to the complicated tokamak geometries and to inherent traits of halo currents.

Chapter 5 is the "showcase" for TSPS-3D, a code custom-designed to solve the full, non-axisymmetric sheet-current equations. The code is benchmarked against the poloidal halo current data taken on Alcator C-MOD, and used to investigate halo current behavior as a function of various parameters. The focus is on the resulting forces in the vacuum chamber, and the important role of toroidal current, both halo and eddy, in driving the forces.

Chapter 6 summarizes the most important results and concludes with some suggestions for the direction of future halo current and disruption modeling.

The sheet-current model is able to achieve its economy, even for non-axisymmetric problems, because there is a great deal of analytic reduction from the general equations. While such steps are vital to the model's success in terms of CPU time, the manipulations are not new and their inclusion in the main work would greatly impair its clarity. Therefore they are relegated to Appendix A, which will be of interest to anyone pursuing related work or to anyone who appreciates the accomplishments of classical mathematics.

One of the suggestions for future work is the proper treatment of the free-boundary problem, which is handled in a rather crude fashion in TSPS-3D. Appendix B offers some thoughts on what may be the best method for incorporating elegant solutions without a major sacrifice in computation time.
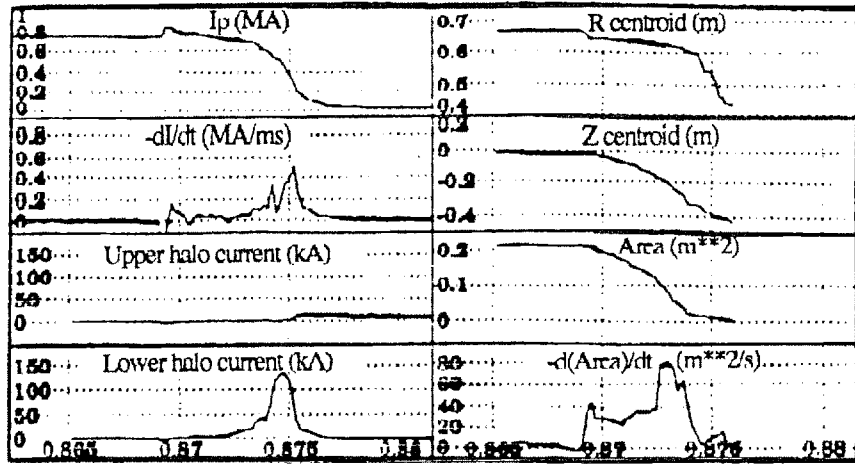
Shot 950112013

Figure 1.2. "Evolution of plasma current, halo currents, position, and cross-sectional area during [an Alcator C-MOD] disruption". This figure from reference [10].
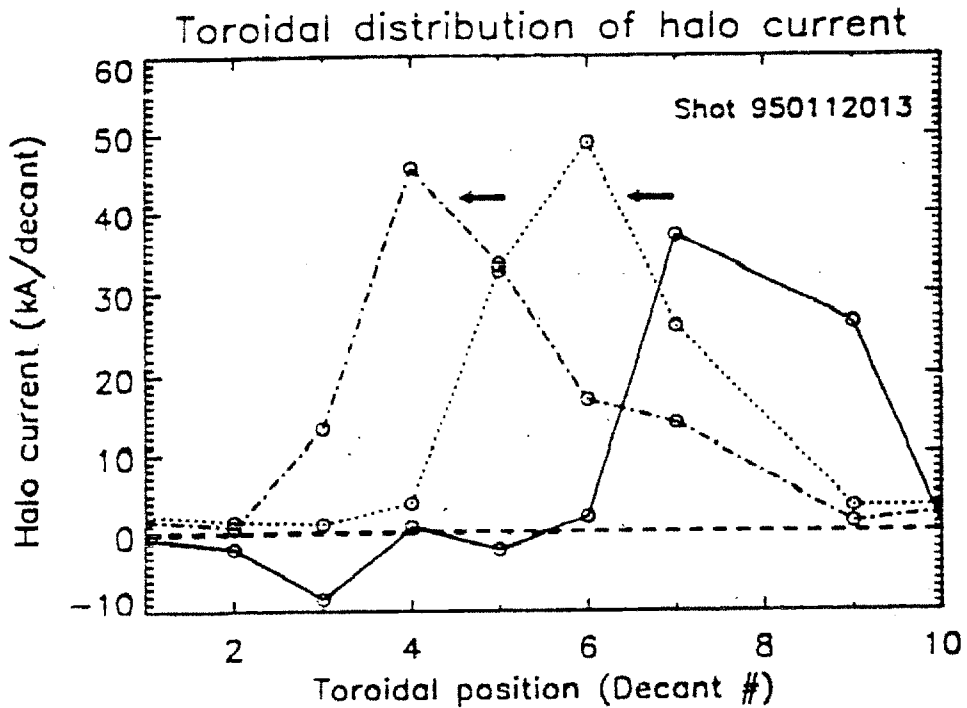

Figure 1.3. "Toroidal asymmetry and rotation of the halo currents for a [C-MOD] disruption. Three successive profiles are shown, separated by time intervals of 100μs." This figure from reference [10].
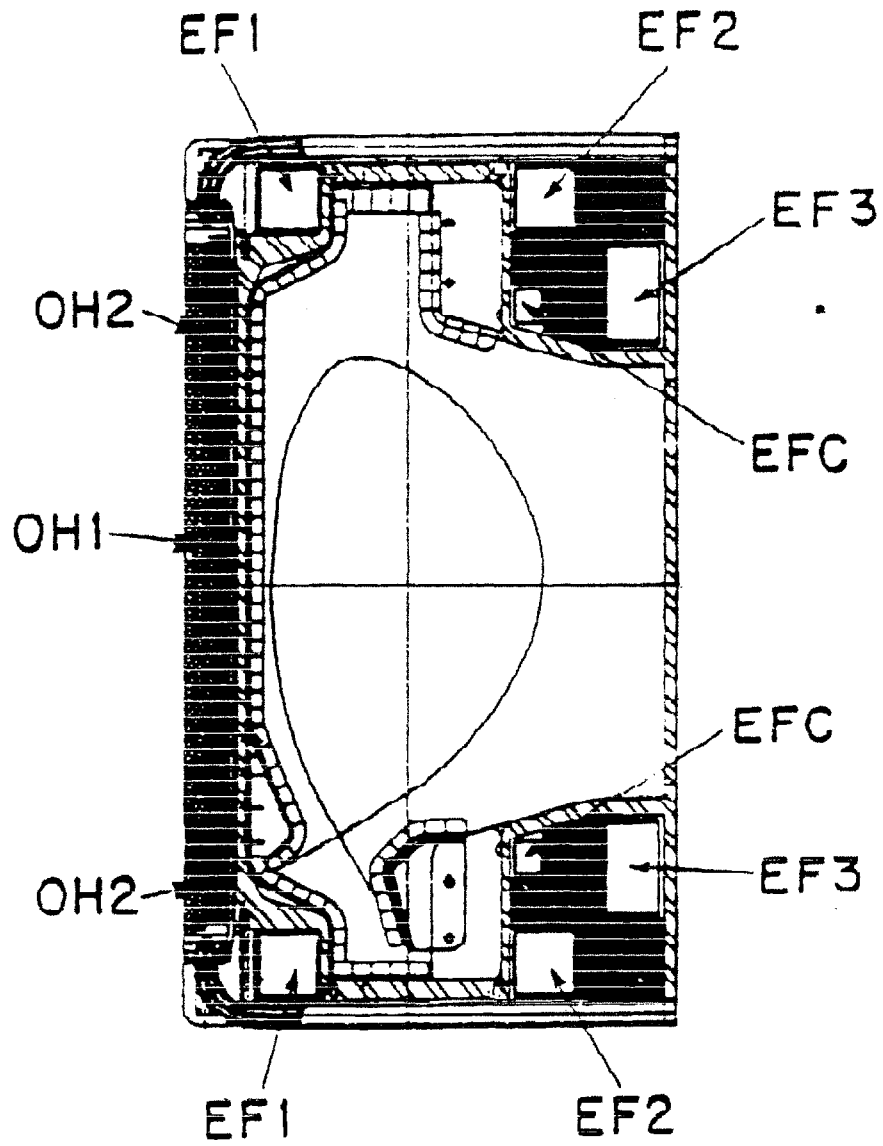
17

Figure 1.4. Cross-section of Alcator C-MOD, showing external field coils and the shape of a typical discharge.

1.6 References

1. N Krall, A. Trivelpiece. *Principles of Plasma Physics.* San Francisco Press, CA. 1986

2. K. Miyamoto. *Plasma Physics for Nuclear Fusion.* English edition: MIT Press, Cambridge, MA. 1989.

3. T. Dolan. *Fusion Research.* Vols I-III. Pergammon Press. 1982

4. R. Gross. *Fusion Energy.* Wiley. 1984

5. Jeffrey P. Freidberg. *Ideal Magnetohydrodynamics,* Plenum Press, New York, NY 1987

6. P. R. Thomas, J. A. Wesson, F. Alladio, et. al. *Plasma Physics and Controlled Nuclear Fusion Research,* 10th Conference Proceedings, Vol. 1, p.353. IAEA Vienna, 1985

7. A. Tanga, et al. "Study of Plasma Disruptions in JET and its Implications on Engineering Requirements." IEEE Proceedings of the 14th Symposium on Fusion Engineering, San Diego, 1991.

8. Y. Neyatani, et al. "Disruption Behavior of Plasma and Vacuum Vessel in JT-60U." 1992 Conference on Plasma Physics, Pt.1, pp138.

9. W.J. Strait, et al. "Observation of Poloidal Current Flow to the Vacuum Vessel Wall During Vertical Instabilities in the DIII-D Tokamak." *Nuclear Fusion,* vol. 31, no. 3, 1991

10. Granetz, Hutchinson, Sorci, Irby, LaBombard, Gwinn. "Disruptions and Halo Currents in Alcator C-MOD." *Nuclear Fusion,* vol. 36, no. 5, p545-56, 1996.

11. H. Becker. "C-MOD Vacuum Vessel Revisited: Effects of Halo Currents on the Inner Wall." MIT PFC Memo HB-3/8/94

12. H. Becker. "Reply to Comments on Halo Current Memo." MIT PFC Memo HB-4/1/94

13. H. Becker. "C-MOD Vacuum Vessel Revisited: Dynamic Effects of Halo Currents on the Inner Wall." MIT PFC Memo HB-5/26/94

14. H. Becker. "Ready-Reference Chart for Assessment of Vacuum Vessel Inner Wall Survivability Under Local Halo Currents." MIT PFC Memo HB-6/20/94

15. H. Becker and P. Titus. "C-MOD Vacuum Vessel Revisited: Effects of Local Halo Currents." MIT PFC Memo 6/21/94

16. P. Noll, R. Aigle, et al. "Stabilization of Vertical Position and Control of Plasma Shape in JET." Proceedings of the 11th Symposium on Fusion Engineering, Austin, 1985, vol.1, pp.33

17. P. Noll, L. Sonnerup, et. al. "Forces on the JET Vacuum Vessel During Disruptions and Consequent Operational Limits." *Fusion Technology*, Vol. 15, Mar. 1989

18. R. Toschi. "ITER Design Overview." IAEA-CN-53/F-1-2, *Plasma Physics and Controlled Nuclear Fusion Research*, 14th Conf. Proceedings, 1990.

19. Lao, St. John, et. al., *Nuclear Fusion* vol. 25, 1985, p.1611

20. S. Jardin, N. Pomphrey, J. Delucia. *Journal of Computational Physics*, no. 66, 1986, p.481

21. F.B. Marcus, et al. "Simulations of Control, Perturbation, Displacement and Disruption in Highly Elongated Tokamak Plasmas." *Nuclear Fusion* Vol. 30, no.8, 1990, pp.1511

22. R.O. Sayer, et al. "TSC Plasma Halo Simulation of a DIII-D Vertical Displacement Episode." ORNL/TM-12281, January 1993

23. D. A. Humphreys. *Axisymmetric Control in Tokamaks*. Ph. D. thesis, Massachusetts Institute of Technology, 1991.

24. G. Tinios. *Axisymmetric Control in Alcator C-MOD*. Ph. D. thesis, Massachusetts Institute of Technology, 1995.

25. L. Bottura, S. Chiocchio, et. al. "Eddy Currents Benchmark Analysis in ITER." *IEEE Transactions on Magnetics*, vol. 28, no.2, March 1992, p.1501

Chapter 2.

Derivation of the Sheet Current Model

Chapter 2. Derivation of the Sheet Current Model

The complexity of a tokamak and the plasma it confines was briefly indicated in the previous chapter. The effort that would be required to model such a system in full detail will appear in the present chapter in the form of the number of steps and assumptions that are required to derive the sheet current model from the general equations. The importance of global modeling techniques in fusion will become clear when it is shown how much information still remains in the sheet current model, in spite of the vast amount that was discarded to get there!

The derivation is straightforward, but does require a lengthy, and at times tedious, path to reach the end. We will begin with Maxwell's equations in general form, and a single-fluid MHD description of the plasma. These will quickly be reduced to the magneto-quasistatic (MQS) limit and a force-free plasma. Next, we switch to the integral form of Maxwell's equations, which allows a very efficient implementation of the sheet current model for a broad class of non-axisymmetric problems. Finally, a brief comparison will be made of the resulting integral equations with the corresponding differential model. Those steps of the derivation which are useful for reference but which do not really fit the context are included in Appendix A, where noted. The MKS system of units is used throughout, with the exception of temperature, as explained later in the text.

2.1 General Equations: Solid Structures

We begin by noting that the electrodynamic behavior of the solid materials in a tokamak is fully classical with respect to the electric and magnetic fields; we then make the first assumption, that the macroscopic charge and current densities are related to these fields through known constitutive laws. We will further restrict ourselves to materials which cannot be significa.tly magnetized; neither C-MOD nor ITER has an iron core. Polarization effects will be excluded for clarity, although it should be noted that the presence of polarizable materials will not affect the final model, as their behavior is unimportant in the magneto-quasistatic limit. Thus we start with the following form of Maxwell's Equations, including charge conservation:

23

$$(2.1) \quad \vec{\nabla} \cdot \vec{E}(\vec{r},t) = \frac{\rho(\vec{r},t)}{\varepsilon_o}$$

$$(2.2) \quad \vec{\nabla} \times \vec{E}(\vec{r},t) = -\frac{\partial \vec{B}(\vec{r},t)}{\partial t}$$

$$(2.3) \quad \vec{\nabla} \cdot \vec{B}(\vec{r},t) = 0$$

$$(2.4) \quad \vec{\nabla} \times \vec{B}(\vec{r},t) = \mu_o \vec{J}(\vec{r},t) + \mu_o \varepsilon_o \frac{\partial \vec{E}(\vec{r},t)}{\partial t}$$

$$(2.5) \quad \frac{\partial \rho(\vec{r},t)}{\partial t} + \vec{\nabla} \cdot \vec{J}(\vec{r},t) = 0$$

In these equations, t denotes time, $\vec{r}$ denotes spatial position, $\vec{E}$ the electric field, $\vec{B}$ the magnetic field, ρ the free charge density, $\vec{J}$ the free current density, and the permeability and permitivity of free space are given by $\mu_o = 4\pi \times 10^{-7}$ H/m and $\varepsilon_o = 8.854 \times 10^{-12}$ F/m respectively. A standard reference on these equations and electrodynamics in general is [1]; a good reference on analysis of continuum electromechanical systems, including polarizable and magnetizable media, is [2].

This set of equations must be closed with a constitutive law relating $\vec{J}$ to the other quantities. Given the presence of a wide variety of conducting materials in a tokamak, and occurrences like metal bolts piercing insulating tiles, it would seem necessary to use some complicated, anisotropic conduction model; however, *complicated* does not imply *accurate* or *useful*, and the complete information (down to the physical condition of each fastener) needed to construct such a model is not necessarily known. Thus we find it more than adequate for our purposes to introduce a linear, isotropic Ohm's Law for a stationary conductor

$$(2.6) \quad \vec{J}(\vec{r},t) = \sigma(\vec{r})\vec{E}(\vec{r},t)$$

where the electrical conductivity σ is a known material property. The possible presence of superconducting coils in the external magnetic field system is treated in this model by taking the limit $\sigma \to \infty$ in Ohm's Law if it is desired to incorporate self-consistent coil currents.

24

Finally, for completeness we give the macroscopic Lorentz force density due to the interaction between currents and magnetic fields [2],

$$\vec{F}(\vec{r},t) = \vec{J}(\vec{r},t) \times \vec{B}(\vec{r},t)$$

The given set of equations is much too general for our needs. We can simplify them greatly by introducing the relevant time and length scales and showing that we can neglect several transient effects which happen much faster than the disruption phenomena of interest.

The first set of scale lengths pertains to the observed characteristics of typical C-MOD plasmas and disruptions. Referring to the schematic in figure (2.1), we have

- r_p, the plasma minor radius, ~ 20 cm;
- r_w, the vacuum chamber minor radius, ~ 30 cm;
- the disruption time scale τ_d, the time it takes the plasma to move radially and impact the wall, typically 1-5 ms.
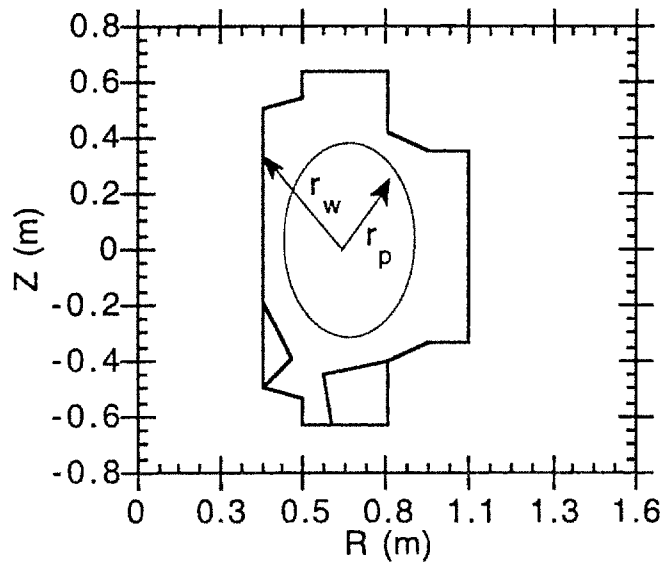
Figure 2.1. Schematic of Alcator C-MOD chamber and plasma dimensions

Inherent in Maxwell's equations in a conducting medium with length scale L, we have

- $\tau_{EM} \equiv L/c$, the electromagnetic wave transit time, where $c = 1/(\mu_o\varepsilon_o)^{1/2}$ is the speed of light in a vacuum;
- $\tau_E \equiv \varepsilon_o/\sigma$, the charge relaxation time;
- $\tau_M \equiv \mu_o\sigma L^2$, the magnetic diffusion time.

Using r_p as a length scale, and the conductivity of stainless steel ($\sigma = 1.43 \times 10^6$ mho/m), we find

$$\tau_E \sim 6.2 \times 10^{-18}\,s \ll \tau_{EM} \sim 3.3 \times 10^{-11}\,s \ll \tau_M \sim 18ms$$

Introducing a normalized gradient operator $\tilde{\nabla} = L\vec{\nabla}$ and a normalized time $\tilde{t} = t/\tau_d$, we can re-write equations (2.4) and (2.5) as

$$(2.7) \quad \tilde{\nabla} \times \tilde{\nabla} \times \vec{B} = \frac{\tau_M}{\tau_d}\frac{\partial \vec{B}}{\partial \tilde{t}} + \frac{\tau_{EM}^2}{\tau_d^2}\frac{\partial \vec{B}^2}{\partial \tilde{t}^2}$$

$$(2.8) \quad \frac{\tau_E}{\tau_d}\frac{\partial}{\partial \tilde{t}}(\tilde{\nabla}\cdot\vec{J}) + \tilde{\nabla}\cdot\vec{J} = 0$$

Therefore, to order τ_{EM}/τ_d we can neglect the displacement current contribution to (2.7), and to order τ_E/τ_d we can assume charge relaxation takes place instantly, leaving only the second term in (2.8). This de-coupling of free charge from the model means that the divergence of $\vec{E}$ given by equation (2.1) does not enter into this ordering.

Note that the value used for τ_M is not unique, since the combination length scale L^2 can take quite a range of values in this problem. For diffusion of current in the wall, $L \sim$ 1cm, we have $\tau_M \sim 0.2ms$; for the toroidal inductive time scale given roughly by the mixed length scales in $\mu_o\sigma r_p R_o$, we find $\tau_M \sim 1s$. This particular limit where

$$\tau_{M,min} < \tau_d < \tau_{M,max}$$

is called the "magneto-quasistatic" limit, and the final set of equations is given by

$$(2.9) \quad \vec{\nabla}\cdot\vec{J} = 0$$

$$(2.10) \quad \vec{\nabla}\times\vec{E} = -\frac{\partial \vec{B}}{\partial t} \qquad \text{(Faraday's Law)}$$

$$(2.11) \quad \vec{\nabla}\cdot\vec{B} = 0$$

26

$$(2.12) \quad \vec{\nabla} \times \vec{B} = \mu_0 \vec{J} \qquad \text{(Ampere's Law)}$$

$$(2.13) \quad \vec{J} = \sigma \vec{E}$$

2.2 General Equations: The Plasma

In order to choose the proper model for the roughly 10^{20} electrically charged, fairly energetic particles of various species which compose the plasma, let us identify some additional plasma parameters.

- v_p, the typical disruption velocity, $\sim \frac{r_w}{\tau_d} \sim 100$ m/s;

- n, the number density of particles per cubic meter, $\sim 10^{20}$ m^{-3};

- ρ, the mass density, $\sim 3.3 \times 10^{-7}$ kg/m^{-3} for a deuterium plasma;

- k_bT, the temperature of the plasma in the energy units *electron-volts*, eV; 1 eV is 1.6×10^{-19} joules, corresponding to 11,600 Kelvin. We take a typical "hot plasma" value to be ~ 1 keV, a typical "cold plasma" value to be ~ 50 eV.

- P, the isotropic portion of the kinetic pressure, $\sim nk_bT \sim 800$ Pa (cold) to 16 kPa (hot);

- I_p, the toroidal plasma current, ~ 1 MA

We are concerned with the bulk motions of the plasma, with length scales of order r_p, and with the macroscopic current density, also resolved only to length scales r_p. Over these distances, we can consider the plasma to be electrically neutral and to form a continuous medium, to be described by a single-fluid MHD (magnetohydrodynamic) model which conserves mass and momentum. A rigorous derivation of this model from kinetic equations and a proper justification of its realm of validity is an entire area of study, a good reference for which is [3].

The MHD equations of mass and momentum conservation are

$$(2.14) \quad \frac{\partial \rho}{\partial t} + \vec{\nabla} \cdot \rho \vec{v}(\vec{r}, t) = 0$$

27

$$(2.15) \quad \rho \frac{\partial \vec{v}}{\partial t} + \rho (\vec{v} \cdot \vec{\nabla}) \vec{v} = \vec{J} \times \vec{B} - \vec{\nabla} P$$

where $\vec{v}$ is the plasma velocity, ρ is the mass density, $\vec{J}$ the current density, $\vec{B}$ the magnetic field, and P the isotropic portion of the pressure tensor. The equation of conservation of energy will not be required, as the number of unknowns in the problem will be reduced shortly.

The disruptions in C-MOD initiate with a thermal quench, where the plasma cools from keV temperatures to ~100eV in a hundred microseconds, with little change in electrical quantities. Comparing the individual terms in the normal component of the momentum equation, we see that

$$\left| J_\theta B_\phi \right| \sim \left| J_\phi B_\theta \right| \sim \left| \frac{\mu_0 I_p^2}{2\pi^2 r_p^3} \right| \sim 4.1 \times 10^7$$

$$\left| \vec{\nabla} P \right| \sim \left| \frac{n k_b T}{r_p} \right| \sim 8 \times 10^3$$

and the pressure gradient term may be neglected. However, even for disruptions which do not have a thermal quench, we see this term may be ignored. A tokamak is a "low-β" device, that is, the ratio of kinetic to magnetic pressure $\beta = 2\mu_0 P / B_\phi^2$ is at best a few percent. Repeating the above calculation for a hot (1 keV) plasma shows

$$\left| \frac{\mu_0 I_p^2}{2\pi^2 r_p^2 n k_b T} \right| \sim 255 \gg 1$$

Thus the pressure and therefore an associated energy equation and equation of state can be neglected for the purpose of studying halo currents.

The next step in simplifying the plasma model is to restrict our attention to "slow" disruptions, where $\tau_d \sim$ 1ms and the plasma velocity is $v_p \sim$ 100m/s. We can compare the inertial term in the momentum equation to the remaining terms and we see

$$\left| \frac{\tau_d \mu_0 I_p^2}{2\pi^2 r_p^3 m_d n v_p} \right| \sim 1.2 \times 10^9 \ggg 1$$

28

By dropping inertia we greatly simplify the description of the plasma, since both the velocity and density no longer appear, leaving

$$(2.16) \quad \vec{J} \times \vec{B} = 0$$

as our only equation. However, we can no longer use this model to study plasma behavior on the ideal MHD time scale, $t_{MHD} \sim 1\mu s$, where inertia plays a considerable role in governing disruption behavior.

Equation (2.16) deserves some comment. In ideal MHD it represents the equation of equilibrium for a pressureless plasma, and yet it appears here in the context of disruptions! It must be emphasized that going from equation (2.15) to (2.16) does not imply that the plasma velocity is zero, but only that inertia does not have a major effect on the reaction of the plasma to applied forces. We will see that equations for the finite plasma velocity v_p will be recovered from (2.16) when we consider some simple examples in Chapter 3. For the cases where (2.16) applies even though the plasma is not in equilibrium, the description "force free" is often used, although it is equally misleading.

To complete the description of the plasma, we need to couple the fields with the current, and return once more to Maxwell's equations. Even a "cold" fusion plasma has a good electrical conductivity (about 7×10^5 mho/m at 50ev), with a corresponding short charge relaxation time $t_E \sim 1.3 \times 10^{-17}$ s $\ll \tau_d$ and long magnetic diffusion time $t_M \sim 9ms$ $\sim t_d$. Thus we may apply the same ordering as before to Maxwell's equations and arrive at equations (2.9)-(2.12). As before, we also need a constitutive law relating $\vec{J}$ and $\vec{E}$. In the single-fluid MHD model, this information comes from the electron momentum equation and shows that, to the extent that the plasma is not a perfect conductor, a simple Ohm's law does not apply. The effect of resistivity is not isotropic with respect to the magnetic field [4] and there are additional terms corresponding to the Hall effect and diamagnetic drifts. However, these issues are related to including some kind of transport model for the plasma, incorporating local gradient information on the pressure and temperature. Such models are notorious for adding marginal accuracy at

the cost of considerable complexity. We will avoid this poor investment by using Ohm's Law anyway, in the correct form for moving media

$$(2.17) \quad \vec{J} = \sigma_p(\vec{E} + \vec{v} \times \vec{B})$$

and by acknowledging that the plasma conductivity σ_p appears as a fitting parameter with respect to existing data, or can be provided by some simple Spitzer-like model

$$(2.18) \quad \sigma_p = 1.9 \times 10^4 \frac{T_{eV}^{3/2}}{Z \ln(\Lambda)} \text{ mho/m}$$

where the temperature must be treated as a known quantity.

Note that in equation (2.17), the plasma velocity appears in a fashion consistent with the ordering:

$$\left| \frac{J}{\sigma_p} \right| \sim \left| \frac{I_p}{\sigma_p \pi r_p^2} \right| \sim 150$$

$$\left| \vec{v} \times \vec{B} \right| \sim \left| v_p B_\phi \right| \sim 500$$

As a final comment about our description of the plasma, note that by using Ohm's Law to eliminate $\vec{E}$ from Maxwell's equations, we have specified both the divergence and curl of $\vec{J}$ and $\vec{B}$ and therefore, by Helmholtz's theorem, determined them uniquely as vector fields. Where, then, is the room to enforce equation (2.16)? This ties in to the plasma velocity and the "free boundary" equilibrium problem, which will be addressed at various points in later chapters.

2.3 The Sheet Current Model

The system of equations we have so far consists of (2.9)-(2.12) in the solid structures and the plasma, and vacuum regions with $\vec{J}$ set to zero; (2.13) in solid structures; (2.16) and (2.17) in the plasma. Across the interfaces of these various regions we have the associated boundary conditions

30

$$(2.19) \quad \left[\hat{n} \cdot \vec{J} \right] = 0$$

$$(2.20) \quad \left[\hat{n} \cdot \vec{B} \right] = 0$$

$$(2.21) \quad \left[\hat{n} \times \vec{B} \right] = \mu_0 \vec{K}$$

where $\hat{n}$ is a unit vector normal to the bounding surface. This system is three-dimensional, non-linear, and coupled across multiple regions with moving boundaries. It contains the right amount of physics for our applications, but is still quite complicated to solve. In order to achieve our goal of a model which is suitable for design and parametric studies, we need to narrow the scope of application, and very carefully tailor the method of solution.

To define the scope of the sheet current model, we need to deal with three issues: describing the geometry; identifying which tokamak components we are most concerned with; and classifying the different types of toroidal asymmetries which enter the problem. Unlike the previous section, we will not introduce a formal ordering to further simplify the equations; we will simply identify what can be handled elegantly in the model, and what cannot.
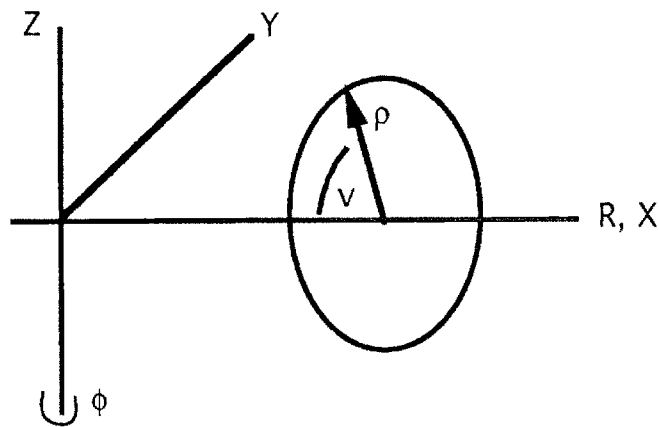
Figure 2.2. Various coordinate systems used in the model

First, let us consider the geometry of a tokamak plasma. Even in the presence of significant asymmetries, the system is dominantly toroidal. The poloidal cross section of the tokamak, however, can be quite complicated; consider the C-MOD design with its

31

intricate divertor structure. The most convenient system to describe this is a cylindrical system (R,ϕ,Z), where the poloidal plane is mapped into the (R,Z) plane. (See figure 2.2). To describe the plasma, it useful to have a local TNB (tangent/normal/binormal) frame, relative to the surface of the plasma and centered at the origin of the poloidal plane in a toroidal system. This system, as labeled in the figure, is given by coordinates (ρ,v,ϕ); in place of the usual poloidal angle coordinate θ, we use an angle defined clockwise from the inboard side of the plasma, v. This gives a right-handed system where the ϕ coordinate maps to the cylindrical system without any change in sign, and points in the plasma can be mapped by transformations $R = R(ρ,v)$, $Z = Z(ρ,v)$. Finally, to handle asymmetries, it will be necessary to resort to a Cartesian system for some intermediate calculations; this is given by sharing the Z axis with the cylindrical system, and rotating the X-Y plane so that the X axis lies along ϕ=0.

Second, let us identify what parts of the tokamak structure concern us most. The closest metallic structure to the plasma, and therefore the most strongly coupled, is the wall of the vacuum chamber (including the contours into divertor chambers and limiters). This is also the structure which suffers the heaviest electrodynamic loads, since it can be in contact with bulk plasma and therefore carry halo current. While there is considerable metallic structure outside the chamber, and by design the chamber does not serve as electromagnetic shielding, we will assume that the dominant interaction is with the wall, and limit our attention to that. The exception, of course, is the coil system which generates the external magnetic fields. At the lowest level, we must know the coil currents in order to model the $\vec{J} \times \vec{B}$ interaction of the plasma with the field, and of I_p with the transformer. At a higher level, it is desirable to solve self-consistently for the coil currents given an external voltage and a set of feedback laws, to model disruption control as well as the structural loads on the coils themselves. We will not, however, introduce this complication with respect to the toroidal field coils. The massive inductance of the TF system and resulting slow response time ($\tau_{L/R} \sim 4s$) means we may treat the toroidal field as constant in time. Thus, our tokamak model will consist of the vacuum chamber and the complete set of poloidal field and transformer coils, immersed in a known toroidal field.

Finally, we come to non-axisymmetric effects. We note that our simplified model of a tokamak is in fact largely axisymmetric about the Z-axis. We will not be concerned with

very localized eddy currents in the external PF coils, but only with the zero-order toroidal current. While vacuum chambers are not truly axisymmetric, the asymmetries appear in high order; for example, Alcator C-MOD has ten-fold symmetry about its access ports. Since we will be focusing on lower-order asymmetries, we will treat the vacuum chamber as being perfectly symmetric, but capable of carrying non-axisymmetric currents.

Tokamak plasmas are, by design, fully axisymmetric when in equilibrium. During a disruption, two types of asymmetry can occur. The first is for the displacement of the plasma to be symmetric with respect to the vacuum chamber, but the distribution of currents in the plasma become asymmetric. The second type is asymmetric in both displacement and current distribution. The first type does not add any special complication to the model, and can be handled in full. The second type presents a number of difficulties, as follows:

- The contact area between the wall and the plasma can occur in unconnected, irregularly shaped patches which vary rapidly in time. Finding these patches is a very complex task; to do so efficiently would be a considerable piece of work by itself.
- The plasma can be rotating toroidally at frequencies up to several kilohertz. When the plasma hits the wall at some local strikepoint, there is no reason to believe that the force-free model holds for the region which lies "ahead" (in toroidal angle) of area which has been scraped off by the wall; as the plasma continues to rotate, this region rapidly becomes large.
- There is no efficient method for calculating the magnetic fields generated by an irregularly shaped three-dimensional geometry.

Because of the first two points, we will not study disruptions of this type past the point in time when the plasma strikes the wall. This still leaves plenty of useful information relating to growth rates and loads due to non-axisymmetric eddy currents in the vacuum chamber. Because of the third point, we will further restrict ourselves to displacements which maintain an axis of symmetry with respect to the plasma ("n=1" modes, in the nomenclature of MHD stability); this consists of all manner of rigid non-axisymmetric displacements, such as shift, tilts, and rotations, as well as pure

33

axisymmetric major and minor radial motion. Denoting the plasma system by S' and the wall system by S, we note that transforming a field or position vector between the two frames can be done with minor algebraic operations, detailed in Appendix A, provided the displacement between the origins of the two Cartesian systems, $(\Delta_x, \Delta_y, \Delta_z)$, is known, as well as the rotation of the Cartesian S' with respect to S $(\phi_{xz}, \phi_{yz}, \phi_{xy})$. Toroidal rotation of the plasma is contained entirely in ϕ_{xy} (see figure 2.3).

1. Translate frame S   2. Rotate in XZ plane

3. Rotate in YZ plane   4. Rotate to S' in XY plane
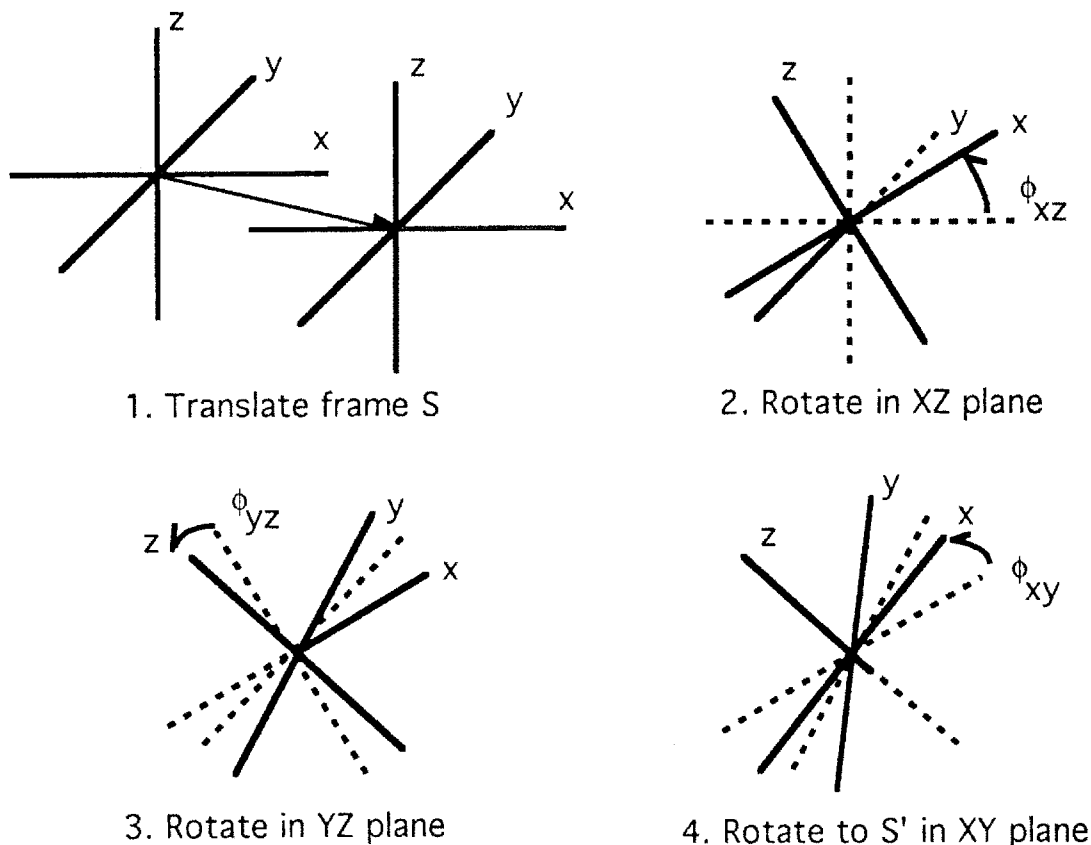
Figure 2.3. Constructing the plasma's locally axisymmetric frame

The restrictions outlined above mean that halo currents can only be studied in the context of the first type of asymmetry. This would seem to be a significant restraint. However, the measurements of the toroidal distribution of halo current show that the "peaking factor", the ratio of peak to zero-order (symmetric) current in toroidal angle, is generally not much higher than 3. This is an indication that the plasma displacement cannot be too strongly non-axisymmetric, as partial contact with the chamber would

result in a small symmetric component to the current (not zero, due to eddy currents), driving the peaking factor very much higher than 3.

We have now established all the foundations necessary to derive the sheet current model. Our goal is to show that the given tokamak/plasma model can be adequately described by assuming all conductors come in the form of thin sheets, with all currents necessarily constrained to the plane of the individual sheets. This model, which can be justified fairly rigorously, strikes an elegant balance between filament models, which do not allow the flow of continuous poloidal currents, and fully distributed conductors, which have too many degrees of freedom to be solved rapidly.
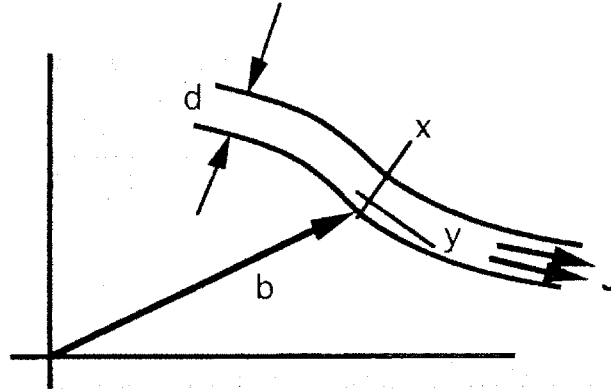
Figure 2.4. Local coordinate frame in a thin sheet

Consider a toroidally axisymmetric conducting sheet with poloidal thickness d and radius of curvature b, carrying a current density $\vec{J}$ (see figure 2.4). We expand the coordinate system into a local Cartesian system, and introduce the scale length d in the $\hat{e}_x$ direction and b in the $\hat{e}_y$ direction. We again normalize time to the disruption time scale $\tilde{t} = t/\tau_d$ and introduce the magnetic diffusion time $\tau_M = \mu_0 \sigma d^2$. Taking σ to be constant, we eliminate $\vec{E}$ from Maxwell's equations, take the curl of (2.10) and substitute (2.9) and (2.11). The result is a diffusion equation for $\vec{J}$, which in normalized form is

$$(2.22) \quad \frac{\partial^2 \vec{J}}{\partial \tilde{x}^2} + \frac{d^2}{b^2} \frac{\partial^2 \vec{J}}{\partial \tilde{y}^2} = \frac{\tau_M}{\tau_d} \frac{\partial \vec{J}}{\partial \tilde{t}}$$

We assume that the sheet is thin both geometrically (d/b << 1) and electromagnetically (τ_M/τ_d << 1). The leading order behavior of this equation

35

$$\frac{\partial^2 \overrightarrow{J}}{\partial \tilde{x}^2} = 0$$

suggest letting $\overrightarrow{J}(x,y,t) = \overrightarrow{J}_o(y,t) + \overrightarrow{J}_1(x,y,t) + \ldots$, where $\left| \overrightarrow{J}_o / \overrightarrow{J}_1 \right| \sim \tau_M / \tau_d$. The boundary condition (2.19) forces $\hat{e}_x \cdot \overrightarrow{J}_o$ to be zero, so that the leading-order current is purely tangential to the sheet.

We define a "sheet current" as $\overrightarrow{K} = d \overrightarrow{J}_o$. Note that this process (including ϕ dependence) takes a set of three unknowns in three spatial variables and reduces it to two unknowns in two spatial variables, a significant reduction.

For a 1 cm thick stainless-steel vacuum chamber with average minor radius b ~ 30cm, we see d/b ~ 0.03 and τ_M / τ_d ~ 0.1, so that the chamber may be modeled with fair accuracy as a thin sheet.

To apply this model to the plasma, note that equation (2.16) implies the existence of closed poloidal flux surfaces, labeled by their flux value ψ, such that

$$(2.23) \quad \overrightarrow{J} \cdot \overrightarrow{\nabla} \psi = 0$$

Recall we consider only those cases where the plasma geometry is toroidally axisymmetric in some coordinate system (not necessarily that of the vacuum chamber). We can parameterize the shape of a flux surface in cylindrical coordinates using the poloidal coordinate from the TNB frame: $R = R(v)$, $Z = Z(v)$, $\phi = \phi$. From these, we can create the unit vectors describing the TNB frame:

$$(2.24) \quad \hat{e}_v = \frac{1}{Q}\left(\frac{dR}{dv}\hat{e}_R + \frac{dZ}{dv}\hat{e}_Z\right), \text{ tangent}$$

$$(2.25) \quad \hat{e}_\rho = \frac{1}{Q}\left(-\frac{dZ}{dv}\hat{e}_R + \frac{dR}{dv}\hat{e}_Z\right) \text{ normal}$$

$$(2.26) \quad \hat{e}_\phi = \hat{e}_\phi, \text{ binormal}$$

36

$$(2.27) \quad Q \equiv \sqrt{\left(\frac{dR}{dv}\right)^2 + \left(\frac{dZ}{dv}\right)^2}$$

and map the current to this local system:

$$(2.28) \quad J_v = \hat{e}_v \cdot \vec{J}, \qquad J_\phi = \hat{e}_\phi \cdot \vec{J}, \qquad J_\rho = 0$$

where the last equation holds from (2.23). Thus, independent of the magnetic diffusion time in the plasma, we can approximate the plasma by a number of sheet currents (say, N of them), defined by

$$(2.29) \quad \vec{J}(\rho,v,\phi,t) \approx \sum_{i=1}^{N} \frac{\vec{K}_i(v,\phi,t)}{\Delta} \delta(\rho - \rho_i), \quad \Delta \equiv r_p(v=0)/N$$

where $\delta(\rho - \rho_i)$ represents the Dirac delta function in the minor radial, locally normal coordinate ρ. Quite accurate representations can be achieved with modest N, as we will see.

Finally, to incorporate the external field coils, we note that all we are concerned with are the axisymmetric toroidal currents flowing in the coils. Thus the coils will be represented by N_c bundled filaments, from whose geometries and material properties we can calculate resistances and inductances.

What we have achieved is elimination of the independent variable ρ by discretizing it into a small number of sheet currents, and of the dependent variable J_ρ by taking advantage of the physical system and using a flexible coordinate system. The last major step in completing the model is to carefully choose the method of solution, so that it will turn out that the set of sheet currents is the complete set of electromagnetic unknowns; no further degrees of freedom will be necessary to describe the magnetic fields.

At this point it will be necessary to establish some notational conventions. Dependence on spatial variables will be suppressed unless absolutely necessary; while several new sub- and superscripts will be introduced and used with consistent meaning, in any particular equation only those necessary for clarity will be shown. To distinguish the

37

different domains, "w" will denote a wall quantity, "p" a plasma quantity, and "c" a quantity in the external coil system. Components of vector quantities will be labeled by subscripts from the particular coordinate system (R,ϕ,Z), (ρ,v,ϕ), or (x,y,z). To single out a particular sheet current in the plasma, the subscript i (ranging from 1 to N) will be used; no subscript will be used, however, to distinguish the associated local TNB coordinates. The wall system S and plasma system S' will be distinguished where necessary. While these conventions may sound confusing, the result will be considerably more clear than if all subscripts were listed in all cases.

The goal of the last step in this derivation is to use Green's functions to rewrite our system of differential equations as a system of integral equations. The advantage of the integral formulation is four-fold:

- The irregular geometry, which is difficult to discretize for differential operators, is inherently easier to handle with integration.
- By taking advantage of the symmetries in the problem, some of the integrals can be carried out analytically, saving considerable numerical computation.
- The magnetic field is eliminated as a separate degree of freedom, which also completely eliminates the vacuum regions from the computational domain.
- All derivatives normal to the surfaces, which are not clearly defined, will be eliminated.

We begin by using equation (2.11) to write $\vec{B}$ as the curl of another vector $\vec{A}$, called the vector potential:

$$(2.30) \quad \vec{B} = \vec{\nabla} \times \vec{A}$$

The divergence of $\vec{A}$ can be chosen arbitrarily without changing $\vec{B}$, so we choose for convenience

$$(2.31) \quad \vec{\nabla} \cdot \vec{A} = 0$$

Using these two equations in (2.12) yields

$$(2.32) \quad \vec{\nabla}^2 \vec{A} = -\mu_0 \vec{J}$$

Through the use of a *Green's dyadic* $\overline{\overline{G}}$, this equation can be solved in closed form, for $\vec{A}$ in terms of $\vec{J}$, for any geometry, based only on the assumption that *all* sources of current (distributed, surface currents, and filaments) are included in $\vec{J}$:

$$(2.33) \quad \vec{A}(\vec{r}) = \iiint \overline{\overline{G}}(\vec{r}, \vec{r}') \cdot \vec{J}(\vec{r}') \, d\vec{r}'$$

A complete derivation of this result, as well as expressions for $\overline{\overline{G}}$, is given Appendix A. This result is extremely useful since it links all the different domains into a single operator; the presence of delta functions with the sheet currents and with the filaments representing external coils means the volume integral can be immediately reduced. Including the contribution from the toroidal field B_ϕ, we can calculate $\vec{A}$ at any time from the expression

$$(2.34) \quad \vec{A}(\vec{r}) = \iint \overline{\overline{G}}_A \cdot \left(\vec{K}_w + \sum_{i=1}^{N} \vec{K}_p \right)' \, dv' \, d\phi' + \sum_{i=1}^{Nc} \hat{G}_A(\vec{r}) \, I_c - RB_\phi \ln R \, \hat{e}_Z$$

And from equation (2.30) we can write

$$(2.35) \quad \vec{B}(\vec{r}) = \iint \overline{\overline{G}}_B \cdot \left(\vec{K}_w + \sum_{i=1}^{N} \vec{K}_p \right)' \, dv' \, d\phi' + \sum_{i=1}^{Nc} \hat{G}_B(\vec{r}) \, I_c + B_\phi \, \hat{e}_\phi$$

where $\hat{G}_B = \vec{\nabla} \times \hat{G}_A$ and $\overline{\overline{G}}_B = \vec{\nabla} \times \overline{\overline{G}}_A$, the curl to be taken in the unprimed coordinates.

The transformation of the equations is almost complete. The remaining step is to integrate (2.10) over a surface, which at this stage is arbitrary save that it must be bounded by a contour that lies entirely on a current sheet:

39

$$(2.36) \quad \int \left(\vec{\nabla} \times \vec{E} \right) \cdot \hat{n} \, dA = - \int \frac{\partial \vec{B}}{\partial t} \cdot \hat{n} \, dA$$

Stokes' theorem may be used to re-write the left hand side as a line integral around the bounding contour:

$$(2.37) \quad \int \vec{E} \cdot d\vec{l} = - \int \frac{\partial \vec{B}}{\partial t} \cdot \hat{n} \, dA$$

Since the contour does lie on a current sheet, we can substitute Ohm's law, keeping in mind that the surface can be moving:

$$(2.38) \quad \int \left(\frac{\vec{K}}{\sigma \Delta} - \vec{v} \times \vec{B} \right) \cdot d\vec{l} = - \int \frac{\partial \vec{B}}{\partial t} \cdot \hat{n} \, dA$$

Rearranging terms and using (2.11) to add the last term on the right hand side,

$$(2.39) \quad \int \frac{\vec{K}}{\sigma \Delta} \cdot d\vec{l} = - \int \frac{\partial \vec{B}}{\partial t} \cdot \hat{n} \, dA + \int \left(\vec{v} \times \vec{B} \right) \cdot d\vec{l} - \int \left(\vec{\nabla} \cdot \vec{B} \right) \vec{v} \cdot \hat{n} \, dA$$

we now apply the generalized Leibnitz rule to re-write the entire right hand side under a total time derivative. This step is crucial and has several computational advantages since the coordinate frame of the integration is always that of a particular sheet, regardless of motion:

$$(2.40) \quad \int \frac{\vec{K}}{\sigma \Delta} \cdot d\vec{l} = - \frac{d}{dt} \int \vec{B} \cdot \hat{n} \, dA$$

Using (2.30) and Stokes' theorem once more, we reach the desired form:

$$(2.41) \quad \int \frac{\vec{K}}{\sigma \Delta} \cdot d\vec{l} = - \frac{d}{dt} \int \vec{A} \cdot d\vec{l}$$

Recognizing that the flux ψ linked by a given contour is $\int \vec{A} \cdot d\vec{l}$, we see that we have in fact reached the traditional form of Faraday's Law where both sides of the equation are evaluated in the same reference frame,

$$(2.42) \quad \int \vec{E} \cdot d\vec{l} = -\frac{d\psi}{dt}$$

The sheet current equations are finally complete. On a given sheet with conductivity σ (σ_w or σ_p), thickness Δ (d_w or Δ_i), and current $\vec{K}$ ($\vec{K}_w$ or $\vec{K}_{p,i}$), we have the system

$$(2.43) \quad \vec{\nabla} \cdot \vec{K} = 0$$

$$(2.44) \quad \int \frac{\vec{K}}{\sigma \Delta} \cdot d\vec{l} = -\frac{d}{dt} \int \left(\left(\iint \overline{\overline{G}}_A \cdot \left(\vec{K}_w + \sum_{i=1}^{N} \vec{K}_p \right)' dv'\, d\phi' + \sum_{i=1}^{N_c} \hat{G}_A(\vec{r}) I_c - RB_\phi \ln R\, \hat{e}_z \right) \cdot d\vec{l}$$

Of the three components of (2.16) in the plasma, only two remain unique:

$$(2.45) \quad K_v B_\phi - K_\phi B_v = 0$$

$$(2.46) \quad B_p = 0$$

For the coil currents, we define the i th coil current $I_{c,i} = \int \vec{J} \cdot \hat{n}\, dA_i$, the self-inductance $L_i = \int \hat{G}_{A,i}(\vec{r}) I_{c,i}\, dA_i$, mutual inductance $M_{ij} = \int \hat{G}_{A,j}(\vec{r}) I_{c,j}\, dA_i$, and denote the resistance by $R_{c,i}$ and applied voltage by $V_{c,i}$. There are then i equations of the form

$$(2.47) \quad I_{c,i} R_{c,i} = V_{c,i} - L_i \frac{dI_{c,i}}{dt} - \sum_{i \neq j} M_{ij} \frac{dI_{c,j}}{dt} - \frac{1}{A_i} \iint \left(\vec{A}_w + \vec{A}_p \right) \cdot \hat{e}_\phi\, dA_i$$

where $\vec{A}_w$ and $\vec{A}_p$ refer to the contributions to the total vector potential from the wall and plasma sheets in (2.34).

Thus, the basic set of equations (assuming for the moment that the PF system is specified) just (2.43-46), repeated here for easier visibility:

41

$$(2.43) \quad \vec{\nabla} \cdot \vec{K} = 0$$

$$(2.44) \quad \int \frac{\vec{K}}{\sigma \Delta} \cdot d\vec{l} = -\frac{d}{dt} \int \left(\iint \overline{\overline{G}}_A \cdot \left(\vec{K}_w + \sum_{i=1}^{N} \vec{K}_p \right)' dv' \, d\phi' + \sum_{i=1}^{Nc} \hat{G}_A(\vec{r}) \, I_c - RB_\phi \ln R \, \hat{e}_z \right) \cdot d\vec{l}$$

$$(2.45) \quad K_v B_\phi - K_\phi B_v = 0$$

$$(2.46) \quad B_\rho = 0$$

Equations (2.43-4) determine the currents, and (2.45-46) determine the shape and position of the sheets.

2.4 Initial Information, Given Parameters, and Calculated Results

The sheet current model consists of a set of coupled non-linear integro-differential equations that requires initial conditions, and a significant body of information which enters parametrically. From this one can use the model to calculate a considerable set of results, which is gratifying to see given the extensive reduction of the equations from their initial to final form. Given the wide range of parameters available as input, the whole system captures a broad range of tokamak behavior, pertaining to the plasma itself, the plasma's interactions with the chamber, the mechanical loads placed on various structures, and the behavior of the PF system. This will all be incorporated into TSPS-3D, the tokamak/shell plasma simulator, described in Chapter 4, but it is useful to outline this information in the present section, in the context of the mathematical requirements of the model.

Boundary conditions usually require significant attention in differential systems. However, formulating the equations with infinite-space Green's functions means that the jump conditions (2.20) and (2.21) appear automatically as properties of the integral operator in (2.44); since all currents in this system come in closed loops, the condition (2.19) associated with equation (2.43) is satisfied automatically.

The first derivative in time requires that values of all currents be known at the initial time when a given system is studied; typically this will be zero current in the wall and a known current in the plasma and the external field coils.

The initial distribution of current in the plasma is not arbitrary, but, in combination with the plasma shape, must begin in a valid equilibrium satisfying (2.45) and (2.46); a brief consideration of techniques to find these equilibria is given in Appendix B. Depending on whether the model is being used to study existing plasma shots or to do design studies for new machines (or new scenarios in existing machines), some subset of the following information is required:

- The total toroidal plasma current.
- The minor-radial profile of toroidal current.
- The desired number of sheets used to represent the plasma.
- The parameterized shape $R_{p,i}(v)$ and $Z_{p,i}(v)$ of the i th sheet.
- The total cross-sectional area of the plasma, or its minor radius at a fixed value of the v coordinate.
- The complete set of information for the external fields, as described below.

The conductivity of the plasma must be known as a function of time. It is assumed to have some toroidally symmetric value on each sheet and the wall. If some simple model is to be used in place of a given constant, all information used in the model must be specified as a function of time (such as temperature). From a numerical standpoint, it is possible to couple the conductivity to some of the unknowns in the sheet current model, but only if coupling is weak enough to "lag" the unknowns in time; however, it is not expected that the sheet current model contains sufficient information to choose an accurate model of this type.

The external field system must be described by the following information:

- The number of coils in the system.
- The centroid (R_c, Z_c) of each coil, its build $(\Delta R, \Delta Z)$, and the desired number of bundled filaments used to represent it.
- The initial current flowing in each coil.

- The conductivity and applied voltage as a function of time for coils whose currents are to be solved self-consistently; the current as a function of time if the coils are to be "fully specified". With respect to numerical solution, feedback models (linear or otherwise) between applied voltage and current in the self-consistent coils can only be used if "lagged" values of the current yield stable results.

The external toroidal field is assumed to be fully axisymmetric in the wall frame, i.e., no ripple; thus, it has the form $B_0 R_0 / R$. The product $B_0 R_0 \equiv \hat{B}$ must be specified. It can be time-dependent, but generally need not be.

The parameterized shape of the wall $R_w(v)$, $Z_w(v)$ must be known, along with a profile of thickness $d_w(v)$ and conductivity $\sigma_w(v)$. The shape of the wall can include any number of closed loops; this is useful for incorporating divertor structures. If the shape is not a closed loop, only axisymmetric toroidal currents can be examined in that piece; such shapes are not supported in the numerical implementation of the model.

From the model one generates the following information, as a function of time:

- Spatial profiles of toroidal and poloidal currents in the wall and the plasma, from equations (2.43) and (2.44). Integrating the toroidal current profile yields the total toroidal current flowing on each sheet, as well as the total plasma current.
- Self-consistent coil currents from (2.47), if desired.
- The position and shape of the sheets representing the plasma, from (2.45) and (2.46).
- The magnetic fields at any point in space can be found from (2.35).
- Flux surfaces can be examined using the vector potential, from (2.34).
- Once the currents and fields are known, the body forces in the wall $(\vec{K}_w \times \vec{B})/d_w$ can be calculated and used as inputs to standard structural dynamics models, to calculate the resulting stresses and strains on the vacuum chamber.

44

2.5 Equivalence with Differential Form

The introduction of integral operators into the sheet current model may not seem desirable, so in this section we will justify why the equations were deliberately put into integral form. This will be done by showing the solution procedure for a simple integral equation, identifying the proper form of the differential system to be used for comparison, and then showing that even though *in principle* the order of operations to solve the equations is the same, *in practice* the systems are very different. Since the details of using Green's theorem are given in Appendix A and the given references, it will be applied without further justification in this section.

Consider that in the vacuum regions between successive sheet currents, $\vec{J} = 0$; thus, according to (2.12) $\vec{B}$ is irrotational and can be written as the gradient of some potential ϕ, so that by using (2.11) we get Laplace's equation,

$$(2.48) \quad \nabla^2 \phi = 0$$

The sheet current model can be considered as a multi-region problem where (2.48) holds in each region, and the current enters through the jump condition (2.21) across the boundary for each region. The use of Green's functions from this starting point will eventually lead to equations (2.43) and (2.44). For the comparison in this section, let us look at a simpler case. Consider a two-dimensional region in the (X,Y) plane bounded by a parameterized curve C, given by $X_c=X_c(v)$, $Y_c=Y_c(v)$ (see figure 2.5). In this region (2.48) holds, and on the boundary we give the value of $\phi = \phi_c(v)$. It can be shown (see, for example, [5]) that $\phi(X,Y)$ can be calculated from the expression

$$(2.49) \quad \phi = \int \frac{\partial G(X,Y;v)}{\partial n} \psi(v) \, dv$$

where our new unknown $\psi(v)$ satisfies the *one-dimensional* integral equation

$$(2.50) \quad \psi(v) = 2\phi_c(v) + 2 \int \frac{\partial G(v;v')}{\partial n} \psi(v') \, dv'$$

45

In both of these expressions, the normal derivative of the Green's function G is fully determined once the parameterization of X_c and Y_c is given. Let us consider how this equation can be solved by the use of orthogonal functions. While there are many numerical variants of this, some of which lower the operations count we will arrive at here, they are not quite as transparent; since those techniques would apply in an identical manner for the differential form, we can make a fair comparison without using them.
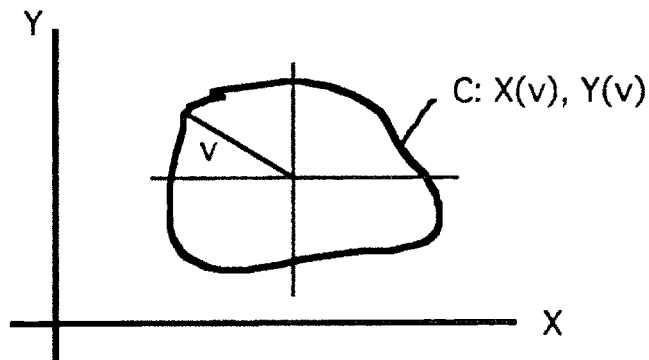
Figure 2.5. Arbitrary curve parameterized in X-Y plane

Suppose we choose to represent ψ by some complete set of orthogonal functions $P_n(v)$, which are assumed to satisfy

$$(2.51) \quad \int P_n(v)P_m(v)\ dv = h_n\ \delta_{mn}$$

where δ_{mn} is the Kronecker delta. We restrict ourselves to N of them:

$$\psi(v) = \sum_{i=1}^{N} \psi_i\, P_i(v)$$

Substituting this into (2.50) and operating with $\int P_m(v)dv$ reduces the problem to the following linear algebra problem

$$M_{ij}\ \psi_i = \phi_i\ ,\text{where}\quad \phi_i\ = 2\int P_i(v)\phi_c(v)\ dv$$

$$M_{ij} = h_n\ \delta_{mn} - 2 \iint \frac{\partial G}{\partial n} P_i(v)P_j(v')\ dv\ dv'$$

46

which consists of an NxN matrix, each matrix element being a double integral, plus N more integrals over ϕ_c. Once ψ is known, ϕ is calculated from (2.49), which is effectively a double summation.

When comparing the integral system with the differential one, it is commonly assumed that the way to proceed is to take the region enclosed by C and discretize ϕ inside it with roughly NxN degrees of freedom. One then applies (2.48) to the discretized form and get a matrix equation whose source term is provided by the boundary conditions. While innovative choices for the discretization can be made by the use of finite elements, so that one can conform to the shape of an irregular boundary with extensive but not excessive effort, one glaring problem becomes evident. NxN degrees of freedom require an (NxN)x(NxN) matrix. The reduction of the problem to a one-dimensional equation (2.60) is clearly more efficient.

However, there is a standard procedure for reducing (2.48) to a one-dimensional problem without resorting to Green's functions, and a fair comparison between the differential and integral forms must involve it. Just as it has been long known in classical mathematics that a Laplace-type operator can be inverted with a Green's function, it has been known that solutions can be written as sums of harmonic functions related to the coordinate system, such as Fourier series. If the shape of the boundary conforms naturally to the coordinates, then in fact this is the simplest method of solution. In general, however, the boundary will be irregular.

In general the solution must be written as a double sum over pairs of functions in each coordinate (e.g., e^{kx}, e^{-kx} and sin ny, cos ny), which we will give general labels $E_n(x)$, $F_n(x)$, $S_m(y)$, $C_n(y)$:

$$(2.52) \quad \phi = \sum_{i=1}^{N} \sum_{j=1}^{M} \left(A_{1,ij} E_i(x) S_j(y) + A_{2,ij} E_i(x) C_j(y) + A_{3,ij} F_i(x) S_j(y) + A_{4,ij} F_i(x) C_j(y) \right)$$

where the four harmonic functions each satisfy relationships of the type (2.51), and (2.52) identically satisfies (2.48) in X,Y coordinates (which need not be Cartesian). (Note we are not addressing the assumed discrete nature of the separation constants.) One then proceeds by setting

$$\phi_c(v) = \sum_{i=1}^{N} \sum_{j=1}^{M} \left(A_{1,ij} E_i(v) S_j(v) + A_{2,ij} E_i(v) C_j(v) + A_{3,ij} F_i(v) S_j(v) + A_{4,ij} F_i(v) C_j(v) \right)$$

and taking the inner product with each of the four families of functions in turn. If the coordinates are separable, the right hand side integrals are known through the orthogonality conditions, and pick out individual coefficients. The problem is then completely solved by doing the $2N+2M \sim 4N$ integrals on the left hand side, and ϕ is evaluated by the double sum (2.52). If the coordinates are not separable with respect to the shape of the boundary, as is usually the case, all constants are coupled and a $4N \times 4N$ matrix of single integrals results.

Without further argument, the case has not been made. The integral form loads an $N \times N$ matrix with double integrals; this means loading the matrix, $N \times N \times N \times N$, actually dominates the process of inverting it (order N^3)! However, there is an additional point to consider. In practice, can the integral form and differential form both use the same order N and get equivalent results? The answer is no. The integral form accounts for the shape of the boundary in the integral over the Green's function in (2.49) and (2.50), whereas the expansion functions need only conform to the smoothness of ϕ_c. The degrees of freedom to accommodate an irregular boundary in the differential case can only come from (2.52), so that N_{diff} must necessarily be greater than N_{int}. Letting N_{diff} equal CN_{int}, the correct comparison is between inverting the differential matrix and loading the integral one: $64C^3 N_{int}^3$ versus N_{int}^4. Even for $N \sim 1000$, if $C>2$ the integral method is superior. In practice, even to represent the C-MOD vacuum chamber, $N \sim 200$, and given the irregular shape one would expect $C>2$.

Finally, there are numerical methods (such as collocation) where it is not at all clear that the reduction of order takes place for both methods; this method would reduce the double integrals to single integrals when loading the matrix for the integral equation. Then the comparison would be unconditionally favorable, $64C^3$ versus 1.

2.7 References

1. J. D. Jackson. *Classical Electrodynamics*, 2nd edition, John Wiley and Sons, New York NY, 1975

2. James R. Melcher. *Continuum Electromechanics*, MIT Press, Cambridge MA, 1981

3. Jeffrey P. Freidberg. *Ideal Magnetohydrodynamics*, Plenum Press, New York, NY 1987

4. Braginskii. "Transport Processes in Plasmas." *Reviews of Plasma Physics*, vol 1, ed. Leontovich. 1965. p.205-311

5. J. Kevorkian. *Partial Differential Equations: Analytical Solution Techniques*. Chapman and Hall, New York, NY 1993

Chapter 3.

Heuristic Models

Chapter 3. Heuristic Models

The sheet current model derived in the previous chapter achieves its economy by concentrating very specifically on the physics of interest. However, the complicated geometry of a tokamak combined with the non-linear nature of the system (2.43)-(2.47) means that closed-form solutions are not feasible. Nevertheless, it is desirable to have some idea about the behavior that can produced by this system, especially in the area of the dependence of halo currents on plasma parameters. Therefore, in this chapter we will consider some extremely simplified models that have little quantitative utility for predicting the behavior of real systems, but which provide some very useful qualitative pictures that go a long way towards clarifying observed phenomena.

We will consider some simple scalings of poloidal halo current, an explicit example of how to extract equations of motion from (2.45), and a simple examination of the distribution of loads on the vacuum chamber. Some of these examples will be carried out as further reductions of the sheet current model; others will be simplifications of systems with a continuously distributed plasma current. The end goal is to provide a heuristic means for visualizing the behavior of the plasma and the currents.

3.1 The Magnitude of Poloidal Halo Current

The dominant reason that poloidal halo currents became an issue of some concern is that the magnitude of the current was measured to be a significant fraction of the equilibrium plasma current, as high as one-half [1]. In the absence of other effects, the dominant contribution to the $\vec{J} \times \vec{B}$ loading of the wall is then $J_v B_\phi$. Since the wall is of fixed dimension, it is often easier to integrate J_v across the wall thickness and around the toroidal direction and work in terms of a measurable quantity, I_v, where I_v is the total poloidal current flowing in the chamber.

Consider a plasma undergoing an axisymmetric radial disruption, at a time when a significant amount of plasma has already impacted the wall (see figure 3.1). In an axisymmetric system, a simple integration of equation (2.9) yields

$$(3.1) \quad R(v)J_v = \text{constant}$$

along any tangential path, including those which link both the wall and the plasma. Therefore, simple continuity arguments require that the total poloidal current flowing through the plasma on the open flux surfaces (bounded by ψ_a and ψ_b in the figure) must also be flowing through the wall, in the region where the wall and those surfaces of the plasma overlap.
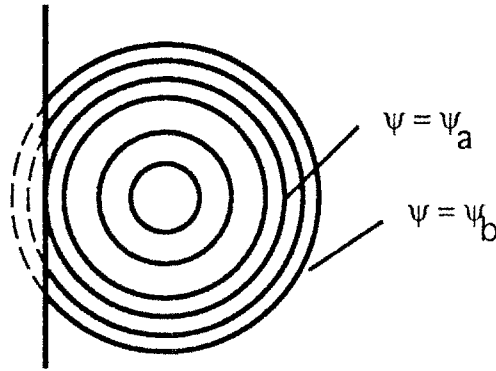
Figure 3.1. Open flux surfaces touching the wall

The natural follow-up to this is to assume that the poloidal halo current in the wall is simply the accumulation of all the poloidal current in the plasma which has "peeled off" from the open flux surfaces as they penetrate the wall. As a crude approximation to this, one can ignore the effects of resistive decay and inductive interaction with the wall, and simply examine the poloidal current profile in the equilibrium plasma.

The MHD formalism for axisymmetric plasma equilibria is given by the *Grad-Shafranov* equation,

$$(3.2) \quad \Delta^* \psi = -\mu_o R^2 \frac{dP}{d\psi} - \mu_o^2 F \frac{dF}{d\psi}$$

which can be quickly derived from Maxwell's equations and the steady-state form of (2.15)

$$(3.3) \quad \vec{J} \times \vec{B} = \vec{\nabla} P$$

by defining $\psi = RA_\phi$ and noting that the $\Delta^*\psi$ operator corresponds to $R(\hat{e}_\phi \cdot \vec{\nabla}^2 \vec{A})$. It follows that the toroidal current density and poloidal magnetic field are given by

$$(3.4) \quad J_\phi = -\frac{\Delta^*\psi}{\mu_0 R}$$

$$(3.5) \quad \vec{B} = \frac{\vec{\nabla}\psi}{R} \times \hat{e}_\phi + B_\phi$$

In (3.2), P is the pressure profile and $\frac{dF}{d\psi}$ is proportional to the poloidal current density in flux coordinates, so that the total poloidal current flowing between two flux surfaces ψ_a and ψ_b is

$$(3.6) \quad I_v \Big|_{\psi_a}^{\psi_b} = 2\pi \int_{\psi_a}^{\psi_b} \frac{dF}{d\psi} d\psi = 2\pi \left(F(\psi_b) - F(\psi_a) \right)$$

We can relate this to something a little more informative by noting that in the "force free" case, the gradient of P is zero and the toroidal current density is given by

$$(3.7) \quad J_\phi = \mu_0 \frac{F}{R} \frac{dF}{d\psi}$$

from (3.4). In an axisymmetric system it is simple to integrate (2.11) and combine it with (2.12) integrated in a toroidal path with Stoke's theorem, leading to

$$(3.8) \quad B_\phi = \mu_0 \frac{F}{R}$$

so that (3.6) becomes

$$(3.9) \quad I_v \Big|_{\psi_a}^{\psi_b} = 2\pi \int_{\psi_a}^{\psi_b} \frac{J_\phi}{B_\phi} d\psi$$

Another form of (3.9) which is more useful for comparison with experimental data can be obtained by switching from flux to spatial coordinates. By dotting equation (3.5) with $\hat{e}_v$ we find

$$(3.10) \quad RB_v = \hat{e}_\rho \cdot \vec{\nabla}\psi = \frac{d\psi}{d\rho}$$

which when substituted into (3.9) gives

$$(3.11) \quad I_v \Big|_{\rho_a}^{\rho_b} = 2\pi \int_{\rho_a}^{\rho_b} \frac{RB_v J_\phi}{B_\phi} \, d\rho = 2\pi \int_{\rho_a}^{\rho_b} \frac{J_\phi}{q} \rho \, d\rho$$

where the limits of integration correspond to the minor radial coordinates ρ_a, ρ_b where the flux has the values ψ_a, ψ_b, and use has been made of a local *safety factor* q, defined by

$$(3.12) \quad q = \frac{\rho B_\phi}{RB_v}$$

Note that even though this safety factor does not require averaging any quantities over the flux surface, it is not a function of the poloidal coordinate, v. This is a result of the form of (3.6), the definition of ρ, and the fact that in an axisymmetric, force-free system RJ_ϕ, RB_ϕ, RB_v, and RJ_v are all constant in v (i.e., on a flux surface). However, the limits of integration in (3.11) are implicitly dependent on v since the actual values of ρ_a and ρ_b will vary with v, even though ψ_a and ψ_b do not. Thus if ρ_a and ρ_b are held fixed as v is varied, the integral itself becomes dependent on v. If ψ_a and ψ_b are held fixed, the integral remains independent of v.

A wide variety of profiles can be used in either (3.9) or the second form of (3.11), but the first form of (3.11) yields the clearest information about scalings, especially when examined in the case of a large aspect ratio and circular flux surfaces. For a plasma of major radius R_o, minor radius a_p, and toroidal plasma current I_p, we can express the toroidal current profile in some parameterized form such as

$$J_\phi(\rho) = \frac{I_p}{2\pi\, a_p^2 \left(\frac{1}{2} - \frac{1}{\alpha+2}\right)} \left(1 - \frac{\rho^\alpha}{a_p{}^\alpha}\right)$$

which would yield a total poloidal plasma current, and therefore maximum poloidal halo current, of

$$(3.13) \quad I_{v,tot} = \frac{\mu_o R_o I_p{}^2}{4\pi\, a_p^2 B_o} \frac{\frac{1}{2} - \frac{\alpha+3}{(\alpha+2)^2}}{\left(\frac{1}{2} - \frac{1}{\alpha+2}\right)^2} = \frac{I_p}{2\, q_{edge}} \frac{\frac{1}{2} - \frac{\alpha+3}{(\alpha+2)^2}}{\left(\frac{1}{2} - \frac{1}{\alpha+2}\right)^2}$$

For values of α between 1 (linear profile) and ∞ (flat profile), the shaping factor ranges from 2 to 1. Thus for tokamaks operating with $q_{edge} \sim 2$, as is typical for stability reasons, it is possible to generate halo currents with fully half the magnitude of the toroidal plasma current; in fact, measurements during shots on Alcator C-MOD with 800kA plasmas have recorded up to 400kA of poloidal halo current. In spite of this apparent agreement, however, it should be noted that too many details have been dropped from this model for it to provide more than a rough envelope of values. It is best to limit (3.13) to the correlations with bulk plasma parameters:

$$I_{v,tot} \sim \frac{R_o I_p{}^2}{a_p^2 B_o} \sim \frac{I_p}{q_{edge}}$$

While the intuition behind this "peel-off" model is straightforward, care must be taken before trying to estimate the influence of other effects, since those effects tend to lead in opposite directions. For example, C-MOD disruptions tend to pull the plasma towards the inner divertor structure, meaning that the plasma must move "up" the toroidal field. Flux conservation would then tend to decrease the poloidal current. However, the plasma also shrinks in cross-sectional area, so that flux conservation would tend to *increase* the poloidal current. Of course, the current cannot remain constant, since the toroidal field is increasing and force-freeness (2.45) must be maintained; this last point emphasizes that the poloidal behavior of the plasma cannot be considered independently of the toroidal behavior. No simple model can correctly balance all these effects. They do, however, lead to the question of how the force-free requirements produce these plasma motions, and how the motions can couple to the current. In the

next section we will consider some simple cases where the plasma displacement can be studied.

3.2 Force-Free Equations of Motion

The system of equations (2.43)-(2.47) is overdetermined if the sheet currents are the only unknowns. The electrodynamic equations (2.43), (2.44), and (2.47) are sufficient in that case. Even though the inertial terms have been dropped from (2.45) and (2.46) it should not be forgotten that these came from equations of motion, and the degrees of freedom originally associated with them were the two components of the local sheet velocity, $v_R(v)$ and $v_Z(v)$, where the v in parentheses is the poloidal coordinate. These quantities do not appear explicitly in (2.45) and (2.46), but implicitly through the integrals used to calculate $\vec{B}$, which contain the parameterized shape of the plasma, $R(v)$ and $Z(v)$. An advantage of the total-derivative form of (2.44) is that only $R(v)$ and $Z(v)$ appear in that equation as well, and thus become the two new degrees of freedom in place of the velocity. Note that $R(v)$ and $Z(v)$ incorporate both "shape" and "position" information.

The expressions for the Green's functions used to calculate $\vec{B}$ can be found in Appendix A; clearly, $R(v)$ and $Z(v)$ enter in a highly nonlinear fashion. Numerical solutions to (2.45) and (2.46) will generally involve reducing $R(v)$ and $Z(v)$ to some limited, discrete set of parameters, and then solving the equations in a "best fit" sense with respect to these parameters. In this section, we will consider a very simple, degenerate geometry where each unknown function is represented by a single parameter, for both the currents and the plasma shape and position. Even in this limit the result will not be closed-form solutions, but a set of nonlinear ordinary differential equations (ODEs) which can be quickly integrated by computer.
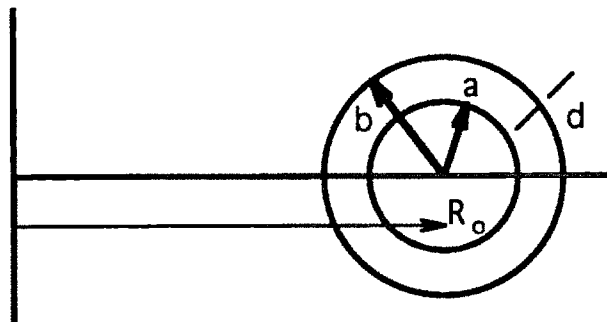
Figure 3.2. Simple two-sheet plasma/chamber model

56

Consider an axisymmetric, large aspect ratio plasma represented by a single sheet current with a circular cross section (see figure 3.2). The sheet has a major radius R_o and minor radius a, and an electrical conductivity σ. It is surrounded by another sheet with minor radius b, thickness d, and conductivity σ_w, representing the wall. Since the plasma is represented by a single sheet, and since a Spitzer-like conductivity is independent of density (see 2.18), the "surface" conductivity of the plasma will be given by the product $a\sigma$. We will consider the plasma to be immersed in a toroidal magnetic field and uniform vertical field, given by

$$(3.14) \quad \mathbf{B} = \frac{\hat{B}}{R}\hat{e}_\phi - B_Z\hat{e}_Z$$

The product $RK_v \equiv \hat{K}$ involving the poloidal current must be constant in v for both the wall and plasma, by (2.43). Taking advantage of the symmetry, we can easily integrate (2.12) to give the toroidal field on the sheet,

$$B_\phi = \frac{\hat{B}}{R} + \frac{\mu_o}{2R}(\hat{K} + 2\hat{K}_w)$$

If we take the toroidal plasma current K_ϕ to be uniform in poloidal angle, then the poloidal field on the surface of the sheet is approximated by $B_v = 0.5\mu_o K_\phi$, neglecting the effects of toroidicity. In both expressions for the fields, the factor of one-half comes from evaluating the field on the sheet itself as opposed to either side of it.

The circuit equations for $\hat{K}$ and $\hat{K}_w$ are derived by taking a poloidal path of integration in (2.44), around the plasma sheet and wall sheet, respectively. Letting $R \sim R_o$ everywhere, and evaluating the right hand side in its original form of $\int \mathbf{B}\cdot\hat{n} \, dA$, we get:

$$(3.15) \quad \frac{2\hat{K}}{\sigma R_o} = -\frac{d}{dt}\left(\frac{a^2\hat{B}}{R_o} + \mu_o a^2\frac{\hat{K}}{R_o} + \mu_o a^2\frac{\hat{K}_w}{R_o}\right)$$

$$(3.16) \quad \frac{2b\hat{K}_w}{d\sigma_w R_o} = -\frac{d}{dt}\left(\frac{b^2\hat{B}}{R_o} + \mu_o a^2\frac{\hat{K}}{R_o} + \mu_o b^2\frac{\hat{K}_w}{R_o}\right)$$

The toroidal circuit equation for K_ϕ and $K_{\phi,w}$ comes from taking toroidal integration paths in (2.44) and averaging the result poloidally around each sheet:

$$(3.17) \quad \frac{R_oK_\phi}{a\sigma} = -\frac{d}{dt}\left(-\frac{B_zR_o^2}{2} + \frac{R_o}{2\pi}\int A_\phi \, dv\right)$$

$$(3.18) \quad \frac{R_oK_{\phi,w}}{d\sigma_w} = -\frac{d}{dt}\left(-\frac{B_zR_o^2}{2} + \frac{R_o}{2\pi}\int A_\phi \, dv\right)$$

The evaluation of the last terms in (3.17-18) requires handling quantities which vary rapidly near the sheet. In Appendix A it is found that the contribution to A_ϕ from a single sheet is

$$(3.19) \quad A_\phi(R,Z) = \frac{\mu_o}{\pi}\int a \, K_\phi' \sqrt{\frac{R'}{Rk}}\left(\left(1 - \frac{k}{2}\right)K(k) - E(k)\right)dv'$$

where $K(k)$ and $E(k)$ are the complete elliptic integrals of the first and second kinds, and

$$(3.20) \quad k = \frac{4RR'}{(R + R')^2 + (Z - Z')^2}$$

Note that this k is not quite the standard quantity; it is equivalent to the quantity m in Abramowitz and Steguin. Letting $R(v) = R_o + a\cos(v)$, $Z(v) = a\sin(v)$, $R_w(v) = R_o + b\cos(v)$, $Z_w(v) = b\sin(v)$, and using the following expansions for the elliptic functions, valid for $k \sim 1$

$$K(k) \approx \left(1 + \frac{1-k}{4}\right)\ln\frac{4}{\sqrt{1-k}} - \frac{1-k}{4} + \ldots$$

$$E(k) \approx 1 + \frac{1-k}{2}\ln\frac{4}{\sqrt{1-k}} - \frac{1-k}{4} + \ldots$$

we find after a short calculation that (3.17-18) become

$$(3.21) \quad \frac{R_oK_\phi}{a\sigma} = -\frac{d}{dt}\left(-\frac{B_zR_o^2}{2} + \mu_oaR_oK_\phi\left(\ln\frac{8R_o}{a} - 2\right) + \mu_obR_oK_{\phi,w}\left(\ln\frac{8R_o}{b} - 2\right)\right)$$

58

$$(3.22) \quad \frac{R_oK_{\phi,w}}{d\sigma_w} = -\frac{d}{dt}\left(-\frac{B_zR_o{}^2}{2} + \mu_oaR_oK_\phi\left(\ln\frac{8R_o}{a} - 2\right) + \mu_obR_oK_{\phi,w}\left(\ln\frac{8R_o}{b} - 2\right)\right)$$

For the two remaining degrees of freedom, R_o and a, we must consider (2.45) and (2.46). Averaging (2.45) around the plasma sheet and using previous expressions for B_ϕ and B_v yields an expression for average minor radial force balance:

$$(3.23) \quad \left(R_oK_\phi\right)^2 = \frac{2\hat{K}\hat{B}}{\mu_o} + \hat{K}^2 + 2\hat{K}\hat{K}_w$$

where the last two terms may be neglected since the perturbation of the vacuum toroidal field in an ohmic tokamak is of order $(a/R_o)^2$.

The geometry is too degenerate to enforce (2.46). There are not enough degrees of freedom to satisfy it exactly, and it is satisfied trivially if averaged over the surface, yielding no information. We will instead consider the linear combination of (2.45) and (2.46) given by $\hat{e}_R \cdot (\vec{K} \times \vec{B})$, and averaged around the plasma sheet. This corresponds to major-radial force balance and requires the presence of the external vertical field. The derivation of Shafranov's formula for the necessary field will not be repeated here; it can be found in texts such as [2] and [3]. The result is

$$(3.24) \quad B_z = \frac{\mu_oaK_\phi}{2R_o}\left(\ln\frac{8R_o}{a} - \frac{3}{2}\right)$$

Examination of equations (3.21-22) shows a serious fault of this "thin filament" limit for the toroidal circuits. It does not contain a distribution of poloidal information; that is, neither the poloidal flux nor toroidal current are defined except at the location R_o. This does not allow the chamber and the plasma to link different amounts of poloidal flux, and more importantly does not allow the generation of image currents, which is the dominant interaction mechanism between a real plasma and wall. In fact, in this limit of $a/R_o \ll 1$, we see that the toroidal circuit reduces to two filaments which occupy the same location in space! We will resolve this by continuing to use the area linked by $R_o(t)$ for the plasma equation, but fix the area used in the wall equation at $R_w = R_o(t=0)$. The

59

problem of image currents cannot be handled even in a simple fashion without a surprising amount of additional algebra, which defeats any illustrative value.

The case considered here differs from the plasma-wall interactions studied in standard MHD stability problems in that there is no true equilibrium, since we are interested in time scales where the resistive decay of the plasma currents is significant. Thus the plasma displacement does not represent an "instability" in the traditional sense, and even a perfectly conducting wall will not "stabilize" the plasma. Thus we can simplify our system further by considering only two limits of equations (3.16) and (3.22): $\sigma_w \to 0$, which represents a case with no wall, and $\sigma_w \to \infty$, to see the maximum influence the wall can exert. In the latter case, equations (3.16) and (3.22) can be integrated to obtain

$$(3.25) \quad \frac{b^2(t)\hat{K}_w(t)}{R_o} = \frac{a^2\hat{K}}{R_o}\bigg|_{t=0} - \frac{a^2(t)\hat{K}(t)}{R_o(t)} \equiv \frac{T_v}{\mu_o} - \frac{a^2(t)\hat{K}(t)}{R_o(t)}$$

$$(3.26) \quad b(L_w - 2)\, K_{\phi,w}(t) = a(L - 2)\, K_\phi\bigg|_{t=0} - a(t)(L - 2)\, K_\phi(t) \equiv \frac{T_\phi}{\mu_o} - a(t)(L - 2)\, K_\phi(t)$$

where $L = \left(\ln\frac{8R_o}{a} - 2\right)$ $L_w = \left(\ln\frac{8R_o}{b} - 2\right)$ and we have assumed that the initial currents in the wall are zero. By substituting (3.25-26) into (3.15) and (3.21) and noting that $\hat{K}$ and K_ϕ appear in simple algebraic form in equations (3.23) and (3.24), the system can be reduced to two first-order ODEs for the major and minor radii of the plasma:

$$(3.27) \quad \frac{c_2 c_1 R_o{}^3}{a^2(L - \frac{3}{2})^2} = -\frac{d}{dt}\left(\frac{a^2}{R_o} + \frac{2c_2 R_o{}^3}{(L - \frac{3}{2})}\left(1 - \frac{\delta a^2}{b^2}\right) + \frac{\delta a^2 T_v}{b^2 \hat{B}}\right)$$

$$(3.28) \quad \frac{c_1 R_o{}^2}{a^2(L - \frac{3}{2})} = \frac{d}{dt}\left(R_o{}^2\left(1 - \frac{4(L - 2)(1-\delta)}{(L - \frac{3}{2})}\right) - \frac{\delta 2 R_o T_\phi}{B_z}\right)$$

where

$$c_1 = \frac{4}{\mu_o \sigma}, \qquad c_2 = \frac{B_z{}^2}{\hat{B}^2}, \qquad L = \ln\frac{8R_o}{a}$$

60

The factor δ has been introduced to more easily compare the case of a perfectly conducting wall ($\delta = 1$) and no wall ($\delta = 0$). Note that without the degrees of freedom to trap varying amounts of poloidal flux on the inboard and outboard sides of the plasma, the toroidal wall-plasma coupling is "perfect" and the self-inductance term vanishes in (3.28) when $\delta = 1$.

These equations can be manipulated to a form that lends itself to numerical integration and further analytic analysis:

$$(3.29) \quad \frac{dR_o}{dt} = \frac{2c_1 R_o}{a \cdot \det}\left[\frac{c_2 R_o^4(1-\delta)}{a^2} + (1+\frac{\delta R_o T_v}{b^2 \hat{B}})(L-\tfrac{3}{2})^3 + \frac{2R_o^4 c_2}{a^2}\left(1+\delta(L-\tfrac{5}{2})\frac{a^2}{b^2}\right)\right]$$

$$(3.30) \quad \frac{da}{dt} = \frac{c_1 c_2 R_o^4}{a^2 \cdot \det}\left[\frac{a^2(L-\tfrac{3}{2})^3}{R_o^4 c_2} + 2(1-\frac{\delta a^2}{b^2})(\tfrac{13}{2}-3L) - (L-\tfrac{3}{2})\left((1-\delta)\left[9-6L+\frac{4(L-2)}{L-\tfrac{3}{2}}\right] - \frac{2\delta T_\phi(L-\tfrac{3}{2})}{R_o B_z}\right)\right]$$

where the determinant is given by the somewhat unwieldy expression

$$\det = 2a\left[(1-\delta)\left(9-6L+\frac{4(L-2)}{L-\tfrac{3}{2}}\right) - \frac{2\delta T_\phi(L-\tfrac{3}{2})}{R_o B_z}\right]\left[1+\frac{\delta R_o T_v}{b^2 \hat{B}}+\frac{2R_o^4 c_2}{a^2(L-\tfrac{3}{2})^3}\left(1+\delta(L-\tfrac{5}{2})\frac{a^2}{b^2}\right)\right]$$
$$+\frac{2a(1-\delta)}{L-\tfrac{3}{2}}\left[(L-\tfrac{3}{2})^3+\frac{2c_2 R_o^4}{a^2}(1-\frac{\delta a^2}{b^2})(\tfrac{13}{2}-3L)\right]$$

Clearly, the simplicity of this system has been obscured by excessive algebra. However, while equations (3.29-30) are exact manipulations of the initial model, they contain terms that are not significant in the a/R_o ordering. Defining $\Lambda = \frac{R_o}{a}$ and noting that the equilibrium vertical field obeys the scaling $\Lambda^2 B_z \sim B_\phi$, some minor manipulations leave the following leading-order equations:

$$(3.31) \quad \frac{da}{dt} = \frac{c_1(L-\tfrac{3}{2})^3}{2a \cdot \det}$$

61

$$(3.32) \quad \frac{d\Lambda}{dt} = \frac{\Lambda c_1 (L-\frac{3}{2})^3}{2a^2 \cdot det}$$

where the remaining terms in the determinant are

$$det = (1-\delta)\left[(L-\tfrac{3}{2})^3 + 9 - 6L + \frac{4(L-2)}{L-\frac{3}{2}}\right] - \frac{4\Lambda_0(L-\frac{3}{2})(L-2)}{\Lambda(L_0-\frac{3}{2})}$$

Λ_o and L_o are the values of Λ and L at t=0, respectively. Interestingly, the effects of the wall on the poloidal circuit do not appear in this order. In addition, the $(1-\delta)$ term in the determinant indicates that the wall can have a very strong effect through the toroidal circuit. The remaining term, which is all that keeps the determinant from vanishing when the wall is present, is the consequence of the geometrical coupling to the external field.
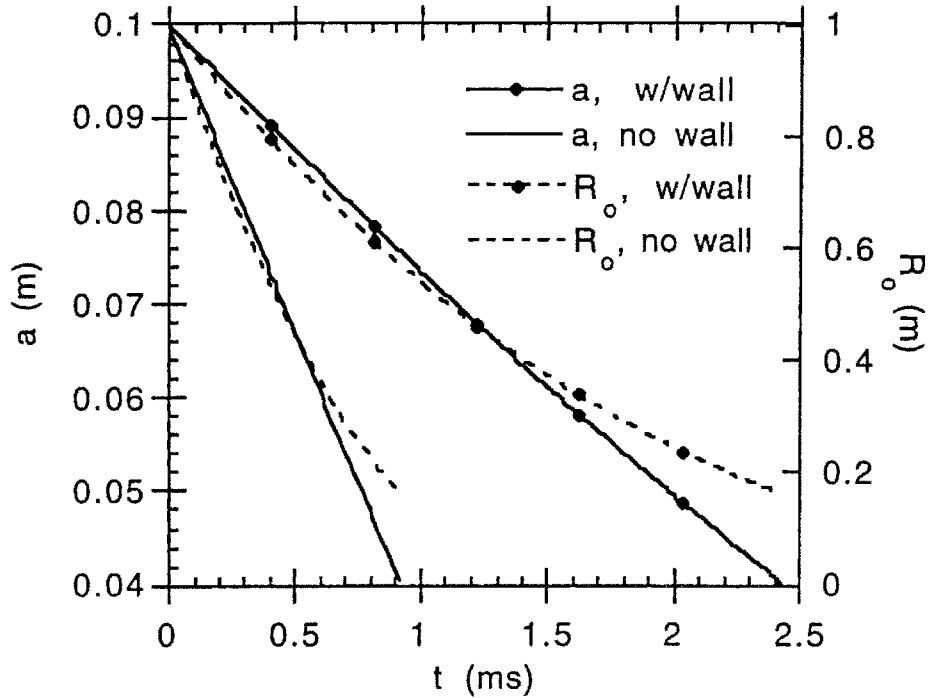
Figure 3.3. Shell geometry over time, with and without a perfectly conducting chamber
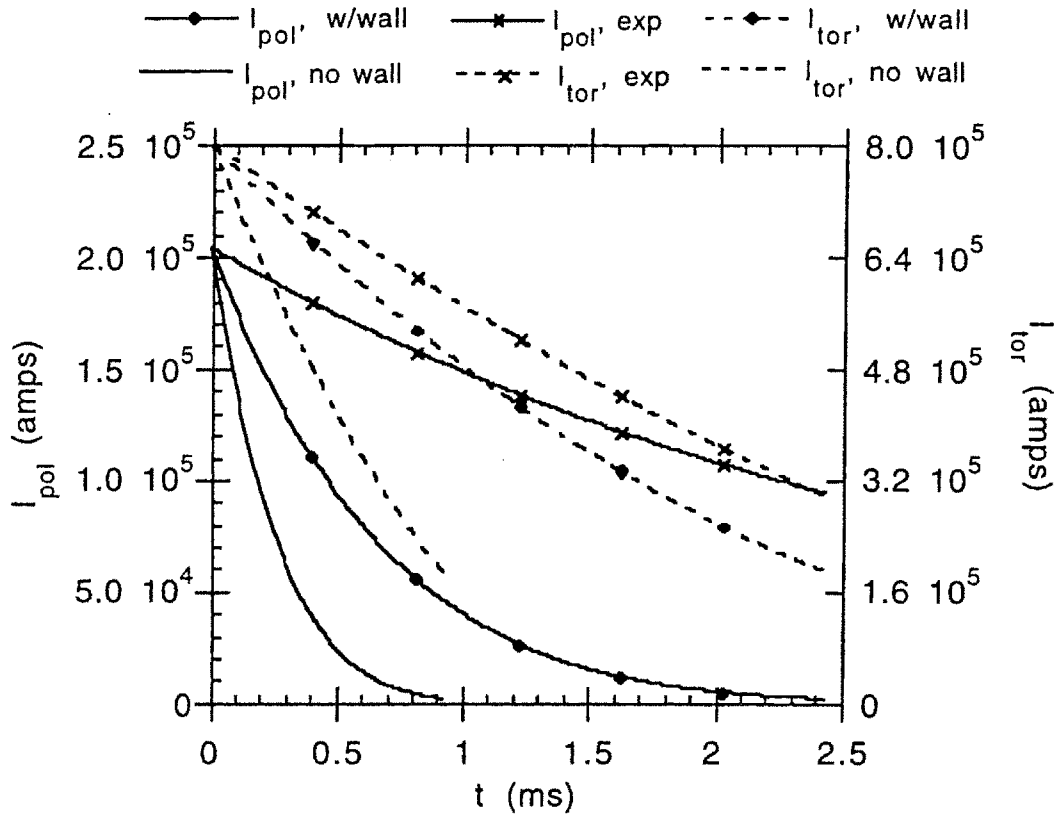
Figure 3.4. Shell currents over time, including simple exponential decay for a fixed geometry

Numerical solutions to these equations are presented in figures (3.3) and (3.4), using the initial conditions $a = 0.1m$, $R_o = 1m$, $B_\phi = 5T$, and $B_z = 0.23T$, which corresponds to initial currents of $\hat{K} = 200kA$, $I_p = 2\pi a K_\phi = 800kA$. The conductivity used is $\sigma = 10^6$ mho/m. Also plotted are the simple exponential decays of the currents that would be seen if the motion of the plasma was not taken into account. To make the trends clear, the simulations are run until Λ, which is supposed to be $>>1$ in this limit, decreases to 4. Notice this corresponds to values of R which have "passed through" the chosen dimensions of the vacuum chamber! The chamber dimensions, however, do not appear in the leading-order equations.

The physical interpretation of the plasma's behavior is as follows. At any given instant of time, resistive decay requires that the flux linked by the plasma decrease by a fixed (differential) amount. For a plasma with a fixed geometry this occurs solely through a proportional decrease in the current. For a plasma which must maintain equilibrium, in

the case with no chamber, a decrease in current requires that the plasma contract in the external field; but since this contraction increases the flux enclosed by the toroidal circuit, the current must decrease faster than in the fixed-geometry case so that the net flux decrease is the same as in the fixed-geometry case. If the chamber is present, the physics is more subtle: the perfect coupling between wall and plasma means that the flux appearing on the right-hand side of Faraday's law is that due to the *initial* flux linked by the plasma, and the external flux; there is no contribution from the plasma current. The purely geometrical changes required to satisfy flux conservation are smaller and therefore slower than in the case with no chamber. The coupling to the currents occurs only through the equilibrium relations.

Qualitatively, this model (including the wall) matches the experimentally observed data on plasma disruptions. Even in disruptions linked to purely vertical instabilities, the plasma shrinks and has an inward component to its displacement. The plasma current typically dumps much faster than a pure L/R decay would allow. However, since the effect of the wall is not realistically represented, we can draw no further conclusions from the model; again, the halo current problem shows strong resistance to purely analytic examination.

3.3 The Distribution of Forces on the Chamber

Now that we have developed at least a pictorial representation of how the plasma moves towards the wall and subsequently has its current "peeled off", can we obtain similar insight about the resulting forces on the chamber structure? The answer is yes, provided that we are again willing to accept greatly reduced models which are meant to provide only qualitative descriptions. Such models are quite useful, however, since they cut through the difficulties associated with incorporating non-axisymmetric effects and other difficult-to-picture processes that often lead to misinterpreting what is allowable halo current behavior.

We begin with a point which, while not as useful as might be hoped, is nevertheless often overlooked in estimations of the effects of halo currents: halo currents *must be force-free* at the time when they first enter the chamber structure. This is independent of any symmetry present (or not) in the problem. It is a simple consequence of the
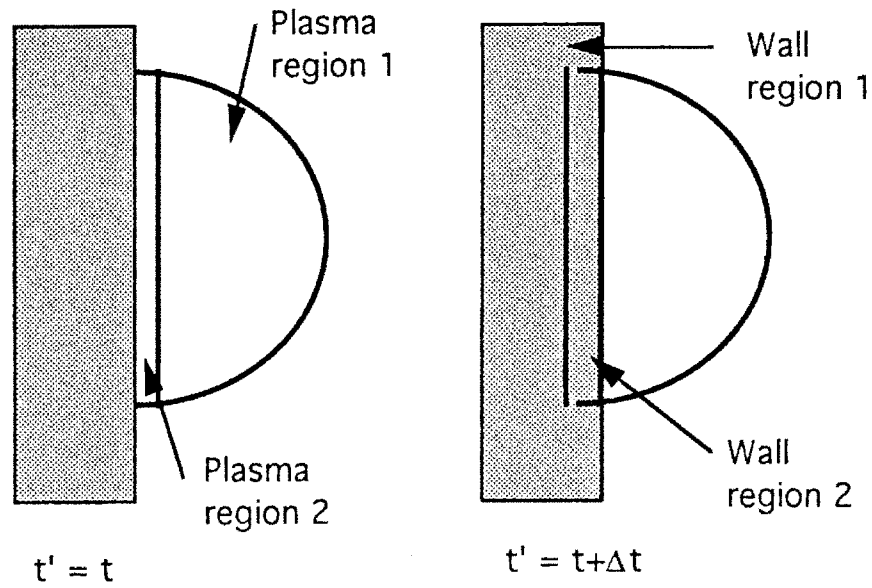
Figure 3.5. Finite plasma layer impacts wall

continuity of Maxwell's equations and the "initial condition" that the currents in the plasma are force-free. Integrating Faraday's Law over an infinitesimal jump in time will quickly show "if you do nothing, nothing happens"; so to show something clearer albeit more ad-hoc, we will consider a situation where we let the system evolve over a finite step in time, Δt. We will let this step be small enough that resistive effects are not important, so that Faraday's Law states simply

$$(3.33) \quad \psi(t) = \psi(t+\Delta t)$$

where the loop through which we are taking the flux is arbitrary. Over this finite step in time, we will assume that a finite amount of plasma has been "peeled off" by the wall. Writing out the fluxes in terms of integrals over the currents and geometry (see figure 3.5), we get

$$\psi(t) = \int \overline{\overline{G}} \cdot \vec{J}_{w,1}'(t) \, d\vec{r}_{w,1}' + \int \overline{\overline{G}} \cdot \vec{J}_{w,2}'(t) \, d\vec{r}_{w,2}' + \int \overline{\overline{G}} \cdot \vec{J}_{p,1}'(t) \, d\vec{r}_{p,1}' + \int \overline{\overline{G}} \cdot \vec{J}_{p,2}'(t) \, d\vec{r}_{p,2}'$$

$$\psi(t+\Delta t) = \int \overline{\overline{G}} \cdot \vec{J}_{w,1}'(t+\Delta t) \, d\vec{r}_{w,1}' + \int \overline{\overline{G}} \cdot \vec{J}_{w,2}'(t+\Delta t) \, d\vec{r}_{w,2}' + \int \overline{\overline{G}} \cdot \vec{J}_{p,1}'(t+\Delta t) \, d\vec{r}_{p,1}'$$

By definition in the latter equation, $\vec{J}_{p,2} = 0$. We take Δt small enough that we can expand the geometry in wall region 1 in terms of plasma region 2, and treat the plasma motion by expanding the plasma geometry at $t+\Delta t$ in terms of the geometry at time t. For example, if we parameterize that region in coordinates defined from its center, which we will call $R_c(t)$, then we may write something like

$$\overline{\overline{G}}\ d\vec{r}_{p,2}(t+\Delta t) \approx \overline{\overline{G}}\ d\vec{r}_{w,2} + \Delta t\ v_p \frac{\partial}{\partial R_c}\overline{\overline{G}}\ d\vec{r}_{p,2}(t) + \dots$$

where v_p is the plasma velocity, so that equation (3.33) becomes

$$\int \overline{\overline{G}}\cdot\vec{J}_{w,1}{}'(t)\ d\vec{r}_{w,1}{}' + \int \overline{\overline{G}}\cdot\vec{J}_{w,2}{}'(t)\ d\vec{r}_{w,2}{}' + \int \overline{\overline{G}}\cdot\vec{J}_{p,1}{}'(t)\ d\vec{r}_{p,1}{}' + \int \overline{\overline{G}}\cdot\vec{J}_{p,2}{}'(t)\ d\vec{r}_{p,2}{}'$$

$$= \int \overline{\overline{G}}\cdot\vec{J}_{w,1}{}'(t+\Delta t)\ d\vec{r}_{w,1}{}' + \int \overline{\overline{G}}\cdot\vec{J}_{w,2}{}'(t+\Delta t)\ d\vec{r}_{w,2}{}' + \int \overline{\overline{G}}\cdot\vec{J}_{p,1}{}'(t+\Delta t)\ d\vec{r}_{p,1}{}'$$

$$+ \int \overline{\overline{G}}\cdot\Delta\vec{J}_{w,2}{}'(t)\ d\vec{r}_{p,2}{}' + O(\Delta t)$$

where the terms represented by $O(\Delta t)$ contain all eddy-current effects. After much cancellation of terms, the solution is simply $\Delta\vec{J}_{w,2} = \vec{J}_{p,2}$. A similar analysis on the magnetic field shows that changes to $\vec{B}$ come in only as $O(\Delta t)$. Since we required $\vec{J}_p \times \vec{B} = 0$ it follows that $\Delta\vec{J}_{w,1}\times\vec{B} = 0$ and we have not added a significant load to the wall in spite of the finite change in current.

The reason that this statement is not completely useful is that "when the currents first enter the chamber" connotes a certain time scale, since obviously once the currents are in the vacuum vessel they are in no way constrained to *remain* force-free. It is often conjectured that, since the cold plasma is a poor conductor relative to the metallic chamber, the currents can "instantly" short to some new path which is not at all force-free. However, no matter how poor a conductor the plasma is, such behavior would violate flux-conservation around the *new* current path. No changes can occur in the current path on any time scale shorter than the toroidal or poloidal L/R time for that path; these times are typically longer than the time scale of the entire disruption itself. We shall return to this point later. A more serious flaw in the force-free argument, however, is in the fact that while the current cannot instantaneously change direction in

66

the sense that poloidal remains poloidal and toroidal remains toroidal, the directions themselves change in relative terms.
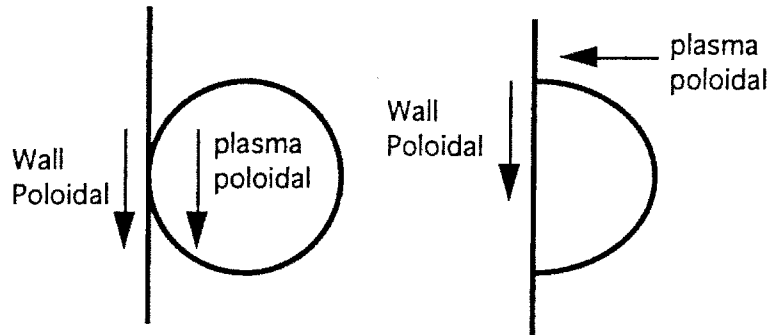
Figure 3.6. Direction changes inherent in a "relative" coordinate system

Consider that as the plasma first touches the wall at a point of tangency (see figure 3.6), the poloidal direction in the plasma and the poloidal direction in the small overlapped segment of wall are the same direction in physical space. Now consider a later time when half of a circular plasma has impinged on the wall. At the upper and lower intersection points, the plasma "poloidal" and wall "poloidal" are at right angles to each other! In the thin-sheet limit we have been using so far, this means the poloidal plasma current does in fact instantly change direction with respect to the magnetic fields. It is not possible for such a change to occur and yet remain completely force-free. However, the current in the portion of the plasma not in contact with the wall must remain force-free; the current entering the wall at the midpoint of the overlap region, where the flux surface is always tangent, is force-free; the local poloidal field is changing rapidly as toroidal current "piles up" in the wall. Is it possible that the two terms in $K_v B_\phi - K_\phi B_v$ still compete strongly with each other, even if they don't cancel?

Let us examine the behavior of a very simple system: a single circular current sheet representing the plasma, and no vacuum chamber. We will deform the sheet in exactly the same manner as if it had impacted the wall by cutting the circle with a moving chord located at major radius $R_w(t)$, while keeping the shell major radius fixed (see figure 3.7). The currents will start initially force-free; as the sheet hits the wall, we will evolve the currents by conserving total toroidal current and forcing the poloidal current to remain force-free in the undeformed segment of the sheet. We will then calculate numerically the fields and forces in the deformed segment.
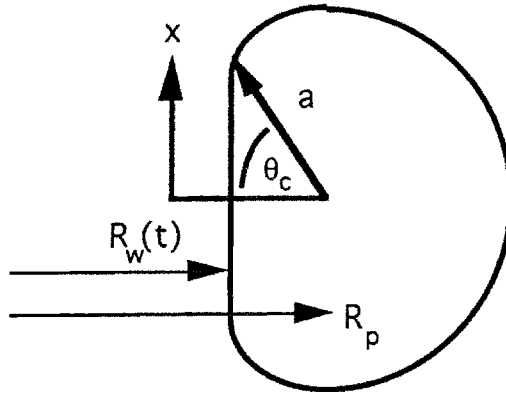
Figure 3.7. Schematic of single-sheet system used to estimate forces

The equations for the system are given by

$$(3.34) \quad \theta_c(t) = \cos^{-1}\left(\frac{R_p - R_w(t)}{a}\right)$$

$$(3.35) \quad x_c(t) = a\,\sin\theta_c(t)$$

$$(3.36) \quad K_\phi\,dx_c\Big|_{\text{"wall"}} = K_\phi\,a\,d\theta_c\Big|_{\text{plasma}} \qquad \text{(cons. of toroidal current)}$$

$$(3.37) \quad RK_v \equiv \hat{K} = \frac{1}{2(\pi - \theta_c)}\int_{\theta_c}^{2\pi - \theta_c} \frac{RK_\phi B_z}{B_\phi}\,dv \qquad \text{(force-free in plasma)}$$

$$(3.38) \quad B_z = \int G_{B,z\phi}\,K_\phi{'}\,a\,dv'$$

and there is also a constant (in time) toroidal field, B_ϕ. We choose $a = 0.15$m, $R_p = 0.6$m, a uniformly distributed toroidal plasma current of 800kA, and $B_\phi(R_p) = 5.3$T. The effective plasma motion is at a velocity of 100m/s. The results of a simulation where the plasma moves almost to the halfway point are in the following graphs.
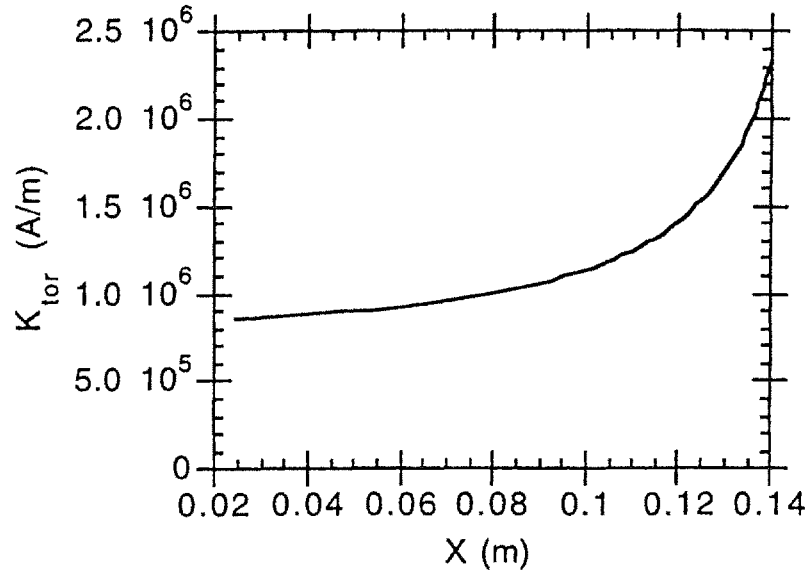
Figure 3.8. Toroidal current profile at end of simulation.
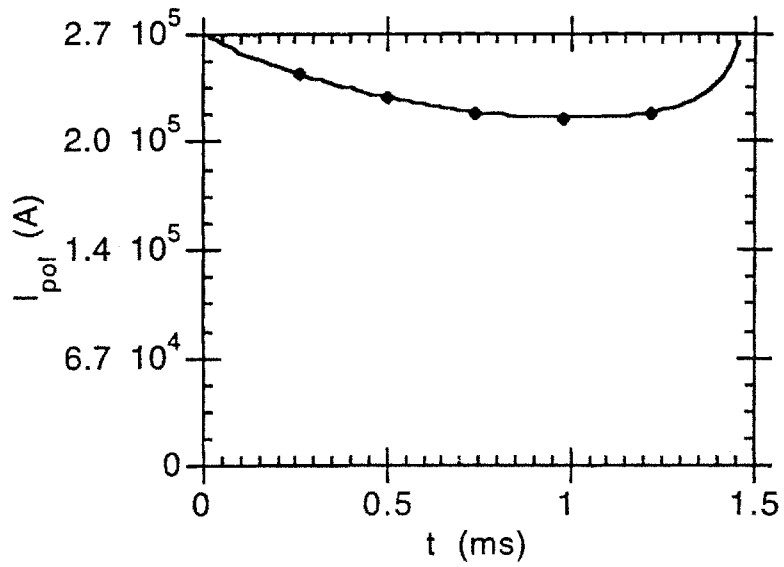
Figure 3.9. Poloidal current over time.

69
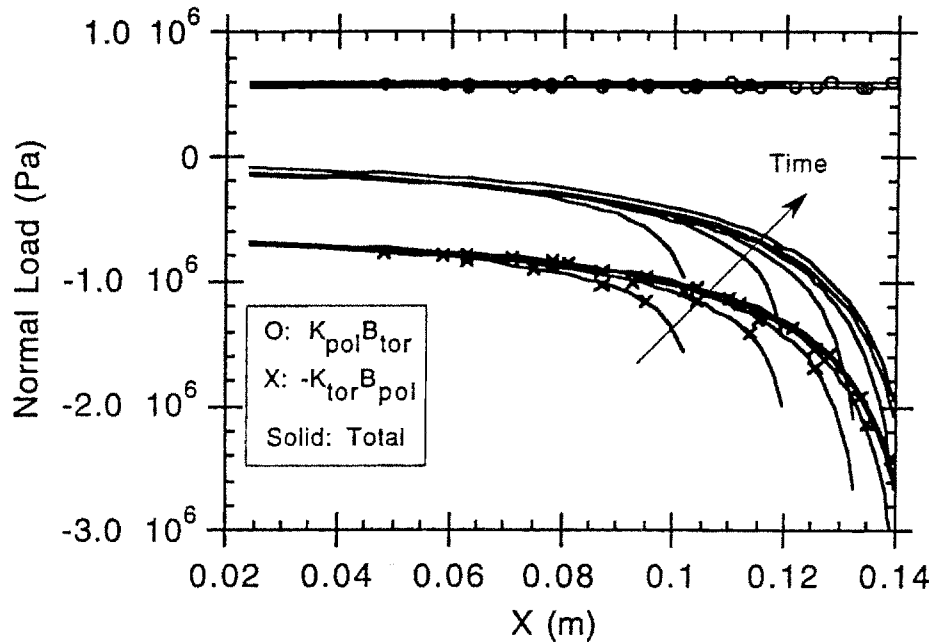
Figure 3.10. The component breakdown and total load profile in the wall, at various times.

The shape of the toroidal current profile does not change over time; it is "drawn" as the contact point slides along the "wall", in the x-coordinate, forming the curve in figure (3.8). Constraining the poloidal current to remain force-free in the undeformed plasma segment does not have a highly significant effect on its magnitude, as seen in the plot of poloidal current versus time in figure (3.9).

By far the most interesting results are the loads, shown in figure (3.10). The individual contributions to the load and the total are profiled at various times; the curves extend farther in X as time increases. Note the following observations:

- The original tangency point (X = 0) remains basically force-free at all times.
- The worst loading is towards the edges of the overlap region.
- The contributions from the toroidal and poloidal currents have opposite signs, so that the net is always between the two.
- The dominant contribution comes from the toroidal currents, not poloidal.

70

- The loads at the edge regions decrease as the plasma continues to move past these points; i.e., note how the total-load curves "unroll" from one time to the next.

Many points could be made about what other significant effects are missing from this simple picture. However, we shall see in Chapter 5 that a big contribution to the load which is not present here is that from the toroidal eddy currents - which flow in the opposite direction to the toroidal halo currents. This would seem to indicate that the halo current loads could be offset or even dominated by eddy currents when taken into account, and that the peak loads might actually occur before the plasma ever hits the wall.
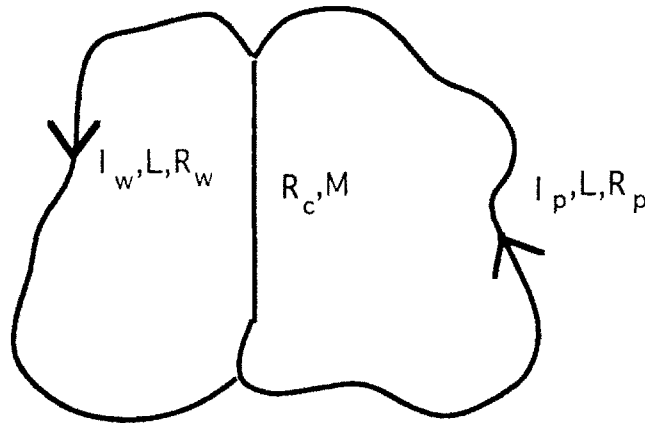
Figure 3.11. Arbitrarily shaped adjoining current loops

The last brief point to consider is whether the poloidal current is constrained to the original path which closed through the plasma, or it is able to transfer to an adjoining loop (such as a path beneath the divertor plates in C-MOD; see figure 2.1) on a fast time scale. Consider two loops of current which share a common segment, so that there is some shared resistance R_c between them (see figure 3.11), and they have a mutual inductance M. We are interested in the case when the resistance through one loop (representing the cold plasma) is much greater than the other (representing the wall). Letting the subscript w denote the wall, p the plasma, and letting the common segment have a resistance R_c, the system is governed by:

$$(3.39) \quad R_w I_w - R_c I_p + L_w \frac{dI_w}{dt} - M \frac{dI_p}{dt} = 0$$

71

$$(3.40) \quad R_p I_p - R_c I_w + L_p \frac{dI_p}{dt} - M \frac{dI_w}{dt} = 0$$

For initial conditions we take $I_w = 0$, $I_p = I_{p,o}$. In the geometries of interest we assume the ordering:

$$L_w \sim L_p \equiv L; \quad \frac{M}{L} \sim \frac{R_c}{R_w} \sim \frac{R_w}{R_p} << 1$$

Using Laplace transforms to solve (3.39-40) in this limit quickly yields the solution

$$(3.41) \quad I(t) = I_{p,o} \frac{M}{L} \left(\exp(-\frac{R_p}{L} t) - \exp(-\frac{R_w}{L} t) \right)$$

The first thing to note is that, for early times, the rise of current in the wall loop is limited by the plasma poloidal L/R time, which even in a cold plasma is at least on the order of the disruption itself. The second and more interesting point is that the true "control" on the magnitude of current flowing in the new path is the ratio of the mutual to self inductance, M/L; even if the wall is a perfect conductor, the new loop will never acquire more than this fraction of the poloidal plasma current. On Alcator C-MOD, given the ratio of plasma-facing segments to "interior" segments for any possible alternate loop, it is difficult to see this ratio exceeding one-third.

To summarize these heuristic results, we expect that:

• The peak axisymmetric halo current is determined simply by calculating the poloidal current available in the plasma, scaling in a clear fashion with equilibrium plasma quantities.

• The halo currents will enter the vacuum vessel in a nearly force-free fashion.

• Even in the presence of a complicated geometry, the halo currents in the vessel will remain force-free over significant periods of time. This opens the door for the possibility of eddy currents dominating the forces.

We have reached the point of diminishing returns for simplified models. While there is a multitude of topics that should be added (eddy currents, etc.), the algebra required to

72

do so would quickly conceal all useful information. The next step is to consider how to find numerical solutions to the complete model, which is the task for Chapter 4.

3.4 References

1 Granetz, Hutchinson, Sorci, Irby, LaBombard, Gwinn. "Disruptions and Halo Currents in Alcator C-MOD." *Nuclear Fusion*, vol. 36, no. 5, p545-56, 1996.

2. Ian H. Hutchinson. *Principles of Plasma Diagnostics.* Cambridge University Press. Reprinted 1992.

3. Jeffrey P. Freidberg. *Ideal Magnetohydrodynamics*, Plenum Press, New York, NY 1987

Chapter 4.

Numerical Methods of Solution

Chapter 4. Numerical Methods of Solution

The heuristic pictures derived in Chapter 3 are useful for giving a basic understanding of halo current and simple disruption behavior, but clearly have no practical application beyond that. In this chapter we return to the full model derived in Chapter 2 and investigate the steps necessary to obtain numerical solutions for realistic tokamak geometries and plasma parameters. The equations are repeated here for easy reference; on a given sheet with conductivity σ (σ_w or σ_p), thickness Δ (d_w or Δ_i), and current $\vec{K}$ ($\vec{K}_w$ or $\vec{K}_{p,i}$), the equations are

$$(4.1) \quad \vec{A}(\vec{r}) = \iint \overline{\overline{G}}_A \cdot \left(\vec{K}_w + \sum_{i=1}^{N} \vec{K}_p \right)' dv' \, d\phi' + \sum_{i=1}^{N_c} \hat{G}_A(\vec{r}) \, I_c - RB_\phi \ln R \, \hat{e}_z$$

$$(4.2) \quad \vec{B}(\vec{r}) = \iint \overline{\overline{G}}_B \cdot \left(\vec{K}_w + \sum_{i=1}^{N} \vec{K}_p \right)' dv' \, d\phi' + \sum_{i=1}^{N_c} \hat{G}_B(\vec{r}) \, I_c + B_\phi \, \hat{e}_\phi$$

$$(4.3) \quad \vec{\nabla} \cdot \vec{K} = 0$$

$$(4.4) \quad \int \frac{\vec{K}}{\sigma \Delta} \cdot d\vec{l} = -\frac{d}{dt} \int \left(\iint \overline{\overline{G}}_A \cdot \left(\vec{K}_w + \sum_{i=1}^{N} \vec{K}_p \right)' dv' \, d\phi' + \sum_{i=1}^{N_c} \hat{G}_A(\vec{r}) \, I_c - RB_\phi \ln R \, \hat{e}_z \right) \cdot d\vec{l}$$

$$(4.5) \quad K_v B_\phi - K_\phi B_v = 0$$

$$(4.6) \quad B_p = 0$$

where the last two equations apply only to the N plasma sheets. The circuit equations (2.47) for the N_c coil currents will not be repeated here.

The first step in the process is to address the nonlinear nature of the system by use of a *penalty function* , such that by minimizing this function we satisfy the force-free requirements imposed by equations (4.5-6). The next step is to perform some additional analytic manipulation of the model, taking advantage of the restricted types of asymmetry, so that Fourier analysis can be used for the toroidal dependence. The third step is to introduce the simplest of possible time-discretizing methods so that the

temporal discontinuities inherent in the problem do not cause difficulties. The last step is to introduce a finite-element expansion of the poloidal dependence, leaving a system of linear algebraic equations which are marched in time.

The complicated tokamak geometry and the contact between the wall and bulk plasma introduce some severe bookkeeping difficulties, which in fact dominate the development of a numerical code to solve the system. Some of the methods to handle the worst problems are discussed in the final section of the chapter. The result is the "Three-Dimensional Tokamak/Shell-Plasma Simulator" or TSPS-3D, a code which enables the simulation of global tokamak behavior, including "slow" disruptions and the generation of halo currents, over long time scales.

4.1 The Penalty Function

Recall that for a single sheet of the plasma, the four equations (4.3-6) are for the four unknowns $K_\phi(\phi,v,t)$, $K_v(\phi,v,t)$, $R(v,t)$, and $Z(v,t)$. While all the equations are coupled, equations 4.3 and 4.4 can be considered linked specifically to K_ϕ and K_v, in the sense that if the currents were treated as "given" information then Maxwell's equations could no longer be enforced uniquely. Thus, equations 4.5 and 4.6 must be connected to R and Z, and examination of the dependence of $\overline{\mathbf{B}}$ on these quantities through $\overline{\overline{G_B}}$ shows that these equations are highly nonlinear. While there are methods to handle "exact" numerical solutions of these equations, as detailed in Appendix B, it turns out that applying these methods to the problem of interest - disruptions where the plasma hits the wall - is beyond the scope of this thesis. Thus, more approximate techniques must be introduced.

Consider a plasma sheet whose shape is given by a small set of parameters, such as

$$(4.7) \quad R(v,t) = R_0(t) - a(t) \cos(v) + d(t) \cos(2v)$$

$$(4.8) \quad Z(v,t) = Z_0(t) + b(t) \sin(v)$$

where d and b can be related to the less numerically convenient but more commonly accepted triangularity δ and elongation κ. This set of parameters can represent quite a

variety of advanced tokamak profiles (see, for example, figure 4.1), and in fact has been used previously in fast equilibrium codes [1]. It can be extended to include the twisting of a plasma towards a single-null divertor by means of a rotation in the poloidal plane given by an angle θ, and the additional parameters $(\Delta_x, \Delta_y, \Delta_z)$ and $(\phi_{xz}, \phi_{yz}, \phi_{xy})$ provide simple non-axisymmetric shifts, tilts, and rotations, as mentioned in Chapter 2.
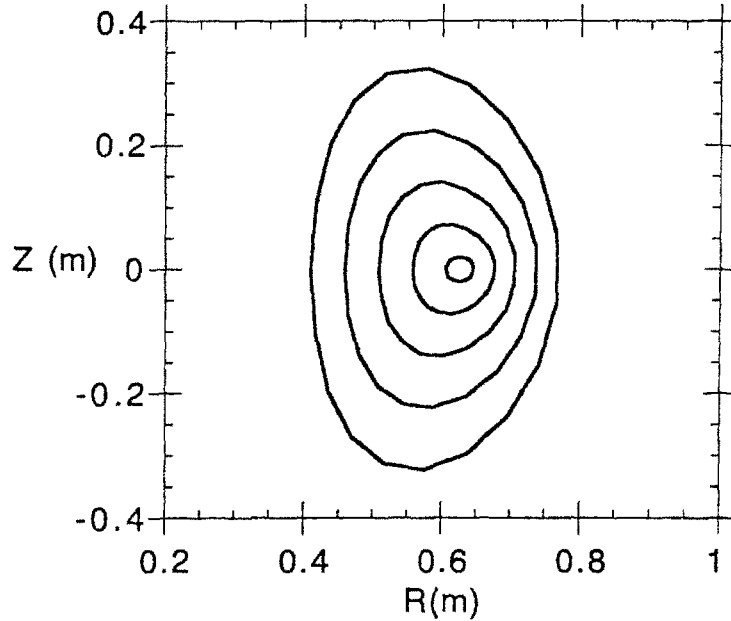
Figure 4.1. Example parameterized plasma shape, with profiled κ and δ.

If the shape of the plasma sheets is known, we can define a "penalty function" which tells us how well the given shapes satisfy equations (4.5) and (4.6):

$$(4.9) \quad P(t) = \frac{1}{2\pi N} \sum_{i=1}^{N} \iint \left[\frac{2\left|K_v B_\phi - K_\phi B_v\right|_i}{\langle RQB_v K_\phi \rangle_N + \langle RQB_\phi K_v \rangle_i} + \frac{\left|B_{p,i}\right|}{\langle RQB_v \rangle_i} R_i Q_i \right] dv_i d\phi_i$$

where the normalization has been chosen so that a "good" value of P is $<< 1$. The notation $\langle X \rangle$ denotes the average of X over the sheet.

It is of course possible to replace (4.5) and (4.6) by a numerical minimization of P(t) at each time step in the code. However, even with just the five parameters R_o, Z_o, a, d, and

b, the process becomes extremely prohibitive in CPU time since the resulting five-dimensional surface does not have a very flat shape over reasonable time steps and the optimizing algorithm can easily wander forever among non-global minima. Since the displacement and distortion of the plasma can be guessed at with fair accuracy based on experimental data, the simplest technique is to specify the parameters as functions of time and track P(t), repeating this for several runs until acceptably small profiles of P are obtained.

While the penalty function technique sounds crude, this "by hand" optimization does yield a net savings in CPU time, since in practice P(t) does not vary rapidly in time and simple temporal parameterizations - usually linear - will suffice. Most importantly, replacing equations (4.5) and (4.6) by this procedure has a profound effect on the remaining system of equations: (4.3) and (4.4) are completely linear in the remaining unknowns K_ϕ and K_v! Certainly no method which replaces a nonlinear system with a linear one should be dismissed without strong reason.

4.2 Fourier Analysis

Recall that we limited our scope of asymmetries to fully axisymmetric displacements which are allowed to hit the wall, and rigid non-axisymmetric displacements which do not hit the wall; in both cases, the currents can be non-axisymmetric. In this restricted scope, the dependence of the currents on ϕ is expected to be smooth since there will be no physical discontinuities in this direction (the case will be quite different in the poloidal direction). We will therefore Fourier-analyze the ϕ dependence, and find that even in the case of non-axisymmetric rigid displacements a good deal of numerical effort can be avoided by analytically integrating over the kernel of our integral equation.

As a warning to the reader, the complete consistent notation for this section would quickly render the work illegible, so only the absolutely necessary subscripts and variable dependence will be shown in any particular equation. Numerical computation is easier with real sines and cosines as opposed to complex exponentials, even though typesetting is more difficult; therefore to save space the proper signs, factors, and sub- or superscripts for the two families of harmonics will be shown as in equation (4.10).

78

We begin by expressing the currents on any given sheet (wall or plasma) in the first n terms of a Fourier series in the toroidal direction. It is important to keep in mind that the plasma and wall can have different coordinate frames, and that we are expanding the toroidal dependence *in the frame of the sheet*.

$$(4.10) \quad \vec{K}(v,\phi,t) = \vec{K}_o(v,t) + \sum_{n=1}^{m} \vec{K}_n^{\substack{c \\ s}}(v,t) \begin{array}{c} \cos(n\phi) \\ \sin(n\phi) \end{array}$$

Substituting this expression into equation (4.3) and doing the necessary overlap integrals yields for the zeroth harmonic

$$(4.11) \quad \frac{d}{dv}(RK_{v,o}) = 0$$

and for the higher harmonics

$$(4.12) \quad \frac{d}{dv}(RK_{v,n}^{\substack{c \\ s}}) \pm nQ\, K_{\phi,n}^{\substack{s \\ c}} = 0, \quad Q = \sqrt{\frac{dR^2}{dv} + \frac{dZ^2}{dv}}$$

Equation (4.11) suggests that it would be convenient to define $RK_v \equiv \hat{K}$, whose zeroth harmonic is a function of time only. Equation (4.12) allows us to eliminate the higher harmonics of toroidal current in terms of the poloidal current. Choosing a purely poloidal integration path in equation (4.4) and integrating the result in ϕ yields the equation for the time dependence of $\hat{K}_o$:

$$(4.13) \quad \hat{K}_o(t) \int \frac{Q}{\sigma \Delta R}\, dv = -\frac{d}{dt} \iint \frac{A_v Q}{2\pi}\, dv\, d\phi$$

where A_v is in general coupled to the poloidal and toroidal currents flowing on all the sheets, as given by (4.1). Choosing a purely toroidal integration path in equation (4.4) yields a one-dimensional (plus time) integral equation for the zeroth-order toroidal currents:

$$(4.14) \quad \frac{RK_{\phi,o}(v,t)}{\sigma \Delta} = -\frac{d}{dt} \int \frac{d\phi}{2\pi}\, RA_\phi$$

To find the equations for the higher harmonics of $\overline{\overline{K}}$ using (4.4) in its present form, it would be necessary to establish a complete set of linearly independent integration paths, and Fourier-analyze the resulting family of equations. However, after all the work that was done to arrive at this set of integral equations, we will now proceed to undo them! The method to the madness is to do so in such a way that only tangential differential operators are introduced, so that we still do not need to include any of the vacuum regions in the calculation, but neither will we include so many integrals.

Consider using an integration path in (4.4) that consists of a small closed loop lying in the surface of a sheet, small enough that we may consider it to enclose a rectangular
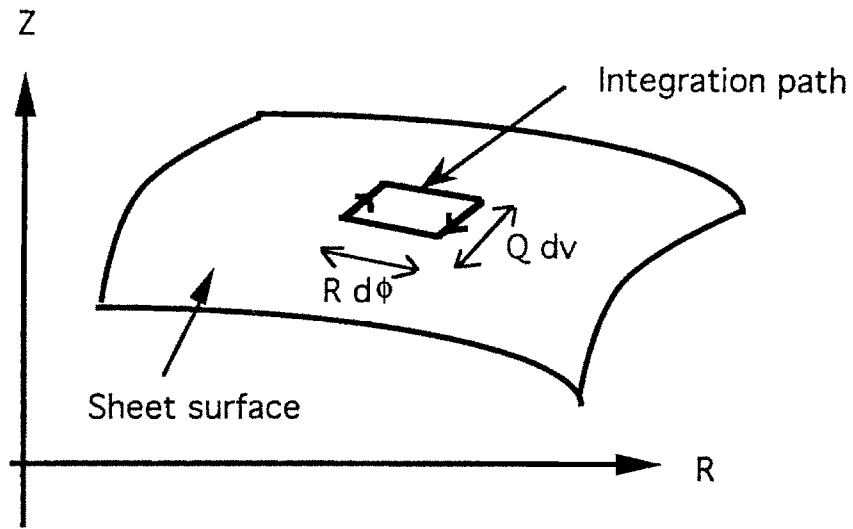
Figure 4.2. Integration path used in equation (4.4)

area $QR\Delta\phi\Delta v$ (see figure 4.2). Temporarily returning to the electric field $\overline{E}$ as an unknown for clarity, the left hand side of the equation would be given by

$$\int \overline{E} \cdot \overline{dl} \approx \int_{\phi}^{\phi+\Delta\phi} RE_{\phi}(\phi',v)d\phi' + \int_{v}^{v+\Delta v} QE_{v}(\phi+\Delta\phi,v)'dv' + \int_{\phi+\Delta\phi}^{\phi} RE_{\phi}(\phi',v+\Delta v)d\phi' + \int_{v+\Delta v}^{v} QE_{v}(\phi,v')dv'$$

As the sides of the rectangle become smaller we can approximate the above expression by the following, returning to $\overline{\overline{K}}$ as the unknown:

80

$$\Delta\phi\frac{RK_\phi(\phi,v)}{\sigma\Delta} + \Delta v\frac{Q\hat{K}(\phi+\Delta\phi,v)}{\sigma\Delta R} - \Delta\phi\frac{RK_\phi(\phi,v+\Delta v)}{\sigma\Delta} - \Delta v\frac{Q\hat{K}(\phi,v)}{\sigma\Delta R}$$

Letting $\Delta\phi$ and Δv shrink to differential size and using the definition of a derivative and the fact that the geometrical quantities are not functions of ϕ, we obtain

$$d\phi\, dv\left(\frac{Q}{\sigma\Delta R}\frac{\partial\hat{K}}{\partial\phi} - \frac{\partial}{\partial v}\left(\frac{RK_\phi}{\sigma\Delta}\right)\right)$$

Note that all scale or Jacobian information is in R and Q; the differentials themselves are not functions of time. Thus the integral on the right-hand side of (4.4) may be treated in an identical manner and the differentials can be pulled from the time derivative and will cancel those on the left hand side. After doing the Fourier integrals over the result and substituting for K_ϕ from (4.12), we obtain a 1-D (plus time) integro-differential equation for each harmonic of the non-axisymmetric poloidal current:

$$(4.15)\quad \frac{d}{dv}\left(\mp\frac{R}{nQ\sigma\Delta}\frac{d\hat{K}_n^{\,s}}{dv}\right)\pm\frac{nQ}{\sigma\Delta R}\hat{K}_n^{\,s}_c = -\frac{d}{dt}\int\frac{d\phi}{\pi}\left(-\frac{\cos(n\phi)}{\sin(n\phi)}\frac{d}{dv}(RA_\phi)\pm nQA_v\frac{\sin(n\phi)}{\cos(n\phi)}\right)$$

By introducing differential operators, we are required to impose jump conditions across any poloidal interfaces. These may be obtained by integrating once across (4.15) and (4.12). Note that (4.16) refers to the *total* poloidal current flowing through an intersection point, which may include a segment shared by several shells if the plasma has impacted the wall. At a Y-branch it consists of just a single constraint; equation (4.17) yields a distinct condition for each branch of the intersection. See figure (4.3) for clarification.

$$(4.16)\quad \left[\,\hat{K}\,\right] = 0$$

$$(4.17)\quad \left[\frac{R}{nQ\sigma\Delta}\frac{d\hat{K}_n^{\,s}_c}{dv}\right] = 0$$

Condition 4.16, 1 Eq:
$$K_2 = K_1 + K_3$$

Condition 4.17, 2 Eqs:
$$C_1 K_1' = C_2 K_2'$$
$$C_2 K_2' = C_3 K_3'$$
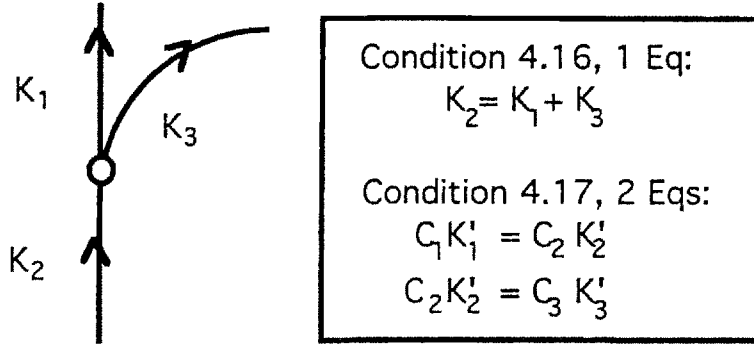
Figure 4.3. Application of boundary conditions

The final step is to consider the Fourier-analyzed forms of (4.1-2). What makes the integral form of the model tractable is that the integration over ϕ' can be done analytically once the series form of $\vec{K}$ is introduced. The algebraic details are less than transparent and will be left for Appendix A; for our purposes here we can express the contribution of a single sheet current to the various components of $\vec{A}$ as

$$(4.18) \quad A_R = \int dv' \left(G_{Rv,o}\hat{K}_o + \sum_n G_{Rv,n}^{\ c\ s}\ \hat{K}_n^{\ c\ s} \mp \frac{G_{R\phi,n}^{\ c\ s}}{nQ'}\frac{d\hat{K}_n^{\ s\ c}}{dv'} \right)$$

$$(4.19) \quad A_Z = \int dv' \left(G_{Zv,o}\hat{K}_o + \sum_n G_{Zv,n}^{\ c\ s}\ \hat{K}_n^{\ c\ s} \mp \frac{G_{Z\phi,n}^{\ c\ s}}{nQ'}\frac{d\hat{K}_n^{\ s\ c}}{dv'} \right)$$

$$(4.20) \quad A_\phi = \int dv' \left(G_{\phi\phi,o}K_{\phi,o} + \sum_n G_{\phi v,n}^{\ c\ s}\ \hat{K}_n^{\ c\ s} \mp \frac{G_{\phi\phi,n}^{\ c\ s}}{nQ'}\frac{d\hat{K}_n^{\ s\ c}}{dv'} \right)$$

There is a corresponding set of equations for $\vec{B}$. The use of the cylindrical components of $\vec{A}$ rather than the TNB is meant to emphasize an important point. The above expressions are valid only when the source coordinates and observation coordinates are in the same frame of reference, which is the frame where the source has an axisymmetric geometry. However, in general the observation point will not be in the same frame as the source (e.g., evaluating the contribution from a plasma shell at a point on the wall during a non-axisymmetric displacement). Thus the components of $\vec{A}$ which appear in equations (4.13-15) are not those which appear above. Let us denote the

82

closed-form results for the case where source and observation point are in the same frame by $\overline{\mathbf{A}}_{cf}$. Then at an arbitrary observation point, $\overrightarrow{\mathbf{A}}$ is calculated from

$$(4.21) \quad \overrightarrow{\mathbf{A}}(\overrightarrow{r}) = \sum_N \overline{\overline{\mathbf{M}}}_N \cdot \overline{\mathbf{A}}_{cf,N}(\overline{\overline{\mathbf{M}}}_N^{-1} \cdot \overrightarrow{r})$$

where $\overline{\overline{\mathbf{M}}}_N$ is the proper transformation tensor from the Nth shell to the observation frame; it is a function of the shift, tilt, and rotation between frames given by the parameters $(\Delta_x, \Delta_y, \Delta_z)$ and $(\phi_{xz}, \phi_{yz}, \phi_{xy})$ introduced in Chapter 2. The exact form is given in Appendix A. The tangential and toroidal components of $\overrightarrow{\mathbf{A}}$ in the observation frame can only be calculated after all three cylindrical components are found in the source frame.

Why is this important? First, it introduces additional bookkeeping to the problem, to insure that the right quantities are calculated in the right coordinate frames. Second and more important, it prevents the analytic Fourier analysis represented by the remaining ϕ integrals in equations (4.13-15). Thus, there is considerable cross-coupling between the different harmonics in the Fourier series and exactly where to truncate the series becomes a delicate issue. For applications where there is a single geometrically axisymmetric coordinate frame, it should be noted that the remaining ϕ integrals in the equations become trivial and the system simplifies greatly.

We see that the Fourier-analyzed equations (4.13-15) accomplish more than a reduction of the ϕ dependence to $2n+1$ functions for each component of current; the zeroth-order poloidal current is reduced to a scalar (but time-dependent) unknown, and the higher-order toroidal current can be expressed purely in terms of the poloidal component. For N sheets and n harmonics, the computational system consists of N functions of time and $N(2n+1)$ functions of time and poloidal angle. The next step in deriving the numerical model is to discretize the time dependence.

4.3 Time Discretization

The standard methods of handling time dependence in computation involve representing time derivatives by combinations of the unknown quantities evaluated at

discrete instants of time, all but one in the "past" relative to the evolution of the simulation. Some schemes are quite clever and involved, enabling the system of equations to evolve over large and arbitrarily sized time increments by taking as much advantage of the assumed smoothness of the system as possible.

For the problem of halo currents, however, we must commit an apparent cardinal sin by completely ignoring all such techniques. In some cases this is because the necessary overhead becomes too expensive given the presence of spatial integral operators; more importantly, in all cases it is because of the assumed smoothness of the system in these schemes. The sheet-current equations are not smooth; in fact, they suffer from finite discontinuities in both time and space as the plasma impacts the wall. In addition, since the plasma shape and trajectory is itself a function of time (and in principle unknown, prior to the introduction of the penalty function), there is no robust method for invoking a high-order technique at times when the system is smooth, then switching to a specialized technique as the jumps occur. Consider the illustration in figure (4.9) of section 4.5: the plasma strikes the wall in discrete steps as subsequent shells impact. The region of overlap also grows in finite increments. Thus, at a fixed poloidal location on the wall, the toroidal current can jump by quite large amounts from one instant of time to the next. Thus we are restricted to the simplest of all possible schemes:

$$(4.22) \quad \frac{dx}{dt}\bigg|_{t=t'+\Delta t} \approx \frac{x(t'+\Delta t) - x(t')}{\Delta t}$$

which will, unfortunately, require that the system be evolved over fairly small time steps (10 μs at best) relative to the time scales of interest (say, 5ms). While a few hundred time steps sounds modest, it must be recalled that each time step will still require the solution of a fairly complicated set of spatial equations, so that each step could take up to several minutes of CPU time on a workstation.

Given that the solutions do exhibit finite discontinuities in time, one may wonder how the time derivative can be defined at all. However, this is really due to the choice of writing this system as differential in time. Since it is first order, one could easily choose to re-write the equation

84

$$(4.23) \quad \frac{dx}{dt} = f(x,t), \; x(t=0) = x_o$$

in the completely equivalent form

$$(4.24) \quad x(t) = x_o + \int_0^t f(x(t'),t') \, dt'$$

where the discontinuity is handled naturally under the integral sign. Applying a first-order accurate numerical scheme to equation (4.24) yields the same set of difference equations as obtained by using (4.22) in (4.23).

As an example of the explicit form of the resulting discretized equations, consider equation (4.14):

$$(4.25) \quad \frac{\Delta t R K_{\phi,o}(v,t')}{\sigma \Delta} + \int \frac{d\phi}{2\pi} RA_\phi \bigg|_{t=t'} = \int \frac{d\phi}{2\pi} RA_\phi \bigg|_{t=t'-\Delta t}$$

where t' is the current time-step in the simulation. Recalling that A_ϕ is itself an integral over the currents, we can see now the form of the purely spatial system that remains: an inhomogeneous Fredholm equation of the second kind, one-dimensional in the coordinate v. We can also see the importance of using the total time derivative: at any time step t', the source term needed on the right is exactly the second term on the left from step t'-Δt, including all geometrical changes. This eliminates the need to re-evaluate all the integrals in the source term, which is in general an extremely expensive operation.

Labeling this "old flux" source term as S , we now have a set of N+N(2n+1) purely spatial equations that are marched through discrete values of $t_i = i \Delta t$, i = 1, 2, 3.... The source term for i=1 is fully specified by the initial conditions. Thus, for each of the N sheets,

$$(4.26) \quad \hat{K}_o(t_i) \int \frac{\Delta t Q}{\sigma \Delta R} \, dv + \iint \frac{A_v Q}{2\pi} \, dv \, d\phi \bigg|_{t_i} = \hat{S}_o(t_{i-1})$$

85

$$(4.27) \quad \frac{\Delta t R K_{\phi,o}(v,t_i)}{\sigma \Delta} + \int \frac{d\phi}{2\pi} R A_\phi \Big|_{t_i} = S_o(v,t_{i-1})$$

$$(4.28) \quad \frac{d}{dv}\left(\mp \frac{\Delta t R}{nQ\sigma\Delta} \frac{d\hat{K}_n^{\tilde{c}}}{dv}\right) \pm \frac{\Delta t nQ}{\sigma\Delta R} \hat{K}_n^{\tilde{c}} + \int \frac{d\phi}{\pi}\left(-\frac{\cos(n\phi)}{\sin(n\phi)}\frac{d}{dv}(R A_\phi) \pm nQ A_v \frac{\sin(n\phi)}{\cos(n\phi)}\right) = S_n^{\tilde{c}}(v,t_{i-1})$$

where the vector potential terms couple all n harmonics of the current on all sheets, as prescribed by equations (4.18-21).

4.4 Poloidal Finite-Element Analysis

The sheet current model has been reduced at this stage to a set of coupled linear one-dimensional equations, which is historically a desirable outcome. However, the model is not yet in a form which can be turned over to standard numerical packages, for two principal reasons. First, there are few commercial integral equation solvers. Second (and most significant), each equation has its own character. Equation (4.26) is purely a difference equation in time, where the spatial dependence under the integral operators is determined by geometry and the other equations; at each time step, it yields a constant, the zeroth-order poloidal current on a sheet. Equation (4.27) is an inhomogeneous Fredholm integral equation of the second kind; it requires no explicit boundary conditions and allows finite spatial discontinuities. It yields a function of poloidal angle, the zeroth-order toroidal current density on a sheet. Equation (4.28) has both an integral operator and a differential operator of second order; it must satisfy two explicit boundary conditions and the solutions, which are the higher-order poloidal current densities as functions of poloidal angle, must be continuous with derivatives that are either continuous or contain jumps fully specified by geometrical properties. The result is that each equation must be handled with a slightly different numerical scheme.

The primary issue is choosing an appropriate poloidal representation of the currents. The zeroth-order toroidal current is inherently discontinuous as the plasma strikes the wall; the higher-order current can exhibit slope discontinuities caused by sharp transitions in the geometry of the vacuum chamber. Thus, spectral methods (Fourier

analysis and orthogonal polynomials, for example) are not applicable. Instead we choose the compact basis functions available with finite-element analysis [2].
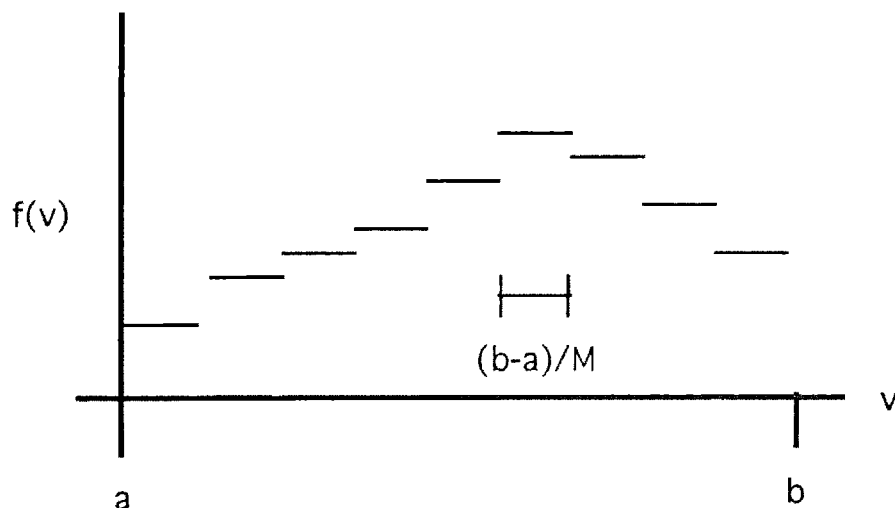
Figure 4.4. Piecewise constant elements

We will see in the following section that a successful computer code will require dynamic remeshing and careful division of the spatial problem into multiple regions, such that the spatial profiles are allowed to "break" at intersections between the wall and the plasma. Even with these capabilities, however, it turns out that even minimal coupling between neighboring elements of toroidal currents will cause severe problems near the discontinuities, mostly because the location of an intersection point can be found with limited precision. We are therefore required to represent the zeroth-order toroidal current by *piecewise constant* elements, so that in a computational domain bounded by poloidal angles a and b, using M elements,

$$(4.29) \qquad K_{\phi,o}(v) = \sum_{i=1}^{M} K_i \, P_i(v); \quad h \equiv \frac{b-a}{M}$$

$$P_i(v) = 1, \, (i-1)h < v < i\,h;$$
$$P_i(v) = 0, \, v < (i-1)h \text{ or } v > i\,h$$

The shape of these elements is shown in figure (4.4).

Since the equation for the higher-order currents has a second-order differential operator, clearly the piecewise constant elements will not suffice. As we will see shortly, however, it is only necessary that the basis functions have a well-defined first derivative. We will therefore use linear finite elements, which have the following form for a domain broken into M+1 elements:

$$(4.30) \qquad \hat{K}_n^{\stackrel{s}{c}}(v) = \sum_{i=1}^{M} \hat{K}_{n,i}^{\stackrel{s}{c}} L_i(v); \quad h \equiv \frac{b-a}{M}$$

$$1 < i < M+1: \quad L_i(v) = \frac{v - (i-2)h}{h}, \ (i-2)h \leq v < (i-1)h;$$

$$L_i(v) = 1 - \frac{v - (i-1)h}{h}, \ (i-1)h \leq v < i\,h;$$

$$L_i(v) = 0, \ v < (i-2)h \ \text{or} \ v > i\,h$$

$$i=1: \quad L_1(v) = 1 - \frac{v - a}{h}, \ a \leq v < a+h;$$

$$L_1(v) = 0, \ v > a+h$$

$$i=M+1: \quad L_{M+1}(v) = \frac{v - (b-h)}{h}, \ b-h \leq v < b;$$

$$L_{M+1}(v) = 0, \ v < b$$
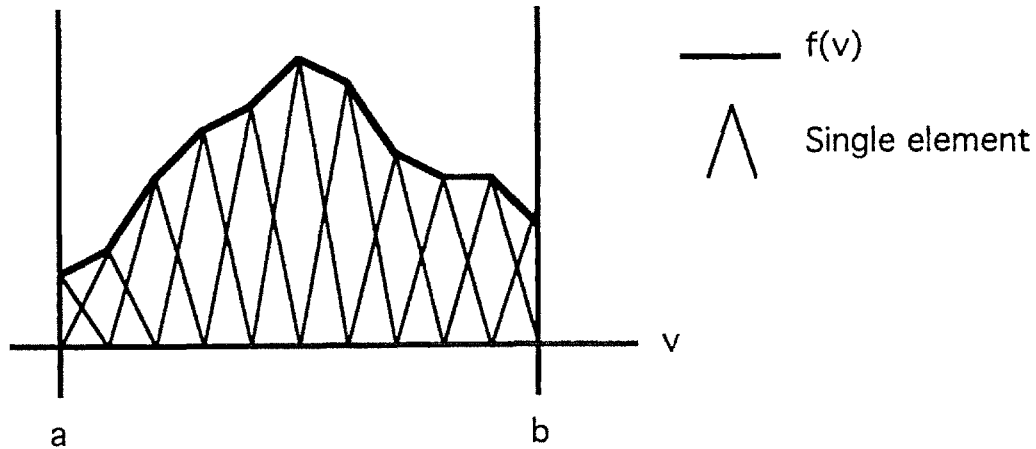
Figure 4.5 Linear finite elements

These elements are illustrated in figure (4.5). Once this functional dependence has been established, it takes just a few more tedious but straightforward steps to turn the equations into a linear algebra system. First, we may substitute the basis functions into

equations (4.18-20), yielding the contribution to the vector potential from a single computational domain on a single sheet (the need for multiple domains on a single sheet will be addressed in the next section):

$$(4.31) \quad A_R = \hat{K}_o \int dv' \, G_{Rv,o} + \sum_M \sum_n \hat{K}_{n,m}^{\substack{c \\ s}} \int dv' \left(G_{Rv,n}^{\substack{c \\ s}} L_m(v') \mp \frac{G_{R\phi,n}^{\substack{c \\ s}}}{nQ'} \frac{dL_m(v')}{dv'} \right)$$

$$(4.32) \quad A_Z = \hat{K}_o \int dv' \, G_{Zv,o} + \sum_M \sum_n \hat{K}_{n,m}^{\substack{c \\ s}} \int dv' \left(G_{Zv,n}^{\substack{c \\ s}} L_m(v') \mp \frac{G_{Z\phi,n}^{\substack{c \\ s}}}{nQ'} \frac{dL_m(v')}{dv'} \right)$$

$$(4.33) \quad A_\phi = \sum_M K_{\phi,m} \int dv' \, G_{\phi\phi,o} L_m(v') + \sum_M \sum_n \hat{K}_{n,m}^{\substack{c \\ s}} \int dv' \left(G_{\phi v,n}^{\substack{c \\ s}} L_m(v') \mp \frac{G_{\phi\phi,n}^{\substack{c \\ s}}}{nQ'} \frac{dL_m(v')}{dv'} \right)$$

If we introduce a vector of unknowns which is composed of all of the undetermined constants in the currents,

$$\vec{U} = \{\hat{K}_{o,1}, \ldots, \hat{K}_{o,N}, K_{\phi,1,1}, \ldots, K_{\phi,M,Nd}, \hat{K}_{0,1,1}^{\substack{c \\ s}}, \ldots, \hat{K}_{n,M+1,Nd}^{\substack{c \\ s}}\}$$

where N is the number of sheets and N_d the total number of computational domains on all sheets, then we can use a $3 \times (N + MN_d + 2n(M+1)N_d)$ matrix $\overline{\overline{a}}$ to calculate $\vec{A}$ at any point. The elements of $\overline{\overline{a}}$ can be identified directly from equations (4.31-33). In general, from (4.21),

$$(4.34) \quad \vec{A}(\vec{r}) = \sum_{Nd} \overline{\overline{M}}_{N(Nd)} \cdot (\overline{\overline{a}}_{cf,N(Nd)}(\overline{\overline{M}}_N^{-1} \cdot \vec{r}) \cdot \vec{U}_{N(Nd)})$$

where $N(N_d)$ refers to the sheet to which a particular domain N_d belongs; similarly, $\vec{U}_{N(Nd)}$ refers to the subset of $\vec{U}$ on a particular sheet. The reasons for letting a good deal of notation remain understood rather than always using it explicitly should now be quite clear; hereafter, the whole issue of different reference frames will be suppressed and we will write simply

$$(4.35) \quad A_v(v,\phi) = \vec{a}_v(v,\phi) \cdot \vec{U}, \quad A_\phi(v,\phi) = \vec{a}_\phi(v,\phi) \cdot \vec{U}$$

A completely analogous process leads to

$$(4.36) \quad B_v(v,\phi) = \vec{b}_v(v,\phi) \cdot \vec{U}, \quad B_\phi(v,\phi) = \vec{b}_\phi(v,\phi) \cdot \vec{U}, \quad B_\rho(v,\phi) = \vec{b}_\rho(v,\phi) \cdot \vec{U}$$

The remaining step is to insert (4.35) into (4.26-28) and discretize the equations themselves so that we have a set of $N + MN_d + 2n(M+1)N_d$ unique equations for that same number of unknowns. Equation (4.26) requires no further work:

$$(4.37) \quad U_j(t_i) \int \frac{\Delta t Q}{\sigma \Delta R} \, dv + \vec{U} \cdot \iint \frac{\vec{a}_v(v,\phi)Q}{2\pi} \, dv \, d\phi \bigg|_{t_i} = \hat{S}_o(t_{i-1})$$

yielding N equations for j = 1,...,N. Applying the method of *collocation*, where an equation is enforced only at discrete points characteristic to the basis functions, to equation (4.27) yields MN_d equations for the discretized zeroth-order toroidal current. The collocation points associated with $P_i(v)$ are the midpoints of the elements, which in the notation used previously are $v_i = a + (i - \frac{1}{2})h$.

$$(4.38) \quad U_j \frac{\Delta t R P_j(v_j,t_i)}{\sigma \Delta} + \vec{U} \cdot \int \frac{d\phi}{2\pi} R \vec{a}_\phi(v_j,\phi) \bigg|_{t_i} = S_o(v_j,t_{i-1})$$

where j cycles through the M elements in each computational domain, j = $N+1,...,N+MN_d$.

Since our basis functions $L_i(v)$ do not have a second derivative, we must treat (4.28) with a slightly different method, the *Galerkin* method [2], which basically involves "projecting" the unknown function onto the L_i's by taking the inner product of equation (4.28) with each of the L_i's in turn. Integration by parts eliminates the second derivative.

For the first term on the left hand side of (4.28), we get in each domain

$$\pm L_i(v)\frac{\Delta tR}{nQ\sigma\Delta}\sum_M \hat{K}_{n,m}^{\overset{s}{c}}\frac{dL_m}{dv}\Big|_a^b \mp \sum_M \hat{K}_{n,m}^{\overset{s}{c}}\int \frac{dL_i}{dv}\frac{dL_m}{dv}\frac{\Delta tR}{nQ\sigma\Delta}dv$$

The second term and last term on the left side become

$$\mp \sum_M \hat{K}_{n,m}^{\overset{s}{c}}\int \frac{\Delta tnQ}{\sigma\Delta R}L_i L_m\, dv \pm \vec{U}\cdot\iint \frac{1}{\pi}d\phi dv\, L_i(v)nQ\vec{a}_v(v,\phi)\frac{\sin(n\phi)}{\cos(n\phi)}$$

The first term under the integral sign of (4.28) is

$$\vec{U}\cdot\left(-L_i(v)\int \frac{d\phi}{\pi}\frac{\cos(n\phi)}{\sin(n\phi)}R\vec{a}_\phi(v,\phi)\Big|_{v=a}^{v=b} + \iint \frac{1}{\pi}d\phi dv\frac{dL_i}{dv}\frac{\cos(n\phi)}{\sin(n\phi)}R\vec{a}_\phi(v,\phi)\right)$$

and the source term is simply $\int L_i(v)S_n^{\overset{s}{c}}(v)dv$.

In common applications of the Galerkin technique, the boundary terms can be implemented explicitly and a given domain actually uses only the interior finite elements, 2...M. As we will see in the next section, linking one domain to its neighbor is not so simple in our application, so the full 1...M+1 elements are maintained. Instead of using the inner products of (4.28) with L_1 and L_{M+1}, we add the boundary conditions (4.16-17) to the system of equations. This actually simplifies the process slightly since the boundary terms in the above expressions never appear, as the interior L_i's are zero at these points. For completeness, then, the final form of the equation is

$$(4.39)\quad \vec{U}\cdot\left(\iint \frac{1}{\pi}d\phi dv\left[\frac{\cos(n\phi)}{\sin(n\phi)}\frac{dL_i}{dv}R\vec{a}_\phi(v,\phi)\pm L_i(v)nQ\vec{a}_v(v,\phi)\frac{\sin(n\phi)}{\cos(n\phi)}\right]\right)\mp$$

$$\sum_M \hat{K}_{n,m}^{\overset{s}{c}}\int\left(\frac{\Delta tnQ}{\sigma\Delta R}L_i L_m + \frac{dL_i}{dv}\frac{dL_m}{dv}\frac{\Delta tR}{nQ\sigma\Delta}\right)dv = \int L_i(v)S_n^{\overset{s}{c}}(v)dv$$

Letting the i's run through all N_d domains, M+1 elements, n harmonics, and sine-cosine pairs completes the set of equations. Grouped together with (4.36-37) they now form a closed linear-algebra system which can be written

$$(4.40) \quad \overline{\overline{A}}(t_i) \cdot \vec{U}(t_i) = \vec{S}(t_{i-1})$$

and solved by standard numerical procedures at each step in time.

4.5 Bookkeeping Issues

The simple fact that the plasma does hit the wall after starting as a distinct object introduces a host of complications when it comes to writing a code capable of handling realistic disruptions. It is rather unfortunate that the majority of effort in writing such a code goes to these "bookkeeping" issues rather than dealing with the inherent mathematical or physical nature of the system. Among the difficulties are resolving
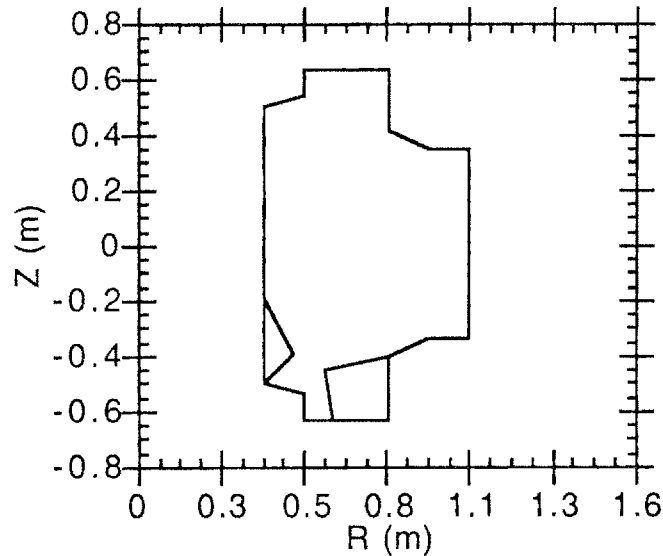
Figure 4.6. Linear-segment, thin-shell model of Alcator C-MOD vessel, with simple divertor structure

complicated time-dependent geometries, the need for dynamic remeshing, the fact that the number of unknowns (physical, not computational!) varies with time, proper implementation of boundary conditions, and above all the need to minimize how often one has to evaluate the triple integrals in (4.39) (especially given that the integrand itself must be calculated by an iterative procedure, as per Appendix A). While all but the last problem are treated to some degree in existing specialized commercial algorithms, there are no such common "black box" routines for integral and integro-differential equations. This section will discuss how some of the more significant issues are handled in TSPS-

3D, both as an illustration for someone pursuing related work and to give some appreciation as to why arriving at equation (4.40) is at most half the battle.

Consider first the thin-shell model of the Alcator C-MOD vacuum chamber shown in figure (4.6). One could describe it as a fairly compartmentalized structure, which therefore requires a multitude of reasonably sharp corners. Even with some artificial smoothing of the corners, it would require a very large number of Fourier harmonics to represent the innermost surface as a function of a single poloidal angle; there would then be the problem of working in the additional structures beneath the segments representing the inner and outer divertor plates. We choose instead to represent the chamber by a set of N_{wall} distinct linear segments, each one parameterized in terms of a normalized arc length (which we can still call v to minimize symbols) ranging from 0 to 1. Thus a segment starting at (R_s, Z_s) and ending at (R_e, Z_e) has the simple representation

$$R(v) = R_s + v \ (R_e - R_s), \qquad \frac{dR}{dv} = (R_e - R_s)$$

$$Z(v) = Z_s + v \ (Z_e - Z_s), \qquad \frac{dZ}{dv} = (Z_e - Z_s)$$

The poloidal derivatives have well defined one-sided limits, which is all that is necessary under the integrals. The values located exactly at a corner are not defined, but do not need to be. Each segment is identified by a number j ranging from 1 to N_{wall}, so the code can access the wall geometry at any time by evaluating user-supplied functions $R_j(v)$ and $Z_j(v)$.

An obvious advantage of using distinct segments is that it ensures that the piecewise constant finite elements will "break" naturally at the corners, which are locations where the zeroth-order toroidal current is free to become discontinuous.

The plasma geometry is parameterized as in section 4.1, so here the user supplies N functions for $R_o(t)$, $Z_o(t)$, $a(t)$, $\kappa(t)$, and $d(t)$ (which is a hybrid of the parameters discussed, a compromise giving κ to the physicists and d to the programmer). The parameter is always the angular coordinate v, but the range cannot be fixed to 0 to 2π. It

must be able to "float" modulo 2π so that, for example, both cases illustrated in figure (4.7) can be treated as unbroken segments.
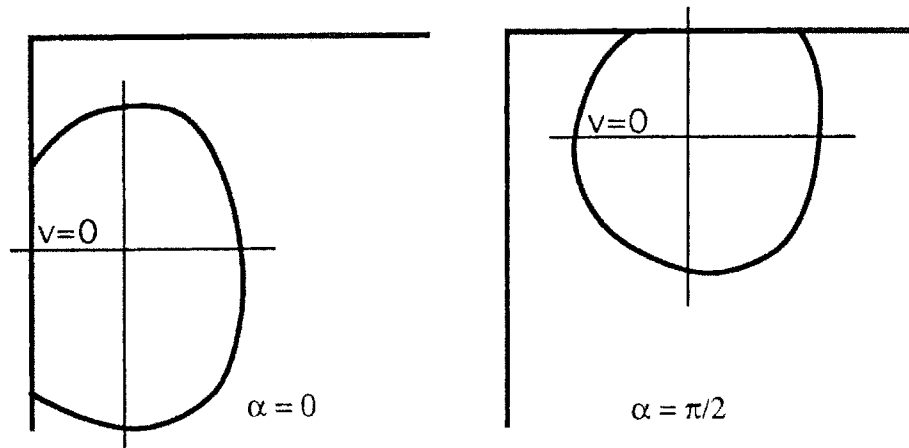
Figure 4.7. Coordinate offset to keep plasma a single segment

The need for dynamic remeshing is twofold. The first is simply to obtain sufficient numerical convergence without unnecessary elements. Consider a plasma whose equilibrium position is close to the inboard wall, as is common on C-MOD. As the plasma disrupts, at its typical disruption velocity $\sim 100\text{m/s}$, a one-millimeter displacement drives the eddy current profile shown to the right in figure (4.8). To the right is a "close-up". A simple rectangular chamber was used for these pictures.
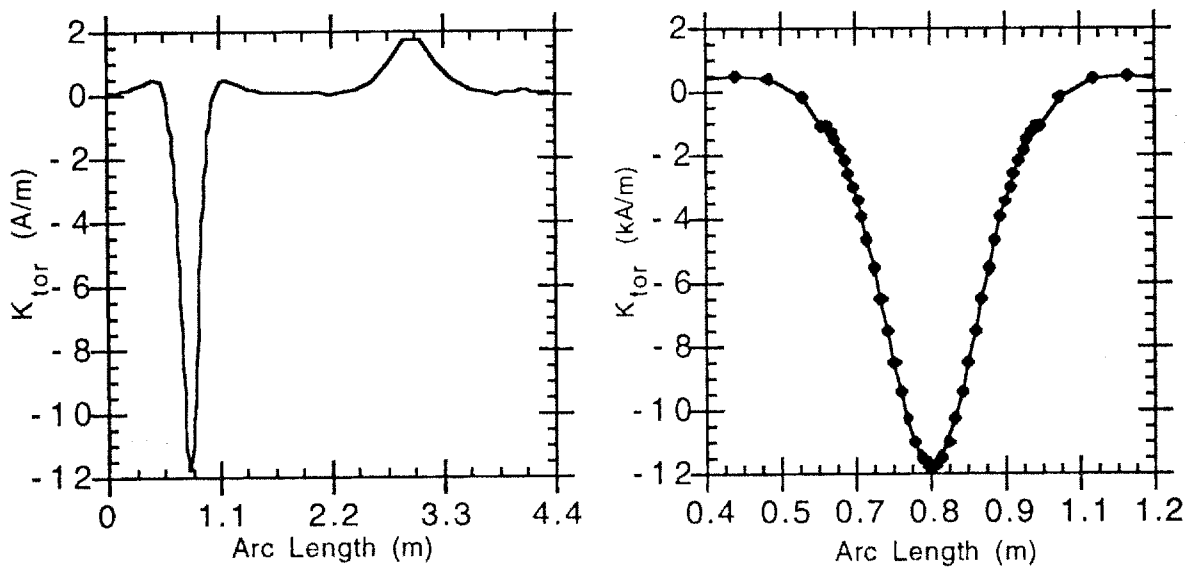
Figure 4.8. Example of sharp eddy-current features, requiring dynamic remeshing.

94

A much stronger reason for using remeshing is evident as the plasma strikes the wall. Recall from Chapter 3 the concept of the *peel-off* model; that is, as the plasma dissipates against the wall, the current which was flowing in that region of the plasma is "absorbed" into the wall as a consequence of continuity and flux conservation. As one moves poloidally along the wall, there is a sharp discontinuity in the wall's current profile at the boundary between regions where the plasma is touching the wall and where it is not. There are at least two such contact points *per shell* in this model (more for complicated wall shapes), and each point moves with time; in order to accommodate the discontinuities, each point must correspond to the boundary of a computational domain. An illustration of this in figure (4.9). In addition, the interior regions may be split into additional domains to resolve the profile, since the number of finite elements per domain is fixed.
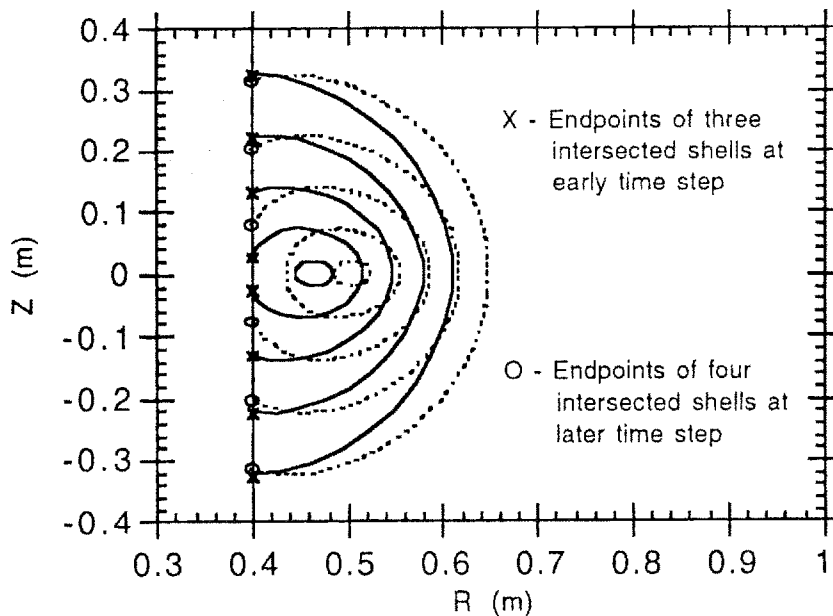
Figure 4.9. As the plasma impacts the wall, regions overlapped by different numbers of shells, associated with jumps in the current profile, are functions of time.

Finding the intersection points is one of many computational issues which are conceptually trivial but in practice not so simple. The problem can be expressed quite clearly: for each shell, an intersection point with the wall is found by solving

$$R_{wall}(v') = R_{plasma}(v); \qquad Z_{wall}(v') = Z_{plasma}(v)$$

for the unknowns v and v'. This is an exercise in nonlinear root-finding [3]. The difficulty is that in any segment of the wall, there could be zero, one, or two roots; of course, the only way to ascertain that the plasma has hit the wall is to try and solve the above equations at every time step and see if proper solutions exist. Prior to plasma impact there is no good way to define the initial guess most root-finding routines require. In an effort to avoid having root-finding dominate each time step, the present version of TSPS-3D limits the wall geometry to linear segments and the plasma to the parameterization given in section 4.1; this way, the root-finding problem is reduced to finding the roots of a fourth-order polynomial. Thus the algorithm always solves for four roots, which can be done efficiently; these are then tested for being real and properly bounded.
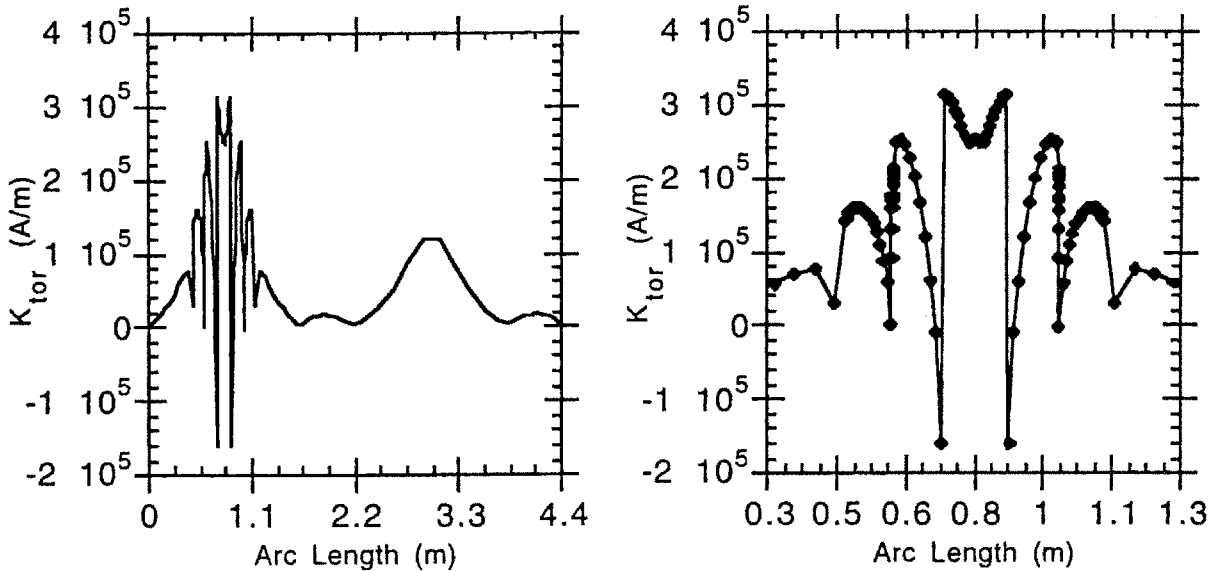
Figure 4.10. Toroidal current profile characteristic of contact with discrete plasma shells

Finally, it is the nature of the halo current problem that the finite jumps in the toroidal current will be superposed on the peaks of the eddy current features - but in the opposite direction! Thus even for a simple rectangular vacuum chamber it is necessary to handle profiles like those in figure (4.10). It takes some practice to see how the region in contact with the plasma (expanded on the right) is composed of a large negative peak

to which a series of three even larger positive steps of different widths have been added, representing the toroidal halo current from three shells. When such features are combined with the geometric effects of the true C-MOD vessel (the case for all results in Chapter 5), where the intersection points can slide over sharp corners, the result is considerably more complicated in appearance (and in the requisite numerical bookkeeping).

Another issue, whose effects are not as drastic as the previous one, is the fact that the number of physical unknowns associated with the model is a function of time. This does not refer to the introduction or destruction of individual computational domains as required by remeshing. It is again purely a consequence of having the plasma strike the wall. Consider the logical evolution of the plasma shells that were depicted in figure (4.9). At some later point in time, it is clear that the innermost shell will be completely "absorbed" into the wall, followed by the next innermost, until the entire plasma has vanished. A complete simulation will need to follow the evolution of the wall currents into their eventual resistive decay, and thus need to accommodate "destroying" the equations associated with a plasma sheet as it vanishes. There are no conceptual difficulties involved in this, but clearly the heavy coupling among all shells through the flux and fields requires that the programmer be very thorough in eliminating all the contributions of an "absorbed" shell. This is complicated by the desire to avoid re-calculating any quantity that need not be, as discussed below.

An additional time-dependence in the system of equations is slightly more subtle but considerably more difficult to handle. Consider the schematic representation of a plasma striking the lower divertor region of the C-MOD vacuum chamber, shown in figure (4.11). Consider that associated with every zeroth-order poloidal current there is a unique poloidal circuit: before the plasma hits the wall, there are $N+N_L$, composed of each sheet and an additional N_L which is the number of geometrical loops in the structure other than the innermost (e.g., two for the C-MOD chamber shown in figure 4.6). When the wall is not very smooth relative to the size of the plasma, however, additional loops are created and destroyed as the plasma hits the wall. In figure (4.11) we have a series starting with the two initial loops formed by the plasma and the wall; a third is created as the plasma "plugs" the divertor well; this third loop splits into two as the plasma hits the bottom of the well; then both of these additional loops vanish as the

plasma "spreads" to fill the divertor. As with the need to destroy equations as discussed above, there is no conceptual difficulty in creating new loops and the associated equations. However, in practice, the code must internally deduce all the quantities associated with the intersection points and boundary conditions.

New loop appears   New loop splits   New loops vanish
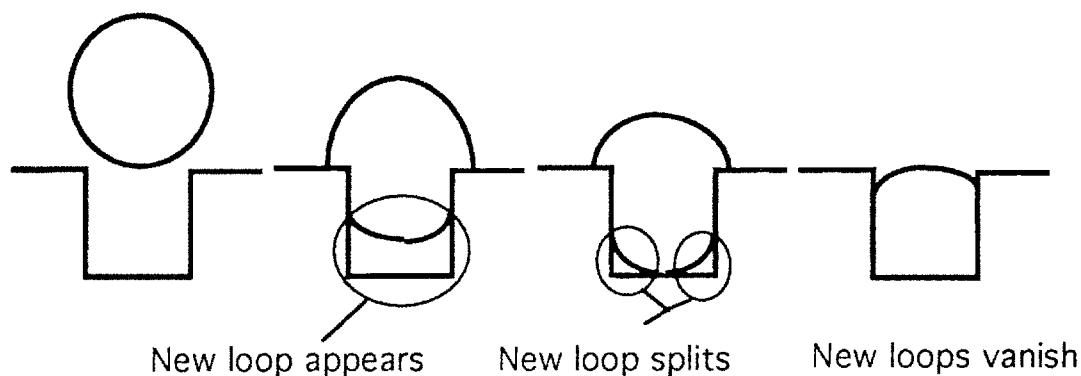
Figure 4.11. Creation and destruction of poloidal circuits

The code does this by treating each poloidal segment separately, rather than by finding all the different closed current paths. By integrating over only a segment instead of a closed loop, one needs to introduce terms representing the integral along a potential. The natural introduction of these "voltages" at each intersection provides the correct number of degrees of freedom to enforce both Faraday's law for the segment and the poloidal continuity boundary conditions.

The main bookkeeping issue is a question of sign. Referring again to figure (4.6), one can see that a positive poloidal current closing through the innermost segments of the wall and a positive poloidal current flowing through the small loop beneath the inner divertor will be flowing in opposite directions through the divertor plate itself! A solid convention must be maintained, especially to account for some of the more complicated wall-plasma intersections in something like the Alcator C-MOD divertor structure.

The non-axisymmetric current and the boundary conditions (4.16-17) that it satisfies introduces several similar issues. A compete explanation would require using too many conventions particular to the choices made when writing TSPS-3D, but a brief list of points can be given:

- Every domain is linked to the next by (4.16) and at least one application of (4.17). At intersection points, one must define which is the "main" path and which is the "spur" which will require an additional application of (4.17), as discussed in section 4.2
- The sign issue occurring with the zeroth-order current occurs here also. One must determine whether the current is flowing *into* the spur or *out* of it.
- As a purely numerical issue, one must make sure the correct sign is applied to element 1 or M+1 in a domain; the "in" and "out" directions of the spur are independent of its poloidal "top" and "bottom".

The last and most important bookkeeping issue relates to computation time. Because equation (4.39) contains triple integrals (v', v, ϕ), it is desirable to avoid any unnecessary recalculation of these terms. When the total number of degrees of freedom has grown large (~1800 or more for five shells and a single Fourier mode in the C-MOD vacuum chamber), the requisite calculation of the 1200x1200 triple integrals, where the integrands themselves require many calculations (especially for the high-order Green's functions, which are calculated through recurrence relations) can consume an amount of CPU time comparable to the subsequent matrix inversion. The major factor in reducing this time is to note that most of the matrix does *not* change from time step to time step; only those elements coupled to the plasma or to wall segments which have been remeshed will change. Thus in TSPS-3D a table is maintained which notes which segments that are "new" at any given time step. Only the matrix elements coupled to those (one row and one column for each - out of over a thousand) are recalculated.

In addition, it was discussed in section (4.2) that the source term is directly related to terms used in the matrix from the previous time step. Thus $\overline{\overline{A}}$ is actually stored as two parts, $\overline{\overline{R}} + \overline{\overline{L}}$, where $\overline{\overline{L}} \cdot \overline{U}$ is the source for the next time step. Only remeshed elements (which have "moved" computationally but not physically) need to have their source terms calculated independently. Splitting the matrix does require that the code use considerable amounts of core memory, but the results are worth it. In addition, due to the compact coupling of the finite elements, $\overline{\overline{R}}$ (roughly a matrix of resistances) is fairly sparse.

99

All of these bookkeeping issues have been resolved in a reasonably robust fashion in TSPS-3D. In the next chapter we will finally examine results of TSPS-3D simulations for realistic cases, and concentrate solely on the answers as opposed to how they were obtained.

4.6 References

1. Scott W. Haney. *Methods for the Design and Optimization of Shaped Tokamaks*. Ph.D. thesis, Massachusetts Institute of Technology. 1988

2. G. Strang, G. J. Fix. *An Analysis of the Finite Element Method*. Prentice-Hall, 1973

3. Press, Teukolsky, Vetterling, Flannery. *Numerical Recipes in FORTRAN: The Art of Scientific Computing*. Second edition. Cambridge University Press, 1992

Chapter 5.

Numerical Results

Chapter 5. Numerical Results

Chipping away at the sheet current model with highly simplified and idealized situations can yield only so much information, especially when one needs to weigh the influences of competing effects which have comparable magnitudes. Eventually one must turn to the computer to produce hard numbers. A fast, flexible computer code called the Three-Dimensional Tokamak/Shell Plasma Simulator, or TSPS-3D, has been written to solve the sheet current equations, using the techniques outlined in the previous chapter. In this chapter we will examine some sample runs, looking at both two and three dimensional effects.

An interesting and old problem will arise: how to present time-dependent, three-dimensional data in a static, two-dimensional form? A variety of plot types will be used; hopefully some subset will appeal to the individual reader and convey the desired information. The best methods for presenting this type of data, using color and interactive animations, are unfortunately not yet incorporated into a printed page!

The proper route for introducing a new computational model is to show that it agrees with existing experimental data before using it as a predictive tool. However, the complicated poloidal cross section of the Alcator vacuum chamber produces data that can be somewhat difficult to interpret without practice; we will therefore break with convention and first examine some alternative TSPS runs which are done with realistic plasmas but a simple rectangular vacuum chamber. Once the reader is familiar with the "feel" of TSPS output we will move on to code verification using Alcator data. We will then return to the simpler vacuum chamber to do scaling runs by varying several tokamak and plasma parameters; non-axisymmetric effects are not as easy to parameterize and so will be considered separately. Finally, we will take a brief look at the computational time required to produce these results.

5.1 The Reference TSPS-3D Run

To examine the behavior of halo currents versus various plasma and tokamak parameters, it is necessary to establish a reference case. We will do this by considering a rectangular vacuum vessel constructed of stainless steel, with a uniform thickness of

one centimeter. The poloidal cross section of the chamber is 50cm wide (in R) and 60cm high (in Z), centered at a major radius of 75cm. The "typical" plasma it contains is circular and has a major radius of 70cm, shifted slightly inwards from the geometric center of the chamber to bring its behavior closer to typical Alcator C-MOD plasmas, which lean quite close to the inboard wall. The corresponding minor radius for the reference case is 18cm. The toroidal field has a value of 5.3T at the plasma major radius. The external poloidal field is dominantly vertical, and held constant in time for simplicity. Since the plasma intersection points in this geometry will consist of a only a single pair per shell, this case makes a nice starting point before moving on to Alcator with its intricate divertor.

The displacement for this reference run is purely axisymmetric, so that we may later compare the decidedly different character of currents generated by non-axisymmetric displacements. Obviously, the only mechanism to introduce asymmetries into an axisymmetric equilibrium is the displacement, so that the currents for this run will also remain purely axisymmetric.

The direction of the displacement is purely vertical, downwards to conform to the typical Alcator VDE although this geometry does not offer a divertor X-point to establish a preferential direction. The plasma velocity is 85m/s. The simulation begins after a presumed thermal quench, so that the bulk plasma temperature is 40eV, corresponding to a Spitzer conductivity of about 0.45 Mmho/m. The simulation lasts for 5.8ms, ending a few hundred microseconds after the last of the plasma has dissipated against the wall. The plasma is represented by five current sheets; snapshots showing the plasma trajectory and chamber geometry are given in figure (5.1).

t = 0 ms

t = 0.58 ms

t = 1.74 ms

t = 2.90 ms
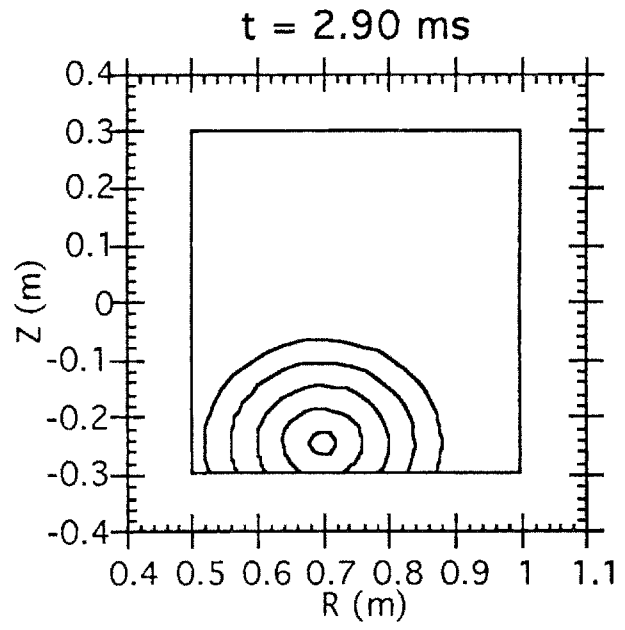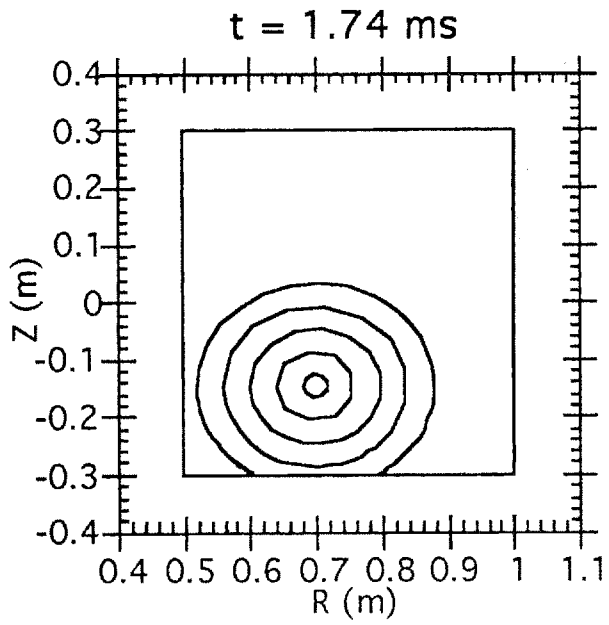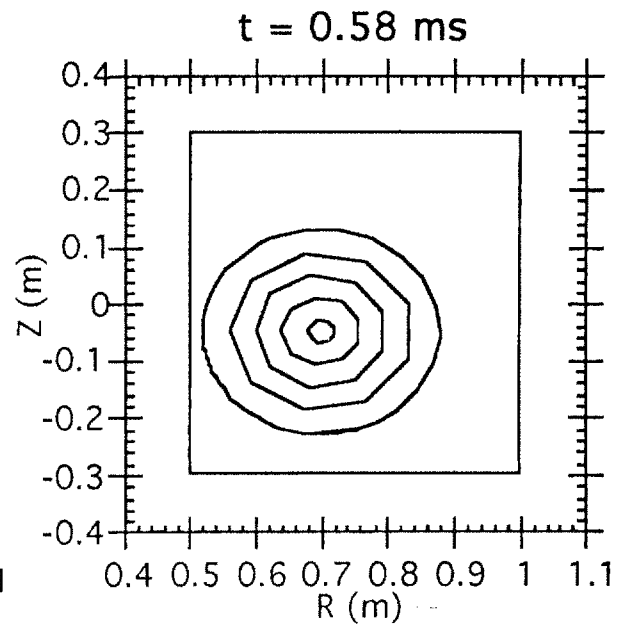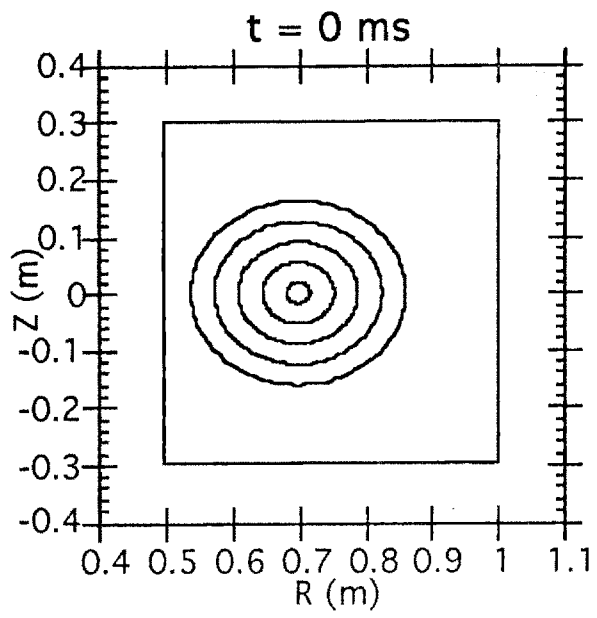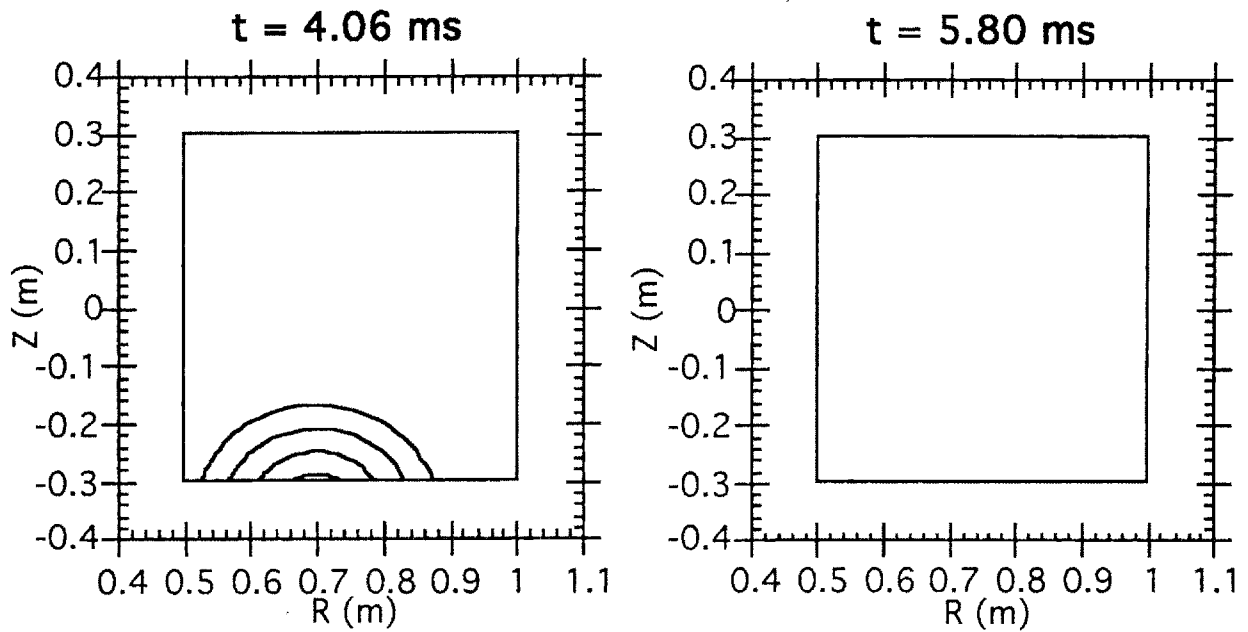
Figure 5.1. Snapshots of the "reference" disruption.
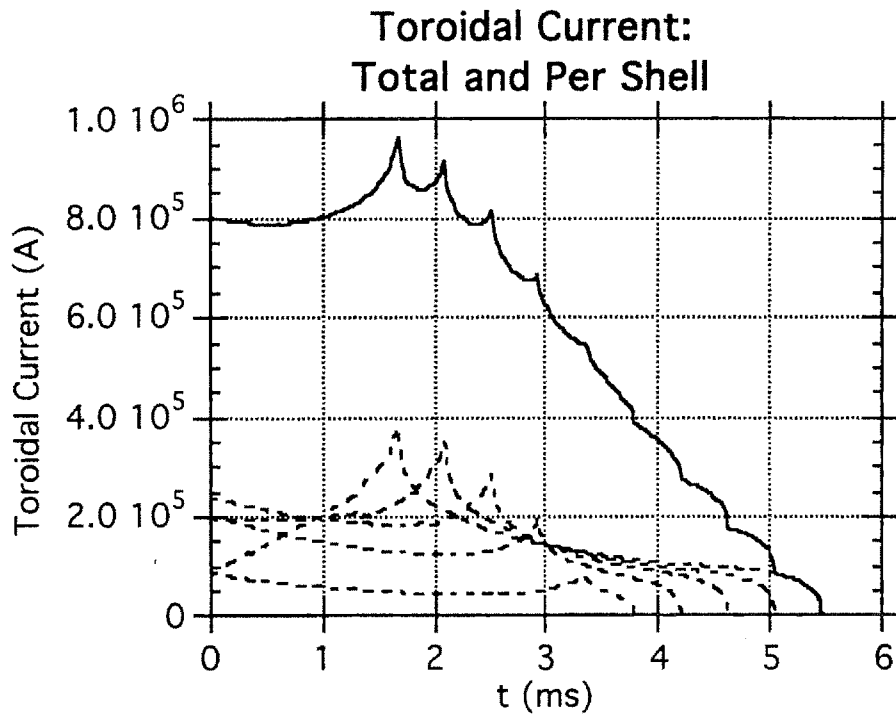
Figure 5.2. Evolution of the toroidal plasma current.

105
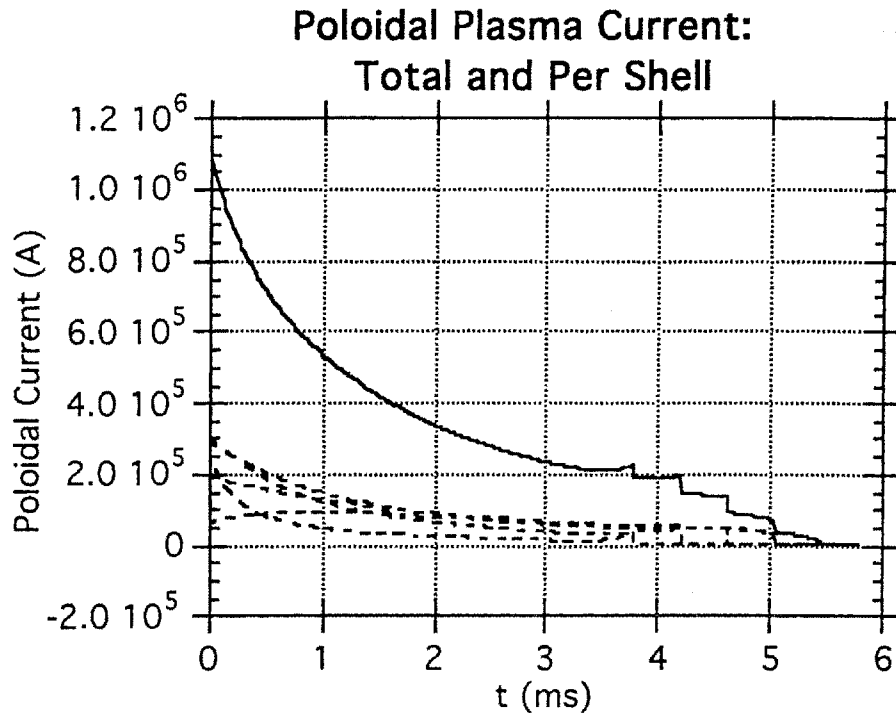
Figure 5.3. Evolution of the poloidal plasma current.

The evolution of the total plasma current as well as the current in each shell is shown in figure (5.2). At very early times, the dominant change in the plasma current is resistive decay. Before long, however, the current begins to grow due to the interaction with the toroidal image currents driven in the chamber (which are substantial, as we will see shortly). This growth peaks just before the plasma hits the chamber, whereupon the current is "peeled off" by the wall; the subsequent drop in the plasma current is then quite rapid, clearly having an average slope much steeper than the initial resistive decay. The approach of each shell is marked by the five small peaks in the total current profile, as each shell generates image currents just before peel-off begins; this is visible in the plots of the current per shell. Similarly, there are five small valleys at the end of the profile as finite pieces of shell disappear "into" the wall. Note that even though only five shells were used, the overall profile shows relatively minor effects of the discretization.

Figure (5.3) shows the corresponding evolution of the poloidal current. Note that even though this example does not have an especially tight aspect ratio, the plasma is in fact carrying a considerable amount of poloidal current.

The dominant behavior is the resistive decay, as the poloidal L/R time is considerably shorter than its toroidal counterpart. Note that the profile remains smooth even after the plasma hits the wall, as the poloidal current still closes continuously through the plasma. Only the curvature changes slightly, so that the current decay is slowed as toroidal flux is compressed as the plasma hits the wall. Since the wall and the shells have comparable surface conductivities in this example, and neither one is very high, the total current curve does not show a striking example of flux compression. Only as the shells are completely absorbed does the curve show any signs of the discrete nature of the shell model.

Now suppose we had a movable, "smart" Rogowski coil in the chamber which would always locate itself at the peak poloidal halo current in the chamber, as a function of poloidal location. A plot of the total current measured by this coil as a function of time is given in the figure below.
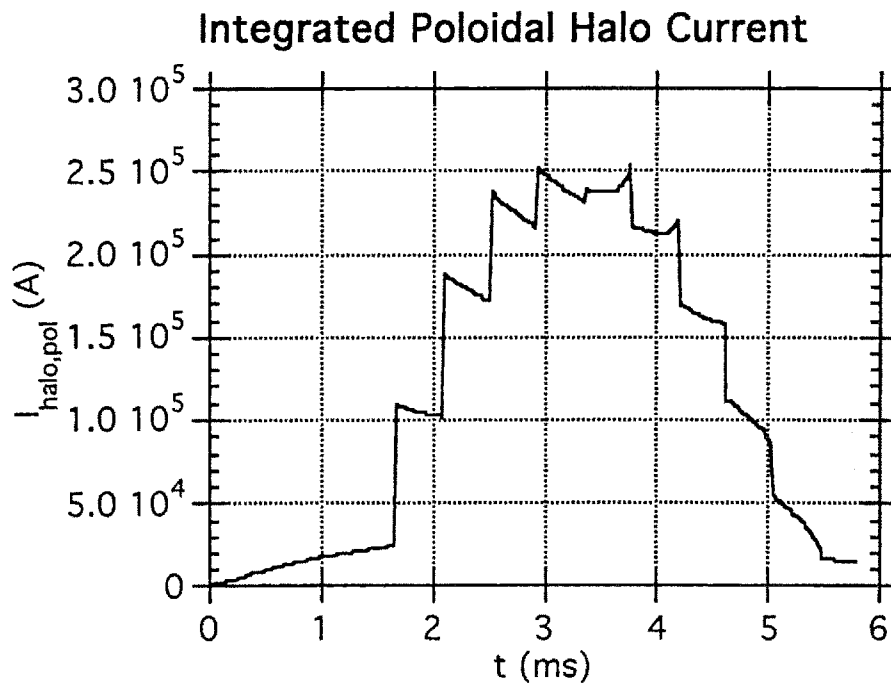
Figure 5.4. Peak poloidal halo current.

We see that in spite of the rapid L/R decay time, a respectable amount of current flows through the wall, nearly a third of the original toroidal plasma current. The discrete jumps as each sheet contacts the wall are clearly visible, but the overall shape of the

profile is quite evident. A nice point demonstrated by this curve is that axisymmetric halo current must decay at least as fast as it rises as complete sheets (or flux lines in a real plasma) vanish into the wall.

The halo current picture is not complete at this point, however. Let us consider the poloidal distribution of the poloidal current flowing in the chamber. We expect strong poloidal localization to the region overlapped by the plasma. Figure (5.5) is a carpet plot of the poloidal distribution of current as a function of time; each shifted curve represents the distribution at an instant of time, increasing in both time and poloidal location from left to right. (For readers not familiar with carpet plots, note that the x-axis does not correspond to any particular independent variable, but a combination of several. The intent is to show trends.) The bottom of the vacuum chamber is the rightmost portion of each curve and is obviously the region which shows the peak currents. Note that the near-vertical lines should not really be present, as the discrete current sheets produce jumps in the current profile in the wall, but they do allow the eye to take in the proper shape of the profile.
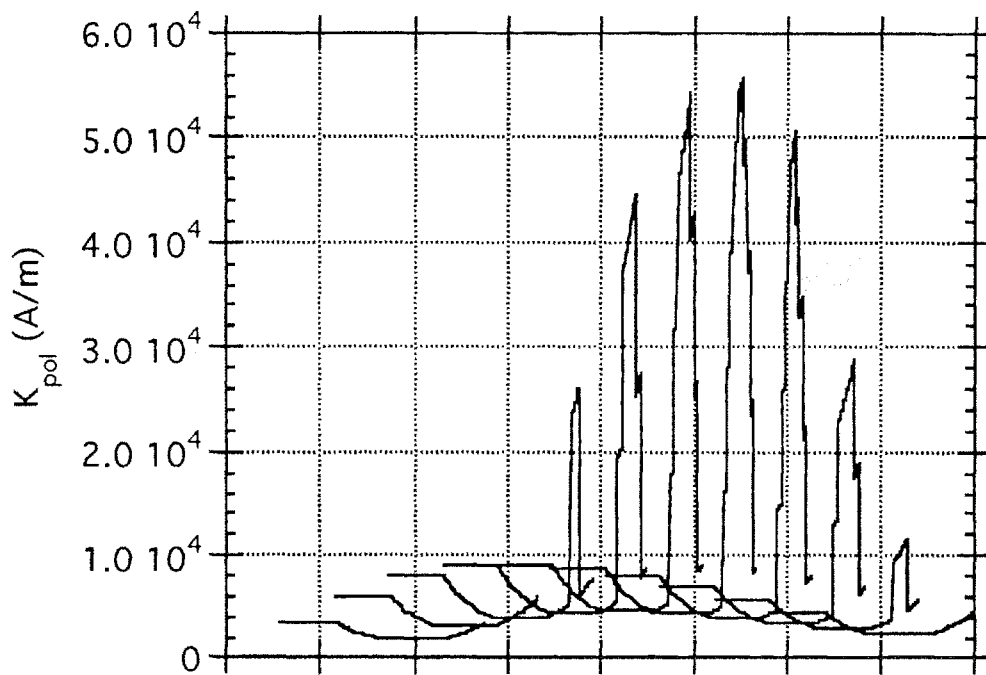
Figure 5.5. Carpet plot of poloidal current distribution over time.

Suppose we now examine the corresponding plot of the toroidal current density. Figure (5.6) shows that there is considerable activity in the toroidal current distribution as well, which will merit a closer look. Figure (5.7) shows that the load on the chamber is dominated by this activity.

The series of figures (5.8) contains snapshots of the toroidal current distribution, focusing on just the bottom of the chamber. The evolution is described as follows: as the plasma approaches the wall, large image currents are driven in the chamber. The speed of the disruption relative to the toroidal L/R time means that the magnitude of these currents as well as the response of the plasma is not negligible; figure (5.2) shows a number on the order of 100kA. However, what makes these image currents very different from those seen in simulations of a fixed-position quench of plasma current is that, since the plasma is nearly touching the wall, the wall currents are confined to a narrow region whose width is comparable to the nearest portion of the bulk plasma. Thus, while 100kA is a modest total current, the toroidal current *density* in the wall over a region of centimeters is quite large. Eventually, of course, the plasma does hit the wall, and in the overlap region a substantial bite is taken out of the current profile as the image currents in the wall and the plasma partly cancel, and a piece of the "original" plasma current flows in the wall. The subsequent shape of the profile in that region depends on the relative conductivities of the wall and plasma, determining how well the image currents cancel. In this case, after all the plasma sheets have vanished into the wall, there is a substantial positive peak of toroidal current in the chamber, representing the remnants of the toroidal plasma current. At intermediate times, the profile looks quite complicated as multiple sheets contact the wall (on a numerical note, notice how what appear to be sharp spikes in the carpet plot are well-resolved in the "zoomed" graphs). As any given sheet continues to penetrate, eddy currents are driven by the approaching "edges" while the segment most recently absorbed cancels them out! The resulting shape (and here the carpet plot shows its usefulness) is very much like a splash, where an object penetrates a surface so that it first dimples inwards and then rebounds outwards.

Evolution of Toroidal Current
Profile in the Chamber
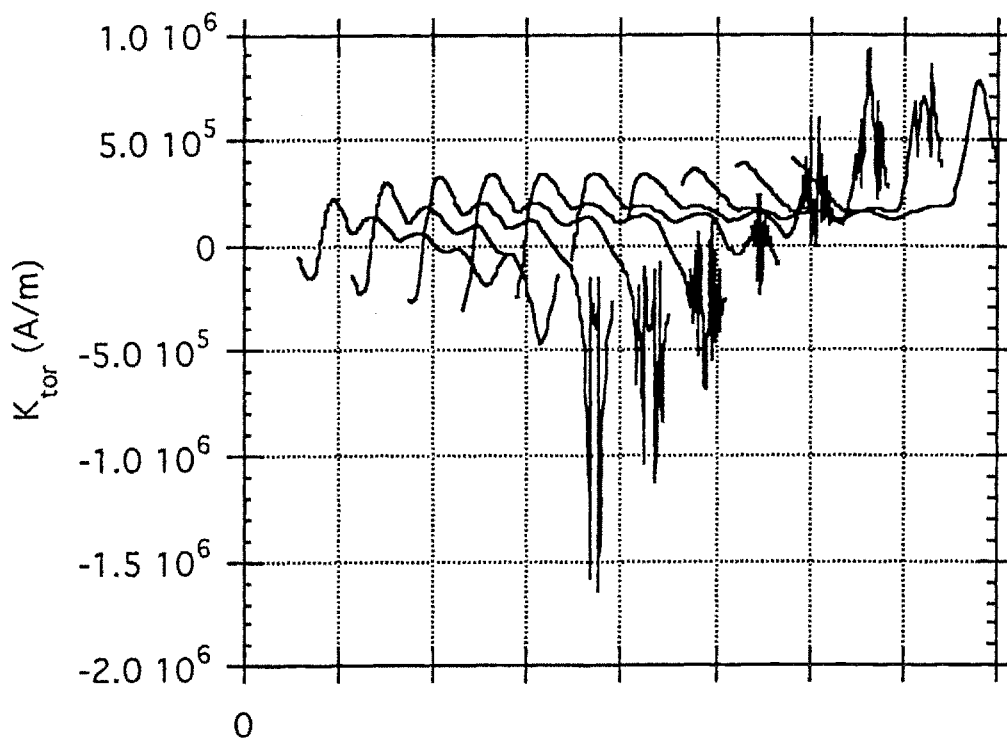
Figure 5.6. Carpet plot of toroidal current density.

As might be expected, since Lorentz forces are based on current densities and not total currents, the load on the chamber is in fact dominated by the eddy currents in this case. A carpet plot of the loads is shown in figure (5.7). Time-series plots of the poloidal current density and the normal load due to Lorentz forces are shown in figures (5.9) and (5.10). Finally, some plots of the relative contributions of poloidal and toroidal currents to the load at various times are shown in figures (5.11). In (5.11), notice that after eddy currents have largely canceled, the effects of the toroidal and poloidal halo currents largely cancel in "pseudo force-free" fashion.

Evolution of Normal Loads
on the Chamber
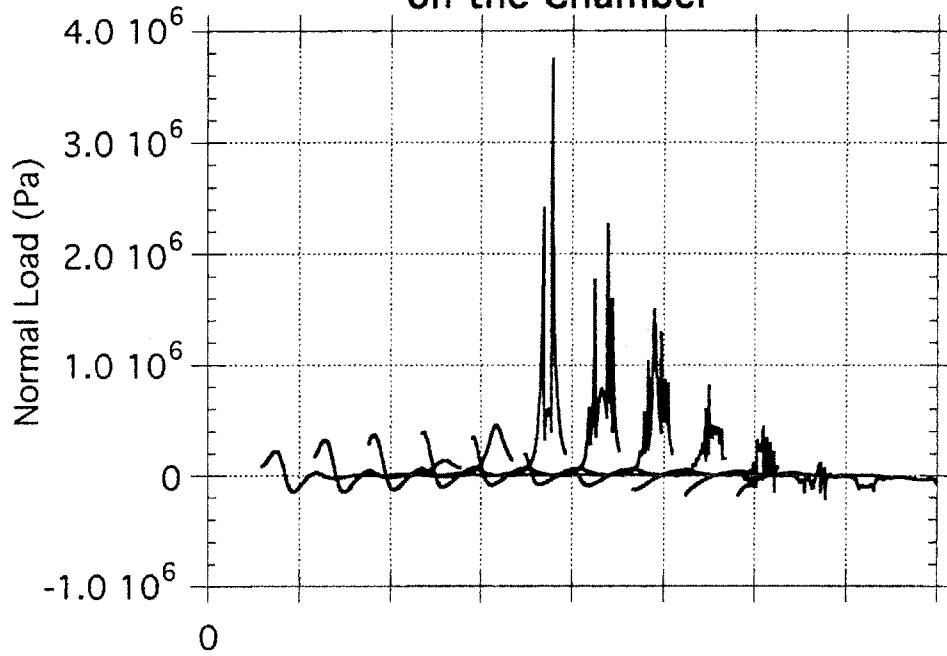
Figure 5.7. Carpet plot of the net load on the chamber.

113
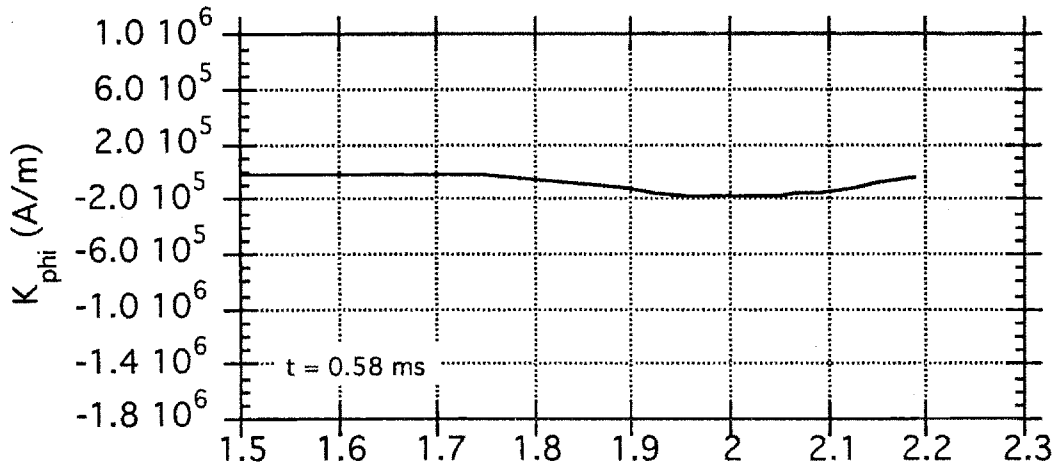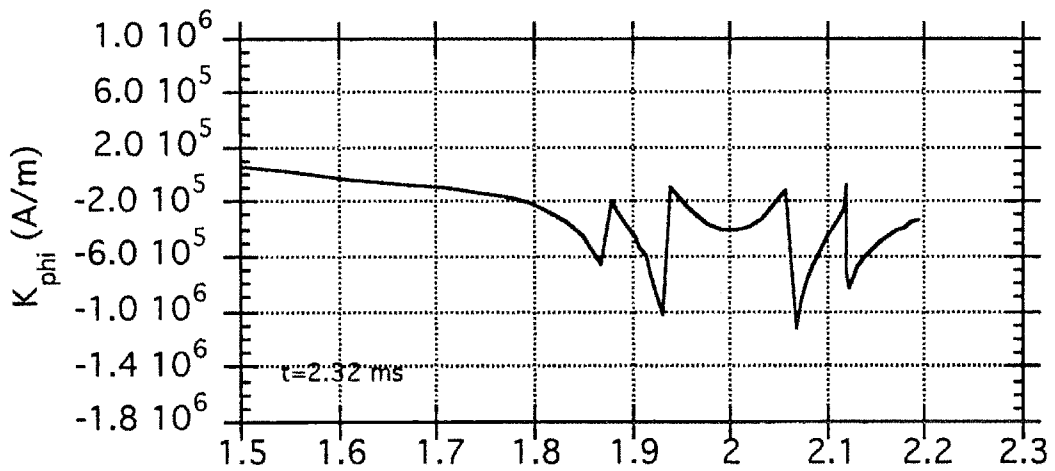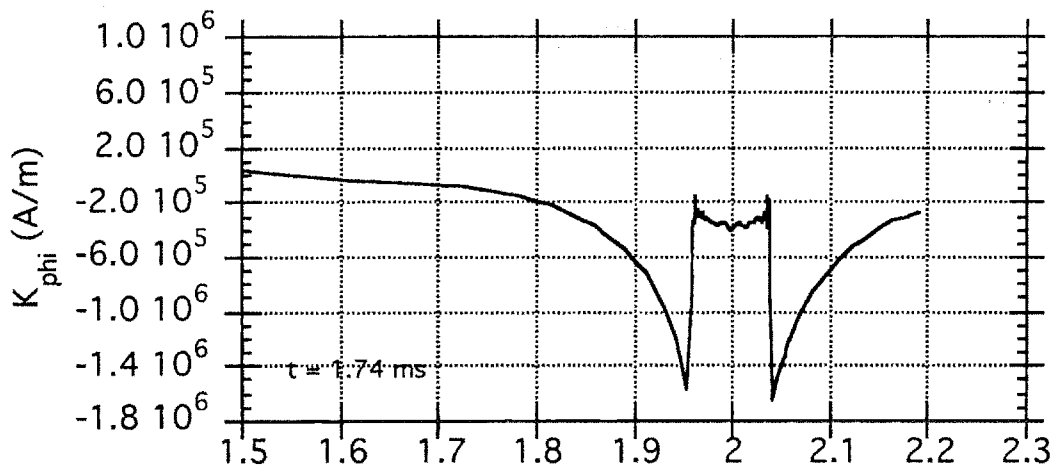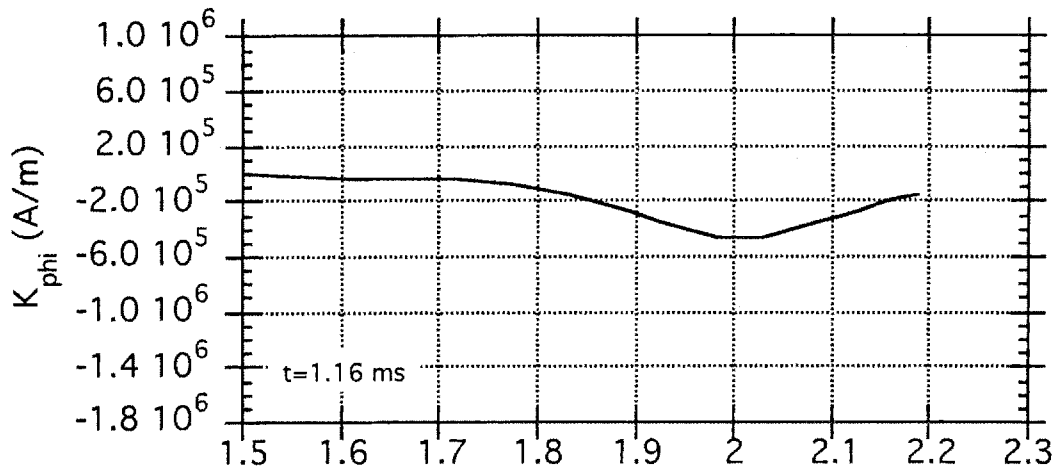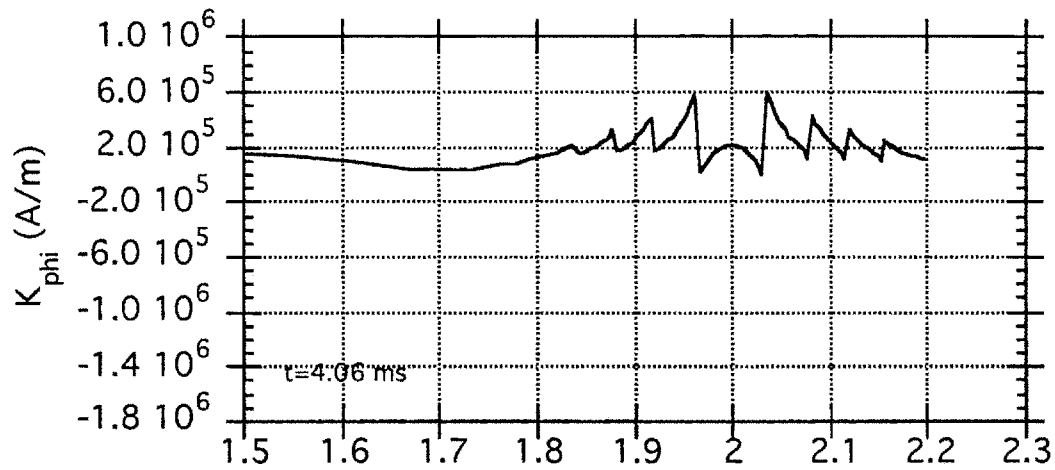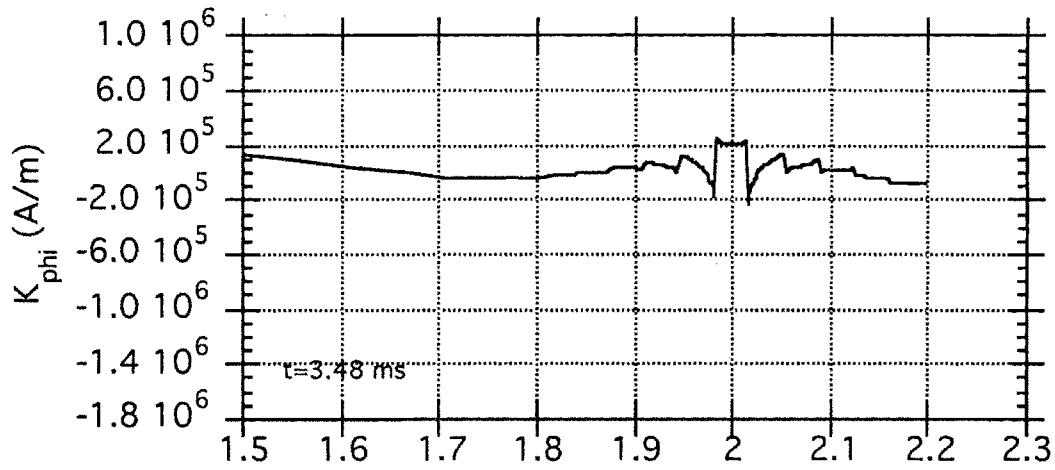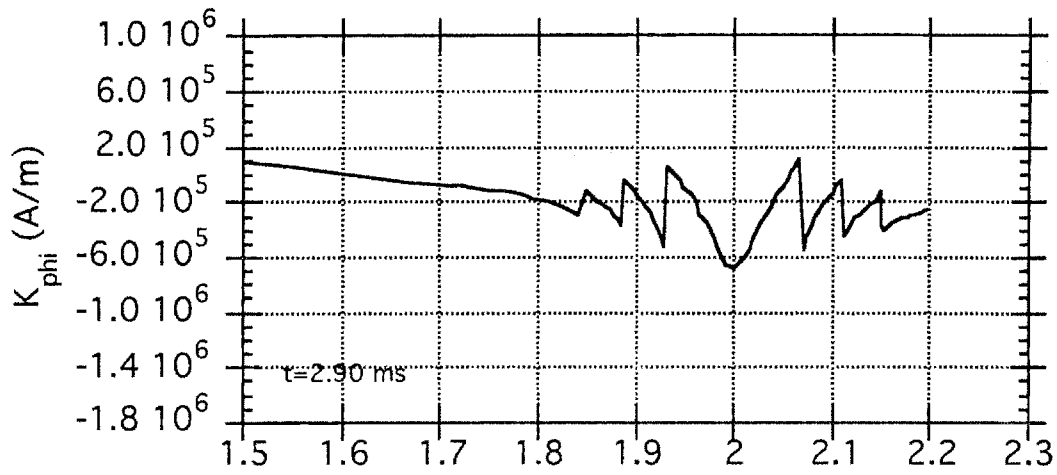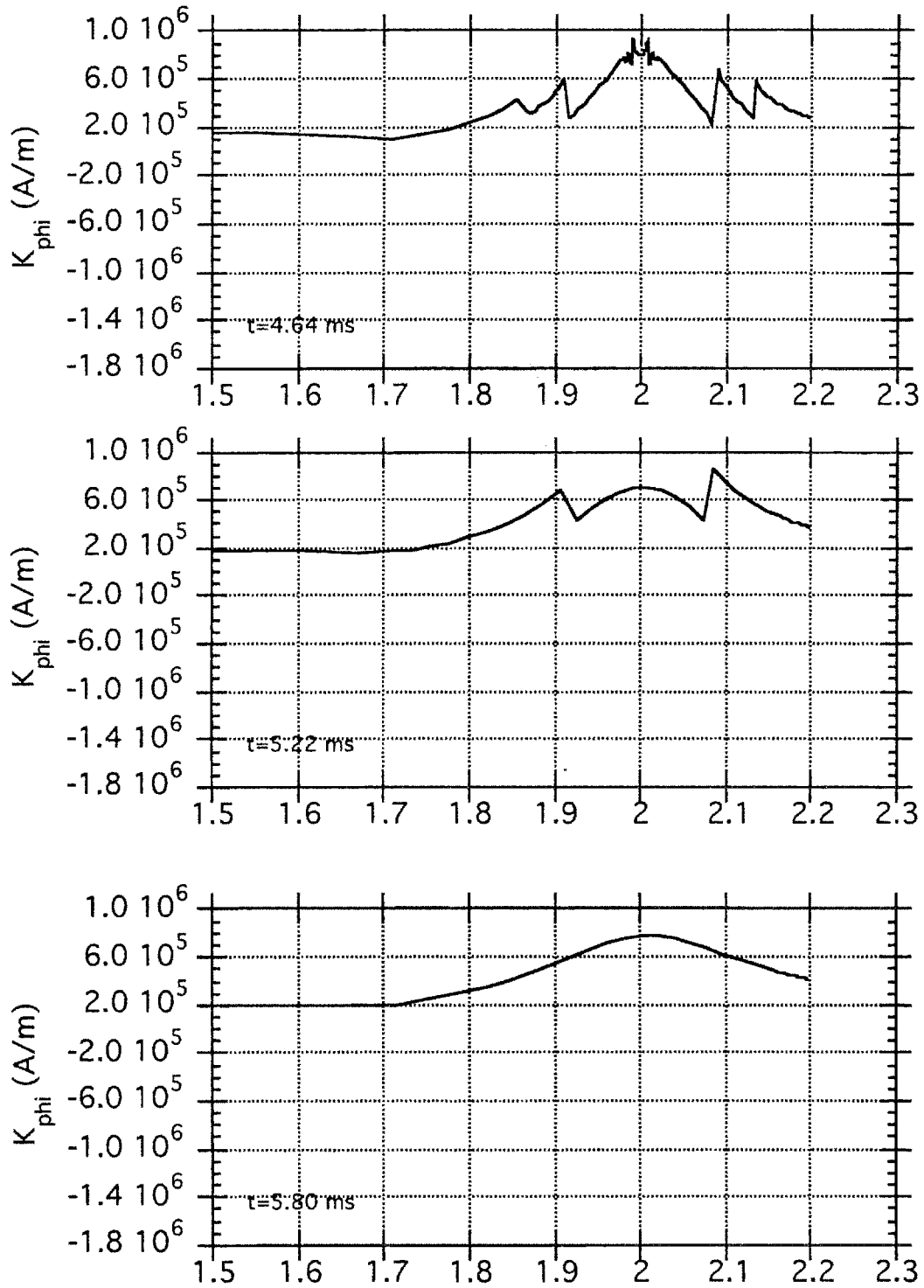
Figure 5.8. Time series of the toroidal current density at the bottom of the chamber. The independent variable on all plots is poloidal arc length (m).

114
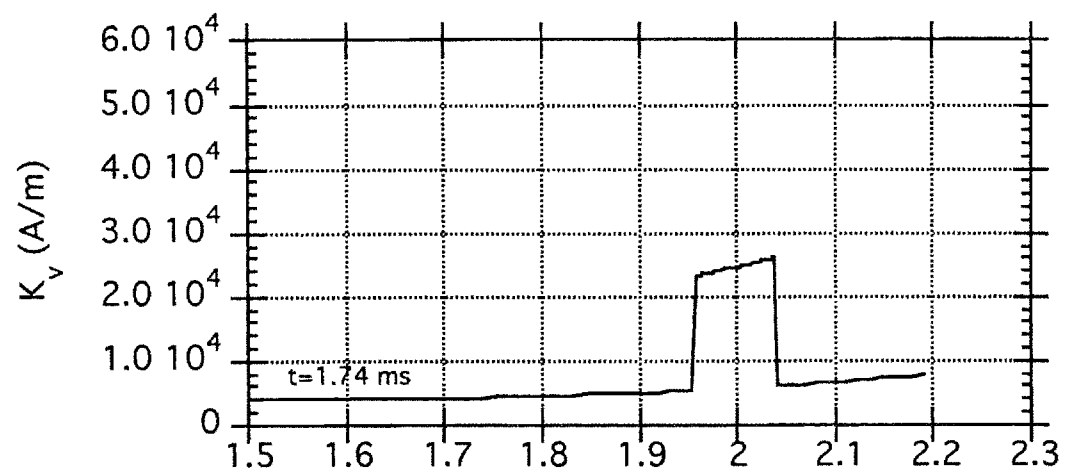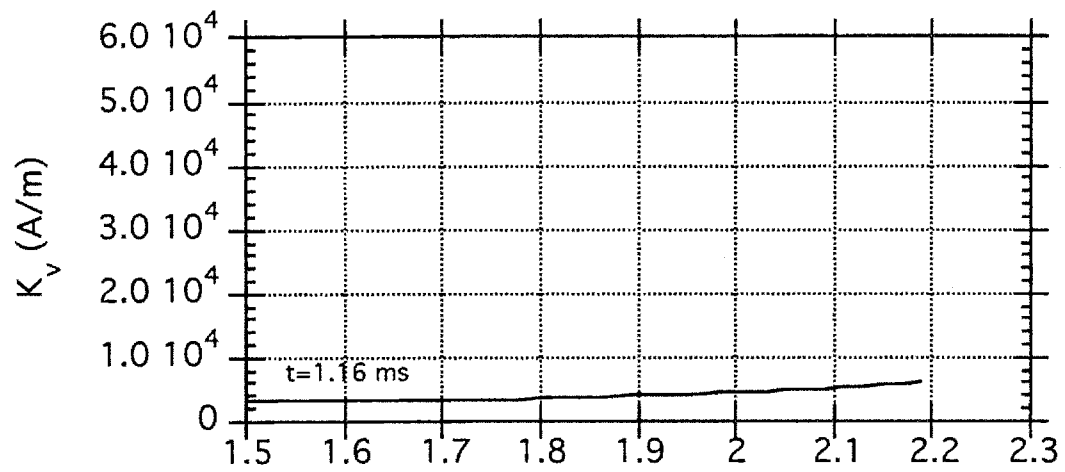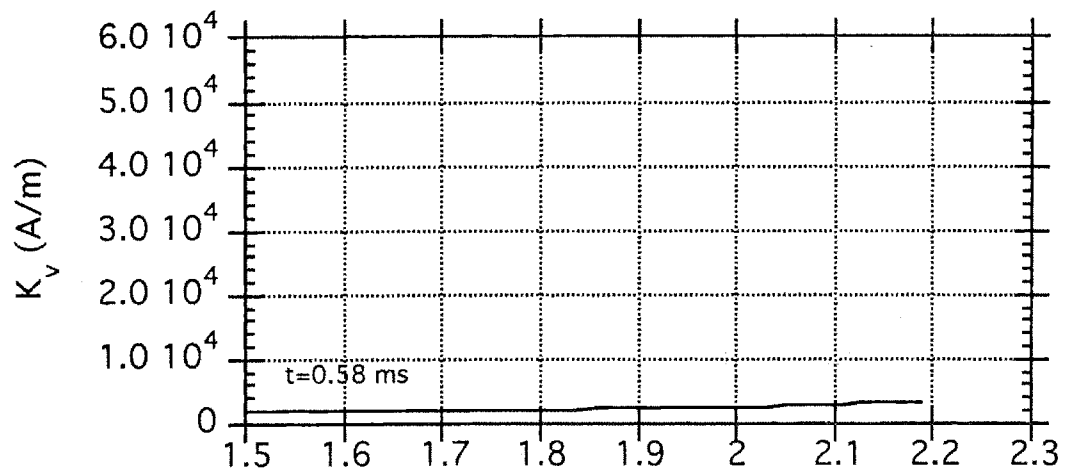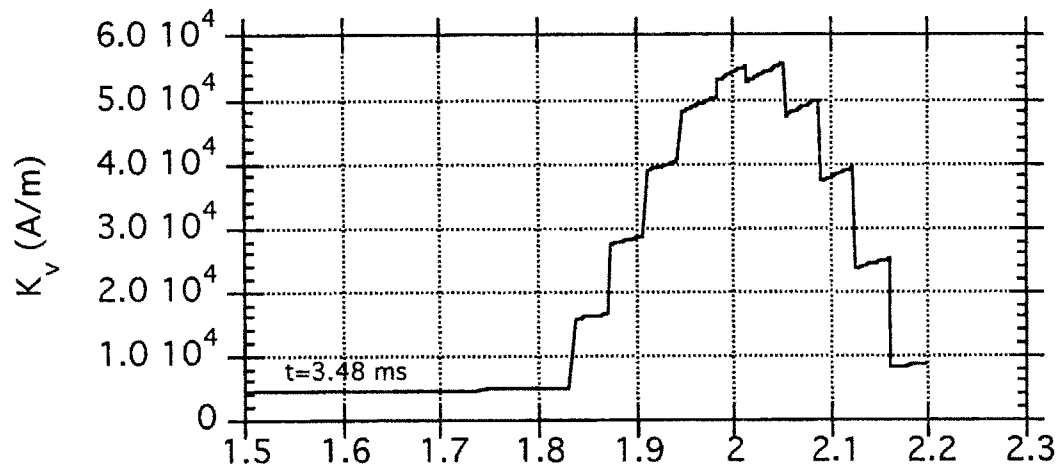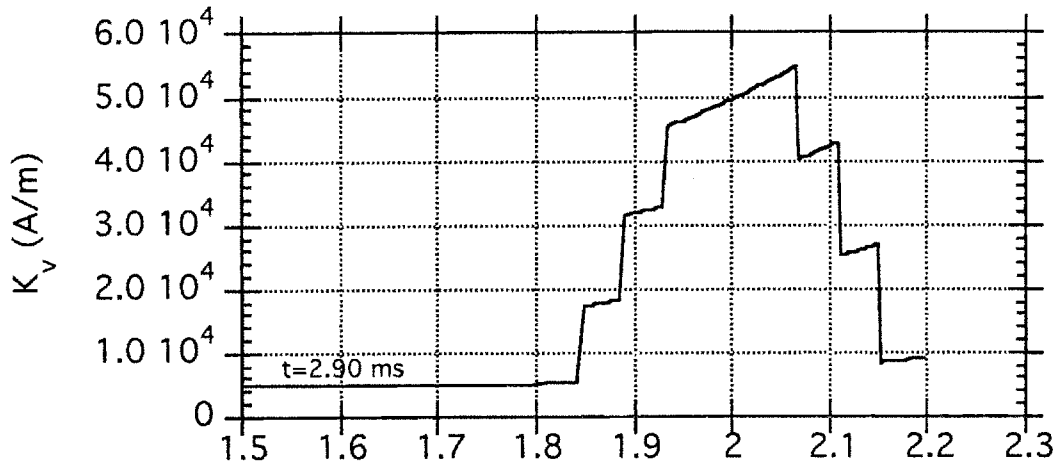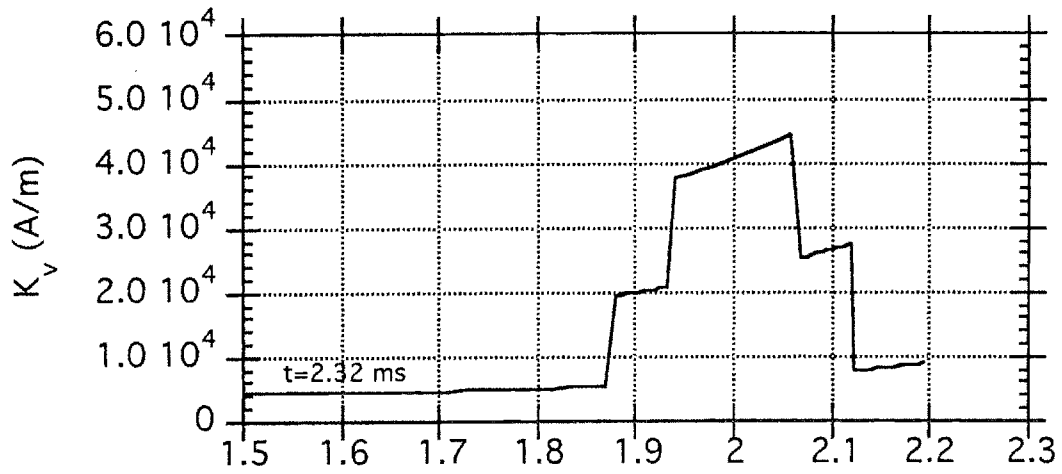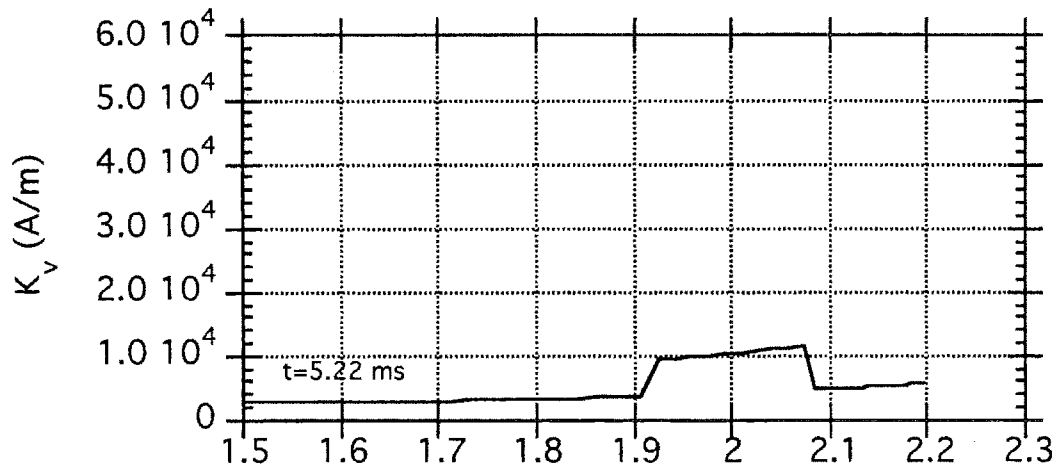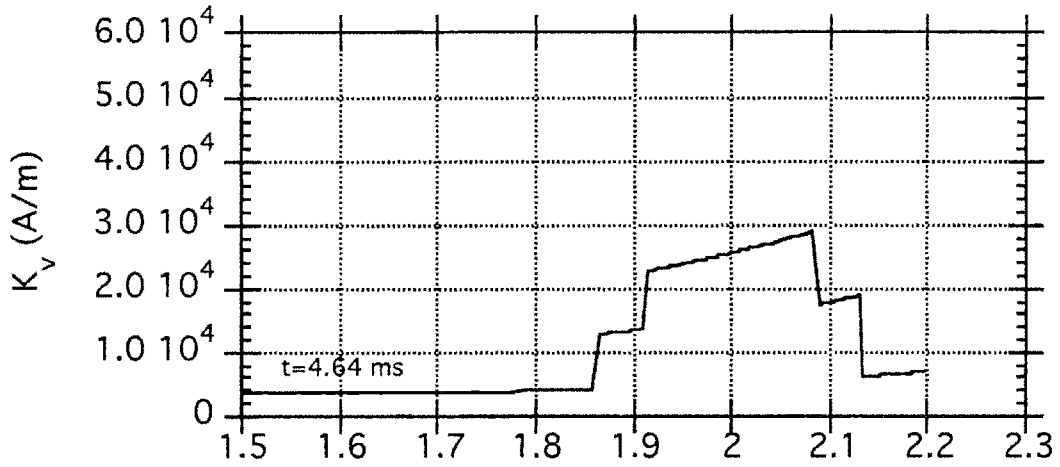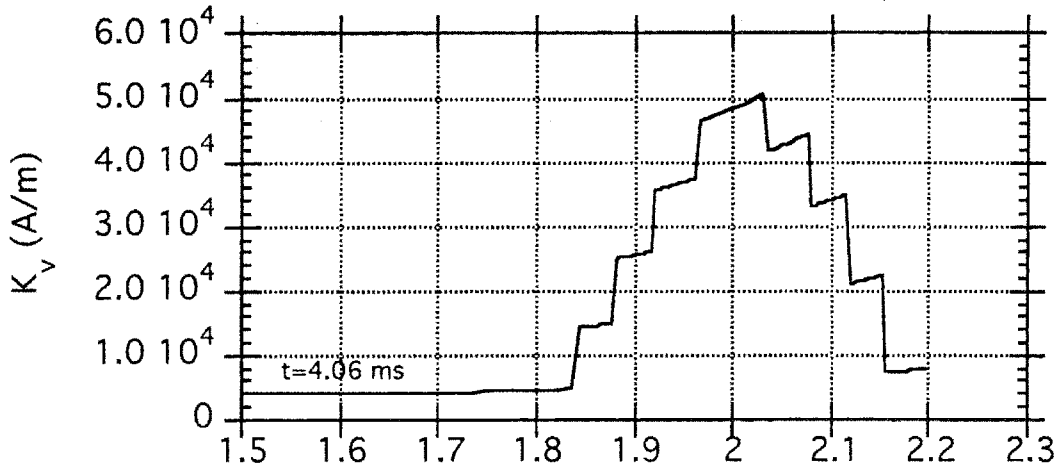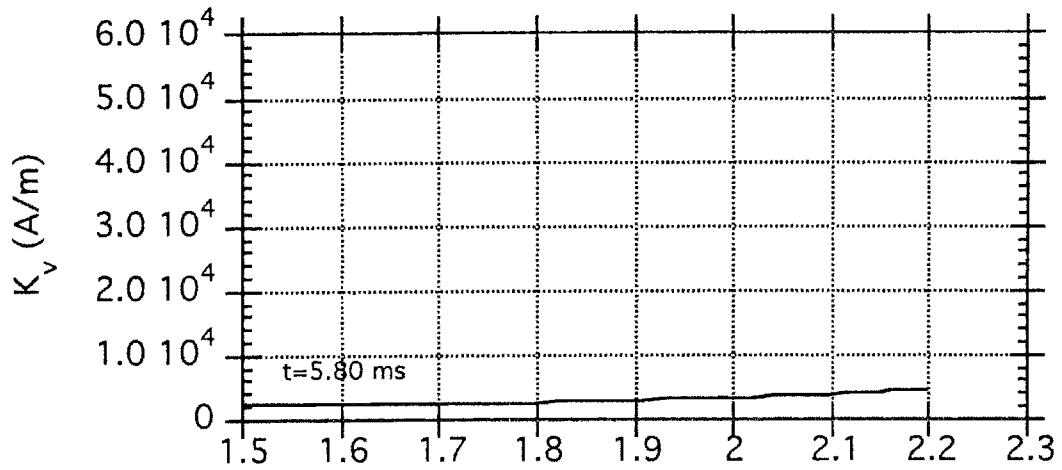
Figure 5.9. Time series of poloidal current density at the bottom of the chamber. The independent variable on all plots is poloidal arc length (m).
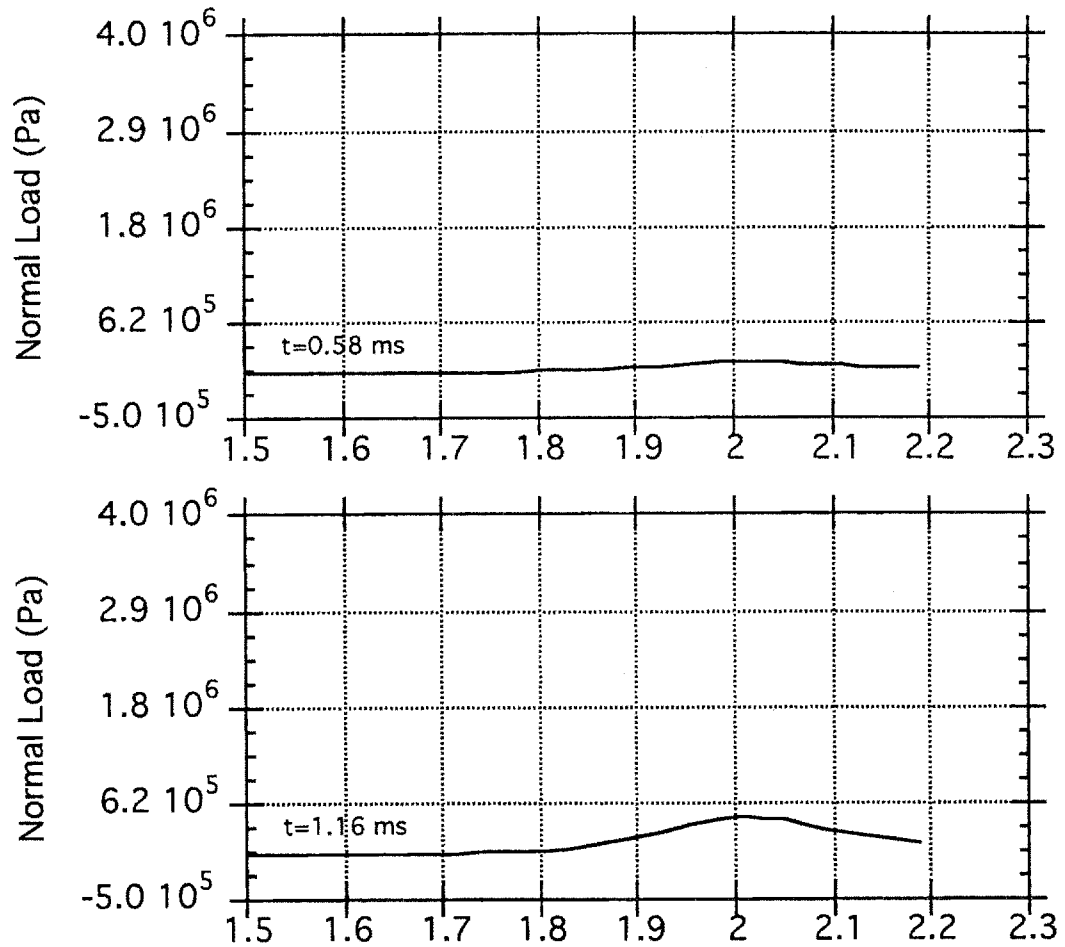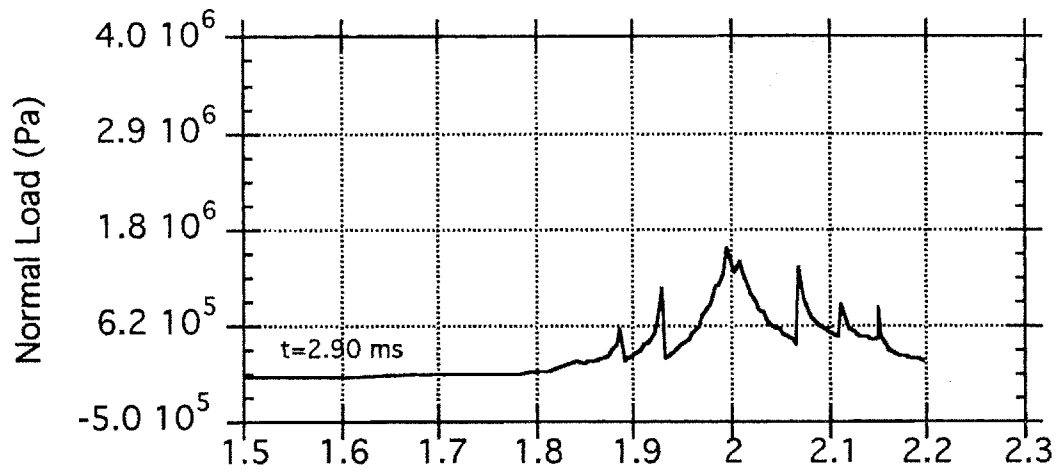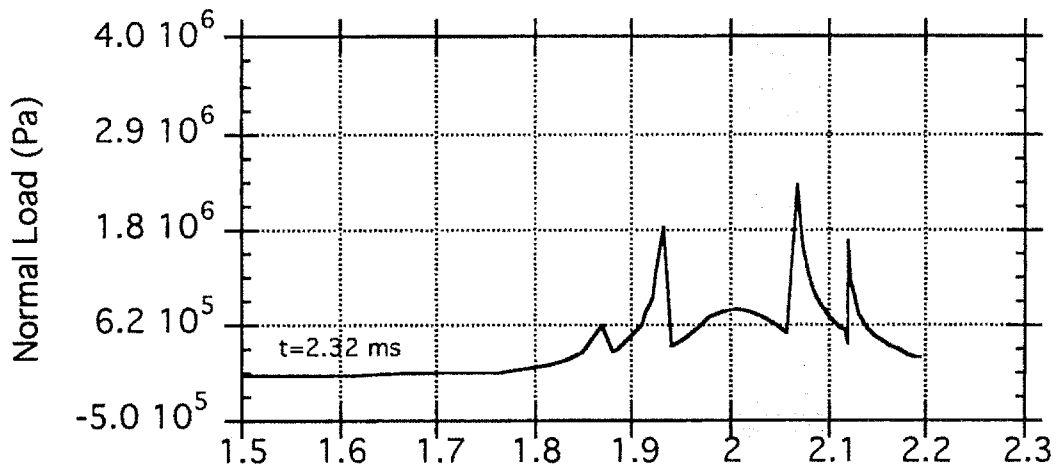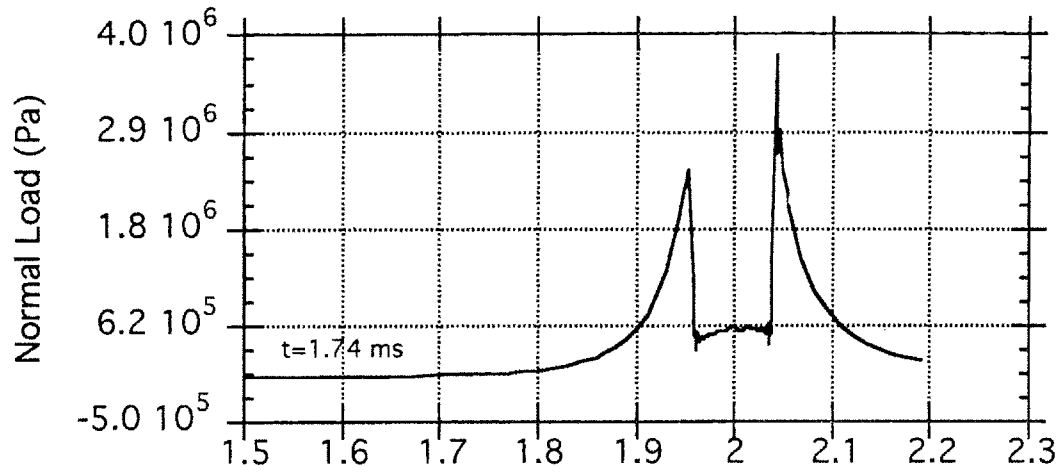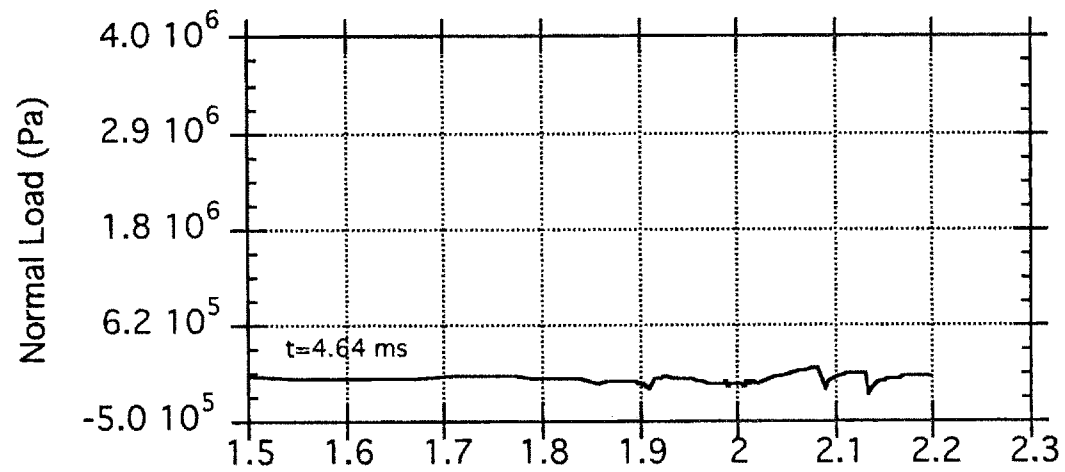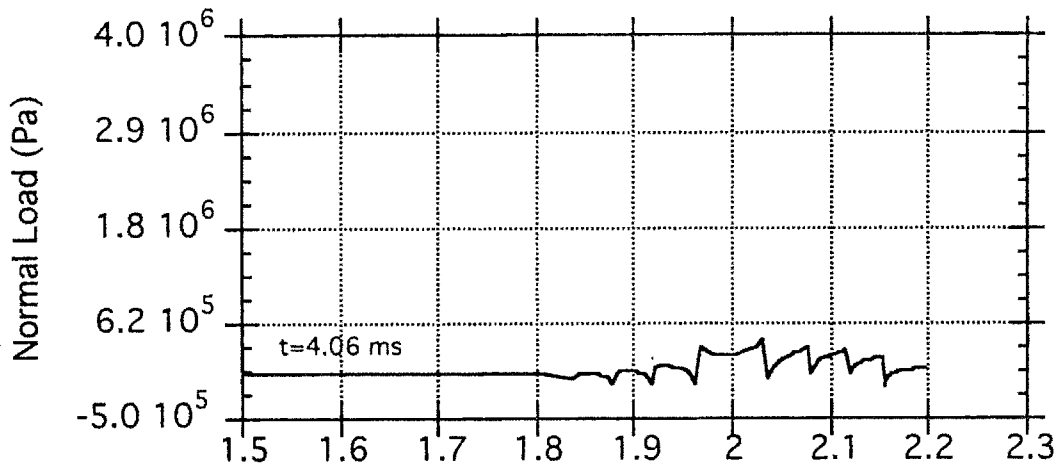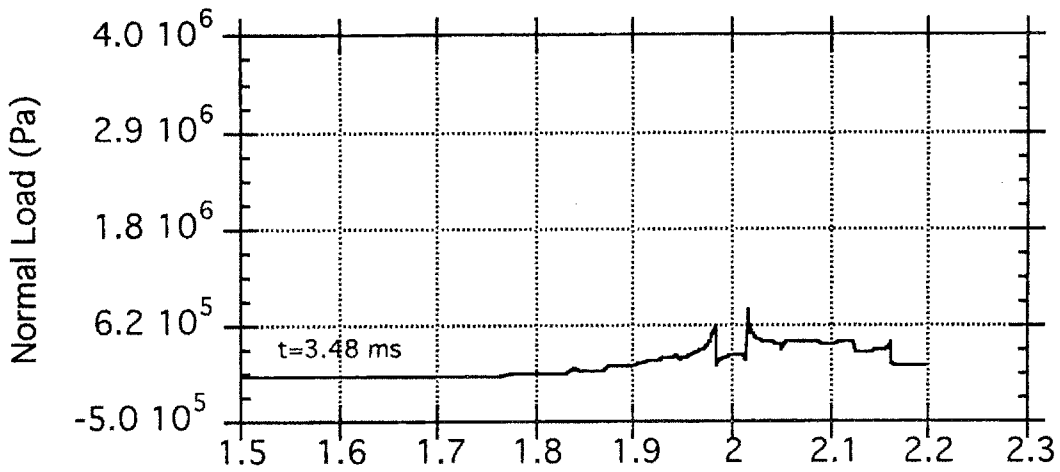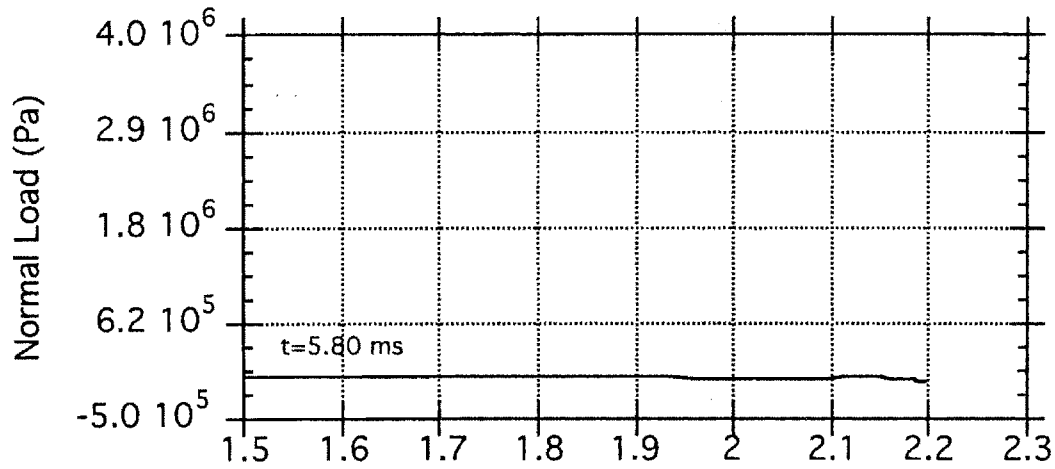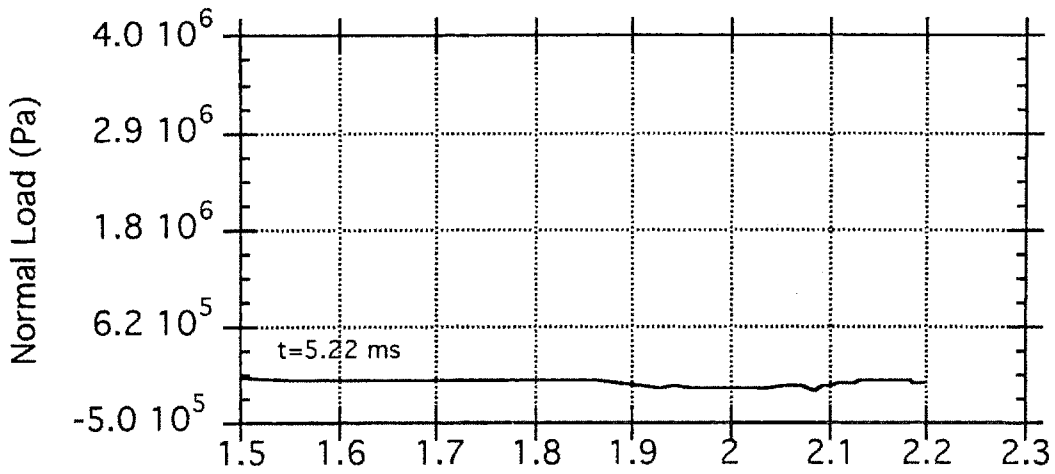
Figure 5.10. Time series of the net load on the bottom of the chamber. The independent variable for all plots is poloidal arc length (m).
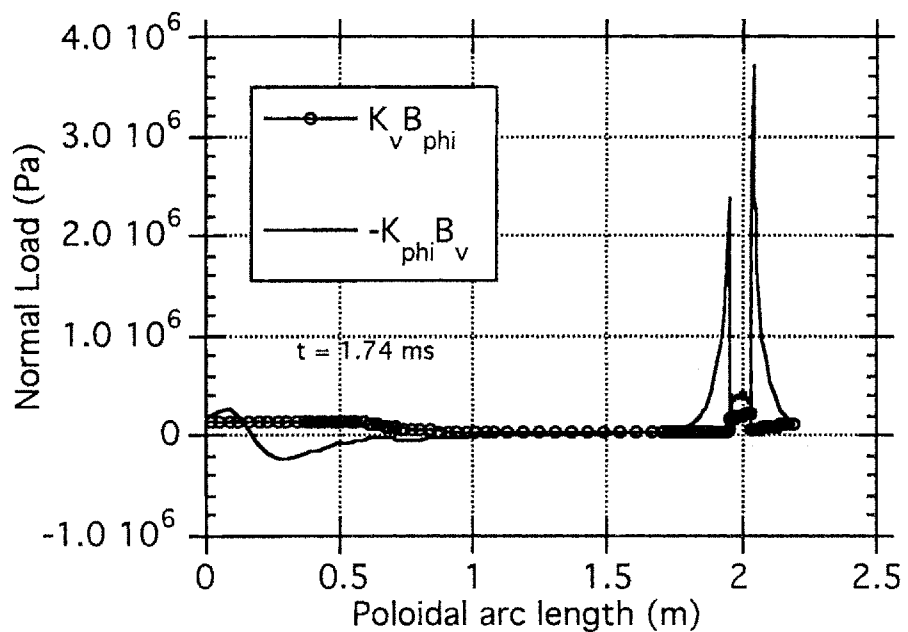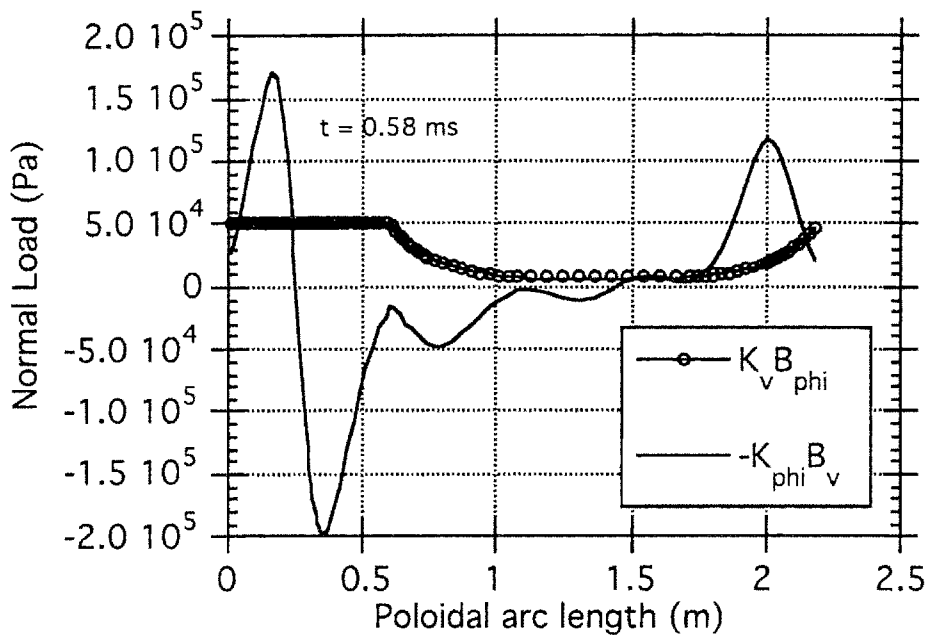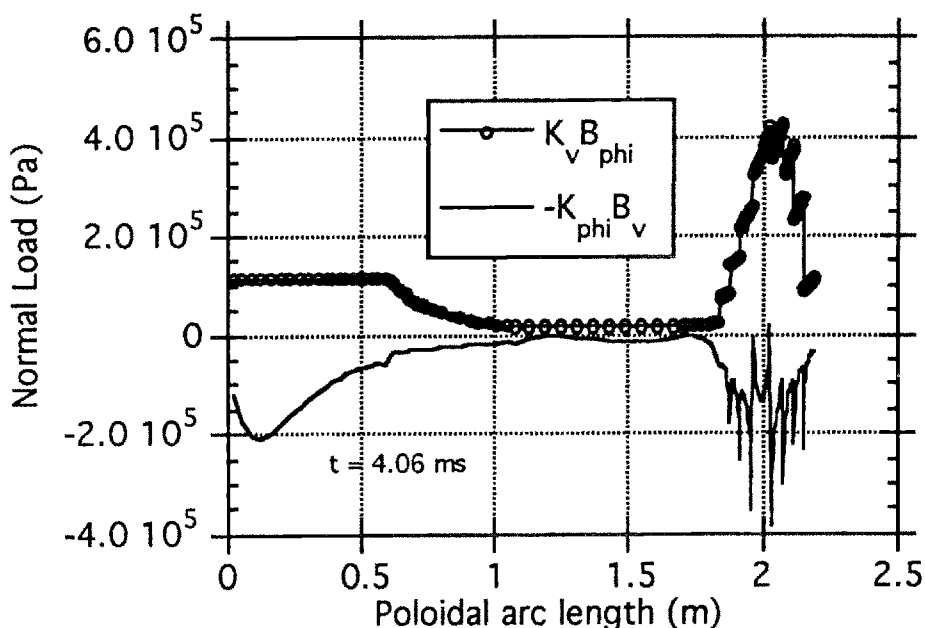
Figure 5.11. Relative contributions to the load on the chamber at various stages of the disruption.

5.2. Code Verification with the Alcator C-MOD Experiment

Now that we have examined a "clean" example of a TSPS run, we will put aside our reference case and turn to verifying that the sheet current model is capable of matching existing experimental data. The test case will be shot number 950112013 on Alcator C-MOD; as mentioned in Chapter 1, the halo current measurements for this shot have been published in the journal *Nuclear Fusion* [1].

This case differs from the reference case of the previous section in a number of ways. The most obvious is that the shape of the vacuum vessel is considerably more complicated. The thickness, and therefore the surface conductivity, is not uniform in poloidal angle. The presence of the inner and outer divertor structure means that there are multiple poloidal current paths. The plasma is strongly shaped and controlled by a system of PF coils, whose currents will be specified from the C-MOD database for this shot. The background toroidal field is held fixed in time, at an on-axis value of 5.3T. The plasma displacement is taken from centroid measurements; the rate at which the plasma shrinks in area is given by a linear fit to the data. The parameterized chamber geometry is taken from the model used by R. Pillsbury in the SOLDESIGN electromagnetics code [2].

123

While there are measurements of the plasma temperature available, this information is not used to determine a plasma conductivity for this shot. Instead, a single conductivity (i.e., the same value for all plasma sheets) which is constant in time is used as the sole fitting parameter in the model. This freedom is introduced to avoid having to discern a temperature profile for the bulk plasma plus some type of transition model as parts of the plasma strike the wall. Given the amount of information which is being replaced by a single parameter, it is felt that this does not introduce undo latitude into the sheet current model.

The only aspect of the disruption not determined by the data is the source of the asymmetry, which in this shot produces a peaking factor of about two in the poloidal halo current. This actually introduces an enormous range of freedom in the plasma motion, which necessitates some method for picking a particular displacement. This was resolved as follows. We first treat the shot as purely axisymmetric, based on the observation that a peaking factor of two is actually quite modest compared to what could be produced in a highly non-axisymmetric event (save for the effect of induced poloidal currents, the peaking factor can theoretically become infinite). Once the plasma conductivity has been adjusted to match the zero-order current measurements, we run the simulation again with the maximum possible non-axisymmetric perturbation which can be returned to an axisymmetric configuration before the plasma hits the chamber (recall the model has this limitation, as discussed in Chapter 2). This consists of a tilt of the plasma's Z-axis with respect to the chamber axis, which can reach a maximum of about twenty degrees. Superimposed on this is a rotation of the plasma at a fixed rate of 2 kHz, which is the measured rotation rate of the halo currents in the wall. If the argument about the magnitude of the actual asymmetric perturbation is correct, the zero-order currents will not change significantly from the 2D run to the 3D one. (Note that what is referred to here as the "maximum perturbation" is still quite small compared to what could be achieved if the displacement was allowed to remain asymmetric as the plasma hit the wall. A good deal of the effects of the twenty-degree tilt will cancel as the tilt is "undone"; only the vertical motion of the plasma towards the divertor, and resistive effects to a much smaller degree, break the symmetry)

It is not expected that this technique will match the amplitude of the measured asymmetries in the currents; it is expected that the asymmetric behavior produced by

the maximized tilt will agree qualitatively with the measurements but exceed them quantitatively. One can then choose from a wide range of lesser perturbations to match the amplitude more closely; this will not be done here, as there is no apparent reason to favor one type of perturbation over another.

The simulation begins just after the plasma experiences a thermal quench, so that the plasma current has jumped from a nominal 800kA to about 840kA. The run ends six and a half milliseconds later in the shot, after most of the plasma current and measured halo current has gone away and all of the bulk plasma has disappeared into the bottom of the divertor. Time is offset by 0.8695 seconds from the actual shot, so that the beginning of the simulation is t=0. Note that the plots of total plasma and halo current have been negated for easier viewing; the plasma current and toroidal field are both actually aligned in the negative ϕ direction in this shot. The plots of current density have not been negated.

The disruption trajectory, along with the geometry used to represent the C-MOD chamber with divertor and PF system, is shown in the following plots.

125
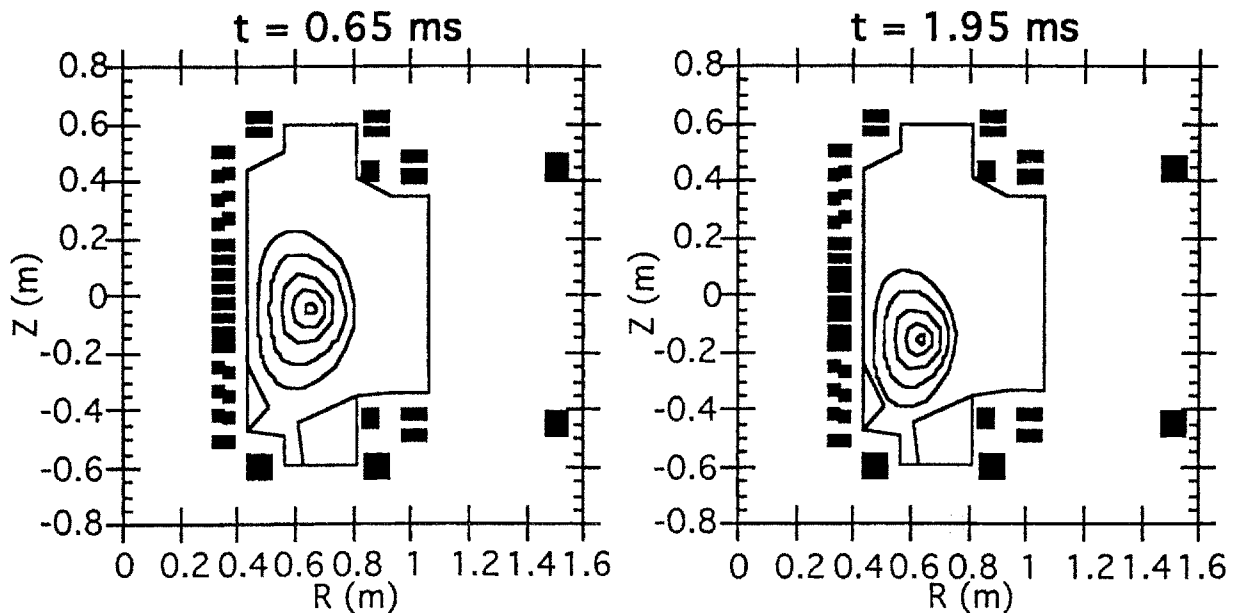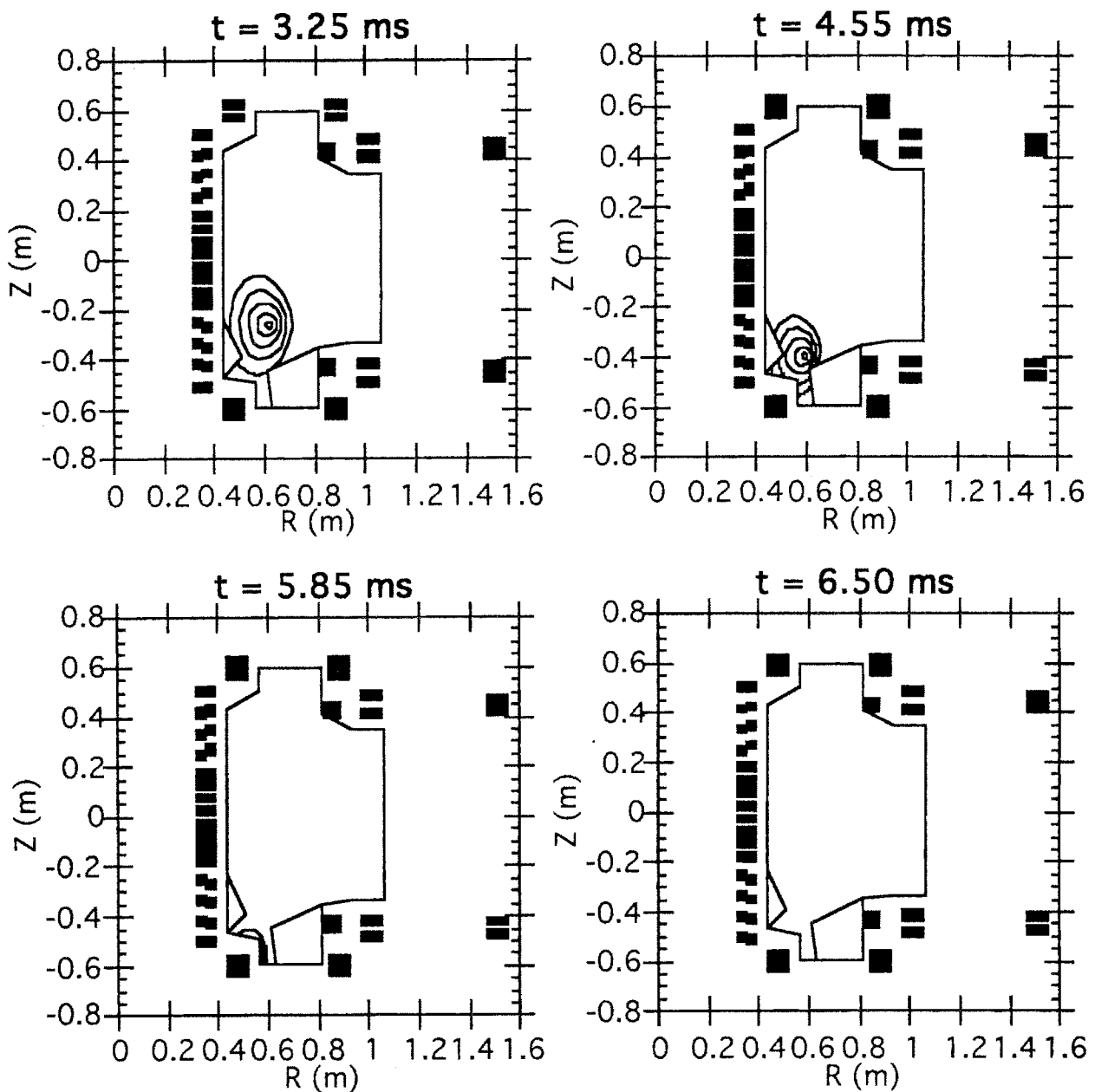
Figure 5.12. Disruption trajectory and geometry used to represent Alcator C-MOD shot 950112013.

The following is a plot of the measured and modeled plasma current, showing quite good agreement given the use of a constant, uniform conductivity of 0.45 Mmho/m, corresponding to a temperature of about 40eV using a Spitzer model (hence the use of this value in the reference case). The figure following that is a plot of the ϕ-integrated poloidal halo current measured by a Rogowski coil located at the bottom of the divertor,

and the peak poloidal halo current from the TSPS run. The use of the peak value rather than the value at the location of the Rogowski in the model will be addressed shortly.
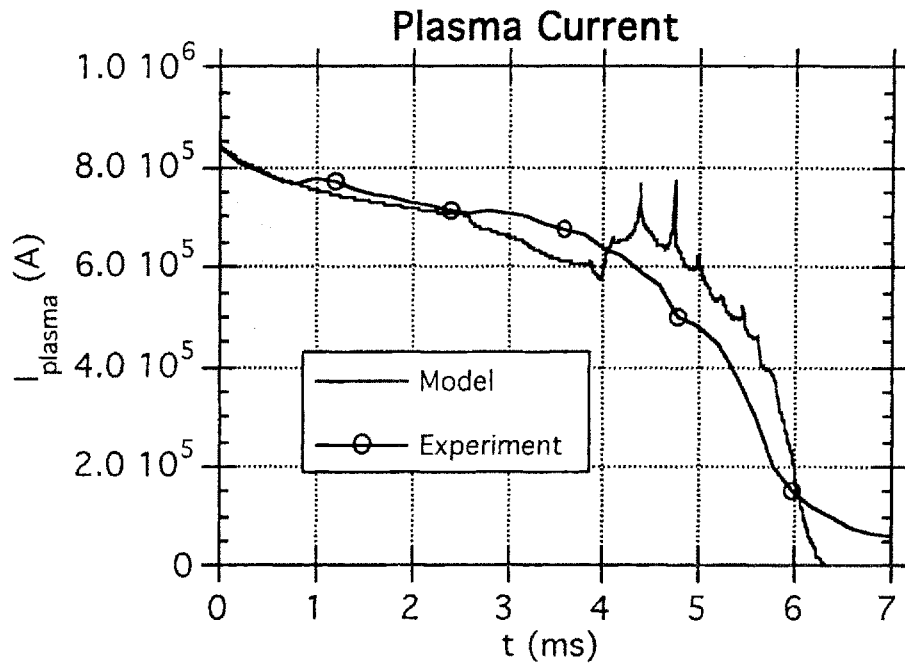
Plasma Current

Figure 5.13. Comparison of TSPS and measured plasma current.

Integrated Poloidal Halo Current
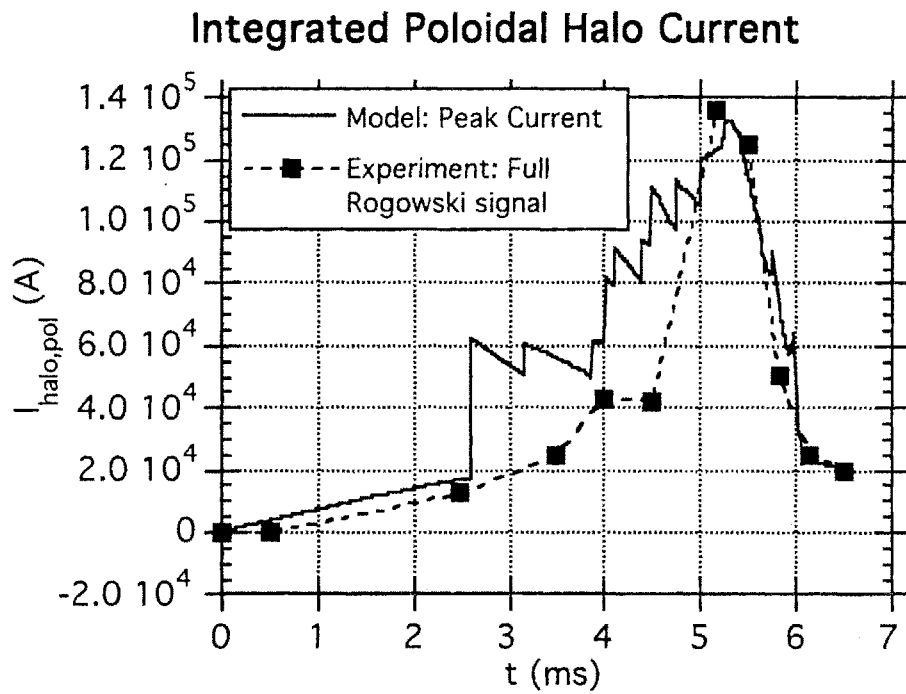
Figure 5.14. Comparison of measured poloidal halo current and peak TSPS value.

127

The use of the peak TSPS value shows a weakness of the sheet current model, which is the fact that the sheet geometry remains "clean" even under circumstances where the real plasma has undergone scrape-off against parts of the chamber. For example, the t=4.55ms frame in figure (5.12) shows that the arcs of the outermost plasma shell are still intact in the segments beneath the inner divertor module and in the divertor well, which is clearly a highly unrealistic situation.

To clarify this point, consider figure (5.15), which compares the experimental data with the TSPS value at the proper location of the full Rogowski coil, as well as at two locations at the opposite edges of the divertor well. In the TSPS simulation, the plasma does not actually strike the bottom of the divertor well until fairly late in the disruption, hence the delay of the simulated Rogowski signal compared to the actual value. At the edges of the divertor well, which are encompassed by the initial strike points of the plasma, the signals match quite well. Since these positions are separated by a gap of only four centimeters, the discrepancy does not lie in having an incorrect plasma trajectory over the course of the run; instead, it is most likely that the real plasma quickly spreads to fill the divertor after scraping against the divertor modules, which the plasma sheets are not permitted to do.

Integrated Poloidal Halo Current
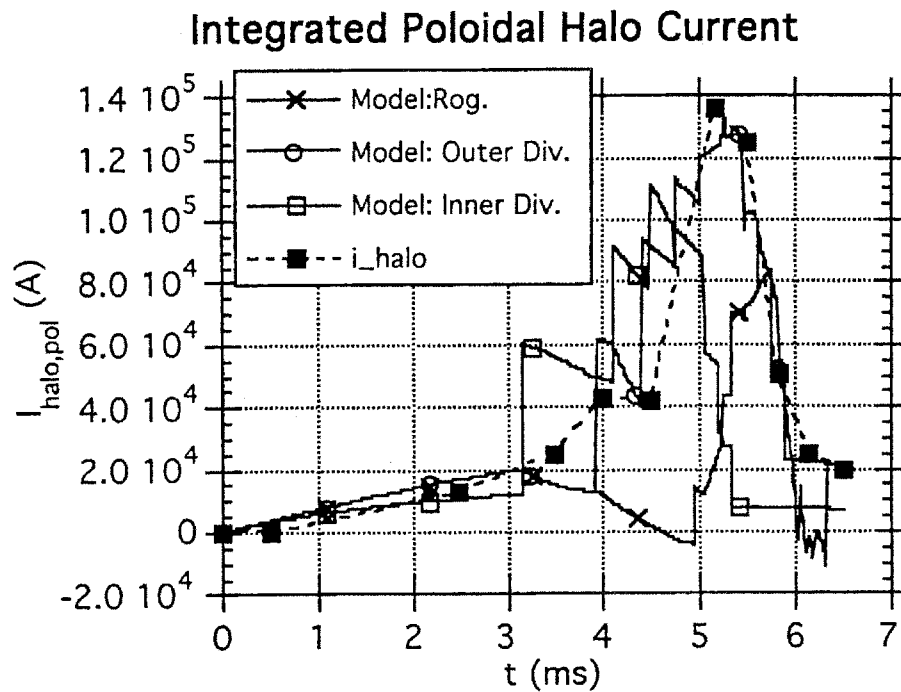
Figure 5.15. Measured poloidal halo current versus the TSPS Rogowski value.

The next step is to consider the non-axisymmetric effects. The three-dimensional displacement is shown in the following frames; the viewpoint is at $\phi=\pi/2$ and slightly elevated with respect to the x-y plane.. The grayscale values indicate toroidal current density, running black to white from minimum to maximum. The chamber and plasma are scaled separately.
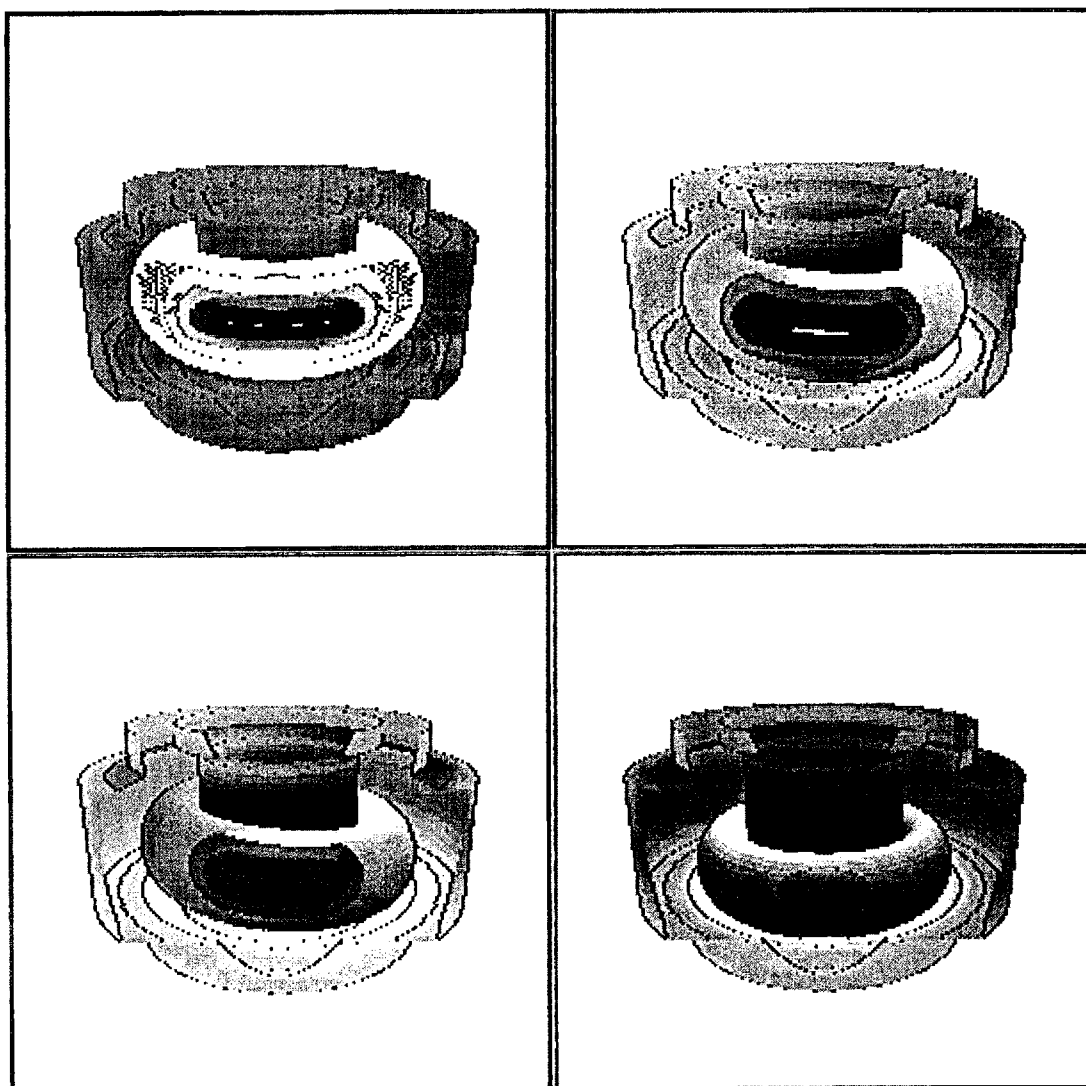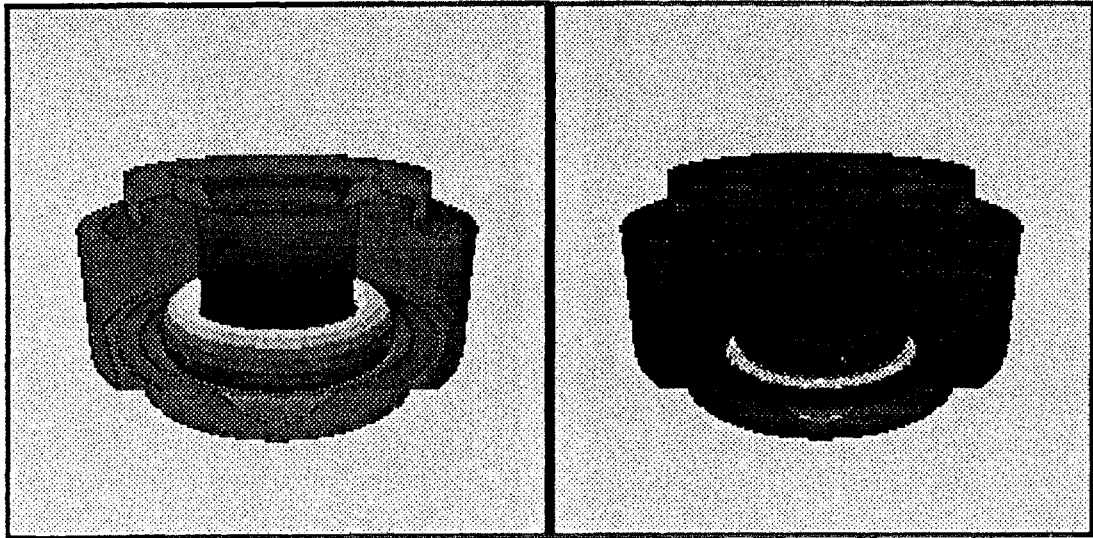
The zero-order plasma current and poloidal halo current do in fact show no discernible difference from the axisymmetric values in figures (5.13-14). However, let us now consider the equivalent measurements that would be made by partial Rogowski coils which each cover one-tenth of the toroidal circumference of the vacuum vessel; these are the corresponding values to the true partial Rogowski measurements for this shot, such as are shown in figure (1.3) of Chapter 1. For a clear description of the diagnostics used to obtain these measurements, the reader is referred to [1] and [3].

The next figure consists of two separate plots to more clearly show four signals, each covering a tenth of the machine, centered at toroidal locations $\phi=0$, $\pi/2$, π, and $3\pi/2$. The signals show a clear oscillation at a frequency of 2 kHz; while it is true that the plasma rotation is specified at this frequency, it is certainly reassuring to see it appear in the fixed geometry of the wall, verifying the proper treatment of boundary conditions in TSPS-3D.

Poloidal Current per Toroidal Decant
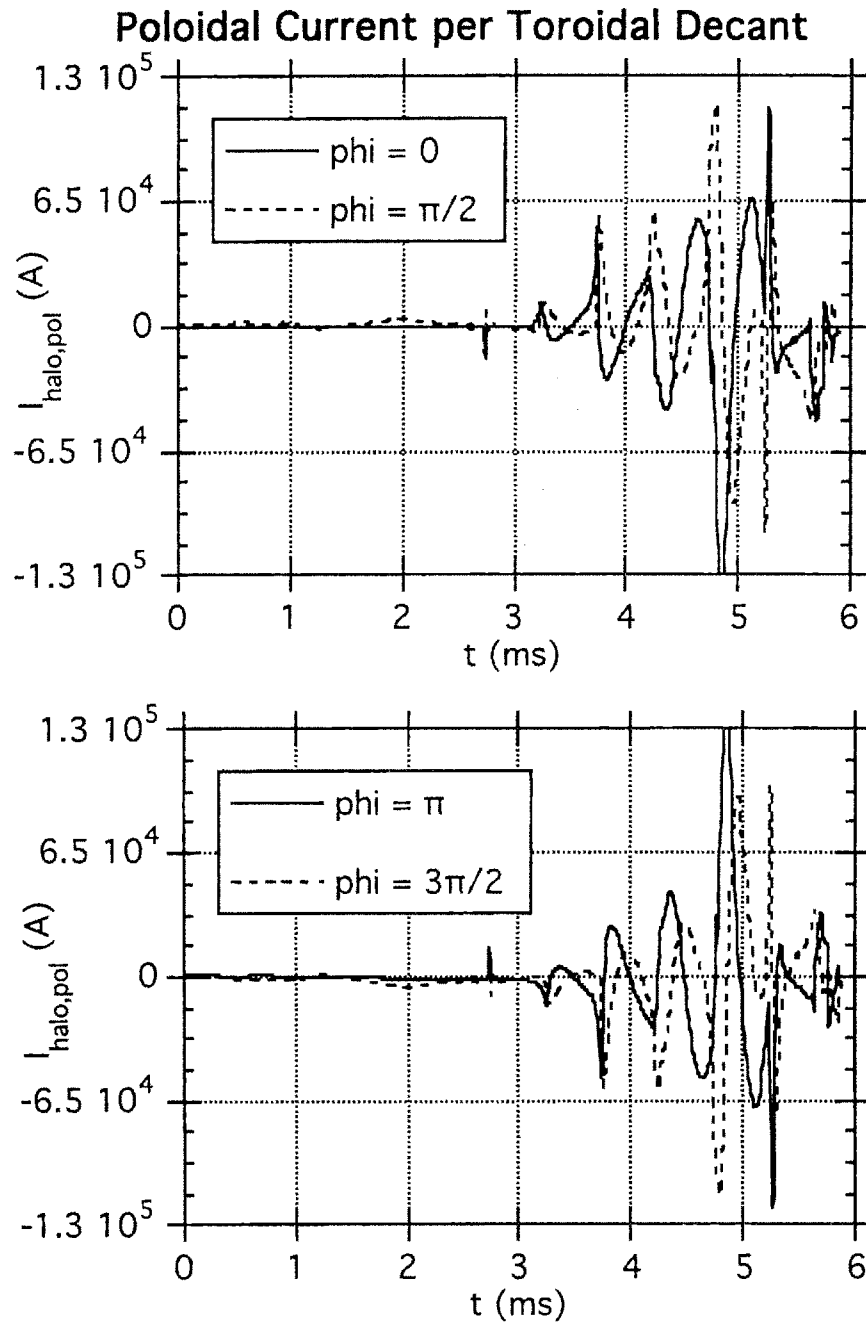
The signals reach their maximum amplitude at the same time the zero-order poloidal halo current peaks. As expected, this amplitude is greater than that which was actually measured in this shot, indicating that the non-axisymmetric nature of the actual displacement was not as severe as the one used in the simulation.

This result emphasizes a fundamental difference between a purely axisymmetric disruption and a non-axisymmetric one. In the axisymmetric case, the only source of poloidal current (or more precisely, rapidly changing toroidal flux) is the equilibrium poloidal current in the plasma. Since this current is small relative to the other currents which flow in the vessel, even when interacting with the large toroidal field, we have seen that it is not a significant contributor to the loads. In the non-axisymmetric case, the toroidal and poloidal directions in the frame of the chamber become coupled in the frame of the plasma, so that the equilibrium toroidal plasma current (or again, poloidal flux) becomes a source of poloidal current. The saving grace is that, even in the absence of the force-free requirement, the spatial distribution of current is constrained to remain divergence-free, satisfying the ordering

$$RK_{\nu,n}^{c,s} \sim n\rho K_{\phi,n}^{s,c}$$

for a given toroidal mode number n, where ρ is a poloidal scale length. Thus for a dominantly n=1 asymmetry, the poloidal currents will be smaller than the toroidal currents by a factor roughly the size of the inverse aspect ratio, a/R. Of course, in the environment of a force-free plasma, one expects $RB_\nu \sim aB_\phi$, so that the contributions to the load will have equal magnitudes. However, unlike pure halo currents which must close through the plasma, eddy currents are not constrained to have these equal-order effects of opposite sign, and a non-axisymmetric disruption can drive large poloidal eddy currents.
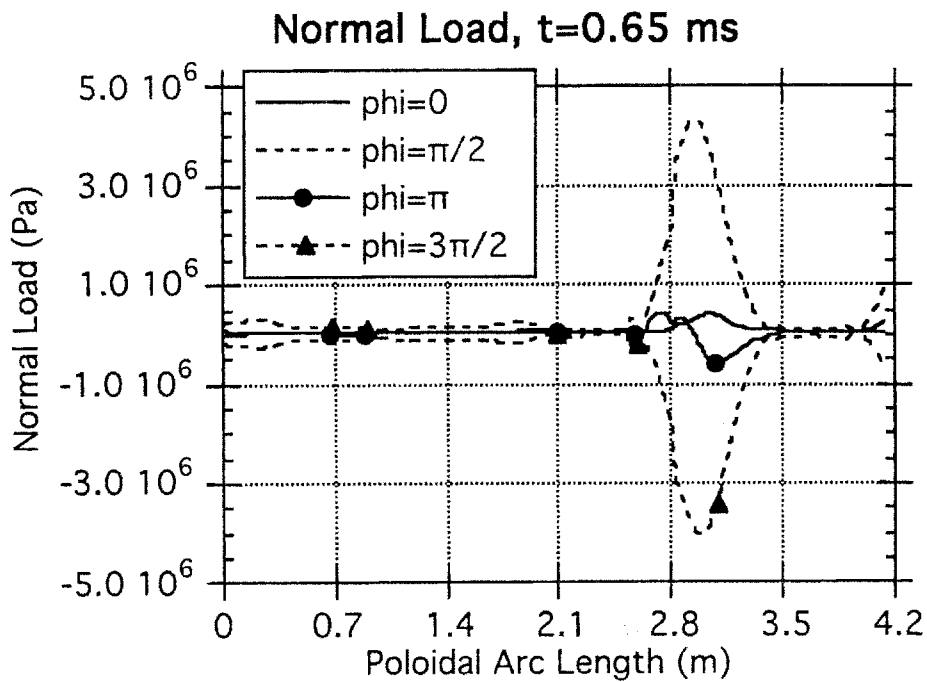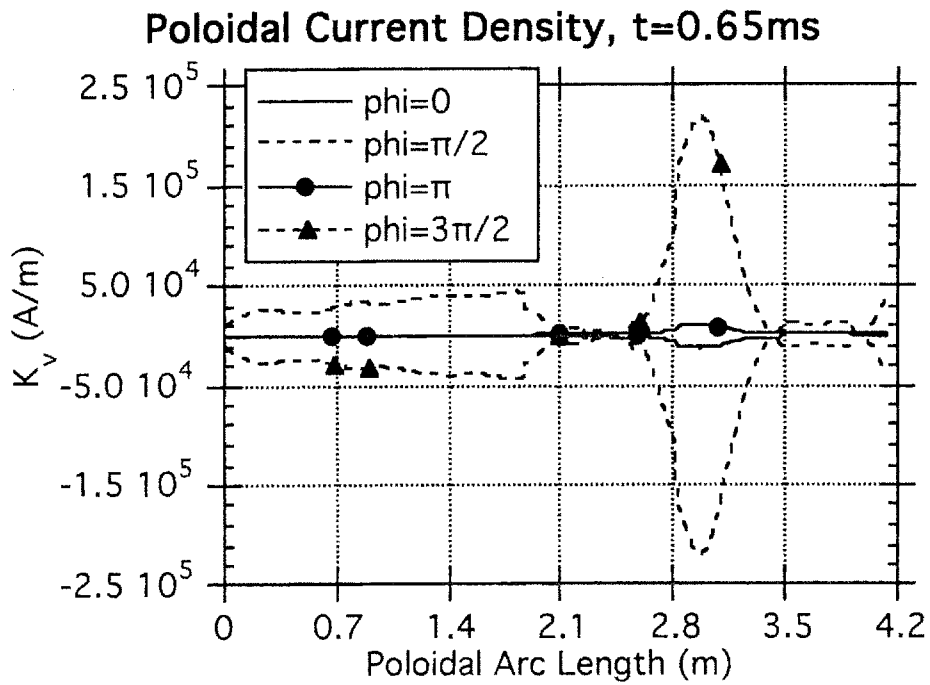
With this in mind, let us now examine the distribution of currents in the vessel, as well as the resulting loads. Early in the disruption, when the plasma is still undergoing a tilt, we get the distributions in the figures that follow; the first is a "map" of the arc length coordinate used in the plots. For ease of viewing, the segments located behind the divertor modules have been mapped to positions beyond the plasma-facing surface.

132

Arc Length "Map" of the C-MOD Vessel

Upper dome • Outer Wall • Outer Divertor Mod. • Divertor Well • Inner Divertor Mod. • Inner wall • Behind Outer Div. • Behind Inner Div.

Toroidal Current Density, t=0.65ms

133
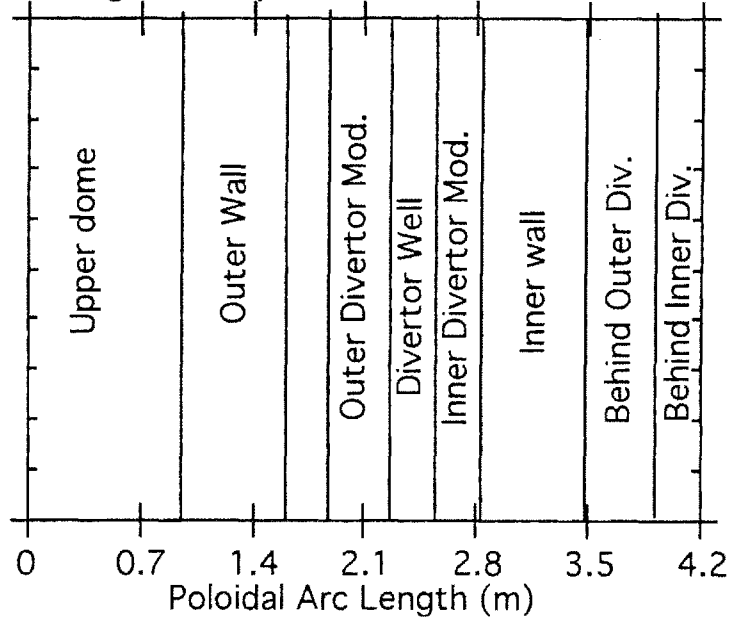
## Poloidal Current Density, t=0.65ms

Normal Load, t=0.65 ms
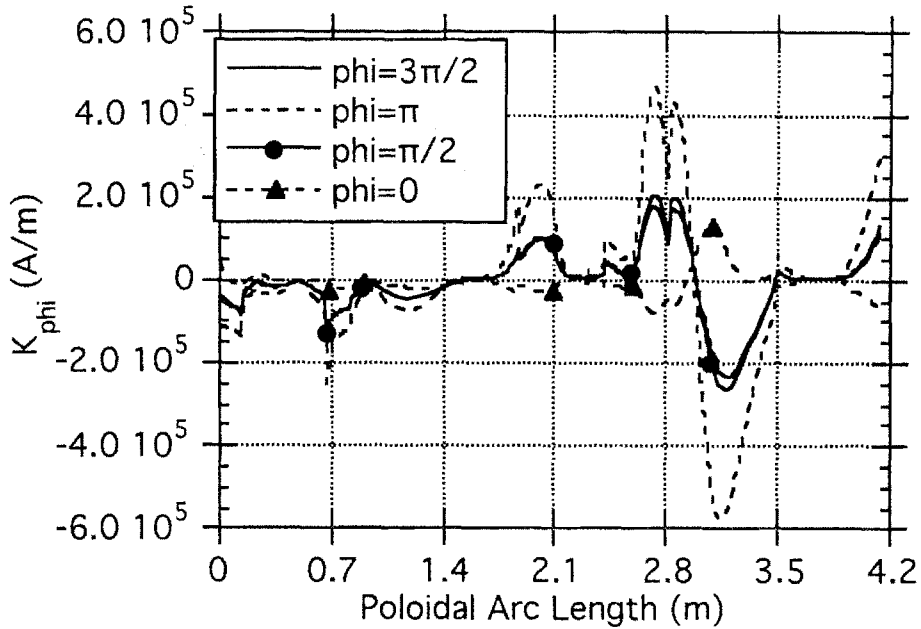
The poloidal and toroidal currents satisfy the appropriate phase and scale relationships, but since the plasma is not yet close enough to the vessel to significantly contribute

to the poloidal field, the loads are at this stage dominated by the $K_v B_\phi$ component. By the time the plasma strikes the wall, the picture has changed:

Toroidal Current Density, t=3.25ms

Poloidal Current Density, t=3.25ms

Normal Load, t=3.25ms
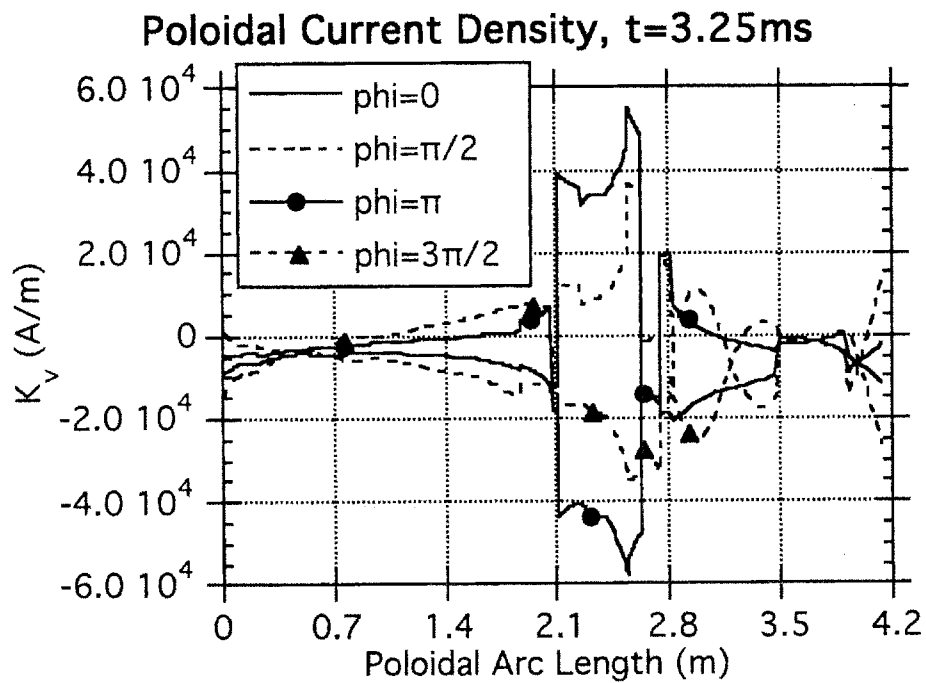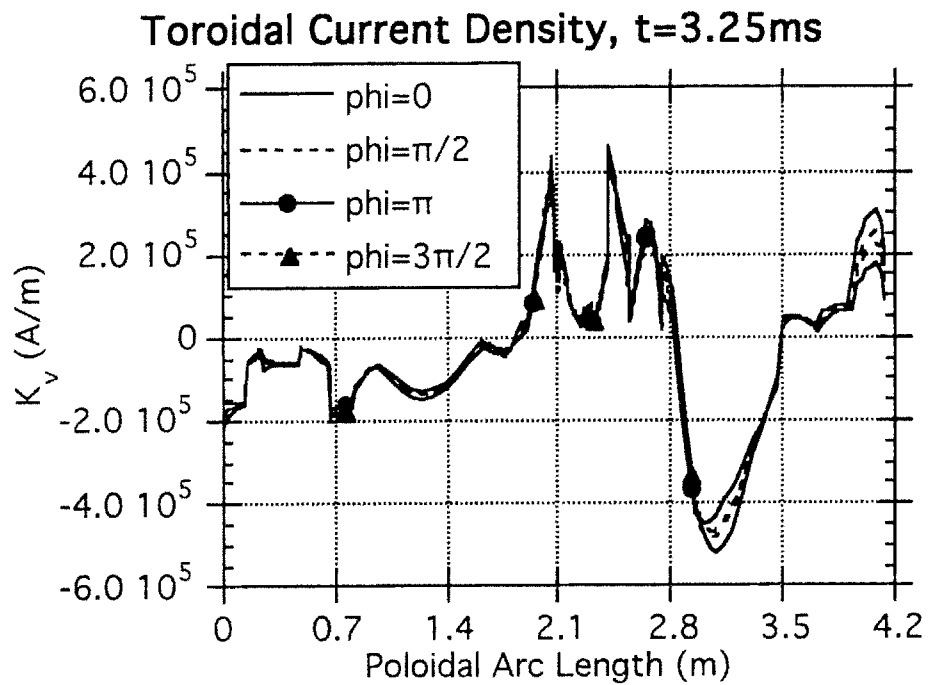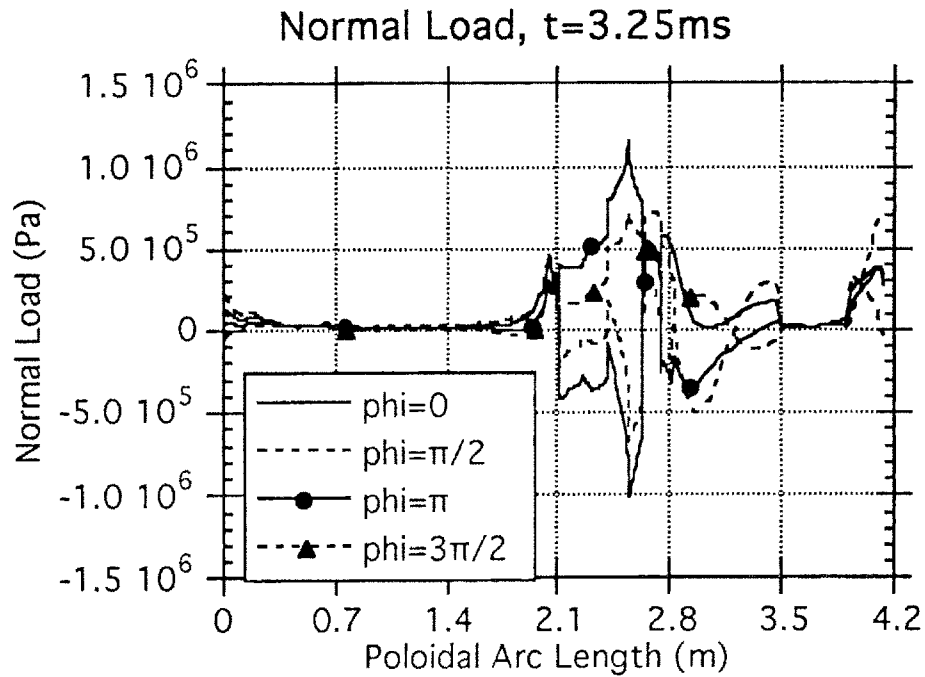
At this stage, the "untilting" of the plasma has produced an interesting result: the toroidal current is nearly symmetric, the zero-order image currents dominating the higher order. The poloidal current is strongly asymmetric, but even though the plasma has hit the wall, the amplitude has *decreased* from the earlier time; the load, still dominated by the poloidal current, has decreased also. This is another indication that it is eddy currents and not halo currents that pose the major threat to the wall.

Toroidal Current Density, t=5.2 ms

Poloidal Current Density, t=5.2 ms

137
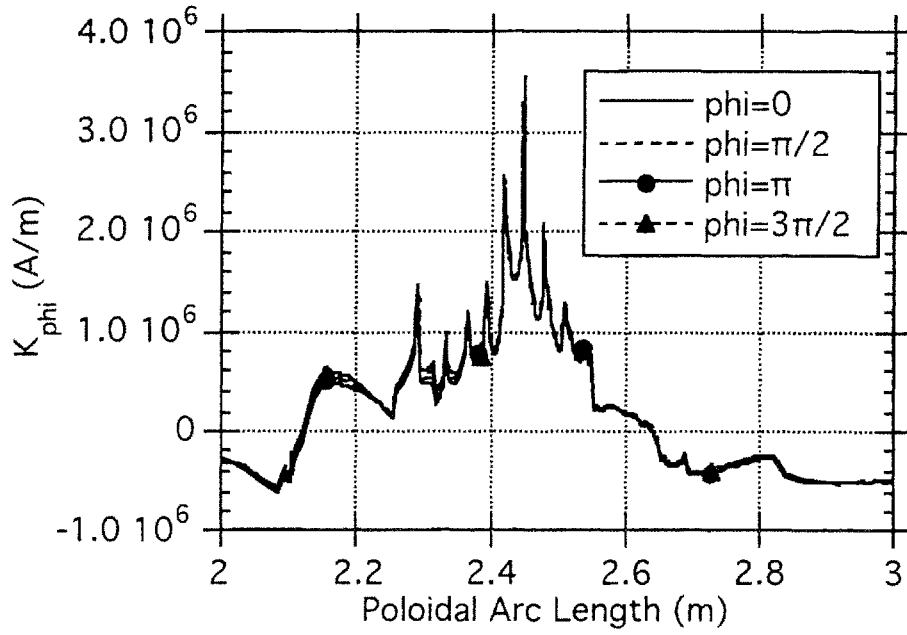
Normal Load, t = 5.2 ms
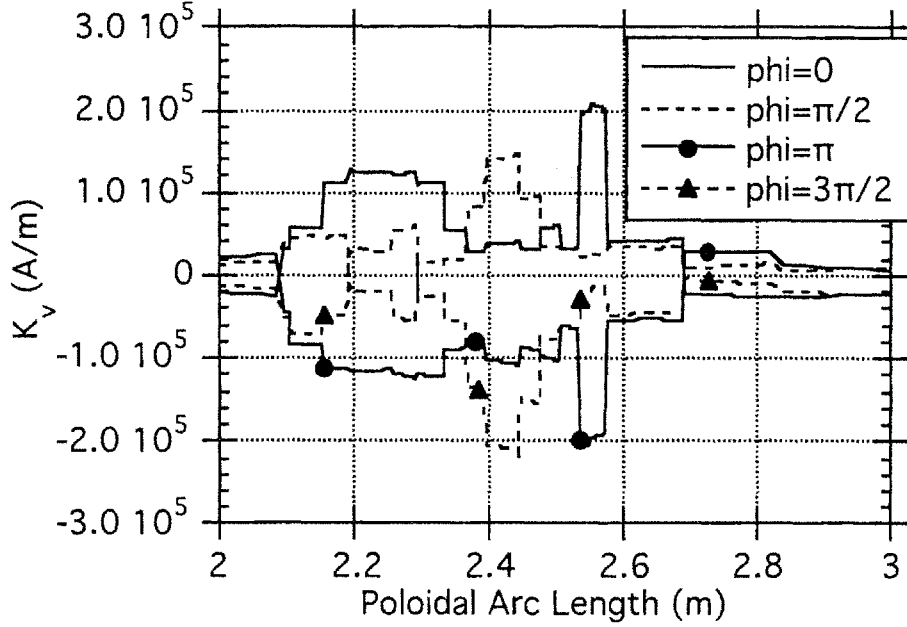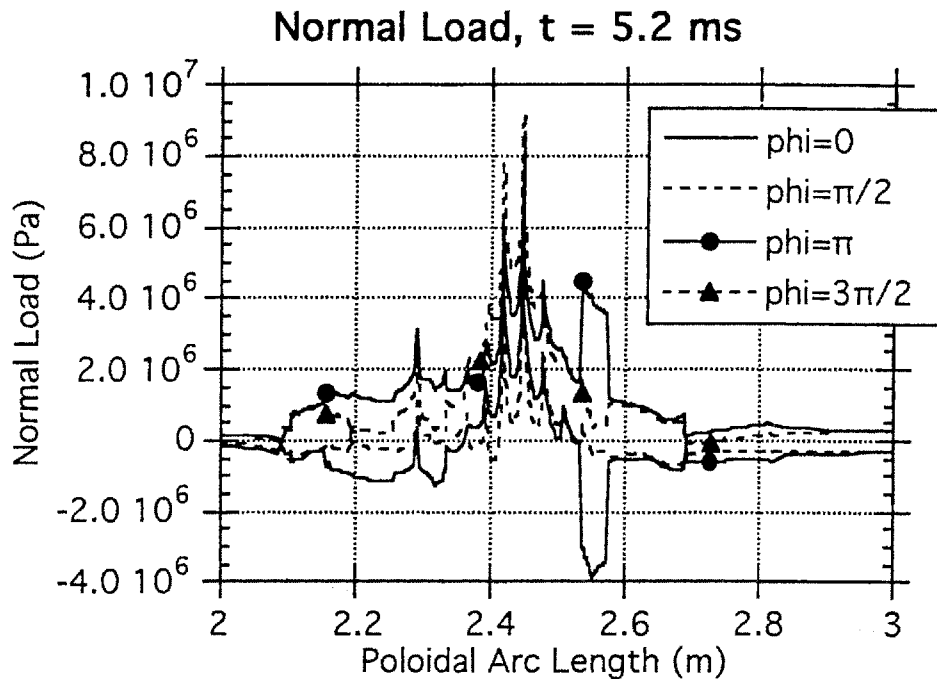
In these pictures we have concentrated on the poloidal region of the lower divertor. Now that the plasma is rapidly approaching the bottom of the divertor well, large zero-order toroidal image currents have started to flow, and have become the dominant contributor to the load on the vessel, so that unlike the reference case the zero-order poloidal and toroidal currents peak at the same time. The part of the chamber which has the large non-axisymmetric load with a negative peak at $\phi=0$ is the corner below the inner divertor module; the plasma "jumps over" this region, so in the sheet current model it has no direct contact with bulk plasma; it is not immediately clear why this has the effect it does on the current flow and resulting load. A more striking example of this behavior will be shown in section 5.4.

Even though the toroidal current is almost completely symmetric, the poloidal current is still strongly non-axisymmetric. It still satisfies the divergence-free condition because the poloidal distribution is nearly flat.

To observe how much the presence of large non-axisymmetric poloidal currents changes the nature of the load on the chamber after the plasma has struck the wall,

138

consider the following plot of the load at the same point in time in the purely axisymmetric simulation:

Normal Load, t=5.2 ms, Axisymmetric
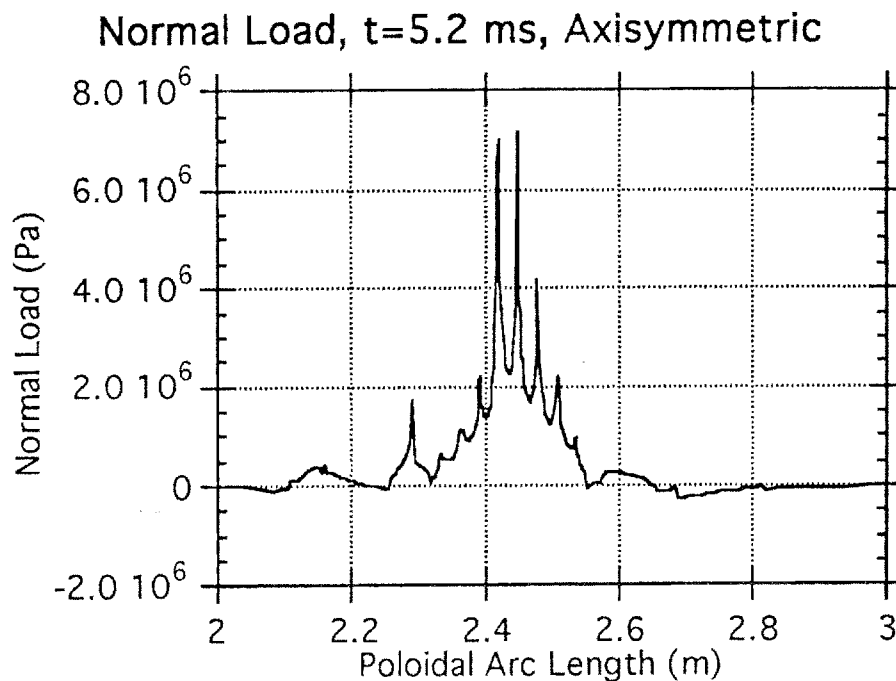
The basic character is the same, except that the axisymmetric case does not experience anything unusual in the region below the inner divertor. However, even though the peak load is dominantly axisymmetric, the chamber obviously experiences highly non-axisymmetric loads in the course of the disruption. This is a clear intersection of paths between the electromagnetic side of the halo current problem and the structural engineering side; further examination of this point will not be considered here. We will instead move to an area within the specific scope of the sheet current model: parametrics.

5.3. Parametric Runs

Having gained considerable confidence in the validity of the sheet current model, we now return to the reference case. We will examine a series of runs where particular plasma parameters are varied to see if there are clear scalings, and if these scalings agree with the heuristic expectations from Chapter 3. Given that we have already seen how much freedom a non-axisymmetric displacement gives the system, we will restrict

our attention to axisymmetric cases, where there are plenty of clearly defined parameters. Further investigation of non-axisymmetric effects will be left for the next section.

The first variation is not a true parametric run, but literally a change of direction: the same plasma as in the reference case undergoes a pure inward-radial displacement, striking the wall at a location of maximum toroidal field. The trajectory is shown in figure (5.16). Since the plasma has a shorter distance to travel before striking the wall, the simulation is obviously over a shorter period of time.

Another consequence of the smaller gap between the plasma and wall is shown in figure (5.17). As poloidal flux is compressed in the gap, the image currents in the plasma are driven higher than in the downwards case. The poloidal halo current (figure 5.18) is also higher as less resistive decay of the poloidal current has taken place, both due to the shorter time and the fact the plasma is now "climbing up" the toroidal field. However, in spite of the larger poloidal current interacting with a higher toroidal field value, the dominant load still comes from the toroidal eddy currents. Carpet plots of the current distributions and the load (figures 19-21) show that the larger image currents produce considerably higher localized forces.
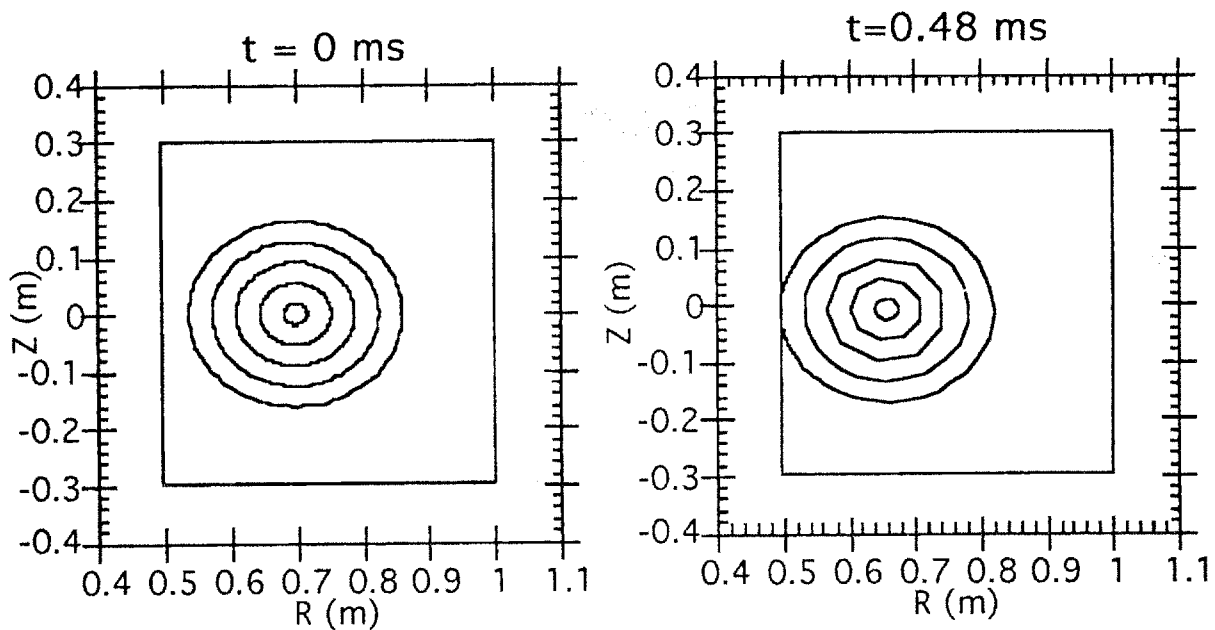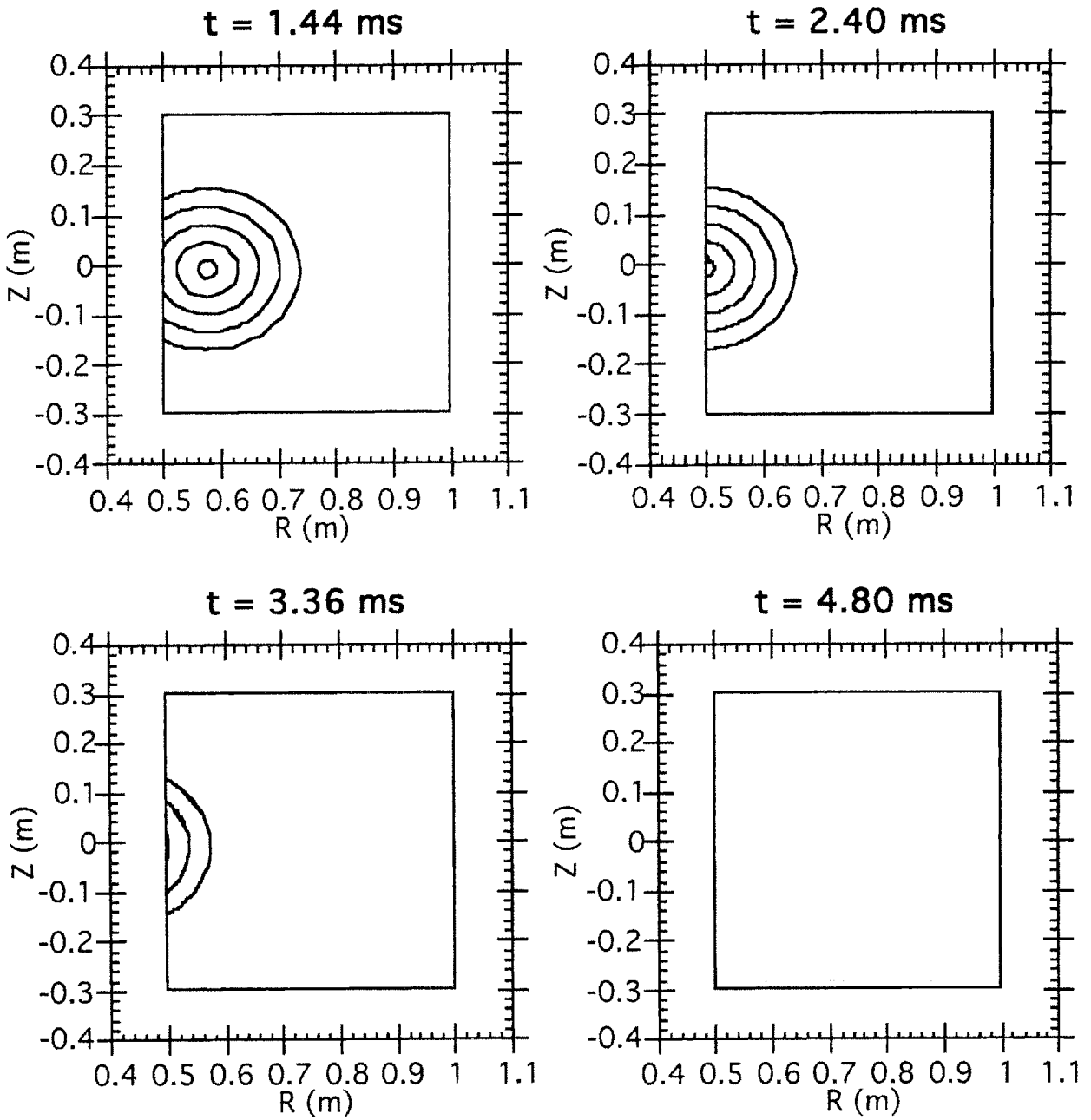
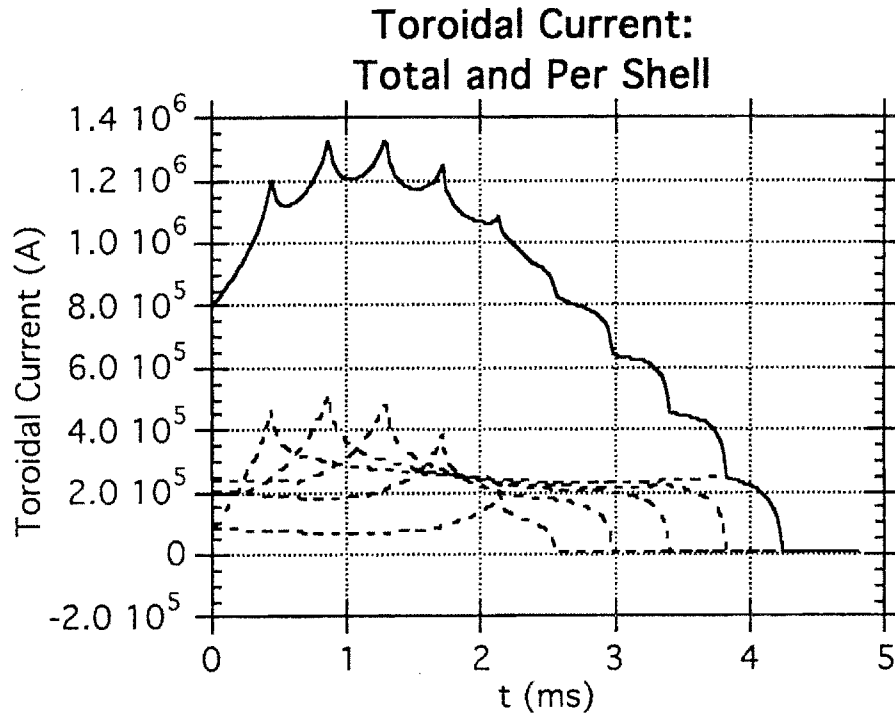**Figure 5.16.** Trajectory of radial disruption.

Toroidal Current: Total and Per Shell

Figure 5.17. Evolution of the toroidal plasma current for the radial disruption.
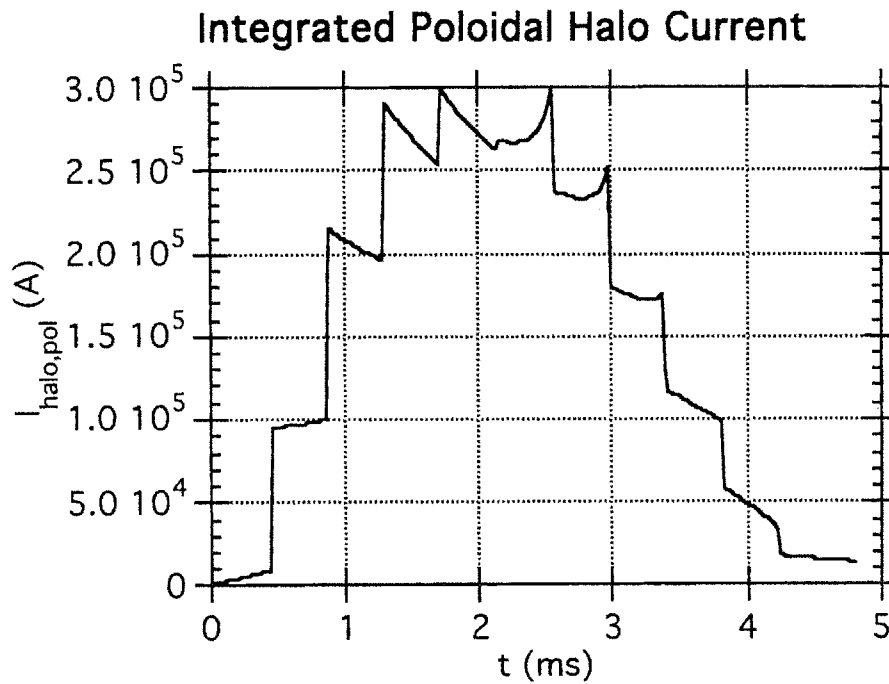
Integrated Poloidal Halo Current

Figure 5.18. Poloidal halo current over time for the radial disruption.
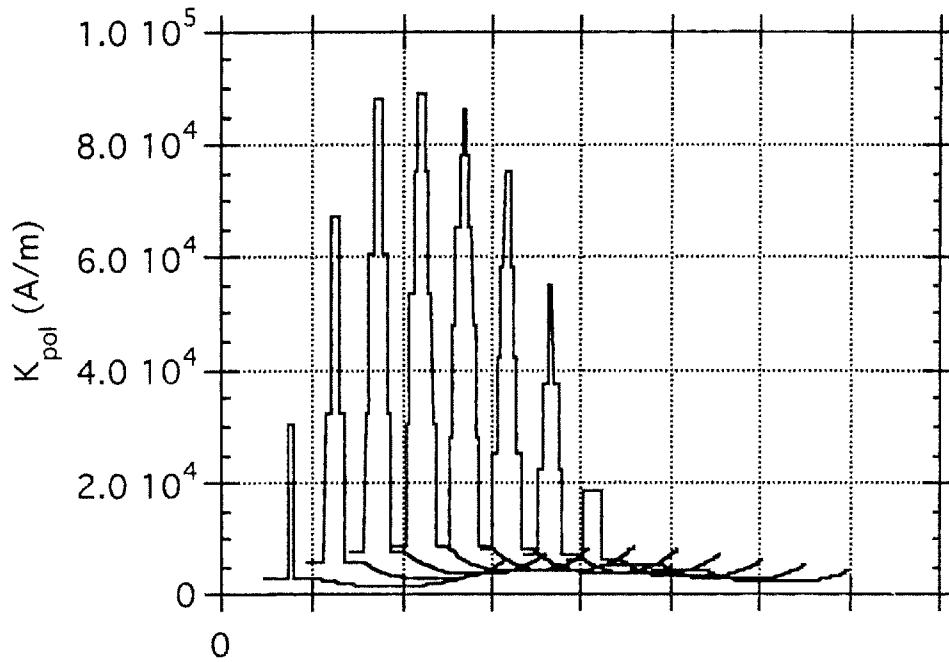
Evolution of Poloidal Current
Profile in the Chamber

Figure 5.19. Carpet plot of the poloidal current density for the radial disruption.

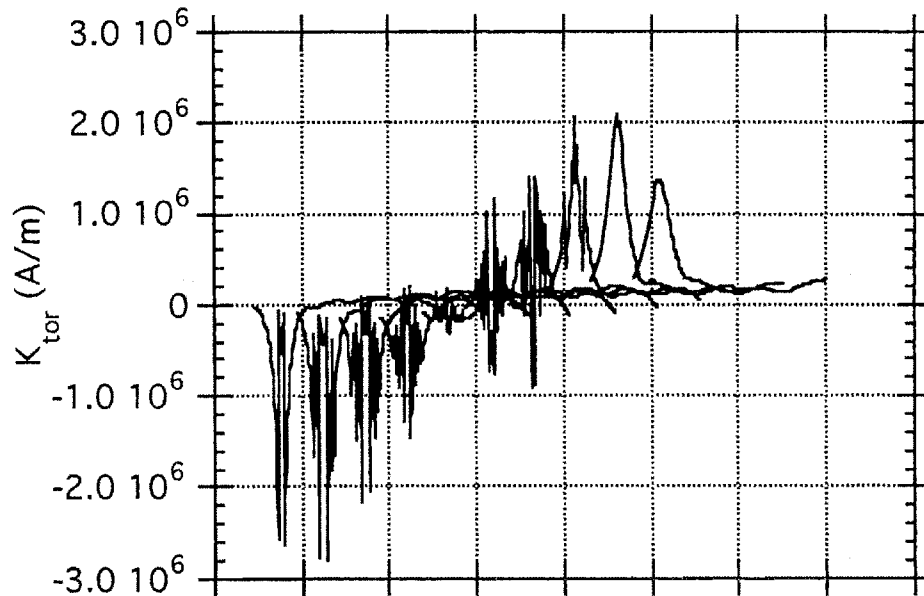## Evolution of Toroidal Current
Profile in the Chamber

Figure 5.20. Carpet plot of the toroidal current density for the radial disruption.

Evolution of the Normal Load
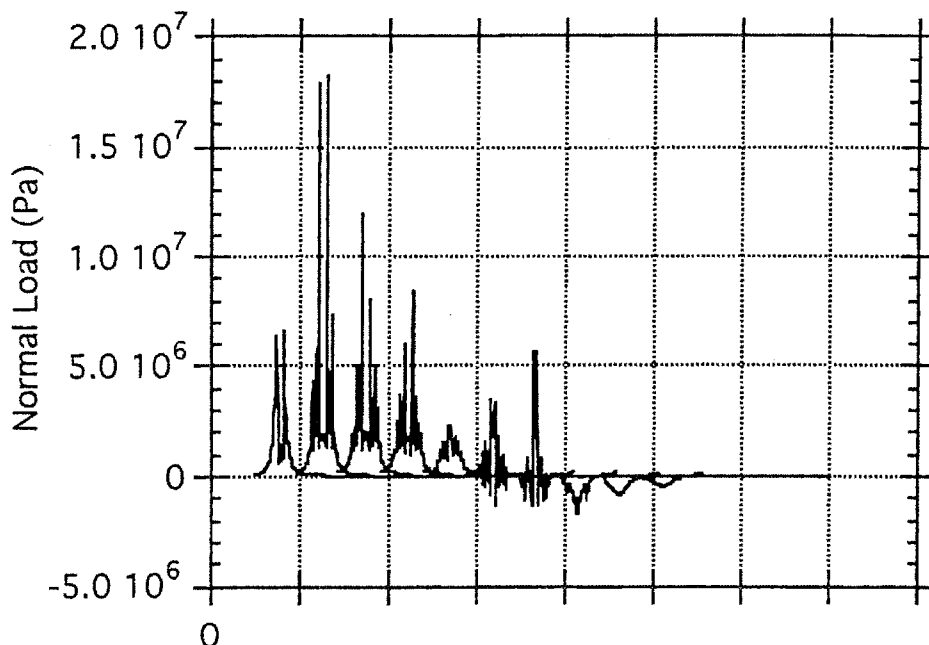## on the Chamber

Figure 5.21. Carpet plot of the normal loads for the radial disruption.

We will now restrict our attention to the peak poloidal halo current, peak toroidal current density, and peak normal load as we vary several plasma parameters. We begin with the most obvious, the plasma current. The results are shown in figures (5.22-24).

The outcome is not surprising. The halo current increases in an almost perfect quadratic, in accordance with the heuristic argument in Chapter 3; however, the precise magnitude is not given correctly by any of the simple expressions derived there. The magnitude of the peak toroidal current density (note the image currents in the wall are negative) increases linearly and remains the dominant contribution to the load. The load itself grows quadratically, as would be expected since the local poloidal field strength will also be proportional to the toroidal current.
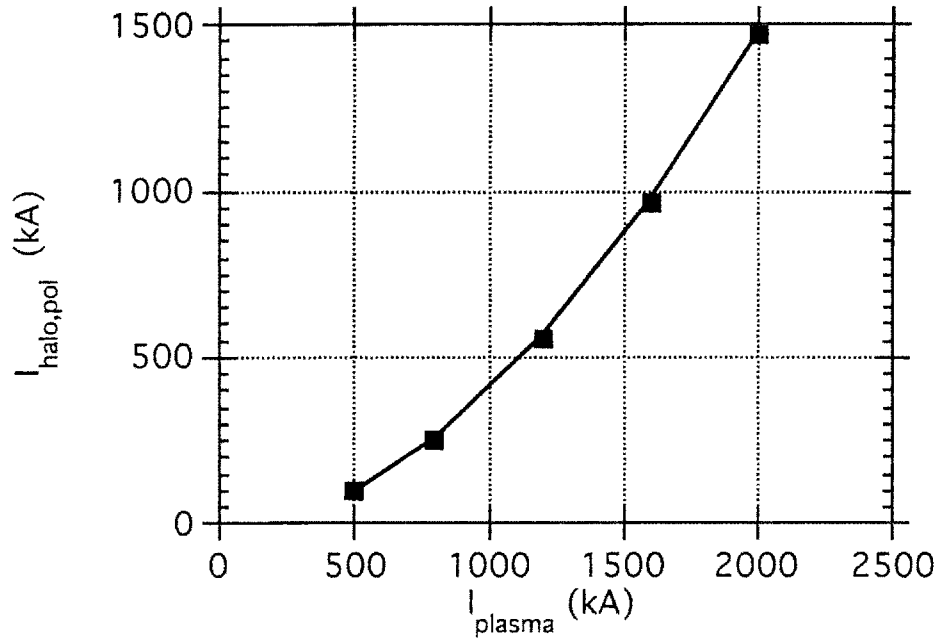
144

Poloidal Halo Current vs. Plasma Current

Figure 5.22.

Peak Toroidal Current Density
in the Chamber, vs Plasma Current
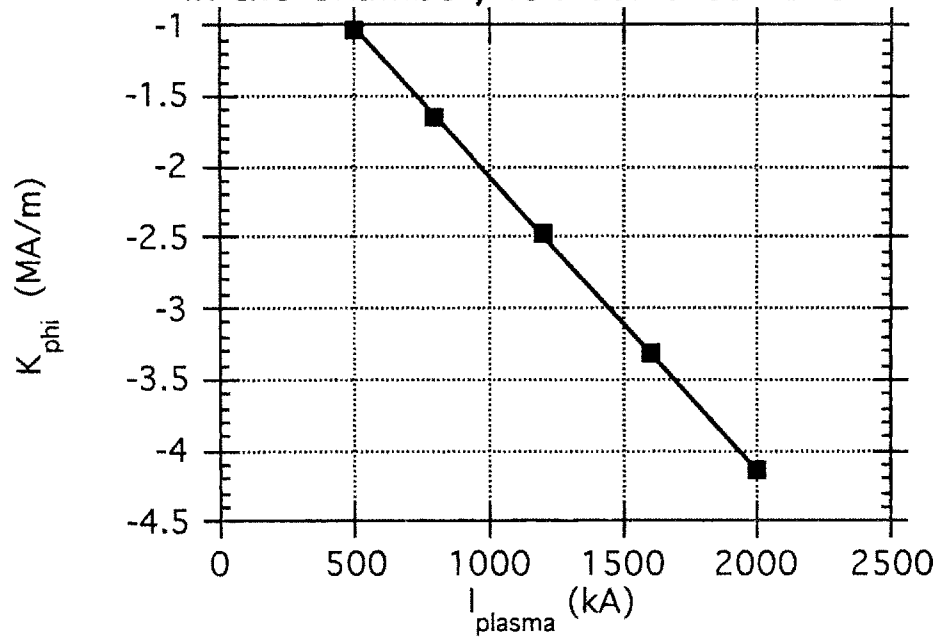

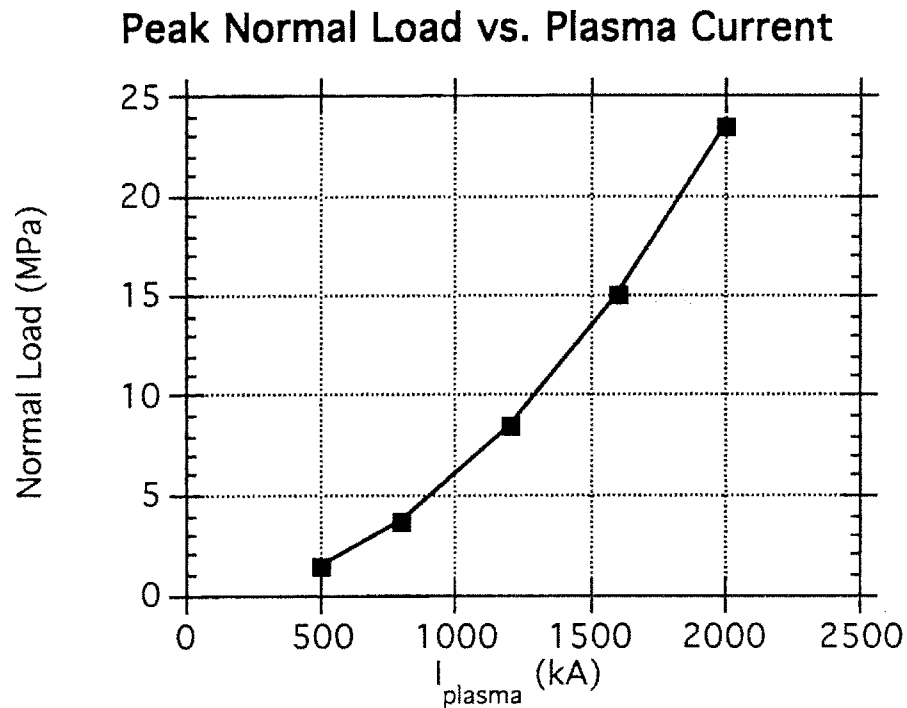Figure 5.23.

Peak Normal Load vs. Plasma Current

Figure 5.24.

In figures (5.25-27) we consider several runs where the major radius of the plasma (and the chamber, accordingly) is varied. This has little effect on the toroidal current density, and therefore the load on the chamber, since the purely vertical displacement is not highly sensitive to the change in radius. The poloidal halo current does change, however, as the equilibrium poloidal current in the plasma increases. The result is not the purely linear one predicted in Chapter 3; a possible reason is the lack of toroidal effects in that model.
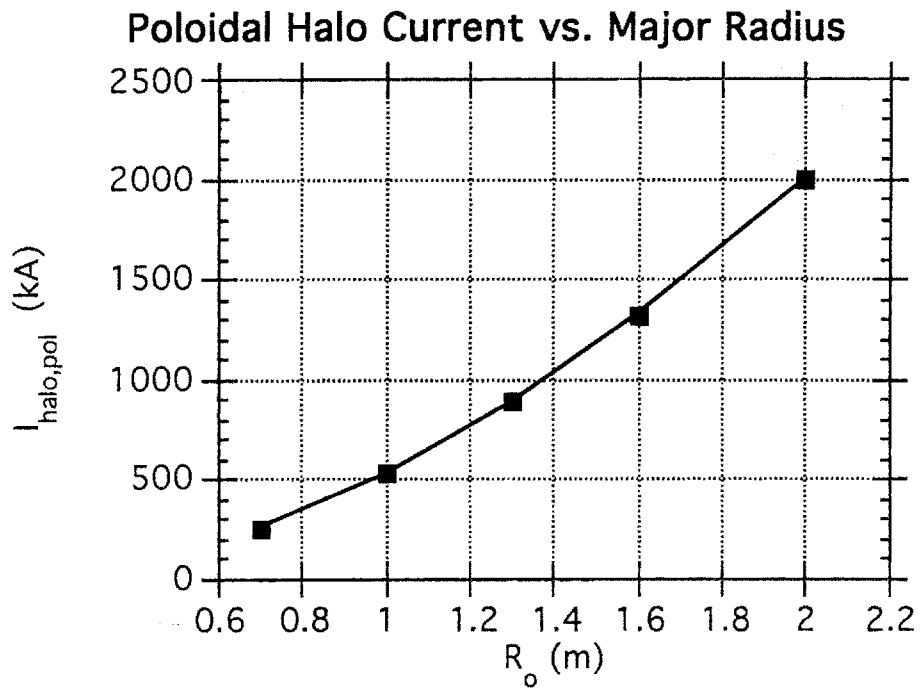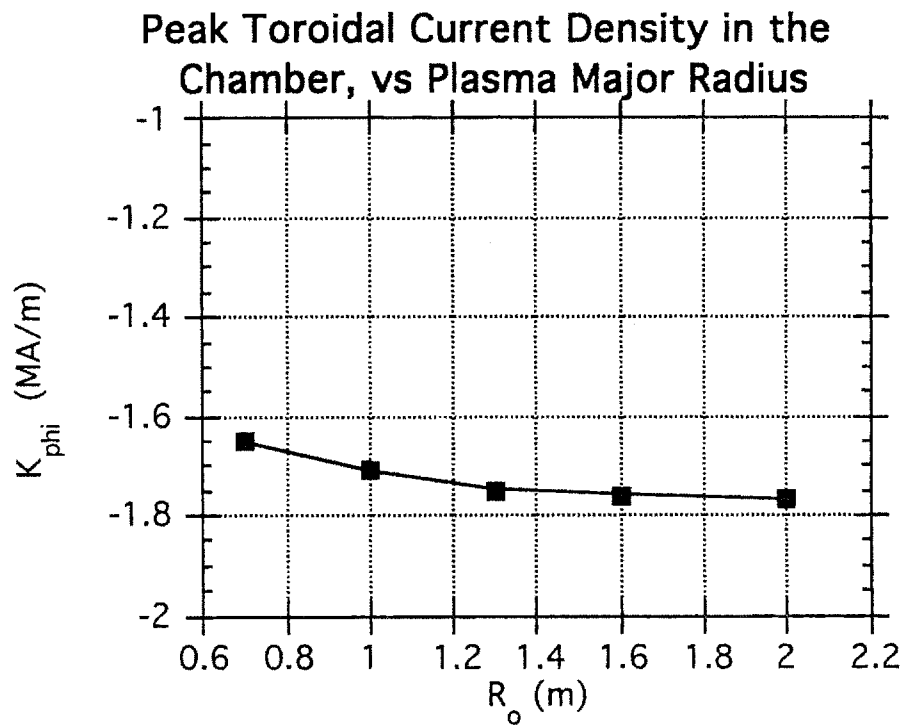
Poloidal Halo Current vs. Major Radius

Figure 5.25.

Peak Toroidal Current Density in the Chamber, vs Plasma Major Radius

Figure 5.26.
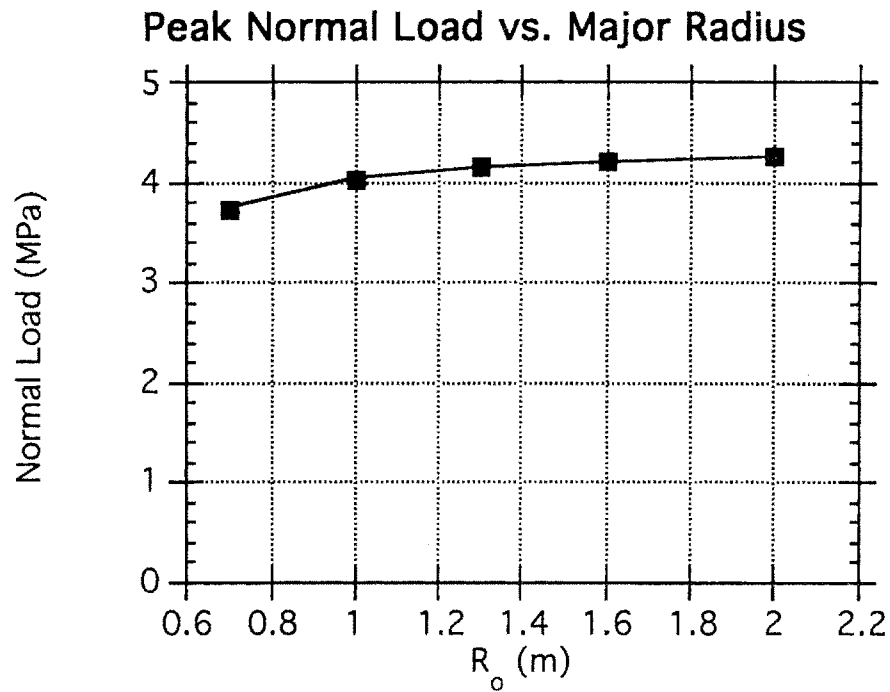
Peak Normal Load vs. Major Radius

Figure 5.27.

We now consider what happens if the disruption velocity is varied. It is expected that this will have the strongest effect on the eddy currents, which were not considered in Chapter 3. The results are shown in figures (5.28-30).
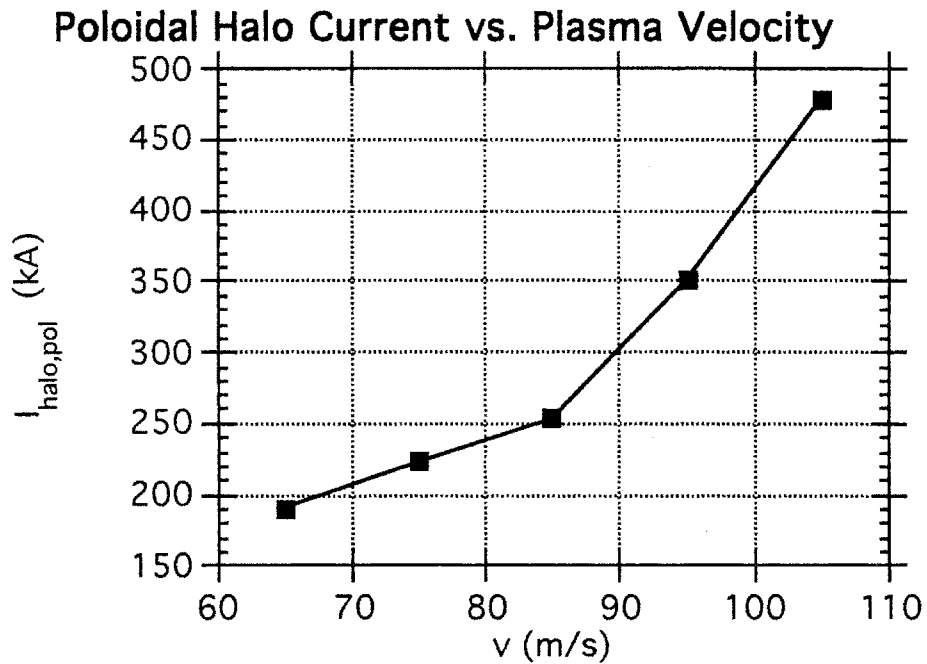
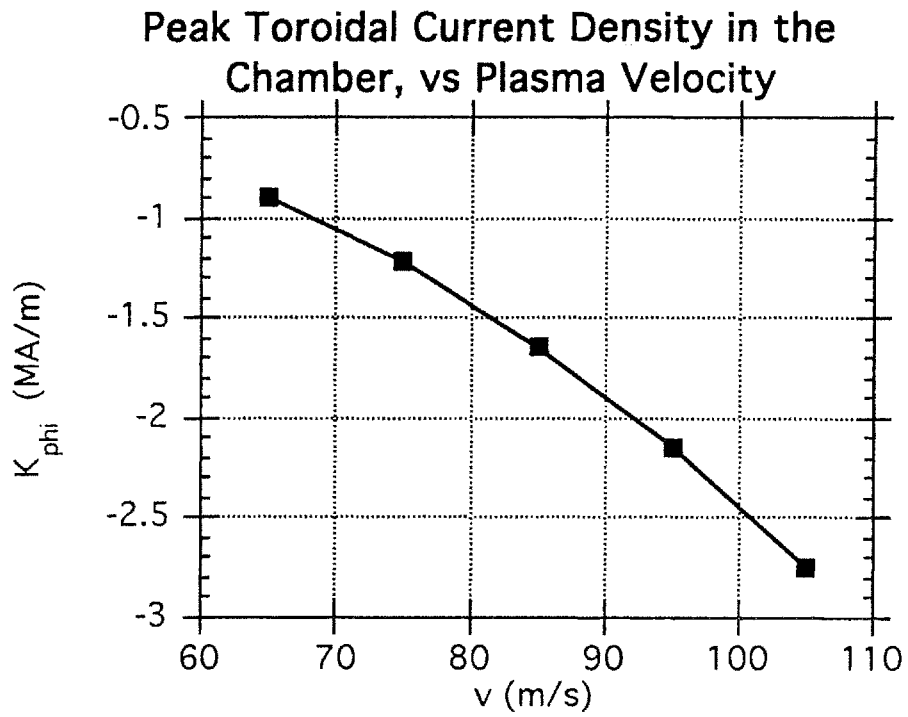## Poloidal Halo Current vs. Plasma Velocity

Figure 5.28.

Peak Toroidal Current Density in the Chamber, vs Plasma Velocity

Figure 5.29.
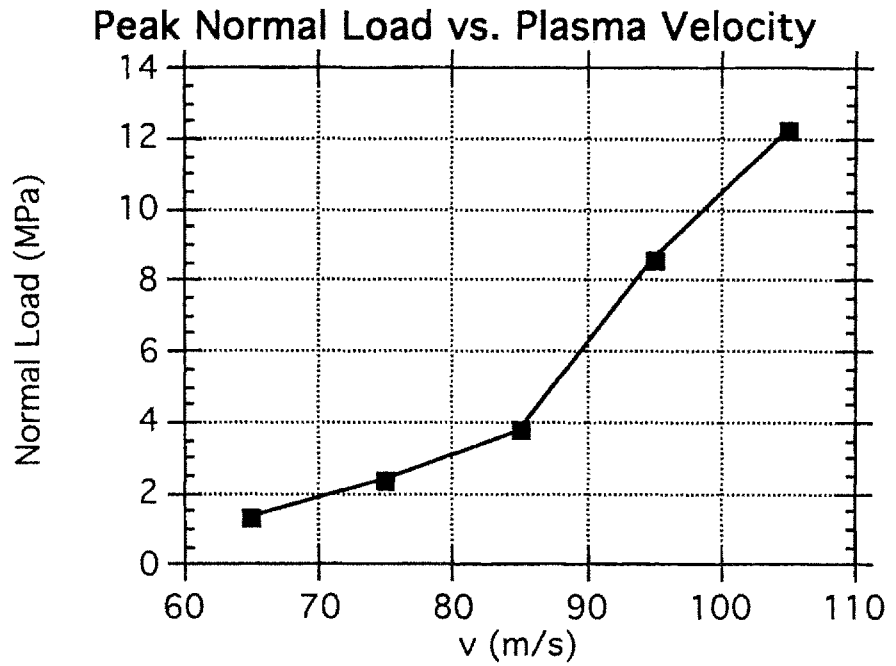
Peak Normal Load vs. Plasma Velocity

Figure 5.30.

149

The poloidal halo currents do increase with velocity, since less resistive decay takes place before the plasma hits the wall, and there is a stronger compression of toroidal flux. The higher velocities also drive larger eddy currents, which again drive the dominant load; as the eddy currents vary by a factor of about three, the loads go as the square, varying by about an order of magnitude. The exact functional relationships, especially in the case of the loads, are not clear.

Even if there is no exact relation appearing from a run, it is at least useful to see a monotonic relationship. However, the following results from varying the plasma minor radius show that when competing effects are involved, no clear relationship may emerge. While figure (5.31) shows a well-behaved relationship between the minor radius and poloidal halo current, it is a completely different curve from the $1/a^2$ heuristic prediction. The toroidal current and load data in figures (5.32-33) show no obvious trend. The fact that the peak toroidal current density is *positive* for small radii is due to the fact that the toroidal halo current "rebound" towards the end of the disruption is actually greater than the negative image currents driven in the wall.
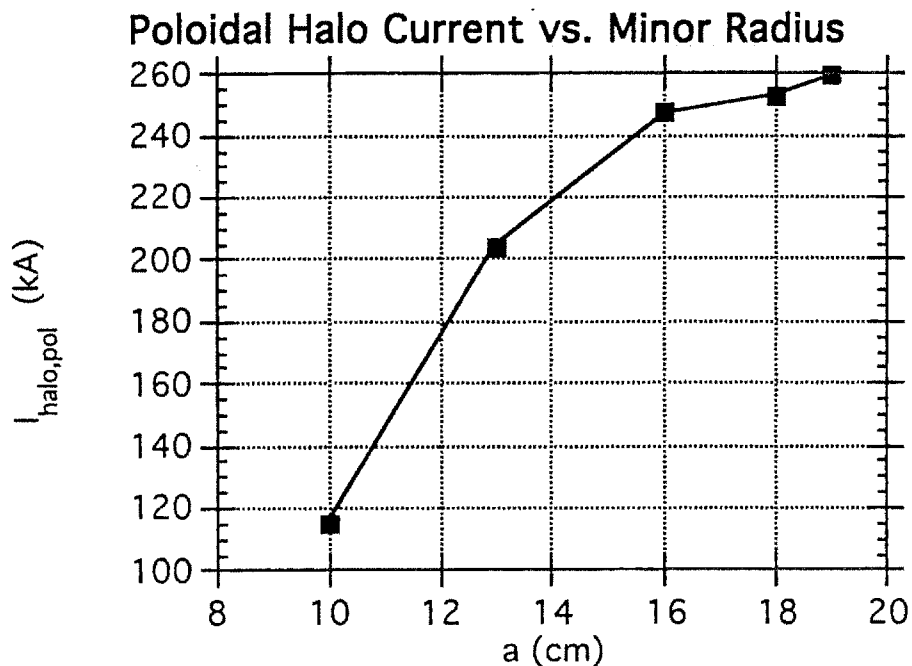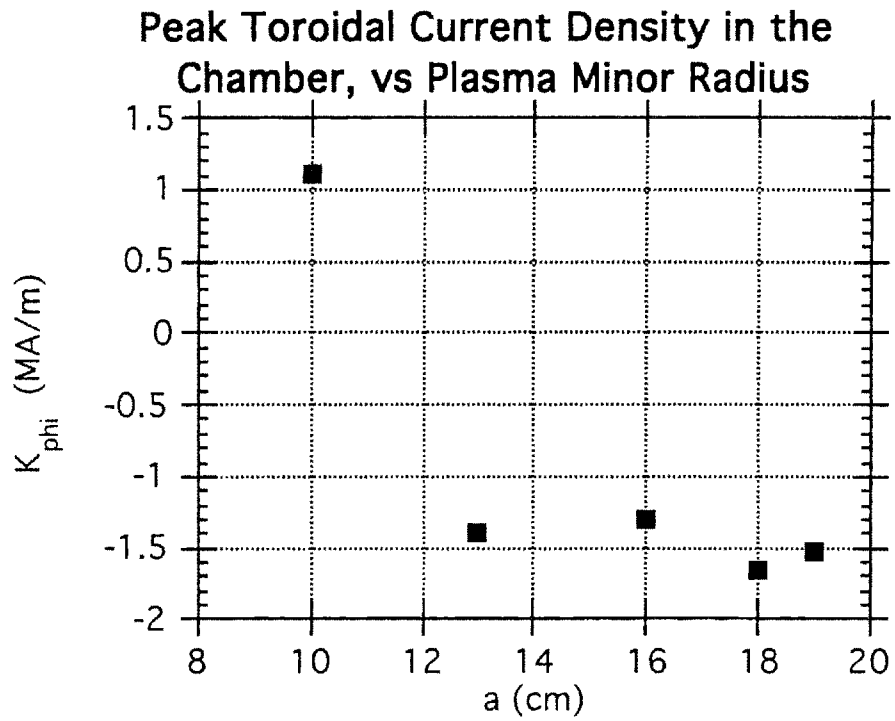

Figure 5.31.

Peak Toroidal Current Density in the Chamber, vs Plasma Minor Radius

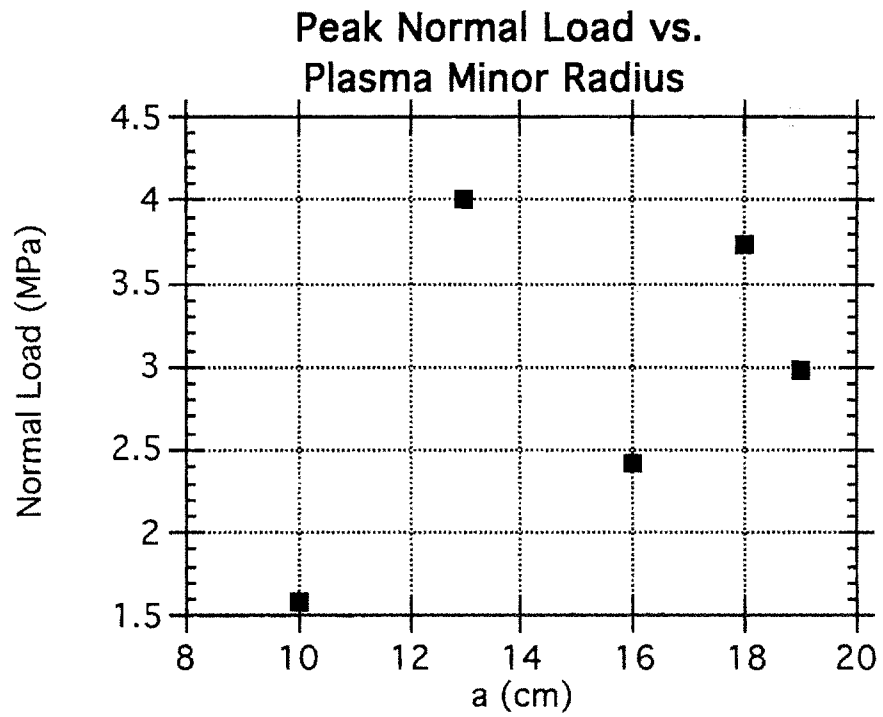Figure 5.32.

Peak Normal Load vs. Plasma Minor Radius

Figure 5.33

The last parameter we will consider is the plasma conductivity. Note that the dependence shown in these curves would appear even stronger if the corresponding Spitzer temperature were used as the independent variable. The implications of these runs are interesting, because the physics required to predict the plasma conductivity or temperature is completely outside the sheet current model. However, even if such predictions were available, they would be of no use for disruptions driven by, say, the sudden failure of a power supply as opposed to the plasma physics of an advanced operating scenario.

Figure (5.34) show the dependence of the poloidal halo current on the conductivity, which looks purely linear. This is somewhat surprising since the disruption lasts long enough for the resistive decay of the poloidal current in the plasma to show its exponential character, and adjusting the conductivity is simply adjusting the ratio of the disruption time to the poloidal L/R time. Since the toroidal L/R time is much longer, the near-linear relationship in figure (5.35) is more acceptable. The anomalous point in the load curve at 0.4 Mmho/m does not have an obvious explanation; that simulation was subject to the same convergence criteria as all the other runs.
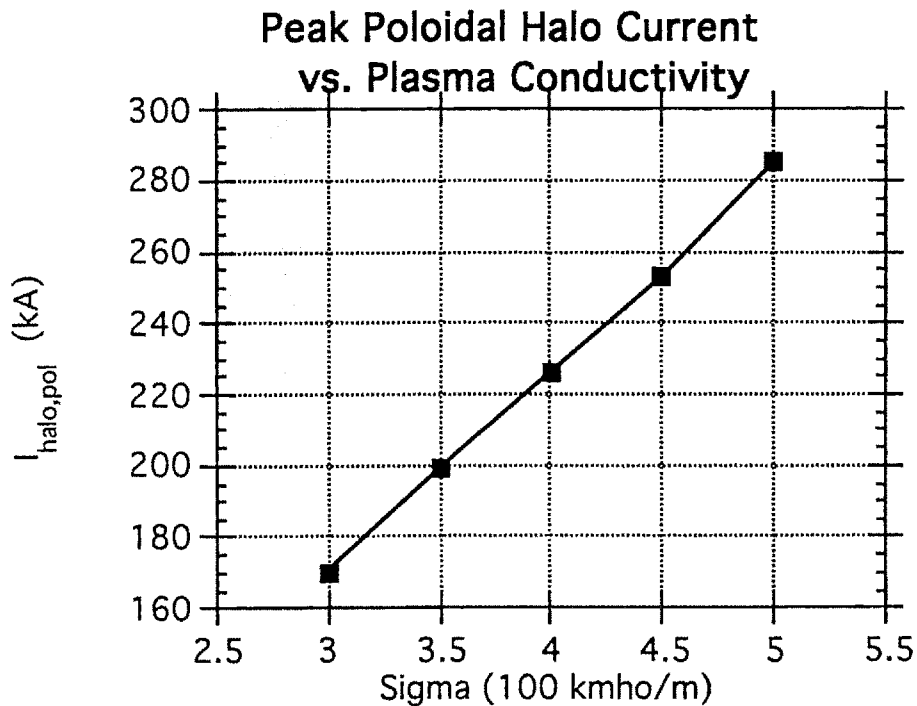
Peak Poloidal Halo Current vs. Plasma Conductivity

Figure 5.34.

Peak Toroidal Current Density
in the Chamber, vs Plasma Conductivity
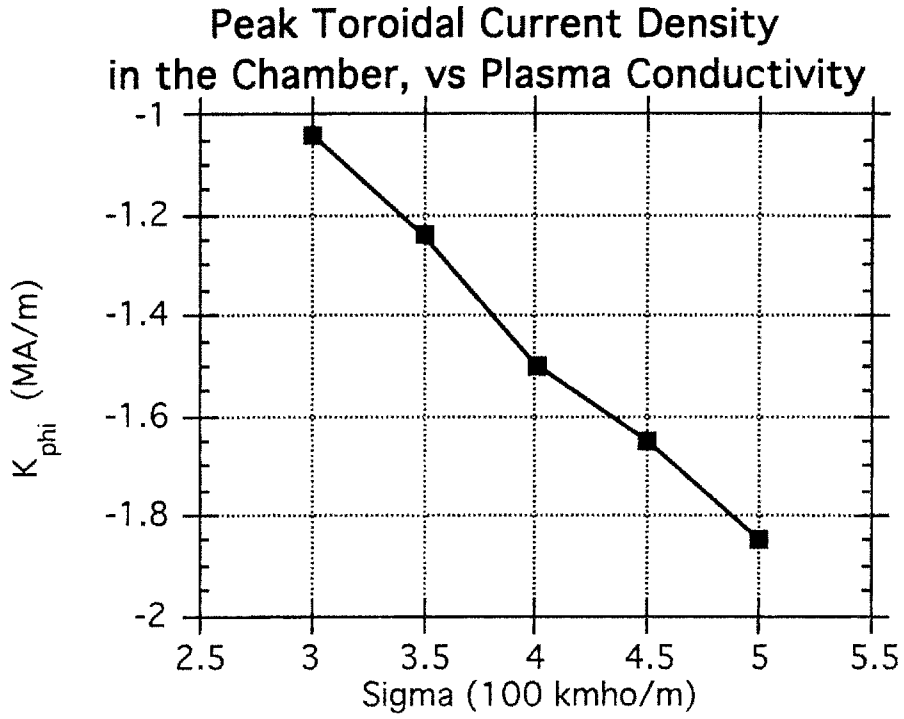
Figure 5.35.

Peak Normal Load vs. Plasma Conductivity
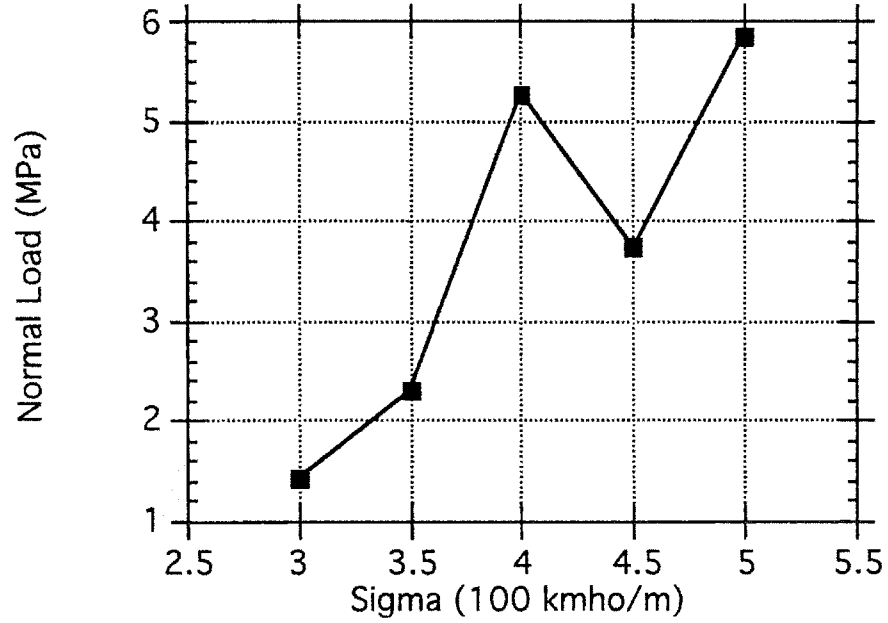
Figure 5.36.

5.4. Non-Axisymmetric Effects

In this section we will examine some consequences of a non-axisymmetric event in the context of the simpler rectangular vacuum chamber, to make the intrinsic features clearer than was possible with the Alcator case. Two cases will be considered: a tilt that is allowed to progress up to the moment before contact with the vacuum vessel, and one like the displacement used for the Alcator shot, where the plasma is returned to an axisymmetric configuration just before impact.

In order to have slightly greater range for the tilt, the plasma is modified slightly from the reference case. The minor radius is decreased to 15cm and the plasma is centered in the chamber, at a major radius of 75cm.

We first consider the unrestricted tilt, whose trajectory is shown in the following frames. As before, the viewpoint is at $\phi=\pi/2$ and slightly elevated.
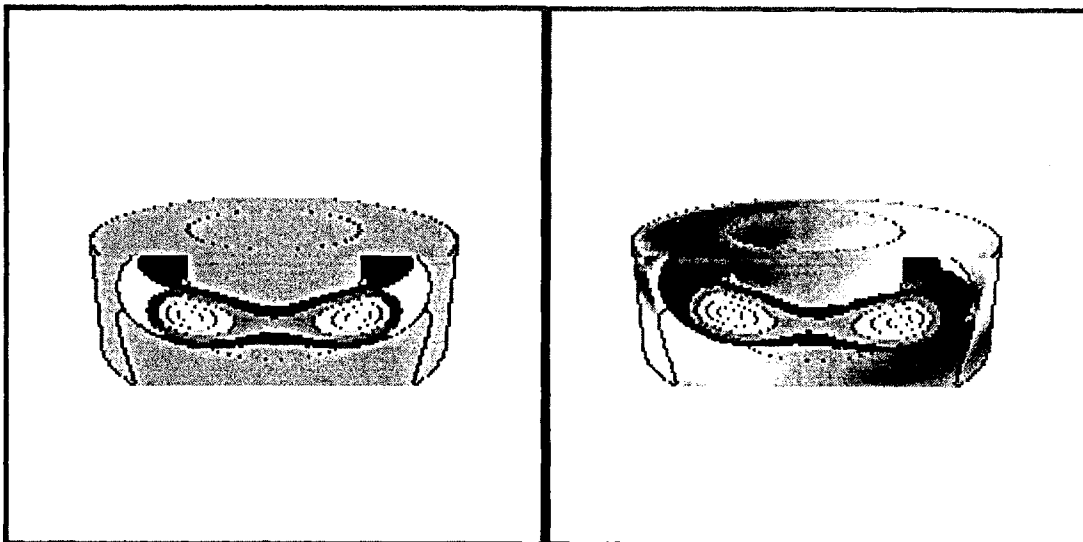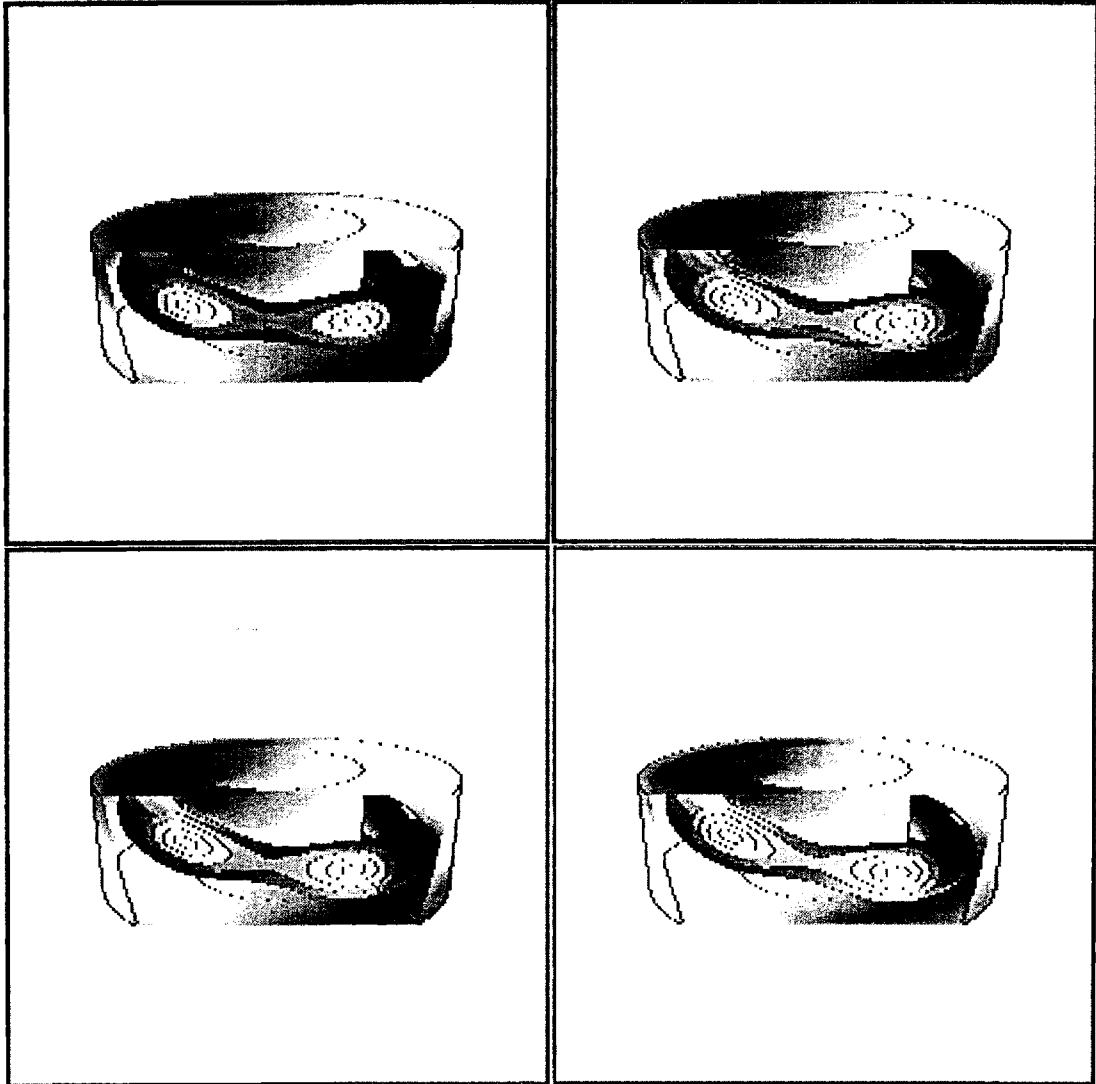
The zero-order plasma current is not strongly affected by this motion and undergoes only a slow resistive decay:

Zero-Order Plasma Current
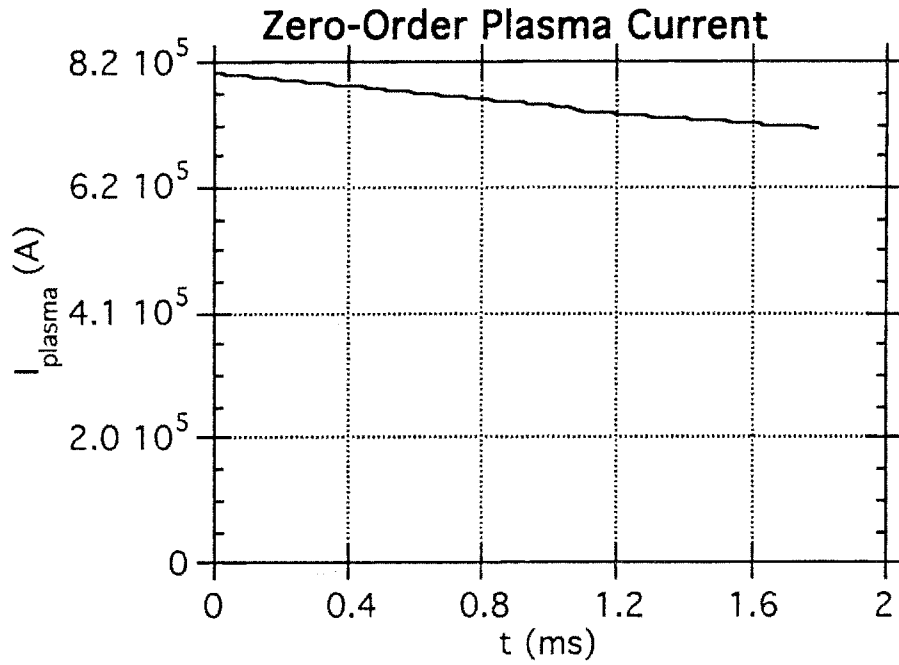
The next set of plots is of the toroidal current density, which shows the strong cosine response to the tilt; the sine components ($\phi=\pi/2$, $3\pi/2$) show only the effects of the resistive decay of the plasma current.
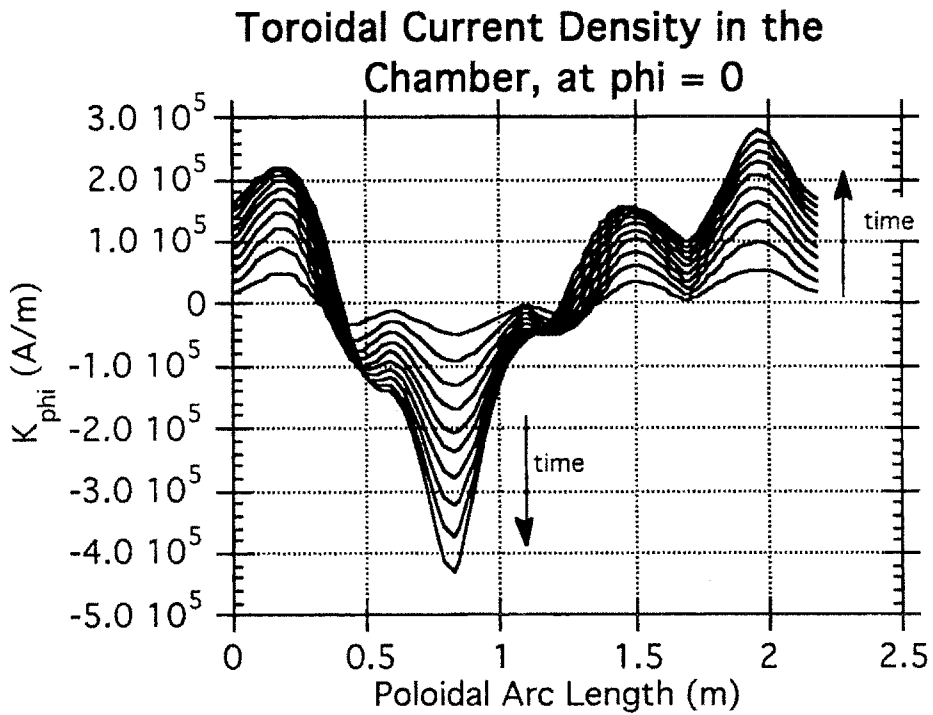
Toroidal Current Density in the Chamber, at phi = 0

156

Toroidal Current Density in the Chamber, at phi = π/2

Toroidal Current Density in the Chamber, at phi = π
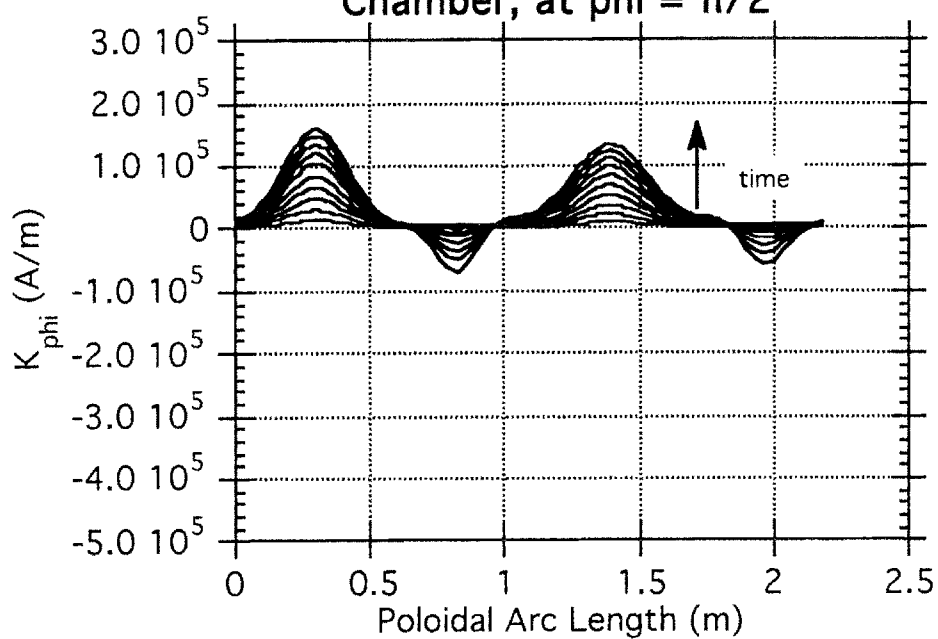
Toroidal Current Density in the Chamber, at phi = 3π/2
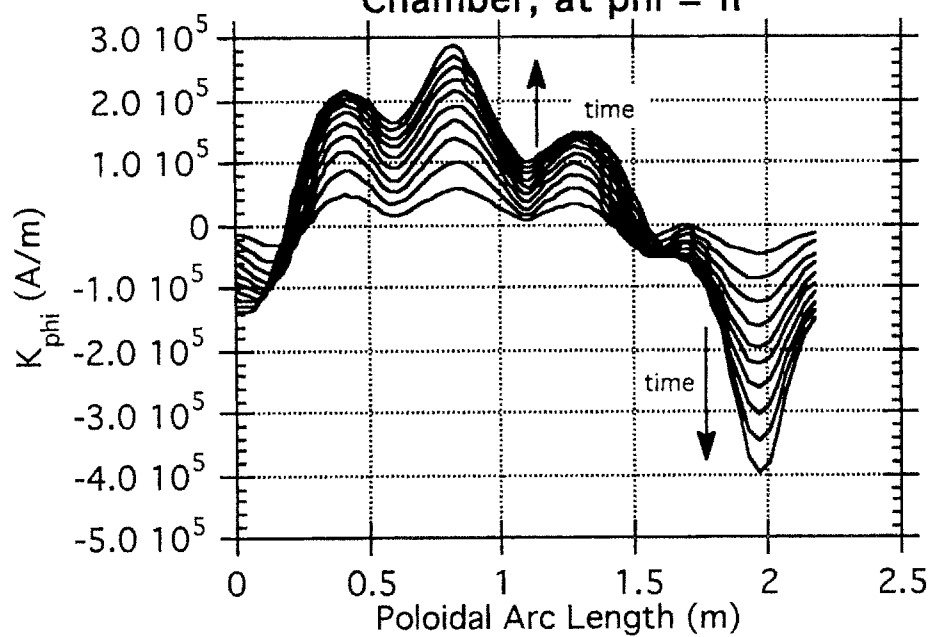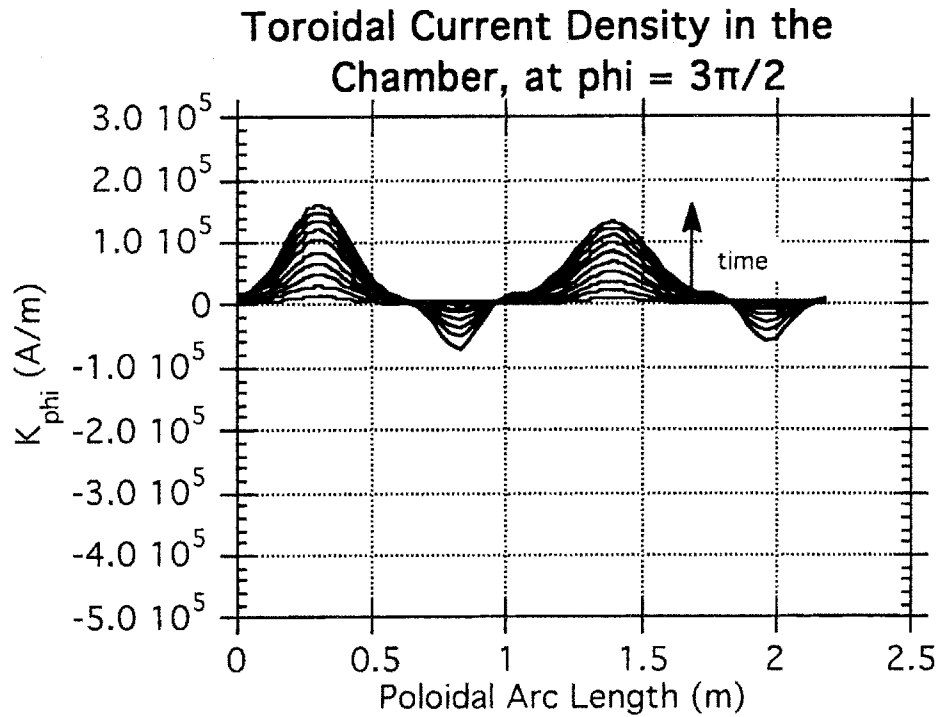
As required to maintain a divergence-free current, the poloidal current is ninety degrees out of phase with the toroidal current. The magnitude is substantial compared to the toroidal current.
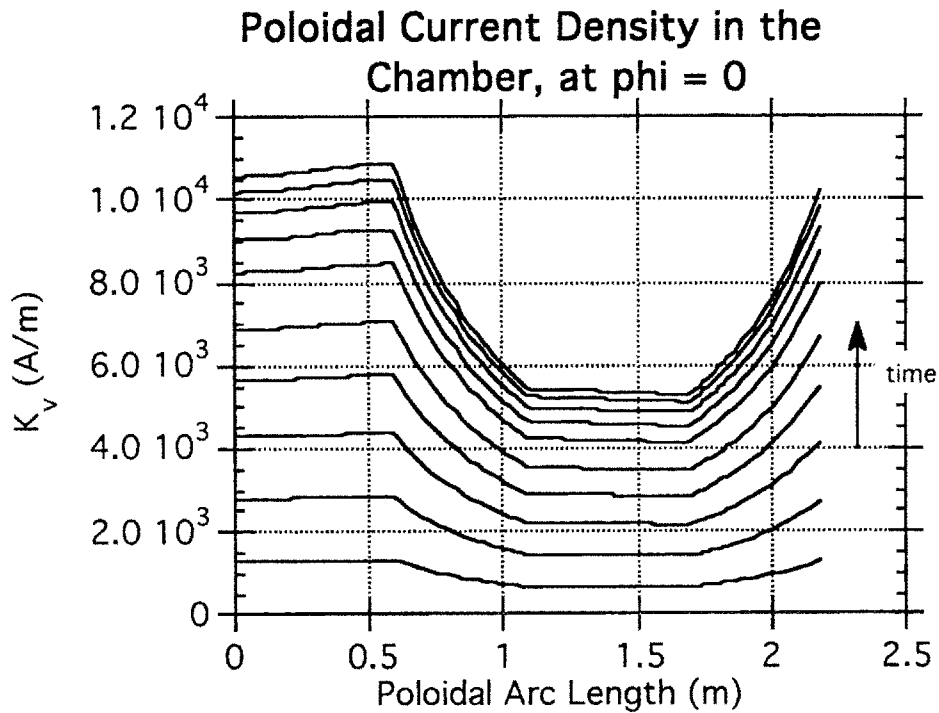
Poloidal Current Density in the Chamber, at phi = 0

Poloidal Current Density in the Chamber, at phi = π/2

Poloidal Current Density in the Chamber, at phi = π
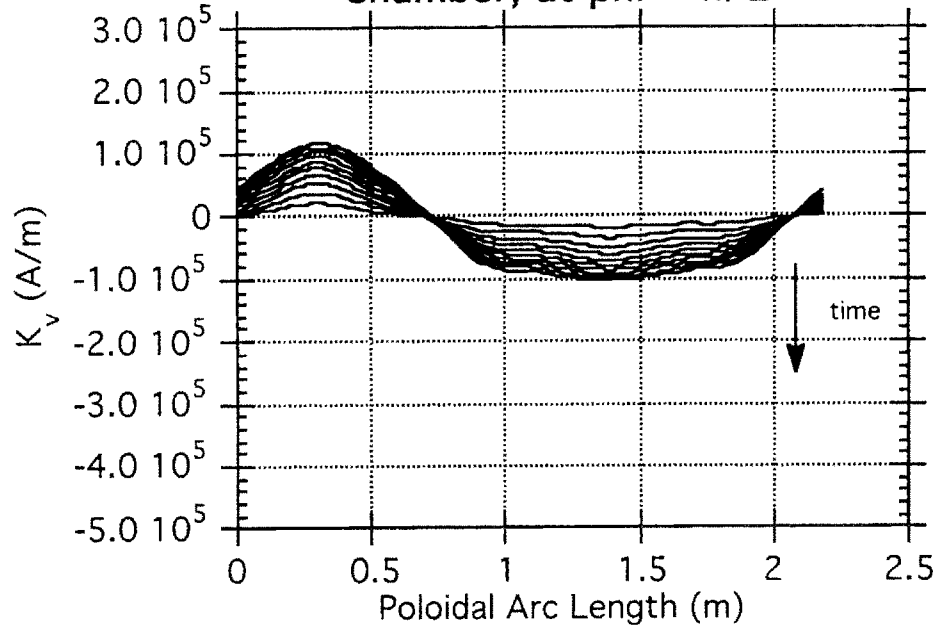
Poloidal Current Density in the Chamber, phi=3π/2
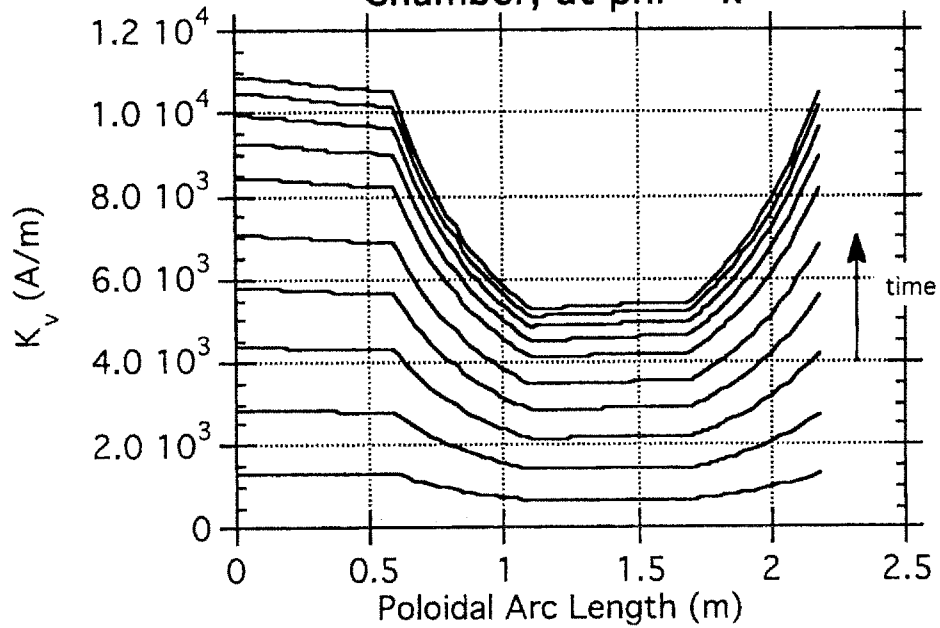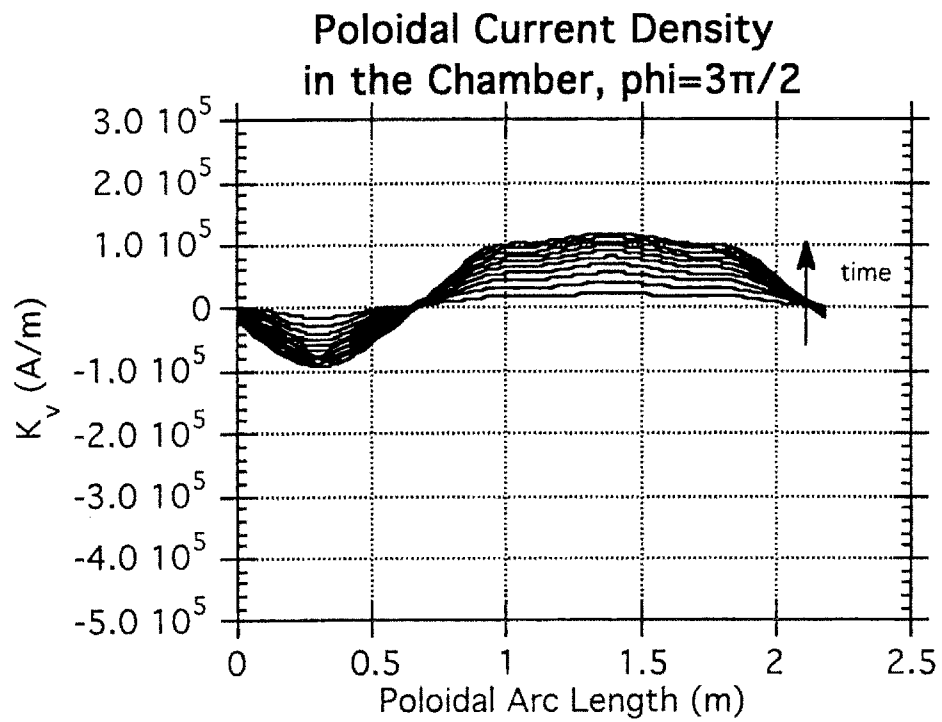
The loads reflect the interaction of the poloidal eddy currents with the toroidal field:

Normal Load on the Chamber, at phi = 0

Normal Load on the Chamber, at phi = π/2

Normal Load on the Chamber, at phi = π

Normal Load on the Chamber, at phi = 3π/2
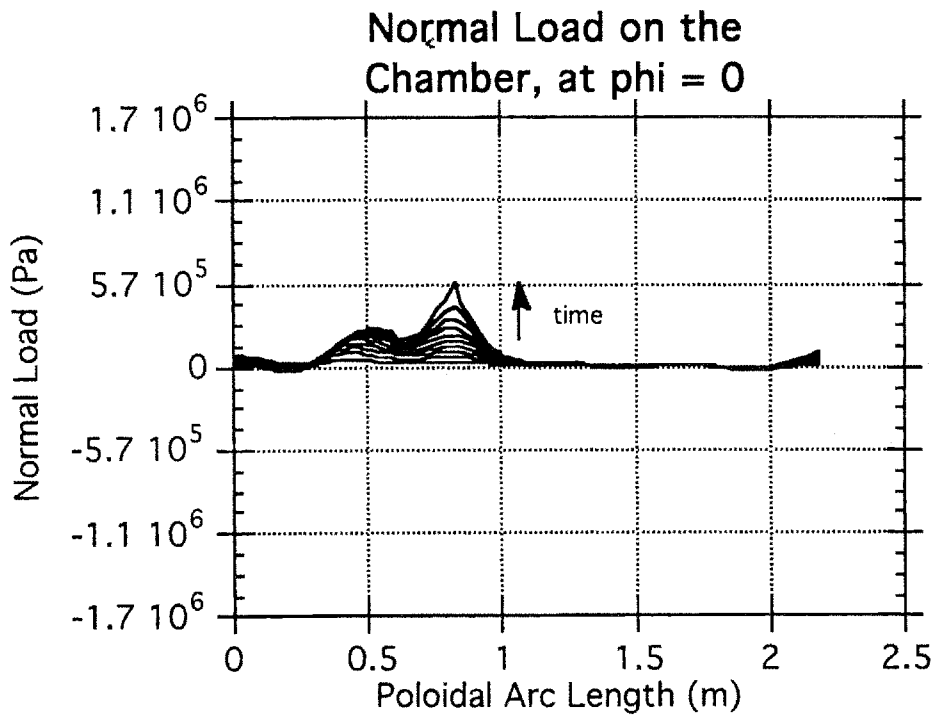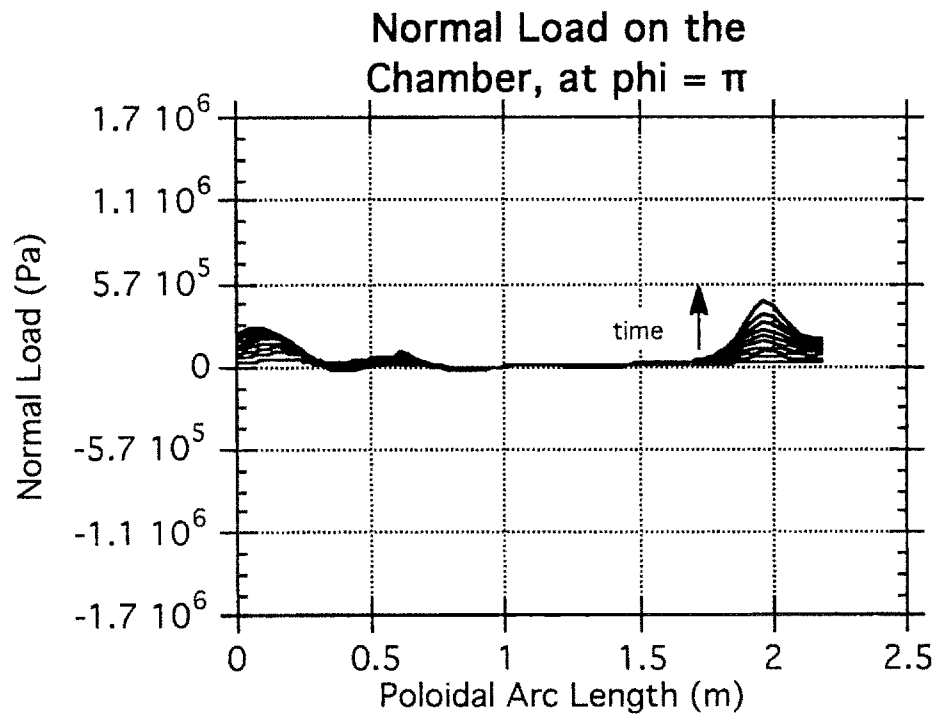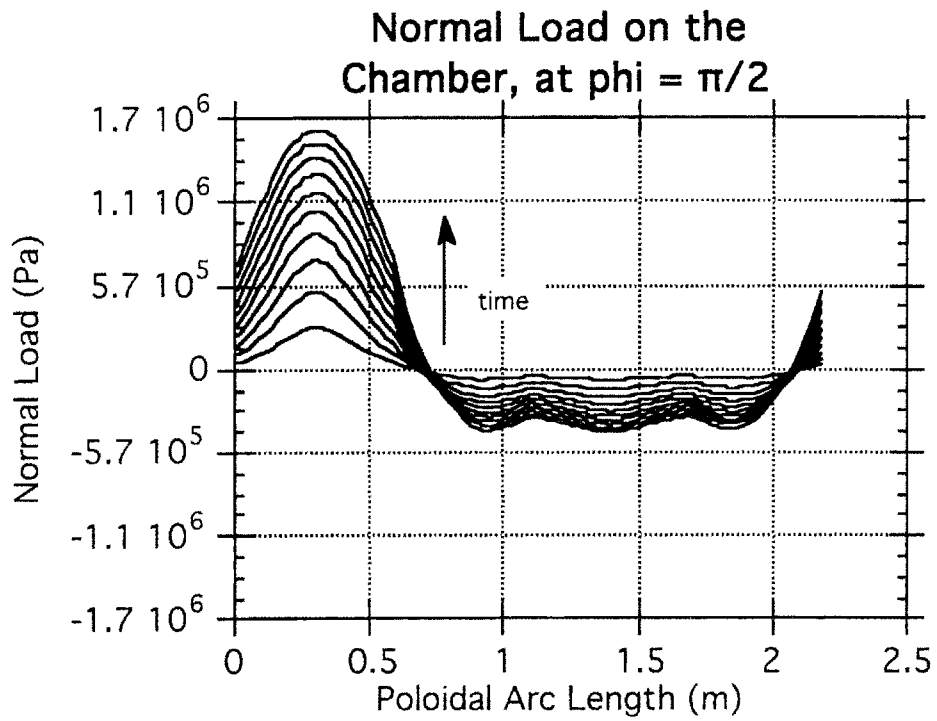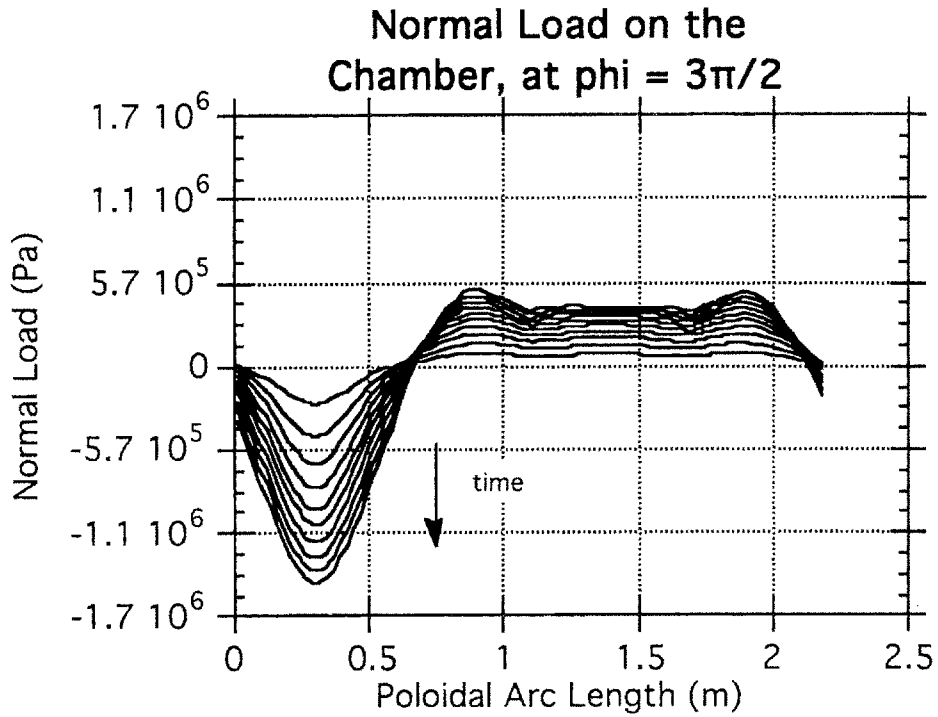
We can compare the contributions of the two currents to the load, looking at just two locations for simplicity; this confirms that the poloidal eddy currents are the most significant. Note that the load varies by an order of magnitude in toroidal angle.

Relative Contributions to Load on the Chamber, at phi = 0

Relative Contributions to Load on the Chamber, at phi = π/2

Legend:
- $K_v B_{phi}$ (dashed)
- $K_{phi} B_v$ (solid)

$t = 1.26$ ms

X-axis: Poloidal Arc Length (m)
Y-axis: Normal Load (Pa)
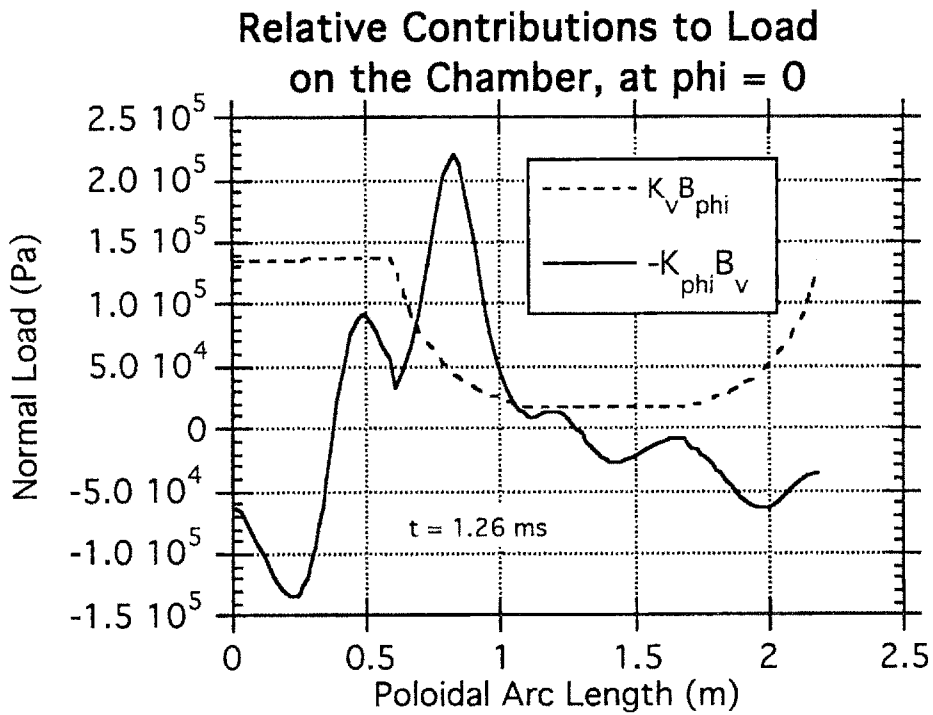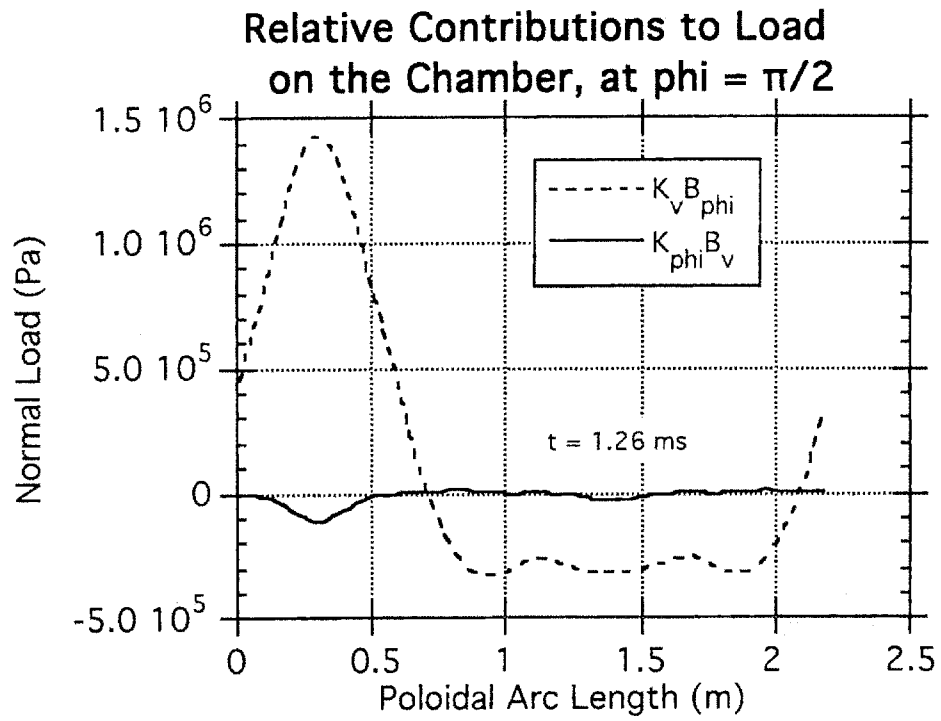
We now consider the case where the tilt is brought back under control so that we can allow the plasma to strike the wall:
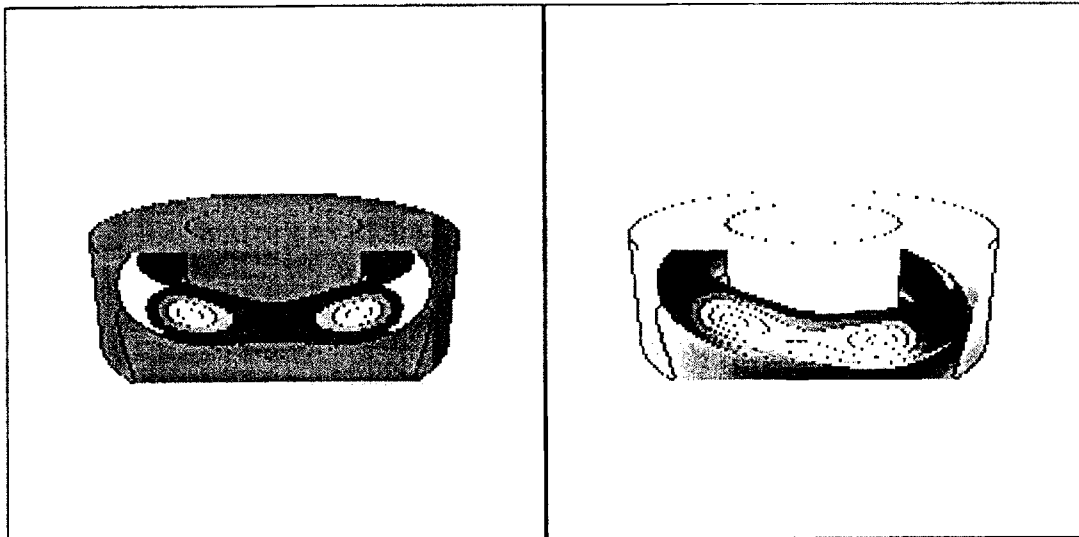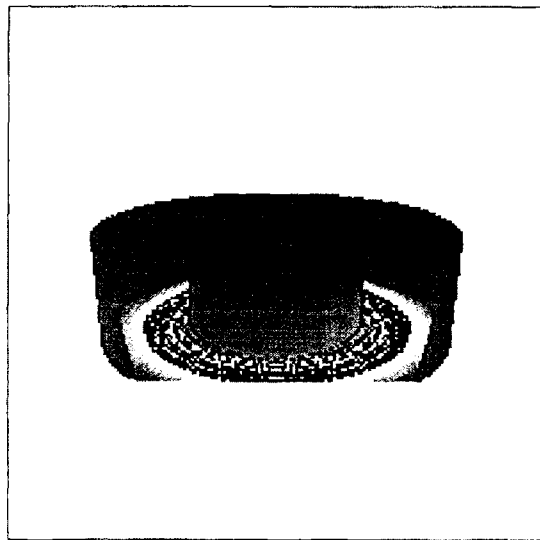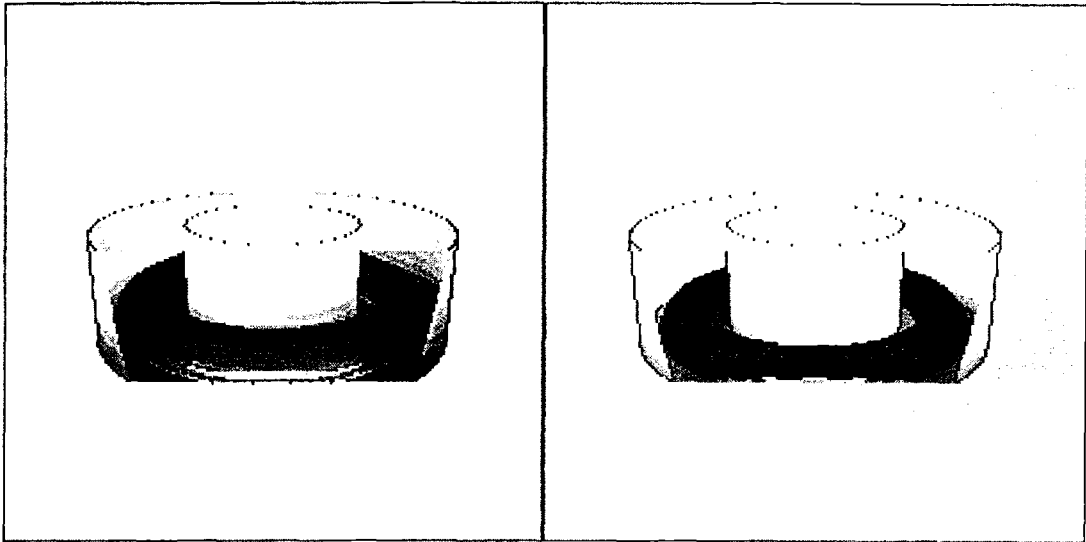
The plasma current shows only minor differences from the reference case (given in figure 5.2):

Zero-Order Toroidal Plasma Current
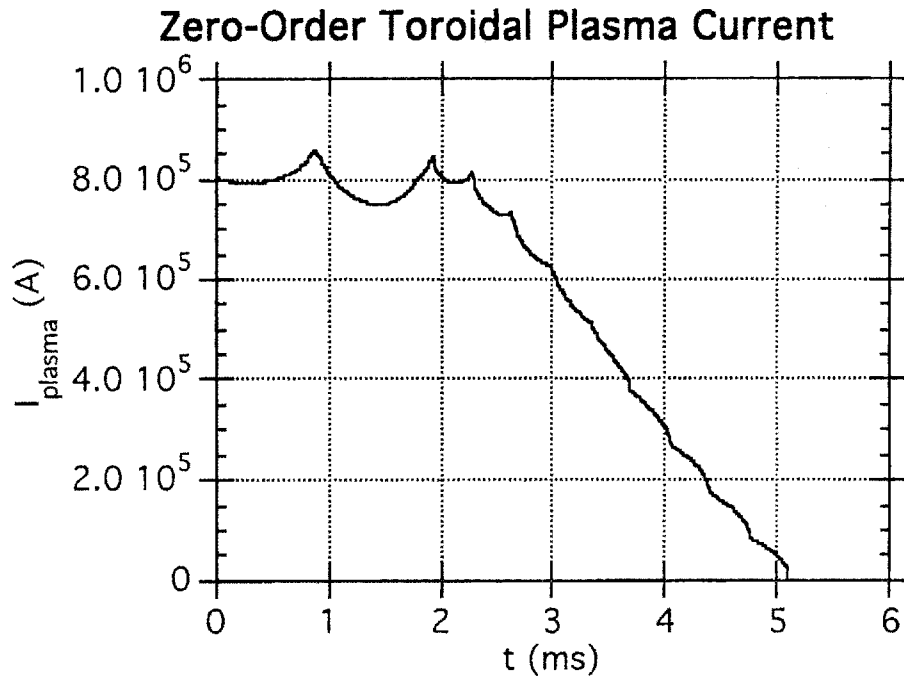
The zero-order poloidal halo current is also unremarkable in appearance; the differences from the reference case are easily attributed to the smaller plasma minor radius:

Zero-Order Poloidal Halo Current
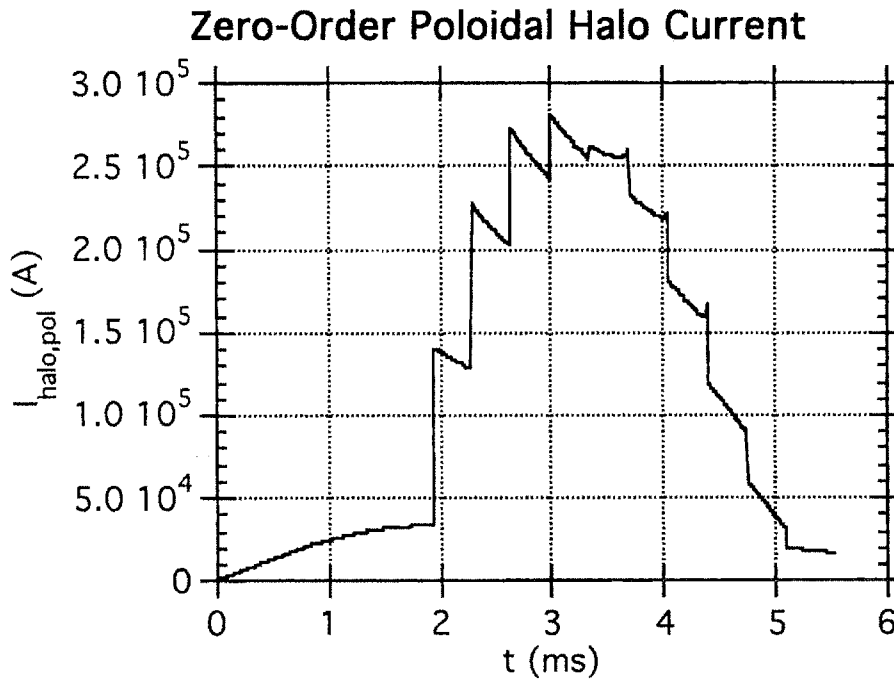
Since this case does not have plasma rotation, the tilting and straightening motion of the plasma is almost symmetrical. However, the non-axisymmetric nature is enough to again show a phenomenon seen earlier in the C-MOD run. Consider first this snapshot of the current and load distributions early in the disruption.

Since the plasma is still undergoing a tilt, the effects of the asymmetry are clear. However, the rise of zero-order toroidal eddy currents quickly dominate, making the disruption look very similar to the reference case during the time of the peak halo currents. Late in the disruption, though, when the plasma has nearly vanished, we see that non-axisymmetric poloidal currents have persisted long enough to contribute a significant amount to the load (again raising the question about choosing the lesser of two evils, a large axisymmetric force or a smaller non-axisymmetric one). However, this is the case mostly at the location of the chamber not in contact with the plasma. In the region still overlapped by a shell, the load is nearly symmetric. The symmetric region is not simply a case of the zero-order current becoming dominant, because it does so in only a localized region; the magnitudes of these symmetric and asymmetric loads is about the same.

Toroidal Current Density, t=0.53ms

Normal Load, t=0.53ms
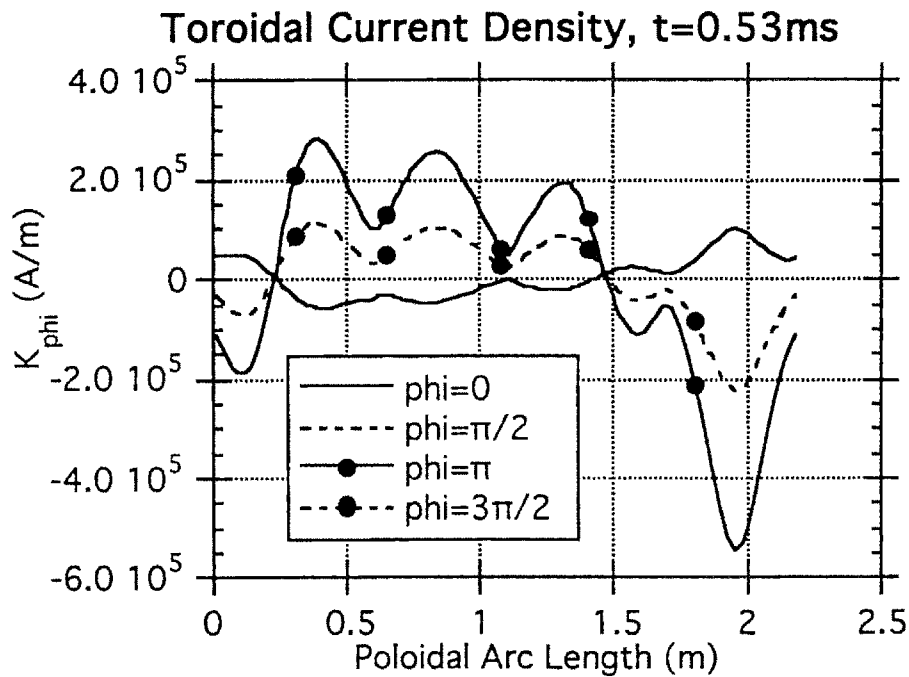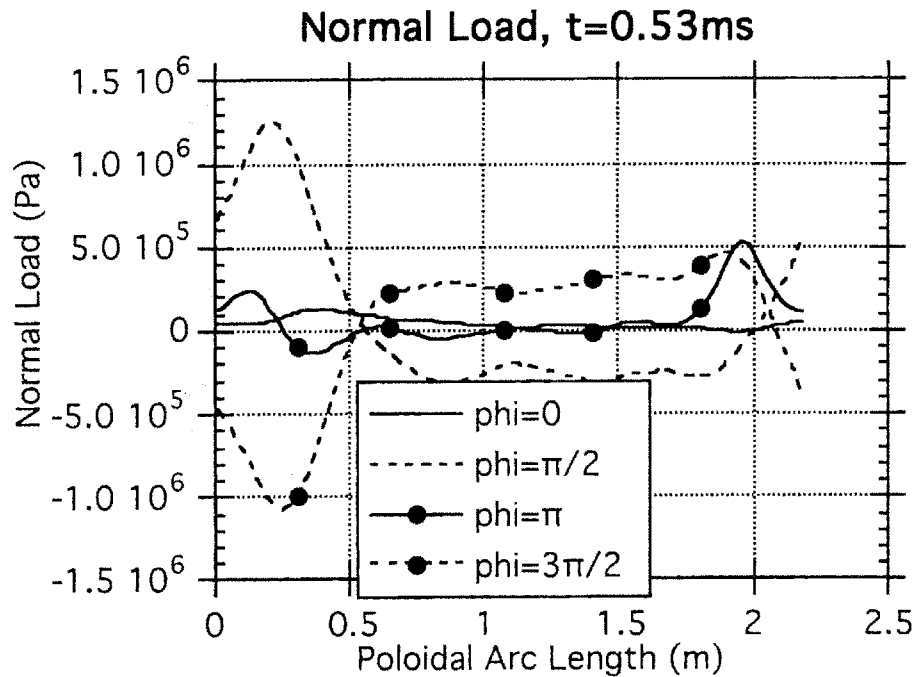
As part of the same phenomenon, note how the poloidal current becomes considerably more symmetric in the region where the plasma hits the wall. If it were the case that the poloidal plasma current remains largely symmetric, and then dominates the wall current as the plasma impacts the chamber, then one must provide a reason why the wall should experience non-axisymmetric poloidal currents before impact while the plasma does not. It seems more plausible to posit the existence of a mechanism which rapidly damps non-axisymmetric currents that are forced to close between moving boundaries; in any event, this is an appealing area for future investigation.

Toroidal Current Density, t=4.77ms

Poloidal Current Density, t=4.77ms

Normal Load, t=4.77ms
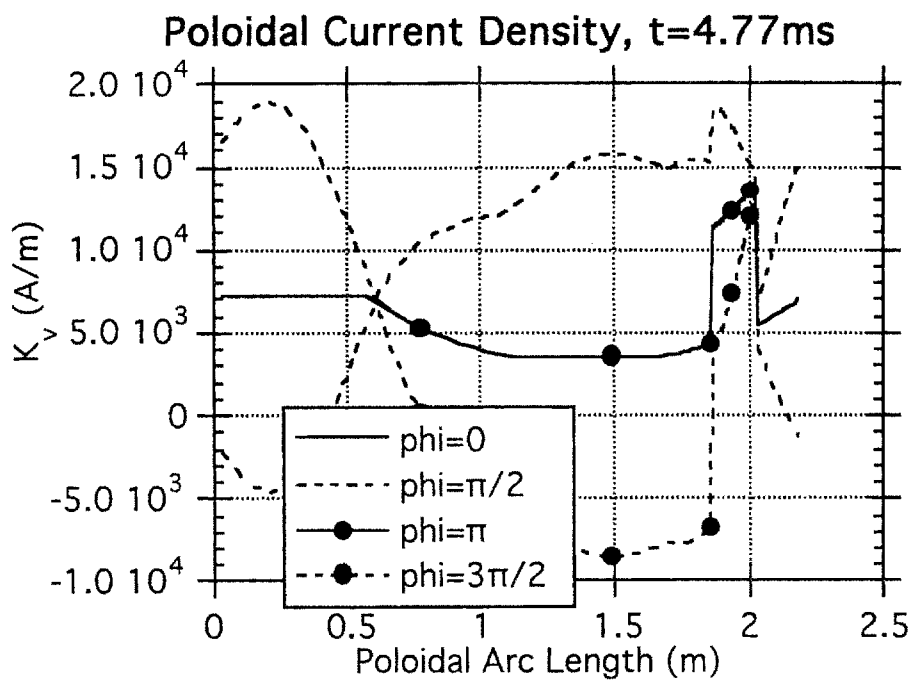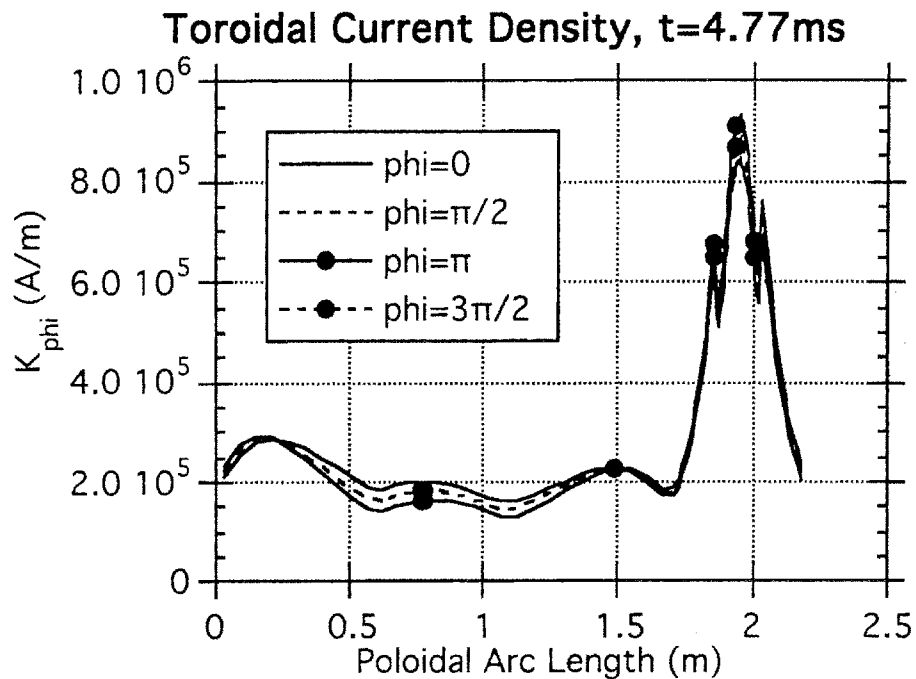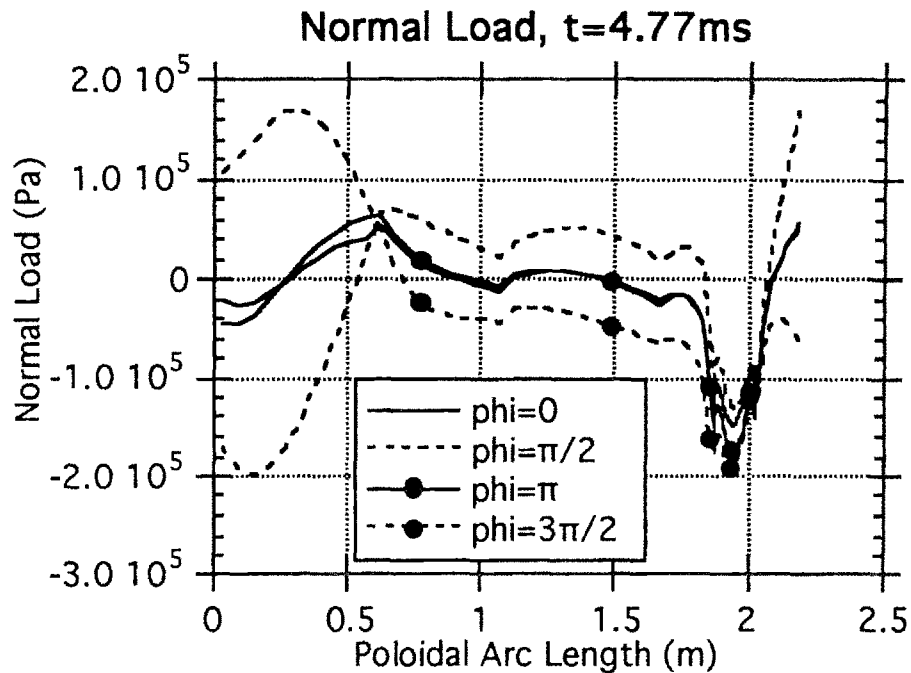
5.5. Computation Time

The last point to consider about TSPS-3D is whether or not it actually achieves a significant advantage in computation speed over other methods. It is hoped that the number of runs required to produce these results is a clear indication that the execution speed is not prohibitive, but of course firm numbers are more reassuring.

In the early stages of benchmarking the code, a simple test simulating an axisymmetric current dump in a filament located in a sharp-cornered chamber was performed with both TSPS-3D and the code ANSYS, which is a finite-element code that solves differential models for a broad range of electrical and mechanical problems [4]. Adjusting for the different platforms used, the TSPS run was *three hundred times* faster than the ANSYS run. The chief difference in this case was clearly the fact that the vacuum region, which encompassed most of the domain in this test run, does not appear explicitly in the integral equations of the sheet current model.

The following times were required for the various runs in this chapter. All runs were done on a DEC Alphastation 500 5/333 computer.

- The reference case took 30 minutes for 580 time steps, each representing 10μs of simulation time.

- The parametric runs took anywhere from 15 to 45 minutes depending on the plasma size and disruption velocity, taking between 470 and 760 time steps.

- The axisymmetric simulation of shot 950112013 in Alcator C-MOD took one hour for 650 time steps.

- The "runaway tilt" case of section 5.4 took one hour for 180 time steps.

- The "restrained tilt" case of section 5.4 took six hours for 530 time steps.

- The non-axisymmetric run for shot 950112013 took a full 48 hours for 650 time steps using an older version of TSPS-3D. The estimated time using the newer algorithm used for the simple "restrained tilt" is about 18 hours.

If a particular geometry requires N degrees of freedom for an axisymmetric case, studying n=1 modes with arbitrary phase requires 3N degrees of freedom. This means that matrix loading times increase by a factor of 9 and - the real limiting factor - matrix inversion times increase by a factor of 27. Iterative N^2 linear algebra routines such as conjugate gradient methods do not help computation time because they take O(N) iterations for these problems; however, they are still useful because they do not require storage space for an inverted or decomposed matrix. Finally, the factor of 27 for non-axisymmetric cases can be reduced if different algorithms are used after the plasma strikes the wall, since once it returns to the same coordinate frame as the chamber the different Fourier modes decouple; this is the enhancement seen from 48 down to 18 hours for the C-MOD simulation. Note that even though the scaling from symmetric to asymmetric cases is disappointing, TSPS-3D is nevertheless the only currently existing tool which can be easily used to study non-axisymmetric halo currents in complex

geometries, so that perhaps the correct time to compare the three dimensional runs to is "infinity"!

We have demonstrated a wide range of the capabilities of TSPS-3D and the sheet current model. In the next chapter we will collect the spread of information into a compact summary, and examine some directions for the future.

5.6. References

1. Granetz, Hutchinson, Sorci, Irby, LaBombard, Gwinn. "Disruptions and Halo Currents in Alcator C-MOD." *Nuclear Fusion*, vol. 36, no. 5, p545-56, 1996.

2. Pillsbury, R. "SOLDESIGN User's Manual." MIT Plasma Fusion Center Report PFC/RR-91-3. 1991.

3. Ian H. Hutchinson. *Principles of Plasma Diagnostics*. Cambridge University Press. Reprinted 1992.

4. Len Myatt, private communication.

Chapter 6.

Conclusions

Chapter 6. Conclusions

The development and initial testing of the sheet current model and the TSPS-3D code have been carried out to the furthest point one can reasonably go without starting to narrow the focus to a specific application. It is obvious that the wealth of information which is generated by just a single three-dimensional run can serve as a starting point for many different follow-on investigations. We therefore consider this to be an appropriate stopping point for this body of work, and in this last brief chapter will summarize the major results and some suggestions for future work.

6.1. Summary

The sheet current model developed in this thesis is a representation of a disrupting tokamak plasma by a set of nested current sheets, which are the most reasonable compromise between computationally difficult non-linear flux surface models, and filament models which do not allow the flow of continuous poloidal currents. Inclusion of poloidal currents is crucial since the experimentally measured large poloidal halo currents will interact with the toroidal magnetic field to produce strong loads on the tokamak vessel. Prior to the development of the sheet current model, there was no efficient tool for performing predictive studies of axisymmetric halo currents and almost no tools whatsoever for non-axisymmetric cases.

By restricting the focus of the model to the global quantities of interest, which are the currents and magnetic fields and the forces resulting from their interaction, the need to resolve complex, short time- and length- scale plasma physics is eliminated. In addition, the resulting integral formulation has been shown to be especially useful in handling realistic tokamak and plasma parameters, such as the complicated tokamak geometries exemplified by the Alcator C-MOD divertor structure. More significantly, the integral form eliminates the need for additional degrees of freedom to represent vacuum fields.

Simple scaling arguments have been considered for the case of axisymmetric halo currents, showing that the currents will have a reasonably persistent force-free character that makes their contribution to the structural loads small compared to that of toroidal eddy currents. This characteristic is particular to axisymmetric disruptions, where the

173

only source of poloidal current is that which evolves from the equilibrium poloidal plasma current.

A numerical code call TSPS-3D has been developed to solve the sheet current equations in arbitrary geometries. The code has been matched against experimental data from the Alcator C-MOD experiment and used to investigate scalings of axisymmetric disruptions with some of the basic plasma parameters. Investigations of the electrical interaction between the wall and plasma have also been performed for non-axisymmetric cases, and reveal a decidedly different character in these events than in the axisymmetric ones. The wall has a new source of poloidal current, as the toroidal current in the plasma couples to this direction as the plasma undergoes a non-axisymmetric displacement. Before the plasma strikes the wall, large eddy currents can be driven both toroidally and poloidally, and eddy currents have no force-free constraint to keep the load small. Curiously, though, these preliminary run show that the region of the wall which is in contact with the plasma does *not* experience large asymmetries in the halo current, so that the peak loads on the vessel are caused by eddy currents in regions not in contact with the plasma, or by large axisymmetric toroidal eddy currents which are generated in the impact regions.

6.2. Suggestions for Future Work

The modeling of halo currents has revealed many other possible lines of investigation, some directly related, some not.

1) Direct application of TSPS-3D to evaluate the structural sufficiency of existing tokamaks or of proposed designs, such as ITER. This work should be combined with finding a better means of taking the loads output by TSPS-3D and using them to perform dynamic analysis on realistically shaped tokamaks, since load information is not useful unless it can be turned into information on stresses.

2) Instrumentation of machines like Alcator C-MOD to provide experimental evidence for strong, poloidally localized toroidal eddy currents.

3) Experimental testing of mock-ups of the chamber wall (of course, the real chamber would do even better!) to confirm or possibly disprove the validity of treating the vacuum vessel as an unbroken, isotropic, single-layered structure. This is by far the weakest assumption in the sheet current model, given the incredibly complex connections between the tiles, brackets, backing plates, etc. It seems very likely that the wall should at least be treated as an anisotropic structure, since the conduction of current into the stainless steel wall through the tiles is very different from conduction along the plane of the wall. It is possible that toroidal current never penetrates to the steel.

4) Theoretical investigation of the apparent suppression of non-axisymmetric currents in the wall in regions touching the plasma. It is quite possible that this is either an artifact of the specific cases used in Chapter 5, or of the sheet current model itself since it imposes stringent boundary conditions on the moving wall/sheet interface.

5) Numerical investigation of incorporating the full free-boundary problem into the model even when the plasma hits the wall. If this is possible without a major excess of computation time, then the sheet current model would become a useful tool for dynamic PF system design as well as more self-consistent disruption studies.

Any of these possibilities would also represent another step towards repairing the existing rift between fusion theory and fusion experiment; the general field of "fusion engineering" requires the skills of the practitioners in both areas.

Appendix A

Algebraic Details

Appendix A. Algebraic Details

The sheet current model achieves its compact form because of the incredible cleverness of classical mathematicians, who fully mastered all nuances of the Laplacian operator. In addition, the lack of high-speed computing forced them to be resourceful enough to find closed-form expressions for things the modern analyst would immediately subject to numerical attack. This is not meant to bemoan the state of modern applied mathematics; certainly many contemporary problems have become sufficiently complex to defy the most clever analytic techniques, and certainly one should always take advantage of labor-saving tools when they become available. However, this philosophy should be used consistently: since there are so many closed-form expressions available from the toils of our predecessors, we should use them rather than wasting computational resources on repeating them.

The following sections provide the some explicit steps used to get results which were treated as "given" in the derivation of the sheet current model. They will not add any physical understanding to the problem, but should serve as a time-saving reference for anyone pursuing related work. Obviously none of the work is new, and all of it is repeated in a large number of math texts. The references listed at the end of this Appendix are simply my personal favorites for Green's functions, integral equations, and techniques for efficiently turning closed-form expressions into hard numbers.

The notation used here is consistent with that in the main thesis; specifically, for a parameterized curve $R(v)$ and $Z(v)$ in cylindrical coordinates, the tangential and normal vectors in the TNB frame are given by

$$\hat{e}_v = \frac{1}{Q}\left(\frac{dR}{dv}\hat{e}_R + \frac{dZ}{dv}\hat{e}_Z\right)$$

$$\hat{e}_\rho = \frac{1}{Q}\left(\frac{dR}{dv}\hat{e}_Z - \frac{dZ}{dv}\hat{e}_R\right)$$

$$Q \equiv \sqrt{\frac{dR^2}{dv} + \frac{dZ^2}{dv}}$$

We further define $\dot{R} \equiv \dfrac{dR}{dv}$, $\dot{Z} \equiv \dfrac{dZ}{dv}$.

Some steps in the derivations use equations taken directly from the references, so an appropriate notation is used to number these equations. For example, (G&R 9.137.2) refers to equation 9.137.2 in Gradshteyn and Ryzhik; the prefix A&S refers to Abramowitz and Stegun.

A.1. Green's Theorem

Consider two scalar functions $f(\vec{r})$, $g(\vec{r})$ and their gradients $\vec{\nabla} f$, $\vec{\nabla} g$. Over some volume of space V, bounded by a surface A with unit normal $\hat{n}$, some simple identities tell us that for the integrand given by $f\vec{\nabla} \cdot \vec{\nabla} g$, we may write

$$\int f \vec{\nabla} \cdot \vec{\nabla} g \, dV = \int \vec{\nabla} \cdot (f \vec{\nabla} g) \, dV - \int \vec{\nabla} f \cdot \vec{\nabla} g \, dV$$

The functions f and g are completely interchangeable at this point, so we may also write

$$\int g \vec{\nabla} \cdot \vec{\nabla} f \, dV = \int \vec{\nabla} \cdot (g \vec{\nabla} f) \, dV - \int \vec{\nabla} g \cdot \vec{\nabla} f \, dV$$

Subtracting these two relations leads to

$$\int \left(g \nabla^2 f - f \nabla^2 g \right) dV = \int \left(\vec{\nabla} \cdot (f \vec{\nabla} g) - \vec{\nabla} \cdot (g \vec{\nabla} f) \right) dV$$

which after applying the divergence theorem to the right hand side can be put in the form of *Green's second identity*,

$$(A.1) \quad \int \left(g \nabla^2 f - f \nabla^2 g \right) dV = \int \left(f \vec{\nabla} g - g \vec{\nabla} f \right) \cdot \hat{n} \, dA$$

Green's first identity is obtained by adding our two starting relations; we will not be using it here. Suppose now we consider two particular functions instead of the arbitrary f and g. Let F be the solution to Poisson's equation,

$$\text{(A.2)} \quad \nabla^2 F(\vec{r}) = S(\vec{r})$$

where $S(\vec{r})$ is a known source term. For the second function, we presume the existence of a special function $G(\vec{r}, \vec{r}')$ which satisfies the particular equation

$$\text{(A.3)} \quad \nabla^2 G(\vec{r}, \vec{r}') = \delta(\vec{r} - \vec{r}')$$

where $\delta(\vec{r})$ is the Dirac delta function, satisfying $\int f(\vec{r}')\delta(\vec{r} - \vec{r}') \, d\vec{r}' = f(\vec{r})$, and the Laplacian operator can be applied to G in either the primed or unprimed coordinates. Plugging (A.2) and (A.3) into (A.1) and integrating over the delta function yields the scalar form of *Green's theorem:*

$$\text{(A.4)} \quad F(\vec{r}) = \int G(\vec{r}, \vec{r}')S(\vec{r}') \, dV' + \int \left(G(\vec{r}, \vec{r}')\vec{\nabla}'F(\vec{r}') - F(\vec{r}')\vec{\nabla}'G(\vec{r}, \vec{r}') \right) \cdot \hat{n}' \, dA'$$

Something remarkable happens in the case when one wishes to solve (A.2) for F in free space, where the boundary surface is at infinity and F is presumed to go to zero. Green's theorem reduces to

$$\text{(A.5)} \quad F(\vec{r}) = \int G(\vec{r}, \vec{r}')S(\vec{r}') \, dV'$$

and equation (A.2) has been solved with no further work whatsoever! This result is independent of the coordinate system; it requires only that G and S be known functions. S presumably depends on the problem at hand; G is in fact a known function. It is possible to derive it by solving (A.3) with Fourier transforms, but we will simply give the result here:

$$\text{(A.6)} \quad G(\vec{r}, \vec{r}') = \frac{-1}{4\pi \left| \vec{r} - \vec{r}' \right|}$$

It is common, and usually physically appropriate, to refer to the point at $\vec{r}'$ as the source point and the point at $\vec{r}$ as the observation point.

179

Green's theorem represents a powerful method to write down closed-form solutions to Poisson equations, or else change them to an integral form which, as demonstrated by this thesis, lends itself to efficient numerical solution when confronted with difficult geometries, especially when compared with solving the equivalent differential equations (see the discussion in the last section of Chapter 2).

A.2 The Green's Dyadic for the Vector Potential

Suppose that instead of the scalar Laplacian operator in (A.2) we have the vector Laplacian; for example, we desire to solve the equation

$$(A.7) \quad \vec{\nabla}^2 \vec{F}(\vec{r}) = \vec{S}(\vec{r})$$

Is there a way to apply Green's theorem and write down the solution as easily as we did in the scalar case? The answer is yes, although the exact form will now be dependent on the coordinate system. However, by knowing the solution in the Cartesian system it is then possible to derive the correct result for any other. Let us consider the Cartesian case.

Since the unit vectors are constant and independent of the coordinates themselves in the Cartesian system, the components of the vector Laplacian have a simple form and the unit vectors themselves can be pulled outside of it:

$$(A.8) \quad (\nabla^2 F_x)\hat{e}_x + (\nabla^2 F_y)\hat{e}_y + (\nabla^2 F_z)\hat{e}_z = \vec{S}$$

Taking the dot product of (A.8) with each of the unit vectors in turn yields three uncoupled scalar equations

$$\nabla^2 F_x = \vec{S} \cdot \hat{e}_x = S_x$$
$$(A.9) \quad \nabla^2 F_y = \vec{S} \cdot \hat{e}_y = S_y$$
$$\nabla^2 F_z = \vec{S} \cdot \hat{e}_z = S_z$$

with the solutions to each equation given by the methods of the previous section:

$$F_x = \int G S'_x \, dV'$$

$$(A.10) \quad F_y = \int G\, S'_y\, dV'$$

$$F_z = \int G\, S'_z\, dV'$$

However, it is only possible to do this since the unit vectors implicit in equation (A.7) are constant and can be pulled outside the operator. This cannot be done for an arbitrary coordinate system. However, if we already know the solution for the Cartesian system, why not just take this solution and express it in the desired system? Suppose the desired system has unit vectors $\hat{e}_1, \hat{e}_2, \hat{e}_3$, and the source term is given in its components S_1, S_2, S_3. The solution is desired in the form F_1, F_2, F_3. The first step is to find the Cartesian components of the source, but expressed in terms of the new coordinate system:

$$F_x = \int G\, \left[(\hat{e}_x \cdot \hat{e}_1)S_1 + (\hat{e}_x \cdot \hat{e}_2)S_2 + (\hat{e}_x \cdot \hat{e}_3)S_3 \right]' dV'$$

$$(A.11) \quad F_y = \int G\, \left[(\hat{e}_y \cdot \hat{e}_1)S_1 + (\hat{e}_y \cdot \hat{e}_2)S_2 + (\hat{e}_y \cdot \hat{e}_3)S_3 \right]' dV'$$

$$F_z = \int G\, \left[(\hat{e}_z \cdot \hat{e}_1)S_1 + (\hat{e}_z \cdot \hat{e}_2)S_2 + (\hat{e}_z \cdot \hat{e}_3)S_3 \right]' dV'$$

Note all quantities in the square brackets are in the primed coordinate system. The next step is to take the appropriate linear combinations of (A.11) to find the components of $\vec{F}$ in the new coordinates; for example:

$$(A.12) \quad F_2 = \int G\, \Big[[(\hat{e}_2 \cdot \hat{e}_x)(\hat{e}_x \cdot \hat{e}_1)' + (\hat{e}_2 \cdot \hat{e}_y)(\hat{e}_y \cdot \hat{e}_1)' + (\hat{e}_2 \cdot \hat{e}_y)(\hat{e}_z \cdot \hat{e}_1)']S_1' +$$
$$[(\hat{e}_2 \cdot \hat{e}_x)(\hat{e}_x \cdot \hat{e}_2)' + (\hat{e}_2 \cdot \hat{e}_y)(\hat{e}_y \cdot \hat{e}_2)' + (\hat{e}_2 \cdot \hat{e}_y)(\hat{e}_z \cdot \hat{e}_2)']S_2' +$$
$$[(\hat{e}_2 \cdot \hat{e}_x)(\hat{e}_x \cdot \hat{e}_3)' + (\hat{e}_2 \cdot \hat{e}_y)(\hat{e}_y \cdot \hat{e}_3)' + (\hat{e}_2 \cdot \hat{e}_y)(\hat{e}_z \cdot \hat{e}_3)']S_3' \Big] dV'$$

Careful attention should be paid to whether a certain quantity is in the primed or unprimed coordinate system. The various dot products in (A.12) and the equivalent expressions for F_x and F_z can be re-written very efficiently as a unitary dyadic operator $\overline{\overline{M}}$. Letting the subscript k range over each Cartesian component x, y, and z, and letting the subscripts i and j range over the components 1, 2, and 3 of the new coordinate system:

$$(A.13) \quad M_{ij} = \sum_k (\hat{e}_i \cdot \hat{e}_k)(\hat{e}_k \cdot \hat{e}_j)'$$

181

The components of $\overline{\overline{M}}$ must be known to carry out the above process; they can be found if the functional relationships between the two coordinate systems are known, as is presumably the case. Examples of this procedure can be found in any text on vector calculus.

If we define $\overline{\overline{G}} = G\overline{\overline{M}}$ then the solution to (A.7) can be written in the compact form

$$\overrightarrow{F}(\overrightarrow{r}) = \int \overline{\overline{G}}(\overrightarrow{r},\overrightarrow{r}')\cdot\overrightarrow{S}(\overrightarrow{r}')\, dV'$$

where the operation under the integral sign is dotting a second-rank tensor with a vector, which yields another vector. The object $\overline{\overline{G}}$ is the *Green's dyadic* for the vector Laplace operator.

To avoid dragging around too many constants, let us redefine the Green's function G to be

$$G(\overrightarrow{r},\overrightarrow{r}') = \frac{\mu_o}{4\pi\left|\overrightarrow{r} - \overrightarrow{r}'\right|}$$

so that it immediately follows that equation (2.32) in the text, $\nabla^2\overrightarrow{A} = -\mu_o\overrightarrow{J}$, has the solution (2.33), $\overrightarrow{A} = \int \overline{\overline{G}}\cdot\overrightarrow{J}'\, dV'$. We will now examine the components of $\overline{\overline{G}}$ in some specific coordinate systems.

In cylindrical coordinates (R, ϕ, Z) with the ϕ=0 plane aligned with the y=0 Cartesian plane, the unit vectors are related back to the Cartesian ones through the relations

$$\hat{e}_R = \cos\phi\,\hat{e}_x + \sin\phi\,\hat{e}_y$$
$$\hat{e}_\phi = -\sin\phi\,\hat{e}_x + \cos\phi\,\hat{e}_y$$

The $\hat{e}_Z$ vector maps to itself. If $\overrightarrow{J}$ is also given in cylindrical components, then after applying (A.13) and the trigonometric identities

$$\cos(a \pm b) = \cos(a)\cos(b) \mp \sin(a)\sin(b)$$
$$\sin(a \pm b) = \sin(a)\cos(b) \pm \cos(a)\sin(b)$$

we get the result

$$\overline{\overline{G}} = G \begin{pmatrix} \cos(\phi\text{-}\phi') & \sin(\phi\text{-}\phi') & 0 \\ -\sin(\phi\text{-}\phi') & \cos(\phi\text{-}\phi') & 0 \\ 0 & 0 & 1 \end{pmatrix}$$

$$G = \frac{\mu_o}{4\pi\sqrt{R^2 + R'^2 - 2RR'\cos(\phi\text{-}\phi') + (Z\text{-}Z')^2}}$$

To deal with the different locally axisymmetric coordinate frames, we saw in Chapter 4 that it is useful to evaluate the cylindrical components of $\overline{A}$ when given the components of $\overline{J}$ in the local TNB frame of a sheet. Note that in this case, the rows of $\overline{\overline{G}}$ yield the ($\hat{e}_R$, $\hat{e}_\phi$, $\hat{e}_Z$) components after the columns are dotted with the ($\hat{e}_\rho'$, $\hat{e}_v'$, $\hat{e}_\phi'$) components of $\overline{J}$:

$$(A.14)\ \overline{\overline{G}} = G \begin{pmatrix} -\dfrac{\dot{Z}'}{Q'}\cos(\phi\text{-}\phi') & \dfrac{\dot{R}'}{Q'}\cos(\phi\text{-}\phi') & \sin(\phi\text{-}\phi') \\[2mm] \dfrac{\dot{Z}'}{Q'}\sin(\phi\text{-}\phi') & -\dfrac{\dot{R}'}{Q'}\sin(\phi\text{-}\phi') & \cos(\phi\text{-}\phi') \\[2mm] \dfrac{\dot{R}'}{Q'} & \dfrac{\dot{Z}'}{Q'} & 0 \end{pmatrix}$$

Finally, if $\overline{A}$ is desired in the TNB frame, so that the rows yield the ($\hat{e}_\rho$, $\hat{e}_v$, $\hat{e}_\phi$) components, we have

$$(A.15)\ \overline{\overline{G}} = G \begin{pmatrix} \dfrac{\dot{R}\dot{R}'}{QQ'} + \dfrac{\dot{Z}\dot{Z}'}{QQ'}\cos(\phi\text{-}\phi') & \dfrac{\dot{R}\dot{Z}'}{QQ'} - \dfrac{\dot{Z}\dot{R}'}{QQ'}\cos(\phi\text{-}\phi') & -\dfrac{\dot{Z}}{Q}\sin(\phi\text{-}\phi') \\[2mm] \dfrac{\dot{Z}\dot{R}'}{QQ'} - \dfrac{\dot{R}\dot{Z}'}{QQ'}\cos(\phi\text{-}\phi') & \dfrac{\dot{R}\dot{R}'}{QQ'} + \dfrac{\dot{Z}\dot{Z}'}{QQ'}\cos(\phi\text{-}\phi') & \dfrac{\dot{R}}{Q}\sin(\phi\text{-}\phi') \\[2mm] \dfrac{\dot{Z}'}{Q'}\sin(\phi\text{-}\phi') & -\dfrac{\dot{R}'}{Q'}\sin(\phi\text{-}\phi') & \cos(\phi\text{-}\phi') \end{pmatrix}$$

To work in terms of sheet currents $\overline{K}$ requires no modifications; K_ρ, of course, is zero.

183

A.3 Analytic Integration of the ϕ dependence

As stated in Chapter 4, the Fourier expansion of $\mathbf{K}$ and the restriction to locally axisymmetric displacements means the f' integration over the Green's dyadic can be evaluated analytically, yielding (4.18-20). To reach this result, we need to calculate the following five integrals:

$$(A.16) \quad \int_0^{2\pi} \frac{\sin(n\phi')\cos(\phi-\phi')}{\sqrt{R^2 + R'^2 - 2RR'\cos(\phi-\phi') + (Z-Z')^2}} \, d\phi'$$

$$(A.17) \quad \int_0^{2\pi} \frac{\cos(n\phi')\cos(\phi-\phi')}{\sqrt{R^2 + R'^2 - 2RR'\cos(\phi-\phi') + (Z-Z')^2}} \, d\phi'$$

$$(A.18) \quad \int_0^{2\pi} \frac{\sin(n\phi')\sin(\phi-\phi')}{\sqrt{R^2 + R'^2 - 2RR'\cos(\phi-\phi') + (Z-Z')^2}} \, d\phi'$$

$$(A.19) \quad \int_0^{2\pi} \frac{\cos(n\phi')\sin(\phi-\phi')}{\sqrt{R^2 + R'^2 - 2RR'\cos(\phi-\phi') + (Z-Z')^2}} \, d\phi'$$

$$(A.20) \quad \int_0^{2\pi} \frac{\cos(n\phi') \text{ or } \sin(n\phi')}{\sqrt{R^2 + R'^2 - 2RR'\cos(\phi-\phi') + (Z-Z')^2}} \, d\phi'$$

In these integrals, R and Z appear only as parameters; since we required the sheets to always remain toroidally axisymmetric about some axis, R' and Z' also have no ϕ' dependence. We define the following:

$$\beta = (R + R')^2 + (Z - Z')^2$$
$$k = \frac{4RR'}{\beta}$$
$$\alpha = \frac{\phi' - \phi}{2}$$

Using these definitions and the trigonometric identities given earlier, along with the additional identity $\cos(x) = 2\cos^2(x/2) - 1$, we can write (A.16) in the form

184

$$\frac{2}{\sqrt{\beta}}\int_0^\pi \frac{(\sin(n\phi)\cos(2n\alpha) + \cos(n\phi)\sin(2n\alpha))(2\cos^2\alpha - 1)}{\sqrt{1 - k\cos^2\alpha}} \, d\alpha$$

Careful examination of the symmetries in the second term shows it to integrate identically to zero. The next step is to use the identity

$$\cos(2n\alpha) = \sum_{j=0}^n C_{n,j}\cos^{2j}\alpha$$

where the $C_{n,j}$ can be found from (G&R 1.331.3). This puts (A.16) in the form

$$(A.21) \quad \frac{4\sin(n\phi)}{\sqrt{\beta}}\int_0^{\frac{\pi}{2}} \frac{\sum_{j=0}^n C_{n,j}(2\cos^{2(j+1)}\alpha - \cos^{2j}\alpha)}{\sqrt{1 - k\cos^2\alpha}} \, d\alpha$$

where the change in the range of integration comes from using the even symmetry of cosine about $\pi/2$ between 0 and π. This brings us to an integral which can be found in tables:

$$(G\&R \ 3.682) \quad \int_0^{\frac{\pi}{2}} \frac{\cos 2j\alpha}{(1 - k\cos^2\alpha)^p} \, d\alpha = \frac{\pi}{2^{j+1}}\frac{(2j-1)!!}{j!} F(j+\tfrac{1}{2}, p; j+1; k)$$

where $F(a, b, c; z)$ is the hypergeometric function (see, for example, G&R chapter 9 or A&S chapter 15) and the notation $(2j-1)!! = 1\cdot 3\cdot 5\cdot \ldots \cdot(2j-1)$. This last notation is defined to be 1 if j is zero.

Since we are interested principally in the case $p=1/2$, we define for convenience

$$\hat{F}^+(j,k) \equiv \frac{\pi}{2^{j+1}}\frac{(2j-1)!!}{j!} F(j+\tfrac{1}{2}, \tfrac{1}{2}; j+1; k)$$

The reason for the "+" superscript will become apparent later. After applying (G&R 3.682) to (A.21) we can finally write (A.16) as

$$(A.22) \quad \frac{4 \sin(n\phi)}{\sqrt{\beta}} \sum_{j=0}^{n} C_{n,j}(2\hat{F}^+(j+1,k) - \hat{F}^+(j,k))$$

A very similar series of steps can be used on the remaining integrals, yielding

$$(A.23) \quad \frac{4 \cos(n\phi)}{\sqrt{\beta}} \sum_{j=0}^{n} C_{n,j}(2\hat{F}^+(j+1,k) - \hat{F}^+(j,k)) = (A.17)$$

$$(A.24) \quad \frac{4 \cos(n\phi)}{\sqrt{\beta}} \left[\sum_{j=0}^{n-1} C_{n-1,j}\hat{F}^+(j,k) - \sum_{j=0}^{n} C_{n,j}(2\hat{F}^+(j+1,k) - \hat{F}^+(j,k)) \right] = (A.18)$$

$$(A.25) \quad \frac{-4 \sin(n\phi)}{\sqrt{\beta}} \left[\sum_{j=0}^{n-1} C_{n-1,j}\hat{F}^+(j,k) - \sum_{j=0}^{n} C_{n,j}(2\hat{F}^+(j+1,k) - \hat{F}^+(j,k)) \right] = (A.19)$$

$$(A.26) \quad \frac{4 \cos(n\phi) \text{ or } \sin(n\phi)}{\sqrt{\beta}} \sum_{j=0}^{n} C_{n,j}\hat{F}^+(j,k) = (A.20)$$

Using these results we may now write the Fourier-anaylzed form of (A.14), yielding the components to be used in (4.18-20) but *without* the scale factors R'Q' from the volume element dV' and *without* adjusting for the use of $\hat{K}$ instead of K_v.

$$G_{Rv,n}^{\,c\,s} = \frac{\cos(n\phi)}{\sin(n\phi)} \frac{\dot{R}'}{Q'} \frac{\mu_o}{\pi\sqrt{\beta}} T_1^+ \qquad\qquad G_{\phi v,n}^{\,c\,s} = \frac{\sin(n\phi)}{-\cos(n\phi)} \frac{\dot{R}'}{Q'} \frac{\mu_o}{\pi\sqrt{\beta}} T_2^+$$

$$G_{R\phi,n}^{\,c\,s} = \frac{-\sin(n\phi)}{\cos(n\phi)} \frac{\mu_o}{\pi\sqrt{\beta}} T_2^+ \qquad\qquad G_{Zv,n}^{\,c\,s} = \frac{\cos(n\phi)}{\sin(n\phi)} \frac{\dot{Z}'}{Q'} \frac{\mu_o}{\pi\sqrt{\beta}} T_3^+$$

$$G_{\phi\phi,n}^{\,c\,s} = \frac{\cos(n\phi)}{\sin(n\phi)} \frac{\mu_o}{\pi\sqrt{\beta}} T_1^+ \qquad\qquad G_{Z\phi,n}^{\,c\,s} = 0, \text{ all orders}$$

where

$$T_1^+ = \sum_{j=0}^{n} C_{n,j}(2\hat{F}^+(j+1,k) - \hat{F}^+(j,k))$$

$$T_2^+ = \sum_{j=0}^{n-1} C_{n-1,j}\hat{F}^+(j,k) - \sum_{j=0}^{n} C_{n,j}(2\hat{F}^+(j+1,k) - \hat{F}^+(j,k))$$

$$T_3^+ = \sum_{j=0}^{n} C_{n,j}\hat{F}^+(j,k)$$

The introduction of the T terms will save much effort when evaluating $\bar{B}$ in the next section. Note that for n=0, the summation up to n-1 in T is zero.

These expressions are not useful without a convenient means of evaluating $\hat{F}^+(j,k)$. It turns out that this function can be calculated through a recursion relation in j, starting with elliptic functions. Suppose we define two "ladder functions" by

$$F^+(j,k) = F(j+\tfrac{1}{2}, \tfrac{1}{2}; j+1; k); \quad F^-(j,k) = F(j-\tfrac{1}{2}, \tfrac{1}{2}; j+1; k)$$

We repeat here some recursion relations between various arguments of the hypergeometric function:

(G&R 9.137.2) $(2a-c-ak+bk)F(a,b;c;k) + (c-a)F(a-1,b;c;k) + a(k-1)F(a+1,b;c;k) = 0$
(G&R 9.137.13) $c(a-(c-b)k)F(a,b;c;k) - ac(1-k)F(a+1,b;c;k) + (c-a)(c-b)F(a,b;c+1;k) = 0$
(G&R 9.137.18) $cF(a,b;c;k) - (c-a)F(a,b;c+1,k) - aF(a+1,b;c+1,k) = 0$

From (G&R 9.137.2) we find an intermediate step:

$$F(j+\tfrac{3}{2}, \tfrac{1}{2}; j+1; k) = \frac{1}{j+\tfrac{1}{2}}\left[j\, F^+(j,k) + \frac{1}{2(1-k)}\, F^-(j,k)\right]$$

which can be substituted into (G&R 9.137.13) to yield the first needed relation:

$$F^-(j+1,k) = \frac{j+1}{(j+\tfrac{1}{2})k}\left[F^-(j,k) - (1-k)F^+(j,k)\right]$$

Using this and (G&R 9.137.18) yields the second:

$$F^+(j+1,k) = \frac{j+1}{j+\frac{1}{2}} F^+(j,k) - \frac{1}{2j+1} F^-(j+1,k)$$

To start the recursion, we can see by examining the original integral (G&R 3.682) that

$$F^+(0,k) = \frac{2}{\pi} K(k), \qquad F^-(0,k) = \frac{2}{\pi} E(k)$$

where K(k) and E(k) are the complete elliptic integrals of the first and second kinds, respectively. These are functions of a single argument and can be evaluated quickly on a computer through high-accuracy parametric curve fits given in [3]. Note that $F^+(j,k)$ and $F^-(j,k)$ are always linear combinations of K(k) and E(k); it is possible to use the recursion relations to track the coefficients of the elliptic functions separately. This is desirable for cases where special techniques are to be used to handle the logarithmic singularity in K(k) as k approaches unity. Care should be taken when using different references on elliptic functions; for example, [4] defines the argument k to be the square root of the one used in [3].

The original function $\hat{F}^+(j,k)$ is given by $\frac{\pi}{2^{j+1}} \frac{(2j-1)!!}{j!} F^+(j,k)$; the function $\hat{F}^-(j,k)$ will be encountered in the next section and is given by the corresponding expression $\frac{\pi}{2^{j+1}} \frac{(2j-1)!!}{j!} F^-(j,k)$.

Some particular values of the various quantities calculated in this section are

$$C_{0,0} = 1$$
$$C_{1,0} = -1 \qquad C_{1,1} = 2$$
$$C_{2,0} = 1 \qquad C_{2,1} = -8 \qquad C_{2,2} = 8$$

$$\hat{F}^+(0,k) = K(k)$$
$$\hat{F}^+(1,k) = \frac{1}{k}\left[K(k) - E(k)\right]$$
$$\hat{F}^+(2,k) = \frac{1}{k}\left[K(k) - E(k)\right] - \frac{2}{3k^2}\left[(1-\frac{k}{2})E(k) - (1-k)K(k)\right]$$

As an example of one of the kernels,

$$G_{\phi\phi,0} = \frac{2\mu_o}{k\pi\sqrt{\beta}}\left[\left(1-\frac{k}{2}\right)K(k) - E(k)\right]$$

which gives the result used in equation (3.19).

A.4 The Green's Dyadic for the Magnetic Fields

Once the expressions for $\overline{A}$ are known, there is no need to evaluate a complete new set of integrals to calculate $\overline{B}$; nor is there a need to calculate any numerical derivatives. Recall that $\overline{B} = \overline{\nabla}\times\overline{A} = \overline{\nabla}\times\int \overline{\overline{G}}\cdot\overline{J}'\ dV'$. Since the curl is taken in the unprimed coordinates in this last expression, only derivatives of $\overline{\overline{G}}$ are required, and a new dyadic which we will call $\overline{\overline{\mathcal{G}}}$ can be calculated analytically, so that $\overline{B} = \int \overline{\overline{\mathcal{G}}}\cdot\overline{J}'\ dV'$. The corresponding cylindrical components of $\overline{\overline{\mathcal{G}}}$ are given by

$$\mathcal{G}_{\phi\phi} = -\frac{\partial G_{R\phi}}{\partial Z} \qquad\qquad \mathcal{G}_{Rv} = \frac{1}{R}\frac{\partial G_{Zv}}{\partial\phi} - \frac{\partial G_{\phi v}}{\partial Z}$$

$$\mathcal{G}_{\phi v} = \frac{\partial G_{Rv}}{\partial Z} - \frac{\partial G_{Zv}}{\partial R} \qquad\qquad \mathcal{G}_{Z\phi} = \frac{1}{R}\frac{\partial}{\partial R}(RG_{\phi\phi}) - \frac{1}{R}\frac{\partial G_{R\phi}}{\partial\phi}$$

$$\mathcal{G}_{R\phi} = -\frac{\partial G_{\phi\phi}}{\partial Z} \qquad\qquad \mathcal{G}_{Zv} = \frac{1}{R}\frac{\partial}{\partial R}(RG_{\phi v}) - \frac{1}{R}\frac{\partial G_{Rv}}{\partial\phi}$$

To evaluate these explicitly, we also require the partial derivatives

$$\frac{\partial k}{\partial R} = k\left(\frac{1}{R} - \frac{2(R+R')}{\beta}\right) \qquad\qquad \frac{\partial k}{\partial Z} = -\frac{2k}{\beta}(Z-Z')$$

$$\frac{\partial\beta}{\partial R} = 2(R+R') \qquad\qquad \frac{\partial\beta}{\partial Z} = 2(Z-Z')$$

and also the derivative $\frac{d}{dk}\left(\hat{F}^{+}(j,k)\right)$. To do this last task we employ the following property of hypergeometric functions:

189

$$(\text{A\&S 15.2.5}) \quad \frac{d}{dk}\left(k^{c-a}\,(1-k)^{a+b-c}\,F(a,\,b;\,c;\,k)\right) = (c-a)\,k^{c-a-1}\,(1-k)^{a+b-c-1}\,F(a-1,\,b;\,c;\,k)$$

From this expression it follows

$$\frac{d}{dk}\left(\hat{F}^{+}(j,k)\right) = \frac{\hat{F}^{-}(j,k)}{2k(1-k)} - \frac{\hat{F}^{+}(j,k)}{2k} \quad \text{and} \quad \frac{dT_n^{+}}{dk} = \frac{T_n^{-}}{2k(1-k)} - \frac{T_n^{+}}{2k}$$

Substituting these various expressions into the partial derivatives of $\overline{\overline{G}}$ given above yields the components of $\overline{\overline{\mathscr{G}}}$; as before, the scale factors R'Q' are not included and no adjustment is made for the use of $\hat{K}$.

$$\mathscr{G}_{Rv,n}^{\;\;c\;s} = \frac{-\sin(n\phi)}{\cos(n\phi)}\,\frac{\mu_o}{\pi\beta^{3/2}}\left[\frac{n\beta\dot{Z}'}{RQ'}\,T_3^{+} + \frac{\dot{R}'(Z-Z')}{Q'(1-k)}\,T_2^{-}\right]$$

$$\mathscr{G}_{\phi v,n}^{\;\;c\;s} = \frac{-\cos(n\phi)}{-\sin(n\phi)}\,\frac{\mu_o}{\pi\beta^{3/2}}\left[\frac{\dot{R}'(Z-Z')}{Q'(1-k)}\,T_1^{+} - \frac{\dot{Z}'\beta}{2RQ'}\,T_3^{+} + \frac{\dot{Z}'}{Q'(1-k)}\left(\frac{\beta}{2R} - R - R'\right)\!T_3^{-}\right]$$

$$\mathscr{G}_{R\phi,n}^{\;\;c\;s} = \frac{\cos(n\phi)}{\sin(n\phi)}\,\frac{\mu_o}{\pi\beta^{3/2}}\,\frac{Z-Z'}{1-k}\,T_1^{-}$$

$$\mathscr{G}_{Zv,n}^{\;\;c\;s} = \frac{\sin(n\phi)}{-\cos(n\phi)}\,\frac{\mu_o\dot{R}'}{\pi Q'\beta^{3/2}}\left[\frac{\beta}{2R}\,T_2^{+} + \frac{n\beta}{R}\,T_1^{+} + \frac{1}{1-k}\left(\frac{\beta}{2R} - R - R'\right)\!T_2^{-}\right]$$

$$\mathscr{G}_{\phi\phi,n}^{\;\;c\;s} = \frac{\sin(n\phi)}{-\cos(n\phi)}\,\frac{\mu_o}{\pi\beta^{3/2}}\,\frac{Z-Z'}{1-k}\,T_2^{-}$$

$$\mathscr{G}_{Z\phi,n}^{\;\;c\;s} = \frac{\cos(n\phi)}{\sin(n\phi)}\,\frac{\mu_o}{\pi\beta^{3/2}}\left[\frac{\beta}{2R}\,T_1^{+} + \frac{n\beta}{R}\,T_2^{+} + \frac{1}{1-k}\left(\frac{\beta}{2R} - R - R'\right)\!T_1^{-}\right]$$

190

A.5 Conversion between Coordinate Frames

The conversion from the wall frame S and the plasma frame S' is specified, as described in Chapter 2, by two sets of parameters. The first is the displacement of the origin of S' relative to the origin of S in Cartesian coordinates, given by the vector $\vec{\Delta} = (\Delta_x, \Delta_y, \Delta_z)$. The second is the set of angles which give successive rotations of the coordinate planes of S' (see figure 2.3), given by $(\phi_{xz}, \phi_{yz}, \phi_{xy})$. To rotate a coordinate system in a particular plane is a simple matter; for example, for a single rotation of ϕ_{xz} in the X-Z plane we would get

$$
\begin{aligned}
\hat{e}_x' &= \cos(\phi_{xz})\,\hat{e}_x + \sin(\phi_{xz})\,\hat{e}_z \\
\hat{e}_y' &= \hat{e}_y \\
\hat{e}_z' &= -\sin(\phi_{xz})\,\hat{e}_x + \cos(\phi_{xz})\,\hat{e}_z
\end{aligned}
$$

Successive rotations look a bit messier but follow in an identical manner. Thus we build up a transformation matrix $\overline{\overline{M}}$ given by

$$
\overline{\overline{M}} = \begin{pmatrix}
\cos\phi_{xy}\cos\phi_{xz}-\sin\phi_{xz}\sin\phi_{yz}\sin\phi_{xy} & \cos\phi_{yz}\sin\phi_{xy} & \cos\phi_{xy}\sin\phi_{xz}+\sin\phi_{yz}\sin\phi_{xy}\cos\phi_{xz} \\
-\sin\phi_{xy}\cos\phi_{xz}-\sin\phi_{yz}\cos\phi_{xy}\sin\phi_{xz} & \cos\phi_{yz}\cos\phi_{xy} & \sin\phi_{yz}\cos\phi_{xy}\cos\phi_{xz}-\sin\phi_{xy}\sin\phi_{xz} \\
-\cos\phi_{yz}\sin\phi_{xz} & -\sin\phi_{yz} & \cos\phi_{xz}\cos\phi_{yz}
\end{pmatrix}
$$

A *position vector* $\vec{r}$ whose coordinates are (R,ϕ,Z) has Cartesian components $\vec{r} = R\cos\phi\hat{e}_x + R\sin\phi\hat{e}_y + Z\hat{e}_z$, and transforms by $\vec{r}' = \overline{\overline{M}}\cdot(\vec{r}-\vec{\Delta})$. The cylindrical coordinates in S' are determined by

$$
\begin{aligned}
\phi' &= \tan^{-1}(y'/x') \\
R' &= \sqrt{y'^2 + x'^2} \\
Z' &= Z'
\end{aligned}
$$

Starting in S' , the inverse transformation is $\vec{r} = \overline{\overline{M}}^{-1}\cdot\vec{r}' + \vec{\Delta}$. Components of a *vector field* $\vec{A}$ transform in almost the same manner, but without the displacement: $\vec{A}' = \overline{\overline{M}}\cdot\vec{A}$, and the inverse through $\vec{A} = \overline{\overline{M}}^{-1}\cdot\vec{A}'$. These manipulations must done on the Cartesian

components of $\overline{\mathbf{A}}$, which can be changed to and from the cylindrical or TNB components as was done in the first section.

Finally, in the sheet-current model it is necessary to know $\dot{R}$ in both frames; it is given by

$$\dot{R}' = \frac{x' \, xp' + y' \, yp'}{R'}$$

after x', y', and R' (or x, y, and R for the inverse) have been obtained as before. The quantities xp' and yp' are the transformed components of the vector $\dot{R}\cos\phi\hat{e}_x + \dot{R}\sin\phi\hat{e}_y + \dot{Z}\hat{e}_z$, which transforms like a vector field, *not* a position vector.

A.6 References

1. P. M. Morse, H. Feshbach. *Methods of Theoretical Physics*, Pts. I-II. McGraw-Hill, New York, 1953.

2. R. Courant, D. Hilbert. *Methods of Mathematical Physics*, Vols.I-II. Wiley Interscience, New York. Reprinted 1989.

3. M. Abramowitz, I. Stegun. *Handbook of Mathematical Functions*. Dover, New York. Ninth Edition, 1972.

4. I. S. Gradshteyn, I. M. Ryzhik. *Table of Integrals, Series, and Products*. Academic Press, San Diego. Fifth Edition, 1994.

Appendix B.

Notes on the Free-Boundary Problem

Appendix B. Notes on the Free-Boundary Problem.

The current implementation of the sheet current model sidesteps an entire area of MHD modeling, namely the solutions to the innocuous-looking equilibrium relation

$$(B.1) \quad \vec{J} \times \vec{B} = 0$$

The amount of detail contained in such a compact expression is surprising, and not immediately clear to those who are not expressly involved in studying it. This brief appendix is meant to provide an "outsider's view" of equation (B.1) in the context of free-boundary problems, and to investigate some interesting methods that were contemplated to incorporate numerical solutions into TSPS-3D. Since the penalty function was ultimately employed in the code instead of exact solutions to (B.1), the reader should be warned that this section is not intended to be a complete review of solving MHD free-boundary equilibria; the numerical method given here may not in fact be the correct choice, and should be taken with a grain of academic salt.

We will begin by defining what exactly we mean by the free-boundary problem, and how it comes about in (B.1), relative to a fixed-boundary problem. The next step is to develop an illustrative model, which will be used in the context of the sheet-current equations developed in the main thesis. The method of "parameter imbedding" will be introduced to find numerical solutions to the model; a simple example of how it works will also be given. Finally, we will show a sample free-boundary sheet-current problem and some numerical results.

B.1. What is the Free-Boundary Problem?

The perspective of the graduate student not intimately involved in MHD equilibria is that MHD equilibrium means the Grad-Shafranov equation and fixed-boundary equilibria. Most introductory MHD texts (in the author's opinion) gloss over the free-boundary problem and do not at all make it clear why some extra degrees of freedom seem to appear out of nowhere. However, the free-boundary problem is not any harder than the fixed-boundary one, or more incomplete; it is simply *different*. Let us examine the problem we would like to solve:

"How do I find a static equilibrium composed of a current-carrying plasma confined in externally applied magnetic fields?"

The answer to this question begins with additional questions. Are you interested in finding what type of plasma can be confined in an existing machine? Do you want to build a machine so that it can confine a particular plasma? Do you have an existing experiment and you want to reconstruct the plasmas it has already generated?

The answers to these questions determine whether it is the fixed- or free-boundary problem that you will need to solve. To briefly list the differences between the two:

In the fixed-boundary problem:

- The shape of the plasma is already known (determined, for example, by its desirable stability or transport characteristics).
- The toroidal plasma current is determined by the MHD momentum equation.
- The external magnetic field system is determined by matching the applied field to the plasma contribution by enforcing $\hat{n} \cdot \vec{B} \big|_a = 0$ at the plasma surface. The exact distribution and magnitude of coil currents which give the desired field must come from other constraints, usually those imposed by engineering necessity.

In the free-boundary problem:

- The shape of the plasma is *not* known. Usually you either want to reconstruct it from existing data, or simulate it (e.g. for halo-current or feedback studies) using the design of an existing machine. It comes from the MHD momentum equation.
- The toroidal plasma current is either specified from existing data, or found by coupling Ohm's Law to Maxwell's Equations.
- The external field system is specified, including the location of the coils and the coil currents.

195

The free-boundary case is actually the more intuitive one when compared to the simplest equilibrium problems we first learn to solve. Consider the spring-mass system shown in figure (B.1), consisting of a block with mass m connected to a linear spring, which is in turn fixed to a wall. The spring is assumed to follow Hooke's Law and to have a spring constant k. Suppose we pull on the block, applying an external force F_{ext}. As the spring is stretched some distance x from its neutral position, it imposes a restoring force, $F_{sp} = -kx$. If the system is in equilibrium, these forces balance and the equation of motion becomes

$$(B.2) \quad m\frac{d^2x}{dt^2} = -kx + F_{ext} = 0$$
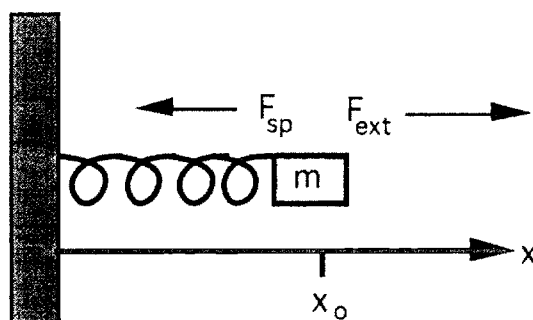
Figure B.1. A simple spring-mass system

We create a free-boundary problem of sorts by asking, "Given a certain spring and a certain external force, where does the block come to rest?" The answer is obviously

$$x = \frac{F_{ext}}{k}$$

We can create a fixed-boundary problem from the same setup by asking, "If I want the block to stay at location x given a certain external force, what kind of spring do I need?" Again the answer is trivial:

$$k = \frac{F_{ext}}{x}$$

There is no other characteristic which makes one type of problem fundamentally "deeper" than the other. In practice, one may be harder than the other if the known and unknown quantities are related in a complicated way; for example, if k in the above example varied non-linearly with position, e.g., $k(x) = k_0(x^3-x)$, then the fixed-boundary problem can still be solved trivially for k_0 but the free-boundary problem would no longer have a single unique solution for x.

Let us see now how this example translates to MHD equilibria.

B.2. Explicit Free-Boundary MHD Equations

We will assume without question that the plasma we seek to confine can be accurately modeled as an ideal MHD fluid. Our complete set of equations will consist of the ideal MHD momentum equation and Maxwell's Equations, with $\vec{J}$ coupled to $\vec{E}$ through Ohm's law with a constant conductivity. Since there are certainly more parameters in this case than in our previous simple example, we will keep a careful count of equations and unknowns to see that the free-boundary problem does not introduce any unusual information.

The ideal MHD momentum equation is

$$(B.3) \quad \rho \frac{D^2\vec{v}}{Dt^2} = \vec{J}(\vec{r}) \times \vec{B}(\vec{J},\vec{r}) - \vec{\nabla}P$$

where D/Dt is the convective derivative. Using the same $\tau_{char} \gg \tau_{MHD}$ ordering as in the main thesis, we drop the inertial term on the left; for a plasma which is cold or low-b, we can neglect the pressure gradient, leaving the familiar

$$(B.4) \quad \vec{J}(\vec{r}) \times \vec{B}(\vec{J},\vec{r}) = 0$$

where the various dependencies have been written explicitly. How many equations is this? Consider writing the velocity as $\vec{v} = \vec{v}_\perp + v_{//}\hat{e}_{//}$ where $\hat{e}_{//}$ is in the direction parallel to the magnetic field. Dotting (B.3) with this unit vector shows that $v_{//}$ is a free function

independent of time; for a static equilibrium, we choose it to be zero. Thus (B.4) is in fact coupled only to the two unknowns in $\vec{v}_\perp$ or, to draw analogy with (B.2), "$\vec{r}_\perp$".

Now we couple this system to Maxwell's equations. Beginning with

$$\text{(B.5)} \quad \vec{\nabla} \cdot \vec{B} = 0$$

$$\text{(B.6)} \quad \vec{\nabla} \times \vec{B} = \mu_0 \vec{J}$$

we see that by Helmholtz's Theorem we have uniquely determined the three unknowns in $\vec{B}$. Substituting Ohm's law into Faraday's Law and taking the MQS limit of charge conservation, we close the system with

$$\text{(B.7)} \quad \vec{\nabla} \cdot \vec{J} = 0$$

$$\text{(B.8)} \quad \vec{\nabla} \times \frac{\vec{J}}{\sigma} = -\frac{\partial \vec{B}}{\partial t}$$

and we have uniquely determined the three unknowns in $\vec{J}$.

The magnetic field can be broken into two parts, the known external fields and the unknown contribution from the plasma current: $\vec{B} = \vec{B}_{ext} + \vec{B}_{pl}$. Using Green's functions with the results in Appendix A, we can eliminate $\vec{B}_{pl}$ in terms of $\vec{J}$ once and for all:

$$\text{(B.9)} \quad \vec{B}_{pl} = \int \overline{\overline{G}} \cdot \vec{J}' \, d\vec{r}'$$

where the dependence of $\overline{\overline{G}}$ on the plasma shape is known.

For clarity, we restrict ourselves at this stage to toroidally axisymmetric equilibria. If we introduce the TNB coordinates used in Chapter 2 and Appendix A, we see that the two unknowns from the quantity "$\vec{r}_\perp$" become the familiar parameterizations $R(\rho,v,t)$ and $Z(\rho,v,t)$. The shape of the plasma surface therefore consists of two unknown functions of a single variable, $R(v,t)$ and $Z(v,t)$.

198

In general, solving this system will require discretizing $\vec{J}$ into some convenient representation; we will do so in the specific form of the sheet current model,

$$\vec{J}(\rho, v) = \sum_n \frac{\vec{K}_n(v)}{\Delta_n} \delta(\rho_n)$$

where Δ is the thickness of sheet n and δ the Dirac delta function. For simplicity, we will hereafter work in terms of only a single sheet carrying a current $\vec{K}$ and having a shape specified by $R(v,t)$ and $Z(v,t)$.

The two unique components of (B.4) are

(B.10) $K_v B_\phi - K_\phi B_v = 0$

(B.11) $B_\rho = 0$

The electrical part of the system simplifies further for the axisymmetric case; from (B.7) it follows that $RK_v(v,t)$ is a function of time only, defined to be $\hat{K}_v(t)$; from (B.5) and (B.11) RB_v is also a spatial constant; from (B.6) so is RB_ϕ. Enforcing (B.10) means that $RK_\phi(v,t)$ has the same property, and we accordingly define that combination to be $\hat{K}_\phi(t)$.

Re-defining $\vec{B}_{ext} = \frac{\hat{B}_\phi}{R} \hat{e}_\phi + \vec{B}_{ext}$ so that the new $\vec{B}_{ext}$ is purely poloidal, and substituting (B.9) and the above definitions into (B.10) and (B.11), we arrive at the two explicit equations for the two unknowns $R(v,t)$ and $Z(v,t)$:

(B.12) $\hat{e}_v(R,Z) \cdot \left[\int (G_{R\phi}\hat{e}_R + G_{Z\phi}\hat{e}_Z)\hat{K}'_\phi + \vec{B}_{ext} \right] \hat{K}_\phi - \hat{K}_v \left(\frac{\hat{B}_\phi}{R} + \frac{\mu_o \hat{K}_v}{2R} \right) = 0$

(B.13) $\hat{e}_\rho(R,Z) \cdot \left[\int (G_{R\phi}\hat{e}_R + G_{Z\phi}\hat{e}_Z)\hat{K}'_\phi + \vec{B}_{ext} \right] = 0$

where

$$\hat{e}_v = \frac{1}{Q}\left(\frac{dR}{dv}\hat{e}_R + \frac{dZ}{dv}\hat{e}_Z \right)$$

$$\hat{e}_\rho = \frac{1}{Q}\left(\frac{dR}{dv}\,\hat{e}_Z - \frac{dZ}{dv}\,\hat{e}_R\right)$$

$$Q \equiv \sqrt{\frac{dR^2}{dv} + \frac{dZ^2}{dv}}$$

$$G_{R\phi}(R, Z, R', Z') = \frac{\mu_o}{2\pi}\,\frac{Q'\,(Z-Z')}{RR'\,\sqrt{(R+R')^2+(Z-Z')^2}}\left(\frac{R'^2+R^2+(Z-Z')^2}{(R-R')^2+(Z-Z')^2}\,E(k) - K(k)\right)$$

$$G_{Z\phi}(R, Z, R', Z') = \frac{\mu_o}{2\pi}\,\frac{Q'}{R'\,\sqrt{(R+R')^2+(Z-Z')^2}}\left(K(k) + \frac{R'^2-R^2-(Z-Z')^2}{(R-R')^2+(Z-Z')^2}\,E(k)\right)$$

$$k \equiv \frac{4RR'}{(R+R')^2+(Z-Z')^2}$$

$K(k)$ and $E(k)$ are the complete elliptic integrals of the first and second kinds, respectively. It is clear that (B.12-13) are highly non-linear in the unknowns R and Z; the quantities $\hat{K}_\phi$ and $\hat{K}_v$ are treated as "known" in these equations, although in practice they must be determined by the coupling with (B.7-8).

Free-boundary numerical solvers commonly employ some kind of iterative technique to solve these equations, either by solving a linearized form at each iteration or by optimization methods. It is often less than obvious how these algorithms work; frequently, after a certain parameterization for $R(v)$ and $Z(v)$ is chosen, the number of equations no longer matches the number of unknowns, and additional constraints must be placed in the system, in a seemingly arbitrary fashion. Furthermore, for problems which are also time-dependent, it is undesirable to require an iterative scheme at each time-step in a simulation. In the halo-current problem, for example, coupling (B.12-13) to the linear-algebra system derived in Chapter 4 would require iterations over the multiple integrals, resulting in slow execution times.

As a possible cure for this problem, we suggest the method of *parameter imbedding*; a brief introduction to this method is given in the next section.

B.3. An Introduction to Parameter Imbedding

Parameter imbedding is not a new technique. It is found in various guises and under various names in the fields of nonlinear dynamics and mechanical engineering, to name just a few. We will consider here a brief description of how it works, as well as a simple example. In the next section we will employ it on a simple MHD free-boundary problem.

Parameter imbedding is based on two simple ideas. The first is that not all nonlinear problems are difficult to solve. There are plenty of nonlinear operators whose inverses are known; x^n, $\exp(x)$, $\cos(x)$ all have their counterparts x^n, $\ln(x)$, $\arccos(x)$, for example. The second idea is that there are systems of equations which can be solved quite easily numerically; linear algebra systems and systems of coupled ODEs can be handled by countless "black box" algorithms which are readily available. The idea behind parameter imbedding is to take a complicated nonlinear system, reduce it to a simpler one whose solution is known, and then evolve the system back to the original one by integrating a system of ODEs. The variable of integration is a parameter which is either natural to the problem (such as time, or a mechanical load in a structural equilibrium problem) or one which is introduced artificially, such as placing a coefficient in front of a particularly troublesome term in the original equations. The key is to choose the parameter so that, for *some* value, the resulting system of equations can easily be solved by standard methods.

Let us consider a simple example. Suppose we desire to find all the roots of a generic nth-order polynomial:

$$(B.14) \quad \sum_{i=0}^{n} a_i \, z^i = 0$$

This is a "hard" problem in the sense that the answer cannot be written down analytically, and numerical solutions require specialized (although, in this example, not difficult) techniques other than matrix operations or ODE integration.

Suppose instead the problem was to find all the roots of the single-term polynomial:

$$(B.15) \quad a_n z^n = C$$

This is a considerably easier problem, with the analytic solution

$$(B.16) \quad z_j = r^{1/n} \exp(i(\theta_0 + 2\pi(j-1))/n), \quad j = 1\ldots n, \quad r \exp(i\theta_0) \equiv C/a_n$$

Let us now introduce a parameter t into (B.14):

$$(B.17) \quad a_n z_j^n + t \sum_{i=1}^{n-1} a_i z_j^i = C, \quad C = -a_0$$

We see that for t=0, we have our easy problem of (B.15), whereas for t=1, we have the original problem of (B.14). If we take the derivative of (B.17) with respect to t, then by definition we get a linear equation for $\frac{dz_j}{dt}$:

$$(B.18) \quad \frac{dz_j}{dt} = \frac{-\sum_{i=1}^{n-1} a_i z_j^i}{na_n z_j^{n-1} + t \sum_{i=1}^{n-1} i\, a_i z_j^{i-1}}$$

Thus, to solve (B.14) we simply integrate (B.18) from t=0 to t=1 with a packaged ODE solver, starting with the initial condition (B.16) at t=0. The results of this process with a randomly chosen fifth-order polynomial are shown in figure (B.2). The solutions in the figure evolve from the Xs to the Os; note how they start as evenly spaced points on a circle in the complex plane, as they should.

The "collapse" of two of the roots to a single repeated root raises an interesting point, which is the fundamental caveat of employing parameter imbedding. It is quite possible that the complete properties of the "simple" operator you start with are still unknown; the existence of multiple solutions may not be immediately evident. Suppose, if one did not know that x^n has n solutions, the following imbedding method was employed:

$$t \sum_{i=2}^{n} a_i z_j^i + a_1 z = C$$

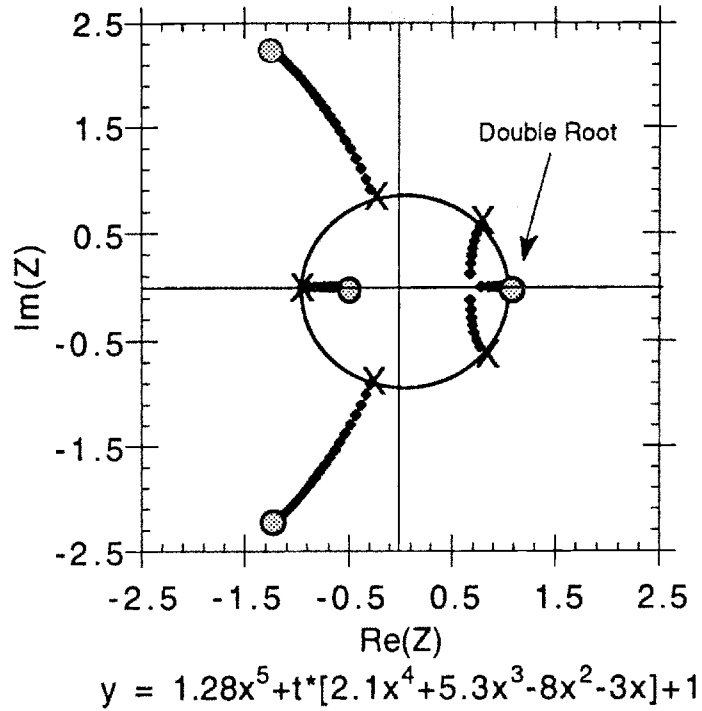$$y = 1.28x^5 + t^*[2.1x^4 + 5.3x^3 - 8x^2 - 3x] + 1$$

Figure B.2. Roots of a fifth-order polynomial evolving with imbedded parameter.

Clearly for t=0 there is only one value of z which solves the resulting linear equation; how can it evolve into n different solutions? The answer is that it cannot. At some point during the integration of the ODE, the path followed by the root would, in principle, undergo a bifurcation. In practice, the right hand side of the ODE develops a pole at the bifurcation point, and the integration breaks down. Thus parameter imbedding in this simple form is only useful if all branches of the solution can followed from the start (which obviously requires that their existence be known *a priori*), or if the evolution of a single solution is known to be smooth.

B.4. An MHD Free-Boundary Problem via Parameter Imbedding

We return now to our original task of solving the MHD free-boundary problem, as given by equations (B.12-13). Suppose we let our unknowns R and Z vary in "time" in response to varying $\vec{B}_{ext}$, $\hat{K}_\phi$, $\hat{K}_v$, or $\hat{B}_\phi$. Here, "time" can be true time dependence from a real PF coil scenario and resistive decay of the plasma currents, or it can be a purely artificial variation from some configuration where the equilibrium is known.

The first step is to differentiate equations (B.12-13), being sure to catch all of the implicit dependencies on time and the plasma shape; for example,

$$\frac{d\vec{B}_{ext}}{dt} = \frac{\partial \vec{B}_{ext}}{\partial t} + \frac{\partial \vec{B}_{ext}}{\partial R}\dot{R} + \frac{\partial \vec{B}_{ext}}{\partial Z}\dot{Z}$$

$$\frac{dG}{dt} = \frac{\partial G}{\partial R}\dot{R} + \frac{\partial G}{\partial Z}\dot{Z} + \frac{\partial G}{\partial R'}\dot{R}' + \frac{\partial G}{\partial Z'}\dot{Z}'$$

The result is two rather complicated-looking but nevertheless *linear* equations for $\dot{R}$ and $\dot{Z}$. They are spatial equations; t is just a parameter. Little illumination would be gained by writing these equations out in full, but they have the form of two coupled linear inhomogeneous Fredholm integral equations, of the second kind:

$$(B.19) \quad f_1\dot{R} + g_1\dot{Z} + \int G_{11}\dot{R}' + \int G_{12}\dot{Z}' = S_1$$

$$(B.20) \quad f_2\dot{R} + g_2\dot{Z} + \int G_{21}\dot{R}' + \int G_{22}\dot{Z}' = S_2$$

It should be noted that f, g, G, and S are highly nonlinear in v, R, Z, t, $\vec{B}_{ext}$, $\hat{K}_\phi$, etc.; however, we are focusing exclusively on $\dot{R}$ and $\dot{Z}$ at this point. Temporarily assuming all other quantities are known, we solve (B.19-20) for $\dot{R}$ and $\dot{Z}$ by any preferred method for linear equations, such as Fourier analysis:

$$\dot{R}(v,t) = \dot{R}_o(t) + \dot{R}_1(t)\cos(v) + \ldots$$

$$\dot{\vec{U}} \equiv \{\dot{R}_o, \ldots, \dot{R}_n, \dot{Z}_o, \ldots, \dot{Z}_n\}$$

After doing the Fourier integrals over (B.19-20), we have a numerically invertible matrix problem consisting of 2(n+1) equations and 2(n+1) unknowns:

$$\overline{\overline{M}}(t, R, Z, etc.) \cdot \dot{\vec{U}}(t) = \vec{S}(t, R, Z, etc.)$$

We can therefore solve the free-boundary problem by integrating a system of ODEs:

$$\text{(B.21)} \quad \frac{d\vec{U}}{dt} = \overline{\overline{M}}^{-1} \cdot \vec{S}(t, \vec{U}, \text{etc.}), \quad \vec{U} \equiv \{R_o, \ldots, R_n, Z_o, \ldots, Z_n\}$$

Once the system is in the form (B.21), t is the independent variable and v appears only as a parameter.

Of course, (B.21) requires initial conditions. These will depend on the application and type of parameter that was chosen. Three possibilities (there are no doubt many others) are

- A true time-dependent simulation through a series of quasi-equilibria (such as with "slow" disruptions) would use t as "real" time. The initial condition would be a real equilibrium reconstructed from a shot, or with parameters constructed from a specialized equilibrium code (possibly fixed-boundary if this is for machine design).

- Finding a single static free-boundary equilibrium by evolving the system from an analytically determined cylindrical system. Here the imbedded parameter would be the inverse aspect ratio, a/R; it would evolve from 0 to some desired value.

- Finding a single static equilibrium by evolving from a "fake" equilibrium. Suppose we have a desired PF scenario, and a plasma with a known total toroidal current and current profile. The poloidal current can be specified, or instead one can let its value float and fix the plasma minor radius (R_1 from the above notation) or some other aspect of the geometry, so long as the proper number of knowns and unknowns are swapped. The correct shape for this plasma is of course unknown, so one can start with any shape (circular, say). The parameter used here is completely artificial. Since the plasma shape was picked arbitrarily, it will not be force free; $\vec{J} \times \vec{B}$ will have some non-zero value. So the equation to be solved is

205

$$\vec{J}(t) \times \vec{B}(t) = (1 - t) \left(\vec{J}(t=0) \times \vec{B}(t=0) \right)$$

which gets integrated from t=0 to t=1.

Either of the last two procedures can be used to generate an initial condition for the first.

As an example of the third procedure, consider a single circular shell immersed in an external magnetic field consisting of a 5.3T toroidal field at a major radius of 1.5m (with 1/R dependence, of course), and a uniform vertical field of -0.15T. We will fix the total plasma current at I_p = 800kA; the plasma has an initial major radius of 1.5m and a minor radius of 0.15m. The initial current densities are found by

$$(B.22) \quad \hat{K}_\phi \int \frac{Q}{R} dv = I_p$$

$$(B.23) \quad \hat{K}_v = \frac{1}{C} \int \frac{\hat{K}_\phi B_v}{B_\phi} Q dv, \quad C = \int Q \, dv$$

As we evolve the parameter t from 0 to 1, we will fix I_p and let $\hat{K}_\phi$ be given by (B.22). To make sure our scenario corresponds to a plasma of an appropriate size once the equilibrium is found, we will fix the circumference C at its initial value, and in exchange for this degree of freedom we will let $\hat{K}_v$ float. Again, it should be emphasized that this is an "even trade" in the number of unknowns; if we were unconcerned about the plasma size we could certainly have held the poloidal current fixed instead.

Solving (B.19-20) with Fourier analysis, using modes up to n=2, and integrating the resulting ODEs gives the evolution of the shape of the plasma sheet shown in figure (B.3).

Clearly in this case, parameter imbedding was not imposed correctly; the solutions show a distinct "buckle" at early "times". In fact, over ninety-five percent of the CPU time for this particular simulation was spent jumping from the third mostly circular shell to the fourth decidedly non-circular one. However, the adaptive integration

scheme used did reduce the step size down to near round-off in this region, so that the complete run took several hours on a fast DEC Alpha workstation.
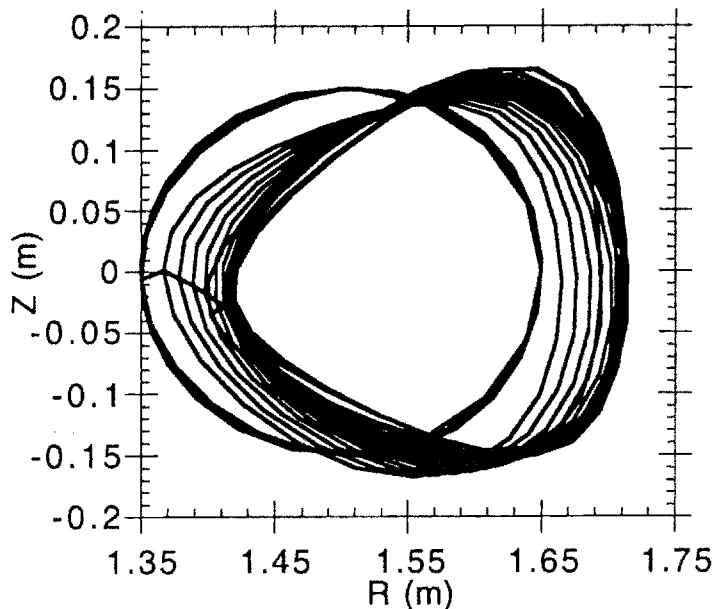

Figure B.3. Shell evolution over "time"

How well does the final shape represent a flux surface? A plot of this shell combined with a contour plot of the flux surfaces (see figure B.4) shows that the match is close but not perfect; near the corners of the triangular shape there is clearly penetration of the flux lines.

However, the shape is definitely reminiscent of the sum of a uniform vertical field and the circular flux contours generated by the initial plasma shape:
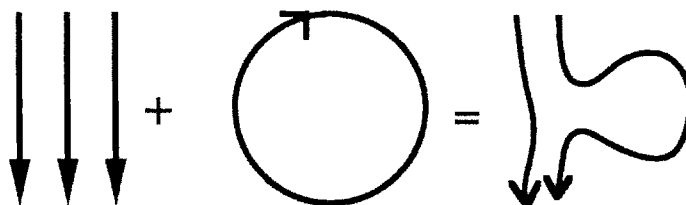
Some possible contributions to the problems are an insufficient number of Fourier modes, a poor choice of constraints (what would happen if the poloidal current were

held fixed, for example?), and the possibility that single current sheets cannot form a static equilibrium in a uniform vertical field.

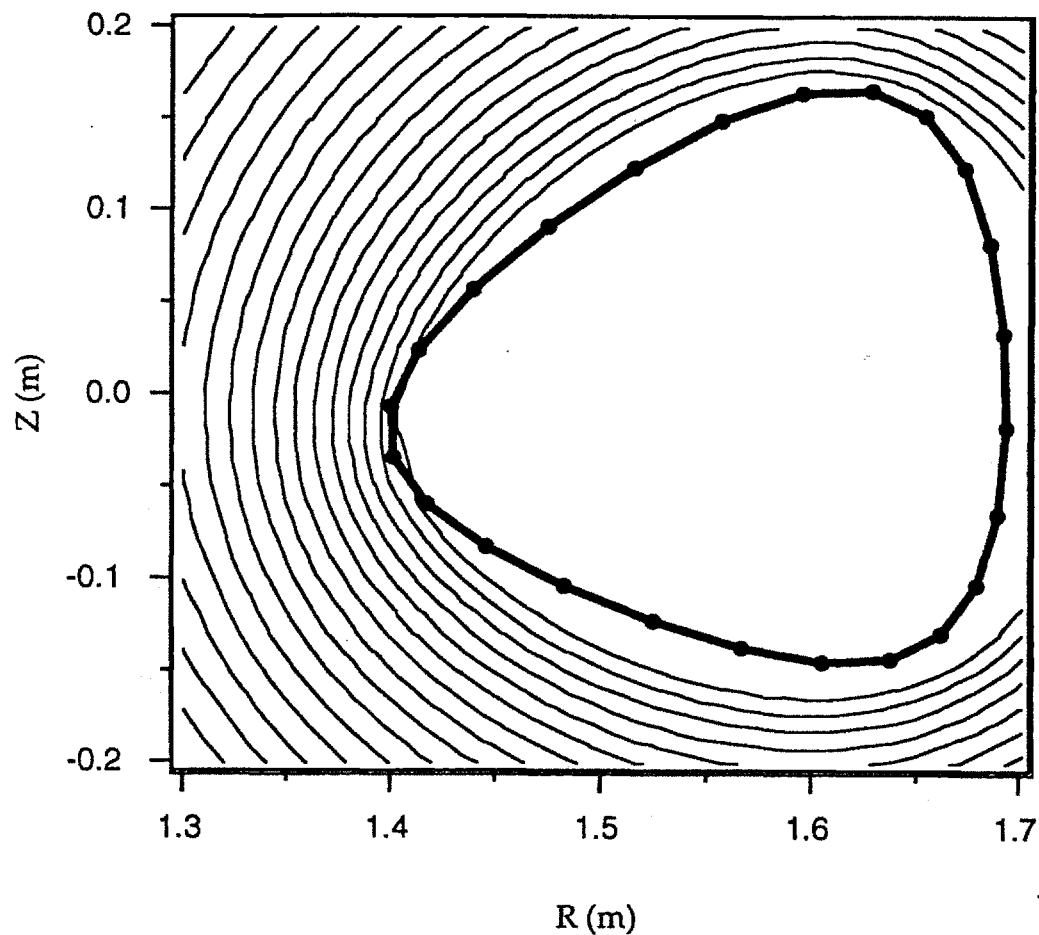## Final Shell w/ Flux Surfaces

Figure B.4. An overlay of flux contours over the final shell

In spite of the problems of this particular example, it is felt that parameter imbedding is still a viable method for solving free-boundary problems in the context of natural evolution through quasi-equilibria. It is unfortunate that the host of other complications involved in impacting a plasma against the wall to generate halo currents prevented these ideas from being implemented in this thesis.